Development of in-situ Rb-Sr isotope measurements by LA-ICP-MS and SIMS for small-scale dating of geological processes

Yujin Jegal

Université de Lorraine, Collegium Sciences et Technologies
Ecole Doctorale SIReNa – Sciences et Ingénierie des Ressources Naturelles

THÈSE

Présentée pour l'obtention du titre de
Docteur de l'Université de Lorraine
Mention « Géosciences »

Par

Yujin Jegal

Développement des mesures isotopiques in situ Rb-Sr par LA-ICP-MS et microsonde ionique pour la datation à petite échelle des processus géologiques

Development of in-situ Rb-Sr isotope measurements
by LA-ICP-MS and SIMS for small-scale dating of geological processes

---

Soutenance publique le 16 Décembre 2022

Membres du jury :

Directeurs de thèse :		
	Etienne Deloule	Directeur de recherche CNRS, CRPG, UL, France
	Julien Mercadier	Chargé de recherche CNRS, GeoRessources, UL, France
Président du jury :		
	Frank Vanhaecke	Professeur, Université de Gand, Belgique
Rapporteurs :		
	Emilie Janots	Maitresse de conférence, Université Grenoble Alpes, France
	Frank Vanhaecke	Professeur, Université de Gand, Belgique
Examinateurs :		
	Cécile Fabre	Maitresse de conférence, GeoRessources, UL, France
	Thomas Zack	Professeur, Université de Götheborg, Suède
Invités :		
	Chantal Peiffert	Ingénieur d'études, GeoRessources, UL, France
	Catherine Zimmermann	Ingénieur d'études, CRPG, UL, France
	Laurie Reisberg	Directrice de recherche CNRS, CRPG, UL, France

Faculté des Sciences et Technologies – Campus des Aiguillettes – 54506 Vandoeuvre-lès-Nancy Cedex

Résumé

Les nouvelles générations d'ablation laser couplée à un spectromètre de masse à plasma induit de type triple quadripolaire (LA-ICP-MS/MS) et de microsonde ionique Cameca IMS-1280-HR2 à haut pouvoir de résolution (~40 000) permettent théoriquement d'analyser rapidement, en contexte et à l'échelle de quelques dizaines de micromètres des rapports isotopiques dont la mesure in-situ souffrait jusqu'ici de problématiques d'interférences isobariques non déconvoluables avec des instrumentations classiques applicables à cette échelle. Cela ouvre des perspectives majeures en particulier pour le système isotopique Rubidium (Rb)-Strontium (Sr) qui est utilisé en géosciences pour dater et tracer les processus affectant les roches. Ce système isotopique est particulièrement adapté aux minéraux riches en Rb (par exemple, les micas et les feldspaths) qui sont complémentaires aux minéraux traditionnellement datés grâce aux systèmes isotopiques Uranium-Plomb par exemple (zircon ou monazite), qui peuvent être absents de certains contextes géologiques (hydrothermalisme par exemple) et/ou être affectés par une altération post-cristallisation qui affecte ce géochronomètre. Ces nouvelles perspectives d'application in-situ de systèmes isotopiques tel que Rb-Sr sont permises respectivement grâce à l'introduction d'un gaz de réaction via une cellule de réaction et à un haut pouvoir de résolution favorisé par une nouvelle configuration instrumentale.

Tester ces approches innovantes pour le système isotopique Rb-Sr est l'objectif principal de cette thèse de doctorat. Plusieurs limitations existent actuellement comme (i) la disponibilité de matériaux de référence (MRs) adaptés aux différentes matrices minérales à analyser pour la calibration des données in-situ des minéraux, (ii) la définition et la compréhension des potentiels effets de fractionnement et de matrice sur analyses isotopique Rb-Sr, et la proposition de méthodes de correction et (iii) l'application de ces développements à un cas d'étude spécifique pour lequel les contextes géologiques et géochronologiques sont connus, afin de définir l'applicabilité du système isotopique Rb-Sr à ces échelles et avec ces instrumentations. Par conséquent, l'objectif de cette thèse est (i) de caractériser et de certifier les valeurs isotopiques Rb-Sr de MRs représentatifs de familles minérales d'intérêt qui conviennent à la datation Rb-Sr in-situ, (ii) de démontrer la faisabilité et capacité des méthodes in-situ par LA-ICP-MS/MS et microsonde ionique pour mesurer les rapports isotopiques d'intérêt dans le cas

du système isotopique Rb-Sr et (iii) d'appliquer la datation Rb-Sr in-situ en utilisant les MRs caractérisés et les conditions analytiques optimisées du LA-ICP-MS/MS à des études de cas géologiques.

Des tests détaillés ont initialement été réalisés sur les deux instrumentations pour définir leurs capacités et les conditions analytiques optimales pour leur application pour le système isotopique Rb-Sr. Ces travaux ont démonté que le LA-ICP-MS/MS est l'instrumentation la plus adéquate pour l'application du système isotopique Rb-Sr in-situ, la microsonde ionique étant par contre la plus adaptée pour la mesure précise des rapports Sr/Sr pour des matrices pauvres en fer. 4 MRs du CRPG comprenant la phlogopite Mica-Mg, la biotite Mica-Fe, la glauconite GL-O et le feldspath potassique FK-N ont été caractérisés comme potentiels matériaux de référence pour les mesures Rb-Sr in-situ. Les rapports isotopiques $^{87}Rb/^{86}Sr$ et $^{87}Sr/^{86}Sr$ des 4 MRs ont été déterminés par dilution isotopique TIMS et MC-ICP-MS. Les résultats suggèrent que Mica-Mg est le plus approprié pour la datation des échantillons de mica, suivi par GL-O et FK-N pour la calibration des glauconites et feldspaths respectivement. Ensuite, les effets de matrice sur l'exactitude et la précision de la datation Rb-Sr ont été étudiés en utilisant différentes matrices et des échantillons de minéraux naturels. Le résultat montre une corrélation entre les compositions des éléments majeurs des matrices et la justesse des rapports $^{87}Rb/^{86}Sr$ mesurés par LA-ICP-MS/MS. Sur la base de ce résultat, une méthode de correction est proposée permettant d'analyser des minéraux sans RM de matrice identique. Enfin, la datation Rb-Sr in-situ par LA-ICP-MS/MS a été appliquée en couplage avec d'autres systèmes isotopiques pour contraindre les âges et la durée des processus magmatiques et hydrothermaux dans la zone de détachement de Quiberon, dans le massif Sud-Armoricain (France).

Mots-clés : datation Rb-Sr, LA-ICP-MS/MS, SIMS, matériaux de référence, in-situ, Zone de détachement Quiberon, interaction fluide-roche

Abstract

The new generation of laser ablation inductively coupled plasma mass spectrometry (LA-ICP-MS/MS) and Cameca IMS-1280-HR2 SIMS with high resolving power (ca. 40,000) theoretically allows to rapidly analyze on a scale of a few tens of micrometers of isotopic ratios whose in-situ measurement has so far suffered from isobaric interference problems that cannot be resolved with conventional instrumentation applicable to this scale. This opens major perspectives, particularly for the Rubidium (Rb)-Strontium (Sr) isotopic system, which has been used in geosciences to date and trace geological processes. This isotopic system is particularly suited to Rb-rich minerals (e.g., micas and feldspars) which are complementary to minerals traditionally dated using Uranium-Lead isotopic systems (e.g., zircon or monazite), which may be absent from certain geological contexts (e.g., hydrothermalism) and/or affected by post-crystallization alteration which affects this geochronometer. These new prospects for in-situ application of isotopic systems such as Rb-Sr are made possible, respectively, by the introduction of a reaction gas via a reaction cell and by a high-resolution power favored by a new instrumental configuration.

The main objective of this PhD thesis is to test these innovative approaches for the Rb-Sr isotopic system. Several limitations currently exist such as (i) the availability of reference materials (RMs) adapted to the different mineral matrices to be analyzed for the calibration of in-situ mineral data, (ii) the definition and understanding of potential fractionation and matrix effects on Rb-Sr isotopic analysis, and the proposal of correction methods and (iii) the application of these developments to a specific case study for which the geological and geochronological contexts are known, in order to define the applicability of the Rb-Sr isotopic system at these scales and with these instrumentations. Therefore, the objective of this thesis is (i) to characterize and propose the Rb-Sr isotopic values of representative RMs of mineral families of interest that are suitable for in-situ Rb-Sr dating, (ii) to demonstrate the feasibility and capability of in-situ LA-ICP-MS/MS and ion microprobe methods for measuring isotope ratios of interest in the case of the Rb-Sr isotopic system and (iii) to apply in-situ Rb-Sr dating using the characterized RMs and optimized analytical conditions of LA-ICP-MS/MS to geological case studies.

Detailed tests were initially carried out on both instruments to define their capabilities and the optimal analytical conditions for their application to the Rb-Sr isotopic system. This work demonstrated that the LA-ICP-MS/MS is the most suitable instrumentation for the application of the Rb-Sr isotopic system by in-situ method, on the other hand, SIMS is the most suitable for the precise measurement of Sr isotopic ratios for iron-poor matrices. Four CRPG RMs, including Mica-Mg phlogopite, Mica-Fe biotite, GL-O glauconite and FK-N potassium feldspar were characterized as potential reference materials for in-situ Rb-Sr measurements. The $^{87}Rb/^{86}Sr$ and $^{87}Sr/^{86}Sr$ isotopic ratios of the 4 RMs were determined by isotope dilution methods using TIMS and MC-ICP-MS. The results suggest that Mica-Mg is the most appropriate for dating mica samples, followed by GL-O and FK-N for the calibration of glauconites and feldspars respectively. Next, the matrix effects on the accuracy and precision of Rb-Sr dating were studied using different matrices and natural mineral samples. The result shows a correlation between the major element compositions of the matrices and the accuracy of $^{87}Rb/^{86}Sr$ ratios measured by LA-ICP-MS/MS. Based on this result, a correction method is proposed to analyze minerals without identical matrix RM. Finally, in-situ Rb-Sr dating by LA-ICP-MS/MS was applied in combination with other isotopic systems to constrain the ages and duration of magmatic and hydrothermal processes in the Quiberon detachment zone, in the South Armorican Massif (France).

Keywords: Rb-Sr dating, LA-ICP-MS/MS, SIMS, reference materials, in-situ, Quiberon detachment zone, fluid-rock interaction

Table of Contents

Remerciements

Je tiens à remercier mes encadrants de thèse qui m'ont accompagné et soutenu tout au long des quatre années de mon doctorat :

Etienne Deloule, mon directeur de thèse, qui a fait confiance en moi et m'a soutenu et qui a constamment transmis ses connaissances des systèmes isotopiques, de la spectrométrie de masse et de la géochimie, en répondant toujours à mes questions, et toujours disponible pour moi. Merci beaucoup de m'avoir fait découvrir la beauté de l'instrument SIMS à haute résolution et de m'avoir fait découvrir mon intérêt pour la méthode in-situ. J'ai la chance et la fierté d'avoir été parmi vos derniers thésards.

Julien Mercadier, mon co-directeur de thèse, qui s'est beaucoup investi dans ce projet et m'a soutenu en étant toujours à mon écoute et en se rendant disponible pour moi. Merci beaucoup de m'avoir fait découvrir la beauté du puissant instrument LA-ICP-MS en partageant vos expériences avec moi, pour que j'établisse la méthode Rb-Sr in-situ à GeoRessources.

A mes deux encadrants, je n'oublierai pas nos discussions lors de nos nombreuses réunions. Vous m'avez toujours donné de bonnes idées et m'avez aidé à développer mes compétences à penser comme un scientifique. Vous avez toujours été disponibles pour ce projet et pour moi, et je vous remercie pour le temps que vous m'avez consacré pendant trois ans et demi. Vous m'avez appris à être chef de projet et à penser et réagir de manière scientifique pour que je devienne une géochimiste. Vous m'avez également donné la force de résoudre les problèmes pour que j'obtienne de meilleurs résultats. A ne pas oublier, les moments agréables qu'on a passés pendant notre pause. Ils m'ont vraiment aidé à me détendre et décharger le stress. Ainsi, Vous n'êtes pas seulement mes directeurs de thèse mais aussi des mentors dans la vie. Cette thèse a pu être achevée grâce à tous vos soutiens.

Je tiens à exprimer mes sincères remerciements aux membres du jury pour l'évaluationde ce travail de thèse :

Madame Emilie Janots et Monsieur Frank Vanhaecke qui ont accepté de juger ce manuscrit de thèse en tant que rapporteurs. Je vous remercie pour les suggestions très intéressantes et pour le grand intérêt pour ce sujet.

Madame Cécile Fabre et Monsieur Thomas Zack qui ont accepté d'être les examinateurs de ce travail de thèse. Je vous remercie pour l'intérêt et les échanges que vous avez portés à mon travail.

Cette thèse est le fruit de nombreuses collaborations (Ghent University, Belgique ; University of Gothenburg, Suède ; Géosciences Rennes, France), et je tiens à remercier chaleureusement toutes les personnes qui ont participé à ce travail. Je remercie les collaborateurs pour les données, les échantillons, les nombreuses discussions et conseils, ainsi que pour la visite de terrain. Cest grâce à toutes ces personnes que ce travail de thèse a pu être réalisé.

CRPG Nancy : Un grand Merci à tout le personnel technique et administratif du labo pour leur gentillesse et leur professionnalisme pour m'avoir aidé à m'installer et à bien travailler au CRPG ainsi que dans le processus de la préparation de cette thèse.

Laurie Reisberg et Catherine Zimmermann, comme une troisième directrice de ma thèse, qui m'a soutenu et qui a toujours partagé ses connaissances de la géochimie analytique et des méthodes de dilution isotopique en répondant toujours à mes questions, et toujours disponible pour moi. C'est un honneur pour moi d'avoir pu travailler avec elle. Un grand merci pour m'avoir fait découvrir la beauté des instruments TIMS et MC-ICP-MS. Je peux rêver de devenir géochimiste isotopique grâce à mes expériences avec vous.

Je remercie également Damien Cividini, Christiane Parmentier et Aimeryc Schumacher pour l'aide et la contribution qu'ils ont apportées aux analyses MC-ICP-MS et aux expériences déroulées dans les salles blanches ainsi que pour les discussions fructueuses. Grâce à vous, j'ai pu approfondir mes connaissances sur le processus expérimental et analytique de la méthode de dilution isotopique.

Christophe Cloquet qui m'a transmis son savoir en répondant toujours à mes questions sur les informations géologiques et géochimiques des matériaux de référence (MR) du CRPG, la méthode analytique et le processus de certification du MR avec le traitement des données. Un grand merci pour votre disponibilité et la discussion que j'ai pu avoir avec vous.

Je remercie Delphine Yeghicheyan, Camille Kieffer, Elise Guerin et Helene Pastel Geny pour les analyses ICP-MS et les expériences de fusion alcaline en répondant à mes questions.

GeoRessources : Merci infiniment à tout le personnel technique et administratif du labo pour leur gentillesse et leur professionnalisme pour votre disponibilité et m'avoir aidé à bien m'installer à GeoRessources.

Je remercie Chantal Peiffert pour son temps, sa patience et ses nombreuses discussions sur le matériel d'analyse LA-ICP-MS et le traitement des données. Sans votre aide, je n'aurais pas pu mener à bien cette thèse.

Christophe Ballouard et Patrick Carr qui ont investi du temps à cette thèse, en étant toujours à mon écoute et en se rendant disponibles pour moi. Bien que vous ne soyez pas le superviseur officiel de ce travail, vous avez été comme mon troisième encadrant à GéoRessources en partageant avec moi vos connaissances, m'apprenant à étudier les échantillons géologiques de la préparation à l'analyse et l'interprétation des données.

Marie Gérardin qui partage avec moi ses connaissances en matière de K-Ar et d'analyse. Merci de ta disponibilité et de l'échange des idées sur les matériaux références et les échantillons afin de résoudre les problèmes survenus.

Un grand remerciement tout particulier à Emeline Moreira, qui a été ma collègue au bureau, ma meilleure amie, parfois comme une professeur qui partageait avec moi ses connaissances en chimie analytique et une compagnon à l'exploration du monde de LA-ICP-MS.

Enfin, je remercie mes amis à Nancy et mes familles et mes amis en Corée du Sud. Je remercie particulièrement à mon mari Yonghwi Kim, qui a toujours été à mes côtés et qui m'a soutenue et encouragée tout au long de cette thèse.

Résumé étendu

La nouvelle génération de spectrométrie de masse à plasma induit par couplage inductif de type triple quadripolaire couplé à un laser (LA-ICP-MS/MS) et la nouvelle génération de microsonde ionique IMS-1280-HR2 à haut pouvoir de résolution permettent d'analyser à haute précision, à l'échelle de quelques micromètres et directement sur les matrices d'intérêt les rapports isotopiques de nombreux systèmes isotopiques, que ce soit en géosciences, en biologie, en archéologie ou en recherche médicale par exemple. Du fait de leurs spécificités, ces instruments permettent de résoudre les interférences isobariques présentes pour de nombreux éléments et systèmes isotopiques et qui ont jusqu'ici limitées leur mesure par les méthodes in-situ. C'est par exemple le cas pour le système isotopique rubidium (Rb) – strontium (Sr), basé sur la décroissance radioactive de l'isotope ^{87}Rb en ^{87}Sr. Ce système isotopique est particulièrement utile dans de nombreux cas d'étude scientifique dans différents domaines, notamment en géosciences, car il permet une double approche de datation des processus par la méthode Rb-Sr, et de traçage isotopique via la mesure des rapports isotopiques du strontium. La mesure des rapports isotopiques du rubidium (^{85}Rb et ^{87}Rb) et du strontium (^{84}Sr, ^{86}Sr, ^{87}Sr et ^{88}Sr) est analytiquement complexe car elle nécessite en particulier la séparation de deux isotopes d'intérêt, ^{87}Rb et ^{87}Sr, pour laquelle un pouvoir de résolution en masse très important ($M/\Delta M > 280\ 000$) est indispensable. Ce pouvoir de résolution est non atteignable par les instrumentations in-situ et l'emploi du système isotopique Rb-Sr pour des phases où les deux éléments Rb et Sr sont présents nécessitait jusqu'à présent le passage par une mise en solution de l'échantillon puis une séparation par voie chimique des deux éléments avant la quantification de leurs teneurs et rapports isotopiques respectifs. Cette problématique peut être aujourd'hui résolue grâce à l'introduction d'un gaz de réaction via une cellule de réaction pour la technologie LA-ICP-MS/MS, et en partie par le haut pouvoir de résolution pour la microsonde ionique IMS-1280-HR2, respectivement. Cela ouvre des perspectives très larges quant à l'application du système isotopique Rb-Sr, ainsi que pour beaucoup d'autres systèmes isotopiques où les interférences isobariques sont significatives (K-Ca ou Re-Os par exemple).

En géosciences, les mesures isotopiques Rb-Sr des minéraux riches en Rb (par exemple, les micas et les feldspaths potassiques) par des méthodes in situ permettent théoriquement de dater ces minéraux dans de nombreux contextes géologiques où les minéraux (zircons ou

monazites pour citer les plus utilisés) datables par les systèmes isotopiques traditionnels (U-Pb par exemple) sont absents et/ou affectés par des processus secondaires qui perturbent les géochronomètres. Tester ces nouvelles approches et établir des protocoles pour l'utilisation in-situ du système isotopique Rb-Sr est l'objectif principal de cette thèse de doctorat. Plusieurs limites affectent actuellement son application in-situ comme (1) la disponibilité de matériaux de référence (MRs) adaptés, c'est-à-dire représentatifs des différentes phases minérales d'intérêt (les familles des micas et feldspaths notamment) et caractérisés isotopiquement pour la calibration des données in-situ de ces minéraux ; (ii) la détermination des effets de fractionnement et de matrice lors des analyses in-situ, et de méthodes pour leur possible correction; (iii) l'absence d'étude pionnière d'applicabilité de l'analyse isotopique Rb/Sr par microsonde ionique. Par conséquent, l'objectif de cette thèse est (i) de caractériser et de certifier les valeurs isotopiques Rb-Sr de matériaux de référence pour différentes familles de minéraux sur lesquelles la datation Rb-Sr in-situ pourrait être appliquée, (ii) de démontrer la faisabilité et la capacité des méthodes in-situ LA-ICP-MS/MS et microsonde ionique pour appliquer in situ le système isotopique Rb-Sr et (iii) d'appliquer la datation Rb-Sr in situ en utilisant les MRs caractérisés et les conditions analytiques optimisées à un cas d'étude géologique test.

Le premier chapitre de cette thèse présente dans une première partie les caractéristiques du couplage LA-ICP-MS/MS et les travaux jusqu'ici publiés sur cette instrumentation, en particulier pour l'analyse des rapports isotopiques Rb-Sr pour des applications en géosciences. Il présente ensuite les tests d'installation et de développement réalisés au laboratoire GeoRessources pour l'établissement de la méthode de datation isotopique Rb-Sr in-situ par LA-ICP-MS/MS. Les nombreux tests ayant servis à la définition des conditions opératoires et à leurs optimisations sont rapportés ici, ainsi que les résultats obtenus. Ce travail a permis d'aboutir à la définition des conditions opératoires optimales propres au couplage LA-ICP-MS/MS disponible au laboratoire GeoRessources. Les problématiques de réduction de données et de correction des biais analytiques et les solutions apportées sont présentées. Une seconde partie présente les tests et mesures faites par microsonde ionique au CRPG. Ces tests ont été réalisés sur un nombre restreint de matériaux, verres silicatés ou minéraux. Ils ont permis de démontrer que l'analyse des rapports isotopiques du strontium est fortement impactée par la composition chimique du matériau analysé, même en conditions de très haute résolution. En effet, les performances en résolution de masse de l'IMS 1280 HR2 permettent une résolution

de masse (M/ΔM) supérieur à 30 000, suffisante pour éliminer des interférences isobariques majeurs telles que celles liées au Calcium (Ca_2) ou au magnésium (Mg_2O_2), mais pas celles liées au Rb, ni celles liées au Fer (FeSi), ce qui n'était pas attendu. Ces interférences limitent considérablement en premier lieu les capacités d'utilisation de la microsonde ionique pour la mesure in-situ des rapports isotopiques du strontium, et donc l'applicabilité du système isotopique Rb-Sr. Il est proposé néanmoins de réaliser de plus amples tests pour valider les champs d'applicabilité de la microsonde ionique pour la mesure des rapports isotopiques du strontium dans les minéraux pour lesquels ces interférences ne sont pas présentes ou fortement réduites, puisque les précisions atteintes sont largement supérieures à celles permises par LA-ICP-MS/MS.

Le second chapitre porte sur la définition de matériaux de référence pour la calibration du couplage LA-ICP-MS/MS pour la datation Rb-Sr in-situ. Ainsi, 4 matériaux de référence (MRs) du Service d'Analyse des Roches et Minéraux (SARM, CRPG, Nancy) comprenant la phlogopite Mica-Mg, la biotite Mica-Fe, la glauconite GL-O et le feldspath potassique FK-N ont premièrement été caractérisés comme matériaux de référence potentiels pour les mesures Rb-Sr in situ. Les rapports isotopiques Rb/Sr et Sr des 4 MRs ont été déterminés par dilution isotopique TIMS et MC-ICP-MS. Les résultats suggèrent que Mica-Mg est le MR le plus approprié pour la datation des échantillons de micas, et que GL-O et FK-N pourraient être utilisés pour calibrer des analyses in-situ sur des glauconites et feldspaths respectivement, bien que présentant une homogénéité plus faible que celle définie pour Mica-Mg. Mica-Fe est trop hétérogène et présente des rapports isotopiques Rb/Sr trop radiogéniques pour être considéré comme utilisable comme matériau de référence. Ce travail a donc permis d'établir les premières valeurs de référence pour des matériaux de référence dédiés à la datation Rb-Sr in-situ en géosciences. Ce travail a fait l'objet un article publié dans la revue internationale Geostandards et Geoanalytical Research (Jegal et al., 2022).

Le troisième chapitre est centré sur les problématiques des effets de fractionnement et de matrice lors de l'utilisation des instrumentations LA-ICP-MS/MS pour la datation isotopique Rb-Sr in-situ. Ce chapitre se focalise sur la caractérisation de ces possibles effets, et de leurs impacts sur l'exactitude et la précision de la datation Rb-Sr in-situ. Pour cela, différents matériaux de référence de matrices variées (verre de silicate synthétique, verre géologique, poudre de minéraux) et des échantillons de minéraux naturels ont été analysés. Les résultats

obtenus montrent que des effets de fractionnement et de matrice existent et affectent en particulier les calculs des rapports isotopiques Rb/Sr, les rapports des différents isotopes du strontium n'étant pas affectés de façon sensible. Les tests réalisés montrent que ces effets de matrice ne sont principalement liés (1) ni à l'état de la matière (verre, poudre compactée de minéraux ou minéraux), (2) ni aux variations des teneurs en Rb, en Sr ou rapports isotopiques Rb-Sr, mais sont dus (3) aux différences de composition en éléments majeurs (Si et Al en particulier) entre les matériaux de référence testés. Une corrélation entre les compositions en éléments majeurs des matrices et la justesse du rapport $^{87}Rb/^{86}Sr$ mesuré par LA-ICP-MS/MS a pu être établie pour Al et Si. Sur la base de ces résultats, une nouvelle approche, utilisant un facteur de correction calculé en fonction des teneurs en Al et/ou Si des minéraux à dater et des matériaux de référence, est proposée et évaluée. Ce travail ouvre la perspective de dater in-situ de façon analytiquement optimale grâce au système isotopique Rb/Sr toutes phases minérales d'intérêt sans nécessairement disposer d'un matériau de référence de composition identique.

Le chapitre quatre présente l'application des développements pour l'instrumentation LA-ICP-MS/MS proposés dans les trois premiers chapitres sur un cas d'étude géologique adapté : la zone de détachement de Quiberon en Bretagne (France). Ce travail réalisé en collaboration avec des chercheurs de Geosciences Rennes visait à appliquer la datation Rb-Sr in-situ dans un contexte géologique connu et contraint temporellement via d'autres systèmes isotopiques (U-Pb, Ar-Ar) et plusieurs phases minérales (zircon, monazite, micas). Pour cela, des échantillons clés ont été prélevés sur le terrain et étudiés au laboratoire, puis ont été datés par la méthode U-Pb sur apatite par LA-ICP-MS à Geosciences Rennes et par la méthode Rb-Sr sur micas, apatite et /ou tourmaline par LA-ICP-MS/MS à GeoRessources à Nancy. Le but était de tester l'applicabilité de la datation Rb-Sr in-situ par LA-ICP-MS/MS pour contraindre les âges et la durée des processus de circulation des fluides dans la zone de détachement de Quiberon, connue comme une zone ou se sont succédées plusieurs épisodes magmatiques et hydrothermaux au cours de la période 320-270 Ma. Sur la base de l'analyse in situ des minéraux dans les leucogranites, les dykes et pegmatites associés, les résultats indiquent des âges Rb-Sr de 300,6 ± 3,8 Ma à 281,2 ± 3,8 Ma. Ces âges sont plus jeunes que les âges connus pour la mise en place de mise en place des leucogranites syn-tectoniques dans ce domaine, ainsi que les épisodes hydrothermaux principaux connus actifs entre 310 et 303 Ma et liés à la percolation d'eau météorique dans la zone du détachement. Les âges Rb-Sr sont par contre contemporains

des âges connus pour les minéralisations uranifères distribuées tout le long du cisaillement sud armoricain (270-300 Ma). Les âges Rb-Sr obtenus correspondent donc à un événement régional de circulation de fluide salée et calcique qui a affecté le Domaine Sud-Armoricain durant cette période et dont on sait qu'ils sont à l'origine de la formation de ces minéralisations. Ils montrent que cet évènement hydrothermal a aussi affecté la zone de cisaillement de Quiberon, sans pour autant avoir affecté l'ensemble des minéraux et des géochronomètres. Ce travail sur la zone du cisaillement sur armoricain démontre que l'utilisation de la datation Rb-Sr in-situ permet indubitablement de mieux comprendre l'évolution de zone géologique complexe et devrait être utilisé de façon généralisée en géosciences pour répondre aux problématiques de scientifiques.

Mots-clés : datation Rb-Sr, LA-ICP-MS/MS, SIMS, matériaux de référence, in-situ, Zone de détachement Quiberon, interaction fluide-roche

Introduction

Introduction

1. General context of the thesis

The subject of this PhD thesis is the development of the in-situ Rb-Sr isotopic analysis by LA-ICP-MS (Laser Ablation Inductively Coupled Plasma Mass Spectrometry) and SIMS (Secondary Ion Mass Spectrometry), and their applications to tracing and dating of geological processes at a scale of a few tens of micrometers. This PhD thesis is part of the scientific project LabEx Ressources21 (Laboratoire d'Excellence RESSOURCES21; https://ressources21.univ-lorraine.fr), funded by the French Government and held at Nancy since 2011. This global project at the scale of the Université de Lorraine aims to understand the cycle of strategic metals and resources for the 21st century. This multidisciplinary project, with a total budget of around 1.4 million euros for 14 years, is a unifying project for the scientific community of Nancy working on Earth sciences. Among the different research topics and objectives, one of the main priority research topics (PRT) is the development of tools for knowledge, and one of its priority research actions (PRA) is the development of analytical methods to constrain the life cycle of strategic metals. In this framework, a significant part of the budget has been dedicated to fund or co-fund new analytical tools at Nancy, and the SIMS and LA-ICP-MS analytical facilities at Centre de Recherches Pétrographiques et Géochimiques (CRPG) et GeoRessources have been reinforced with the arrival of new instrumental generations, like Agilent ICP-MS/MS 8900 and Cameca IMS-1280-HR2. To develop the use of these new instrumental capacities, Etienne Deloule (CRPG) and Julien Mercadier (GeoRessources) have proposed a subject for a PhD thesis dedicated to their application with a focus on the Rb-Sr isotopic system. This proposal was accepted, and a grant from the French Ministry of Higher Education and Research was attributed, with an analytical support from Labex Ressources21.

1.1. Importance of Rb-Sr isotopic system to study geological processes

Dating the processes affecting the Earth's crust since its formation 4.4 billion years ago (e.g., U-Pb age of Jack Hills zircons, Wilde et al., 2001) through the evolution of the Earth has been an objective for generations of scientists. Different long half-lives radioactive isotopes have been used for dating these processes, dependent on the type of investigated rock and mineral samples. The geological processes have been studied through traditional isotopic

systems such as uranium-lead (U-Pb). U-bearing accessory minerals occurred in a wide range of rocks in continental crusts such as zircon (Deloule et al., 2002; Kröner et al., 1996; Liu et al., 2012; Page, 1978), monazite (Liu et al., 2020; Parrish, 1990), rutile (Kooijman et al., 2010) or apatite (Kirkland et al., 2018). The ability to date the events using such minerals and isotopic systems is sometimes limited since they are not always present, and/or influenced by alteration that affect resetting or new growth of the minerals. Therefore, it is critical to date these rocks and/or processes by using mineral phases that are ubiquitous and could provide a record of processes which shape the zone of interest. Coupling different isotopic systems applied to different mineral phases allows to consider not only the ages but also the duration of the processes, which is of high interest in geosciences.

The rubidium-strontium (Rb-Sr) isotopic system is ideal as a geochronometer. Rubidium (Rb) is indeed abundant in many potassium (K)-bearing minerals (e.g., micas and K-feldspars) which are common in many geological contexts, so the Rb-strontium (Sr) β-decay scheme is used in geochronology studies of magmatic, metamorphic and/or hydrothermal rocks and minerals (e.g., Glodny et al., 2002; Page, 1978; Riley & Compston, 1962; Willigers et al., 2004; Nebel & Mezger 2008; Hurst et al., 1975; Yang & Zhou, 2001). Strontium (Sr) is an alkaline earth element, including three non-radiogenic isotopes of ^{84}Sr (0.56% abundance), ^{86}Sr (9.86% abundance) and ^{88}Sr (82.58% abundance) and one radiogenic isotope of ^{87}Sr (7.00% abundance). Rb is an alkali metal and has two naturally occurring isotopes of ^{85}Rb (72.17% abundance) and ^{87}Rb (27.83% abundance) (Rosman & Taylor, 1998), common in K-rich minerals such as potassium feldspar, muscovite, biotite and illite where Rb^+ substitutes for K^+. The abundance of ^{87}Sr varies over time due to the β-decay of ^{87}Rb with a half-life of 49.76 billion years (Nebel, 2014). The decay constant has been recently revised from $1.42 \pm 0.01 \times 10^{-11}$ a (Steiger & Jäger, 1977) to $1.3972 \pm 0.0045 \times 10^{-11}$ a (Villa et al., 2015). Via decay process, the radiogenic atoms such as Sr starts to be generated and to accumulate when a mineral system has reached its closure temperature (Dodson, 1973; Waight, 2013). This radioactive process records the age information of the minerals. It has been reported that closure temperature for the Rb-Sr system in white micas range from 500 ºC to >600 ºC (Glodny et al., 2002, 2008; Inger et al., 1996). Other micas such as biotite have lower closure temperature of ca. 300 ºC (Jenkin et al., 2001; Villa, 1998). At rapid cooling conditions, the age of these minerals can be considered as crystallization age corresponding to other isotopic

systems (Naumenko-Dèzes et al., 2018; Nebel et al., 2011; Waight, 2013) with higher closure temperature such as U-Pb zircon systems (ca. 900 ºC, Lee et al., 1997). On the other hand, in slow cooling system, the minerals with higher closure temperatures crystallize and become a closed system prior to minerals that have lower closure temperatures (Waight, 2013). In such conditions with different closure temperatures of minerals, minerals with lower closure temperature still experience the diffusive exchange of atoms until the temperature achieves at their closure temperature, recording a cooling history with a potential detectable discrepancy of ages from different isotopic systems (Bosse & Villa, 2019; Fletcher et al., 1997; Tichomirowa et al., 2019; Van Daele et al., 2020). Rb-Sr isotopic systems of these Rb-rich minerals also can be perturbed and reset by low-temperature events such as metasomatism or metamorphism that diffuse Rb and Sr in the system (Bosse & Villa, 2019).

In a closed system, the Rb-Sr isotopic compositions of mineral and rock samples can be expressed by the decay equation (Equation (1)) (Nebel, 2014):

$$(^{87}Sr/^{86}Sr)_t = (^{87}Sr/^{86}Sr)_{t0} + (^{87}Rb/^{86}Sr)_t \times (e^{\lambda t}-1) \quad (1)$$

where ^{87}Sr (t0) is the initial Sr amount at a time (t0) when mineral or rock forms, ^{87}Sr (t) is the Sr amount at present or specific time (t), ^{87}Rb is the amount of radiogenic Rb at present or specific time (t), e is Euler's number (≈ 2.71828), and λ is the decay constant for Rb-Sr system. As measuring precise amount of ^{87}Rb and ^{87}Sr isotopes in samples is challenging, the ^{87}Sr (t), ^{87}Sr (t0) and ^{87}Rb (t) are expressed relative to the abundance of stable isotope ^{86}Sr as the equation (1). Then, age (t) can be calculated by the equation (2):

$$t = 1/\lambda \times \ln [1+((^{87}Sr/^{86}Sr)_t - (^{87}Sr/^{86}Sr)_{t0}))/ (^{87}Rb/^{86}Sr)_t] \quad (2)$$

If $^{87}Rb/^{86}Sr$ and $^{87}Sr/^{86}Sr$ data are obtained from multiple cogenetic whole rock samples or mineral phases, the age (t) and Sr initial isotopic ratio at (t0) can be calculated by plotting on a Nicolaysen diagram as $^{87}Rb/^{86}Sr$ versus $^{87}Sr/^{86}Sr$ (Nicolaysen, 1961). Through the data on the plots, the best fit line (i.e., Isochron, York, 1968) can be calculated using a maximum likelihood linear regression (York et al., 2004) as a formula of $y = ax + b$, where y is $^{87}Sr/^{86}Sr$, x is $^{87}Rb/^{86}Sr$, b is the intercept at $x = 0$ that provides the initial $^{87}Sr/^{86}Sr$ ratio, and a is the slope of the isochron. Slope of this line is proportional to the age of the samples, then the age can be calculated using

the equation (3) (Waight, 2013):

$$t = 1/\lambda \times \ln (1 + Slope) \quad (3)$$

Based on the Rb-Sr decay system, Rb-Sr dating techniques have been established and widely used as a geochronological tool for many decades (Nebel, 2014). This dating method is useful particularly for rock samples that lack datable U-bearing minerals.

1.2. General problematic of the PhD thesis

The conventional Rb-Sr dating techniques such as thermal ionization mass spectrometry (TIMS) or multicollector inductively coupled plasma mass spectrometry (MC-ICP-MS) offer high precision and accuracy for Rb/Sr ratio measurements with ca. 0.1-0.2% precision (Nebel et al., 2005; Nebel & Mezger, 2006; Waight & Peate, 2002; Waight & Willigers, 2002; Willigers et al., 2004). One of major obstacles for these methods is the measurement of β decay product isotopes due to isobaric interferences of the daughter isotope on their related parent isotope. In the Rb-Sr decay system, the experimental and analytical processes of separation of ^{87}Sr from ^{87}Rb are required to avoid the isobaric spectral overlap at mass 87. Previous studies using conventional techniques (e.g., TIMS and MC-ICP-MS) have conducted to date pure minerals at small scale (more than 100 μm) by careful hand-picking (Chen et al., 1996; Eberlei et al., 2015; Li et al., 2005) and magnetic separation (Farina et al., 2014; Fletcher et al., 1997; Hefne et al., 2008). These methods based on physical separation and dissolution are encountered by limitations to date pure mineral separates and can be time-consuming and analytically challenging. Furthermore, some Rb and K-rich micas and feldspars are susceptible to alteration that perturbed their isotopic systems. This can lead to difficulties to avoid inclusions, alterations and/or age zonation in small and complex minerals such as hydrothermal vein fragments. In-situ methods able to measure isotopic ratios and applied at tens of micrometer scale directly on minerals like LA-ICP-MS and SIMS can be thus good alternative solutions together with the advantages of relatively short preparation time and minimal damage for samples. However, the limitation of Rb-Sr geochronology for conventional in-situ dating is the isobaric interference of ^{87}Sr and ^{87}Rb that cannot be solved by conventional in-situ mass spectrometry. In a conventional ICP-MS, chemical resolution to resolve isobaric interferences has been advanced

by flowing a reaction gas of CH_3F through a dynamic reaction cell to produce ^{87}Sr as $^{87}Sr^{19}F^+$ (m/z = 106) and leave ^{87}Rb as ^{87}Rb (m/z = 87) (Moens et al., 2001; Vanhaecke et al., 2003), but the precision is ca. 0.1-0.2% (Vanhaecke et al., 2003).

2. Objectives of the PhD thesis

To address the problematic, the new generation of ICP-MS where one reaction cell is situated between two quadrupoles (ICP-MS/MS) and SIMS with high resolving power (ca. 40,000) can cope with the isobaric interference by introducing reaction gases and high resolving power, respectively. The main objectives of this PhD thesis are the development of in-situ methods for Rb-Sr geochronology by LA-ICP-MS/MS and SIMS, and their application to date and trace geological processes in various contexts. This PhD thesis aims three main objectives:

(i) The first aim is to characterize and recommend the Rb-Sr isotopic values of reference materials (RMs) suitable for calibrating in-situ Rb-Sr dating of minerals. With recent advent of techniques such as LA-ICP-MS/MS, in-situ approaches have been increasingly used for Rb-Sr dating. Homogeneous and well characterized RMs with precise Rb-Sr isotopic values are however required for data calibration of Rb-Sr isotopic ratios in minerals of interest. Such matrix-matched RMs is currently lacking for the Rb-Sr isotopic dating of various families of minerals. Thus, characterization of Rb-rich mineral reference materials as calibration materials for in-situ Rb-Sr dating of natural minerals is a pre-requisite and is the first objective of this PhD thesis.

(ii) The second objective is the establishment of the analytical conditions for the in-situ Rb-Sr isotope measurements by LA-ICP-MS/MS and SIMS at GeoRessources and CRPG, respectively. Over the past few years, LA-ICP-MS/MS studies have demonstrated the feasibility of in-situ analyses to measure Rb-Sr isotopic system using LA-ICP-MS/MS. For SIMS methods, few reference works exist on in-situ Sr isotopic analysis, and none with the new SIMS with high resolving power. Referring to the previous works, both methods are sensitive to matrix effect and instrumental fractionation that affect analytical precision and accuracy during the measurement of the isotopic data. The optimization of operating conditions and tests for the capacities of both instruments available at Nancy will be conducted using the

characterized RMs.

(iii) The third aim is the test and application of in-situ Rb-Sr dating methods to a geological case study. The Quiberon detachment zone (Brittany, France), located in the Southern domain of the Variscan Armorican massif, French Variscan belt, was selected. This zone has been studied by previous works and known as a representative of the diversity of geological processes experiencing crustal thickening, high-pressure metamorphism deformation and fluid circulation in the Armorican Massif during the Carboniferous and Permian. This zone has been a natural laboratory for several years, with several works done to define the detailed geological context and evolution. Isotopic dating has been intensively applied to temporally constraint this geological evolution, using different isotopic systems (U-Pb, Ar-Ar) applied to different mineral phases (zircon, monazite, phosphates or micas for example). In this framework, the in-situ Rb-Sr dating of minerals from the Quiberon area by LA-ICP-MS/MS is conducted to test the applicability of this approach and to better understand the temporal relations during the development of such detachment zone affected by multiple geological events through time.

To approach and reach to these scientific goals, collaborations with Ghent University (Belgium) and the University of Gothenburg (Sweden) was conducted, the two institutions being reference laboratories for analytical chemistry and LA-ICP-MS analyses and pioneering for Rb-Sr isotopic analyses. The collaboration with these two institutions was however significantly affected by the Covid-19, and stays of several months initially planned in these two institutions to strengthen the present PhD research program and collaborative works were cancelled. For the application study to the Quiberon detachment, a field mission and collaborative work were done with Geosciences Rennes (Philippe Boulvais, Nathan Cogné and Yannick Branquet).

3. Organization of the thesis manuscript

This PhD thesis manuscript is structured in the following four main chapters, as shown in **Fig. 1**:

The first chapter is dedicated to methodological developments for the applicability of in-situ Rb-Sr dating of natural minerals. It comprises two parts, for LA-ICP-MS/MS and SIMS

respectively. Referred to the previous studies on in-situ Rb-Sr and Sr isotopic analyses by these two methods, the capability and feasibility of these two methods were tested, with optimization of operating conditions.

The second chapter is dedicated to development of reference materials for calibration of LA-ICP-MS/MS and SIMS for in-situ measurements of Rb-Sr isotopic ratios. In this chapter, four CRPG geostandards including phlogopite Mica-Mg, biotite Mica-Fe, glauconite GL-O and potash feldspar FK-N were characterized as potential reference materials for in situ Rb-Sr measurements by LA-ICP-MS/MS. Rb/Sr and Sr isotopic ratios of the four RMs were determined by isotope dilution TIMS and MC-ICP-MS. This work was published in *Geostandards and Geoanalytical Research (GGR)* in 2022 and titled 'Characterisation of Reference Materials for In Situ Rb-Sr Dating by LA-ICP-MS/MS' (Yujin Jegal, Catherine Zimmermann, Laurie Reisberg, Delphine Yeghicheyan, Christophe Cloquet, Chantal Peiffert, Marie Gerardin, Etienne Deloule, Julien Mercadier).

The third chapter is focused on the in-situ Rb-Sr dating method by LA-ICP-MS/MS using the various matrix samples with the characterized RMs and geological samples. The objective is to examine different types of RMs with various matrices in order to investigate matrix effects and their effects on the accuracy and precision for Rb/Sr isotopic values and age dating.

The fourth chapter focuses on one geological case study to test the applicability of in-situ Rb-Sr dating by LA-ICP-MS/MS to constrain polyphased geological zones, on the example of the Quiberon detachment zone (Brittany, France).

The PhD thesis manuscript ends up with **general conclusion** by integrating and summarizing the results and giving further perspectives for in-situ Rb-Sr dating methods by LA-ICP-MS/MS and SIMS for small-scale dating of geological processes.

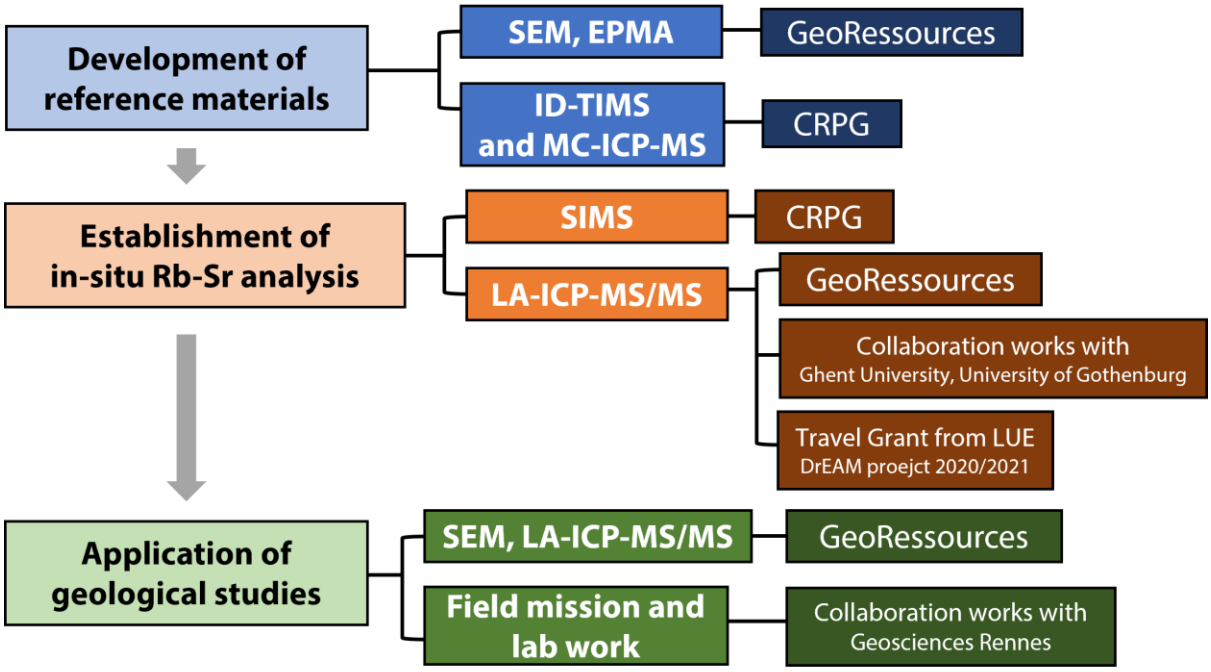

Fig. 1. Structure of the PhD thesis works.

References

Bosse, V., & Villa, I. M. (2019). Petrochronology and hygrochronology of tectono-metamorphic events. *Gondwana Research*, *71*, 76–90. https://doi.org/10.1016/j.gr.2018.12.014

Chen, C.-H., DePaolo, D. J., & Lan, C.-Y. (1996). RbSr microchrons in the Manaslu granite: implications for Himalayan thermochronology. *Earth and Planetary Science Letters*, *143*(1), 125–135. https://doi.org/10.1016/0012-821X(96)00122-7

Deloule, E., Alexandrov, P., Cheilletz, A., Laumonier, B., & Barbey, P. (2002). In-situ U–Pb zircon ages for Early Ordovician magmatism in the eastern Pyrenees, France: the Canigou orthogneisses. *International Journal of Earth Sciences*, *91*(3), 398–405. https://doi.org/10.1007/s00531-001-0232-0

Dodson, M. H. (1973). Closure temperature in cooling geochronological and petrological systems. *Contributions to Mineralogy and Petrology*, *40*(3), 259–274. https://doi.org/10.1007/BF00373790

Eberlei, T., Habler, G., Wegner, W., Schuster, R., Körner, W., Thöni, M., & Abart, R. (2015). Rb/Sr isotopic and compositional retentivity of muscovite during deformation. *Lithos*, *227*, 161–178. https://doi.org/10.1016/j.lithos.2015.04.007

Farina, F., Dini, A., Rocchi, S., & Stevens, G. (2014). Extreme mineral-scale Sr isotope heterogeneity in granites by disequilibrium melting of the crust. *Earth and Planetary Science Letters*, *399*, 103–115. https://doi.org/10.1016/j.epsl.2014.05.018

Fletcher, I. R., McNaughton, N. J., Pidgeon, R. T., & Rosman, K. J. R. (1997). Sequential closure of K–Ca and Rb–Sr isotopic systems in Archaean micas. *Chemical Geology*, *138*(3–4), 289–301. https://doi.org/10.1016/S0009-2541(97)00005-3

Glodny, J., Bingen, B., Austrheim, H., Molina, J. F., & Rusin, A. (2002). Precise eclogitization ages deduced from Rb/Sr mineral systematics: The Maksyutov complex, Southern Urals, Russia. *Geochimica et Cosmochimica Acta*, *66*(7), 1221–1235. https://doi.org/10.1016/S0016-7037(01)00842-0

Glodny, J., Kühn, A., & Austrheim, H. (2008). Diffusion versus recrystallization processes in Rb–Sr geochronology: Isotopic relics in eclogite facies rocks, Western Gneiss Region, Norway. *Geochimica et Cosmochimica Acta*, *72*(2), 506–525. https://doi.org/10.1016/j.gca.2007.10.021

Hefne, J., Aldayel, O., Amr, M. A., & Alharbi, O. (2008). Rb-Sr and U-Pb age dating of granite rocks by inductively coupled plasma mass spectrometry. *International Journal of Physical Sciences*, *3*(1), 28–37. https://doi.org/10.5897/IJPS.9000472

Hurst, R. W., Bridgwater, D., Collerson, K. D., and Wetherill, G. W., (1975). 3600 m.y. Rb–Sr ages from very early Archean gneisses from Saglek Bay, Labrador. *Earth and Planetary Science Letters*, 27(3), 393–403. https://doi.org/10.1016/0012-821X(75)90058-8

Inger, S., Ramsbotham, W., Cliff, R. A., & Rex, D. C. (1996). Metamorphic evolution of the Sesia-Lanzo Zone, Western Alps: time constraints from multi-system geochronology. *Contributions to Mineralogy and Petrology*, *126*(1–2), 152–168. https://doi.org/10.1007/s004100050241

Jenkin, G. R. T., Ellam, R. M., Rogers, G., & Stuart, F. M. (2001). An investigation of closure temperature of the biotite Rb-Sr system: The importance of cation exchange. *Geochimica et Cosmochimica Acta*, *65*(7), 1141–1160. https://doi.org/10.1016/S0016-7037(00)00560-3

Kirkland, C. L., Yakymchuk, C., Szilas, K., Evans, N., Hollis, J., McDonald, B., & Gardiner, N. J. (2018). Apatite: a U-Pb thermochronometer or geochronometer? *Lithos*, *318–319*, 143–157. https://doi.org/10.1016/j.lithos.2018.08.007

Kooijman, E., Mezger, K., & Berndt, J. (2010). Constraints on the U–Pb systematics of metamorphic rutile from in situ LA-ICP-MS analysis. *Earth and Planetary Science Letters*, *293*(3), 321–330. https://doi.org/10.1016/j.epsl.2010.02.047

Kröner, A., Braun, I., & Jaeckel, P. (1996). Zircon geochronology of anatectic melts and residues from a highgrade pelitic assemblage at Ihosy, southern Madagascar: evidence for Pan-African granulite metamorphism. *Geological Magazine*, *133*(3), 311–323.

LabEx RESSOURCES21 Strategic metals of the XXIst century, Auunal report 2020/2021 (ressources21.univ-lorraine.fr)

Lee, J. K. W., Williams, I. S., & Ellis, D. J. (1997). Pb, U and Th diffusion in natural zircon. *Nature*, *390*(6656), 159–162. https://doi.org/10.1038/36554

Li, Q., Chen, F., Wang, X., Li, X., & Li, C. (2005). Ultra-low procedural blank and the single-grain mica Rb-Sr isochron dating. *Chinese Science Bulletin*, *50*(24), 2861–2865. https://doi.org/10.1360/982005-984

Liu, L., Wang, C., Cao, Y.-T., Chen, D.-L., Kang, L., Yang, W.-Q., & Zhu, X.-H. (2012). Geochronology of multi-stage metamorphic events: Constraints on episodic zircon growth from the UHP eclogite in the South Altyn, NW China. *Lithos*, *136–139*, 10–26. https://doi.org/10.1016/j.lithos.2011.09.014

Liu, Y.-H., Lee, D.-C., You, C.-F., Takahata, N., Iizuka, Y., Sano, Y., & Zhou, C. (2020). In-situ U–Pb dating of monazite, xenotime, and zircon from the Lantian black shales: Time constraints on provenances, deposition and fluid flow events. *Precambrian Research*, *349*, 105528. https://doi.org/10.1016/j.precamres.2019.105528

Moens, L. J., Vanhaecke, F. F., Bandura, D. R., Baranov, V. I., & Tanner, S. D. (2001). Elimination of isobaric interferences in ICP-MS, using ion–molecule reaction chemistry: Rb/Sr age determination of magmatic rocks, a case study. *J. Anal. At. Spectrom.*, *16*(9), 991–994. https://doi.org/10.1039/B103707M

Naumenko-Dèzes, M. O., Nägler, T. F., Mezger, K., & Villa, I. M. (2018). Constraining the 40K decay constant with 87Rb-87Sr – 40K-40Ca chronometer intercomparison. *Geochimica et Cosmochimica Acta*, *220*, 235–247. https://doi.org/10.1016/j.gca.2017.09.041

Nebel, O., & Mezger, K. (2006). Reassessment of the NBS SRM-607 K-feldspar as a high precision Rb/Sr and Sr isotope reference. *Chemical Geology*, *233*(3–4), 337–345. https://doi.org/10.1016/j.chemgeo.2006.03.003

Nebel, O., Mezger, K., Scherer, E. E., & Münker, C. (2005). High precision determinations of 87Rb/85Rb in geologic materials by MC-ICP-MS. *International Journal of Mass Spectrometry*, *246*(1–3), 10–18. https://doi.org/10.1016/j.ijms.2005.08.003

Nebel, Oliver. (2014). Rb–Sr Dating. In W. J. Rink & J. Thompson (Eds.), *Encyclopedia of Scientific Dating Methods* (pp. 1–19). Dordrecht: Springer Netherlands. https://doi.org/10.1007/978-94-007-6326-5_116-1

Nebel, Oliver, Scherer, E. E., & Mezger, K. (2011a). Evaluation of the 87Rb decay constant by age comparison against the U–Pb system. *Earth and Planetary Science Letters*, *301*(1–2), 1–8. https://doi.org/10.1016/j.epsl.2010.11.004

Nebel, Oliver, Scherer, E. E., & Mezger, K. (2011b). Evaluation of the 87Rb decay constant by age comparison against the U–Pb system. *Earth and Planetary Science Letters*, *301*(1–2), 1–8. https://doi.org/10.1016/j.epsl.2010.11.004

Nicolaysen, L. O. (1961). GRAPHIC INTERPRETATION OF DISCORDANT AGE MEASUREMENTS ON METAMORPHIC ROCKS. *Annals of the New York Academy of Sciences*, *91*(2), 198–206. https://doi.org/10.1111/j.1749-6632.1961.tb35452.x

Page, R. W. (1978). Response of U-Pb Zircon and Rb-Sr total-rock and mineral systems to low-grade regional metamorphism in proterozoic igneous rocks, mount Isa, Australia. *Journal of the Geological Society of Australia*, *25*(3–4), 141–164. https://doi.org/10.1080/00167617808729025

Parrish, R. R. (1990). U–Pb dating of monazite and its application to geological problems. *Canadian Journal of Earth Sciences*, *27*(11), 1431–1450. https://doi.org/10.1139/e90-152

Riley, G. H., & Compston, W. (1962). Theoretical and technical aspects of Rb-Sr geochronology. *Geochimica et Cosmochimica Acta*, *26*(12), 1255–1281. https://doi.org/10.1016/0016-7037(62)90055-8

Rosman, K. J. R., & Taylor, P. D. P. (1998). Isotopic Compositions of the Elements 1997. *Journal of Physical and Chemical Reference Data*, *27*(6), 1275–1287. https://doi.org/10.1063/1.556031

Steiger, R. H., & Jäger, E. (1977). Subcommission on geochronology: Convention on the use of decay constants in geo- and cosmochronology. *Earth and Planetary Science Letters*, *36*(3), 359–362. https://doi.org/10.1016/0012-821X(77)90060-7

Stein, H. J. (2014). Dating and Tracing the History of Ore Formation. In *Treatise on Geochemistry* (pp. 87–118). Elsevier. https://doi.org/10.1016/B978-0-08-095975-7.01104-9

Tichomirowa, M., Käßner, A., Sperner, B., Lapp, M., Leonhardt, D., Linnemann, U., et al. (2019). Dating multiply overprinted granites: The effect of protracted magmatism and fluid flow on dating systems (zircon U-Pb: SHRIMP/SIMS, LA-ICP-MS, CA-ID-TIMS; and Rb–Sr, Ar–Ar) – Granites from the Western Erzgebirge (Bohemian Massif, Germany). *Chemical Geology*, *519*, 11–38. https://doi.org/10.1016/j.chemgeo.2019.04.024

Van Daele, J., Dewaele, S., Melcher, F., Onuk, P., Spikings, R., Glorie, S., et al. (2020). Geochronology of metamorphism, deformation and fluid circulation: A comparison between Rb-Sr and Ar-Ar phyllosilicate and U-Pb apatite systematics in the Karagwe-Ankole Belt (Central Africa). *Gondwana Research*, *83*, 279–297. https://doi.org/10.1016/j.gr.2020.02.008

Vanhaecke, F., De Wannemacker, G., Balcaen, L., & Moens, L. (2003). The use of dynamic reaction cell ICP mass spectrometry to facilitate Rb-Sr age determination. *Geological Society, London, Special Publications*, *220*(1), 173–181. https://doi.org/10.1144/GSL.SP.2003.220.01.10

Villa. (1998). Isotopic closure. *Terra Nova*, *10*(1), 42–47. https://doi.org/10.1046/j.1365-3121.1998.00156.x

Villa, I. M., De Bièvre, P., Holden, N. E., & Renne, P. R. (2015). IUPAC-IUGS recommendation on the half life of 87Rb. *Geochimica et Cosmochimica Acta*, *164*, 382–385. https://doi.org/10.1016/j.gca.2015.05.025

Waight, T. (2013). Rb–Sr Geochronology (Igneous Rocks). In W. J. Rink & J. Thompson (Eds.), *Encyclopedia of Scientific Dating Methods* (pp. 1–8). Dordrecht: Springer Netherlands. https://doi.org/10.1007/978-94-007-6326-5_105-1

Waight, T., Baker, J., & Willigers, B. (2002). Rb isotope dilution analyses by MC-ICPMS using Zr to correct for mass fractionation: towards improved Rb–Sr geochronology? *Chemical Geology*, *186*(1–2), 99–116. https://doi.org/10.1016/S0009-2541(01)00420-X

Waight, T., Baker, J., & Peate, D. (2002). Sr isotope ratio measurements by double-focusing MC-ICPMS: techniques, observations and pitfalls. *International Journal of Mass Spectrometry*, *221*(3), 229–244. https://doi.org/10.1016/S1387-3806(02)01016-3

Wilde, S. A., Valley, J. W., Peck, W. H., Graham, C. M. (2001) Evidence from detrital zircons for the existence of continental crust and oceans on the Earth 4.4 Gyr ago. *Nature, 409*, 175-178. https://doi.org/10.1038/35051550

Willigers, B. J. A., Mezger, K., & Baker, J. A. (2004). Development of high precision Rb–Sr phlogopite and biotite geochronology; an alternative to 40Ar/39Ar tri-octahedral mica dating. *Chemical Geology*, *213*(4), 339–358. https://doi.org/10.1016/j.chemgeo.2004.07.006

Yang, J. H., and Zhou, X. H., 2001. Rb–Sr, Sm–Nd, and Pb isotope systematics of pyrite: Implications for the age and genesis of lode gold deposits. Geology, 29(8), 711–714. https://doi.org/10.1130/0091-7613(2001)029<0711:RSSNAP>2.0.CO;2

York, D. (1968). Least squares fitting of a straight line with correlated errors. *Earth and Planetary Science Letters*, *5*, 320–324. https://doi.org/10.1016/S0012-821X(68)80059-7

York, D., Evensen, N. M., Martínez, M. L., & De Basabe Delgado, J. (2004). Unified equations for the slope, intercept, and standard errors of the best straight line. *American Journal of Physics*, *72*(3), 367–375. https://doi.org/10.1119/1.1632486

Chapter 1.
Methodological approach

Chapter 1. Methodological approach

1. Laser ablation-tandem ICP-MS (LA-ICP-MS/MS)

1.1. Principle of ICP-MS/MS

Existing quadrupole ICP-MS (ICP-QMS) instruments consists of single mass filter formed by the quadrupole, usually localized after a collision-reaction cell. In the reaction mode on ICP-QMS, masses are not selected before the cell and all ions can pass through the cell and partially react to form new reacted product ions. This process results in the measured signals contributed by many different ions and can gives error in variable samples (Agilent manual G3270-90106). The main difference of triple quadrupole ICP-MS (ICP-QQQ) from the ICP-QMS is that a tandem mass spectrometer (MS/MS) consists of double mass filters (first and second quadrupole) before and after the cell (the Octopole Reaction System; ORS), controlling directly isobaric overlaps and enable accurate isotopic analysis by using reaction processes in the cell as shown in **Fig. 2** (Agilent technical overview 5991-6942EN).

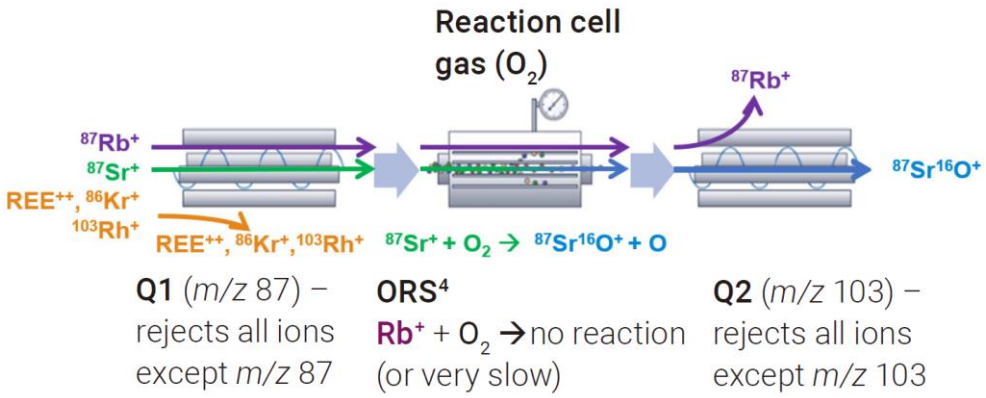

Fig. 2. A schematic image adapted from Liu et al. (2020), displaying the principle of operating the tandem mass spectrometry which consists of the two quadrupoles and the reaction cell that determine Sr isotopes as SrO^+ product by operating in mass-shift mode (MS/MS mode) with O_2 reaction gas.

The ICP-QQQ can be operated in either single quad (SQ) mode or MS/MS mode. When first quadrupole (Q1) and the ORS cell are used as an ion guide, the mode is called as 'SQ' mode, and second quadrupole (Q2) is used as a mass filter. In 'MS/MS' mode, ICP-QQQ allows

elimination of isobaric overlaps by controlling the quadrupoles set to targeted mass-to-charge (m/z) ratios and reaction cell filled with a gas (**Fig. 2**). After the formation and extraction of ions from samples in ICP and interface, Q1 can reject all ions at masses other than target analyte ion mass that enter the cell. Ions react with reaction gases by introducing the gases in the reaction cell and are neutralized or moved, then product ions are formed. Q2 selects the target analyte mass, allowing interference-free analyte ions passed to EM detector. EM detector then measures the ions that pass through Q2. In this reaction mode, the ICP-MS can be used as 'on-mass' or 'mass-shift' mode (Balcaen, 2015). 'On-mass mode' is used when reaction gas is more reactive with the interference than with the analyte, measuring target isotope at its original mass. When reaction gas is more reactive with the analyte than the interference, 'mass-shift mode' is used to measured target isotope as a reaction product ion. The use of an appropriate reaction gas enables the advanced method development for Rb-Sr and isotopic analyses.

1.2. Previous works of Rb-Sr isotope measurements by LA-ICP-MS/MS

In the recent years, Rb-Sr isotope measurements by LA-ICP-MS/MS have been performed to examine and demonstrate its potential and to optimize operating parameters for the in-situ Rb-Sr isotopic analysis of geological applications by using the different reaction gases such as O_2, CH_3F, N_2O or SF_6 (Bolea-Fernandez et al., 2016b; Gorojovsky & Alard, 2020; Hogmalm et al., 2017; Redaa et al., 2021; Zack & Hogmalm, 2016). The selection of a suitable reaction gas is important for method development. From the initial work by Moens et al. (2001), it has been demonstrated that Sr^+ selectively reacts with CH_3F by forming SrF^+ ions in an ICP-MS equipped with a dynamic reaction cell (DRC). Vanhaecke et al. (2003) also documented that chemical separation of ^{87}Rb from ^{87}Sr by using CH_3F gas to produce SrF^+ through a DRC with the precision of ca. 0.1-0.2%. The experimental study of Cheng et al. (2008) shows the efficiencies of reactions between Sr^+ and Rb^+ and different reaction gases, including O_2, CH_3F, CH_3Cl, N_2O and SF_6. From the experiments, Sr^+ is much more reactive than Rb^+ with CH_3F and SF_6 by F-atom transfer, CH_3Cl by Cl-atom transfer and N_2O and O_2 by O-atom transfer (Cheng et al., 2008). Largest difference in reactivity between Sr^+ and Rb^+ among these gases is shown when using SF_6 with a factor of 10^4, allowing to solve the isobaric interference between Rb^+ and Sr^+ (Cheng et al., 2008).

Bolea-Fernandez et al. (2016b) have established the in-situ Sr isotopic analysis by using a mixture of CH_3F and He (10% CH_3F in He) as a reaction gas for determining Sr isotope ratios of solid samples with high Rb/Sr ratios by using LA-ICP-MS/MS (193 nm Analyte G2 coupled with an Agilent 8800 ICP-QQQ). Via reaction with CH_3F/He mixture (0.90 mL min^{-1}) and wet plasma mode, it was possible to achieve signal stability (RSD) of $^{87}Sr/^{86}Sr$ isotope ratios for glass standard (NIST SRM 610) of ca. 0.05 %, better than that in dry plasma mode (ca. 0.17 RSD%). NIST 610 glass was used as an external standard for mass bias correction of $^{87}Sr/^{86}Sr$ isotope ratios. The results show that five replicate analyses of variable geological RMs (BHVO-2, NKT-1G, TB-1G, BCR-2G, T1-G, GSD-1G, ATHO-G) yield the precision (RSD) with the range of 0.024-0.054 % and the good agreement of $^{87}Sr/^{86}Sr$ ratios with the preferred values of the RMs. This study demonstrates that this approach could be applied to variable geological materials with a wide range of Rb/Sr ratios and Sr contents for Sr isotopic analyses.

Zack and Hogmalm (2016) have described a method for determination of Rb-Sr isotopic ratios of Rb-rich mineral phases (e.g., K-feldspar, biotite, muscovite) using LA-ICP-MS/MS (ESI 213NWR connected to an Agilent 8800 ICP-QQQ) in combination with O_2 as a reaction gas. The optimized conditions were found when using an 80 µm laser spot and 0.25 mL min^{-1} O_2 gas, enabling separation of Sr from Rb and application to in-situ Rb-Sr dating. Plagioclase and K-feldspar samples were calibrated externally using BCR-2G and NIST 610, respectively. Natural biotite from La Posta granodiorite was used as an external standard for biotite samples. The precision of $^{87}Rb/^{86}Sr$ and $^{87}Sr/^{86}Sr$ for geologic glass standards was obtained in ca. 0.5% and ca. 1%, respectively. Isochron ages of magmatic rocks were obtained with an accuracy of <1.5%.

A similar approach was performed for Rb-Sr and K-Ca isotope measurements for micas by Hogmalm et al. (2017) using LA-ICP-MS/MS (ESI 213NWR connected to an Agilent 8800 ICP-QQQ) with N_2O and SF_6 gases, compared with O_2 gas as reaction gases. They evaluated that N_2O and SF_6 react more with Sr with a higher sensitivity of ca. 10 times in N_2O and ca. 8 times in SF_6 compared to that of O_2, leading to smaller spot sizes of 50 µm when using N_2O and SF_6. Less sensitivity of SF_6 than N_2O with Sr was observed due to the higher collisional scattering of ions from dense and complex of SF_6. They also illustrated the potential of using SF_6 to measure K-Ca isotopes, showing that the use of SF_6 in combination with H_2 can overcome the interference of $^{40}Ca^+$ on $^{40}K^+$ and $^{40}Ar^+$ by analyzing $^{40}Ca^+$ in mass-shifted mode

to $^{40}Ca^{19}F^{+}$ without decreasing the reaction sensitivity.

The method of Hogmalm et al. (2017) using N_2O as a reaction gas has been applied to in-situ Rb-Sr geochronological analyses of K-bearing mica and/or feldspar minerals in various case studies: in hydrothermal vein and fault systems (Tillberg et al., 2017, 2020), in ore (Olierook et al., 2020; Şengün et al., 2019) and mineral deposits (Redaa et al., 2021), for kimberlites (Gorojovsky and Alard, 2020), and for the characterization of Archaean to Proterozoic crustal rocks (Li et al., 2020). In the study of Rösel and Zack (2022), various mica reference materials (RMs), used for Rb-Sr and Ar-Ar dating, have been analyzed for the validation of single-spot Rb-Sr ages for the RMs and examined as potential secondary standards by using the approach of Hogmalm et al. (2021). Gorojovsky and Alard (2020) and Redaa et al. (2021) have studied various analytical parameters of laser and ICP-MS to optimize the conditions for in-situ Rb-Sr dating using LA-ICP-MS/MS. They also investigated matrix effect of reference materials on the precision and accuracy of analyses. The details of their studies on matrix effects by Gorojovsky and Alard (2020) and Redaa et al. (2021) are described in **chapter 3**.

1.3. Analytical procedure and conditions for Rb-Sr isotope measurements by LA-ICP-MS/MS

Over the three years of this PhD thesis project, in-situ Rb-Sr isotopic analyses were performed by using the latest generation of ICP-QQQ (Agilent 8900 triple quadrupole ICP-MS) coupled with an ArF excimer laser ablation (LA) system at the GeoRessources laboratory (Vandoeuvre-lès-Nancy, France). Compared to the first generation ICP-QQQ (Agilent 8800), the Agilent 8900 offers increased sensitivity (10^9 cps/ppm), lower instrumental background (detectable detection limit of ca. 50 ppt for S and Si), and faster detector with minimum dwell times of 0.1 ms (Agilent technical overview 5991-6942EN, Agilent Handbook 5991-2802EN). An ESI 193 nm LA system (Elemental Scientific Lasers, US) with a two-volume 'TwoVol2' ablation chamber was used. This laser system provides high performances in accuracy and precision by using the wavelength of 193 nm with better coupling efficiency and translucent samples, very narrow particle size distribution and good fractionation effects among the existing laser types (Horn and Günther, 2003). In the main chamber (100 mm × 100 mm) of

the LA system, the ablation was performed in a helium (He) environment. Prior to the analysis, the glass RMs were prepared by embedding into epoxy resin, and mineral RMs such as Mica-Mg were prepared in the form of powder pressed tablet. In order to establish and optimize the analytical conditions of the ICP-MS/MS and LA systems for in-situ Rb-Sr isotope measurements, various operating parameters were tested as shown in **Fig. 3**.

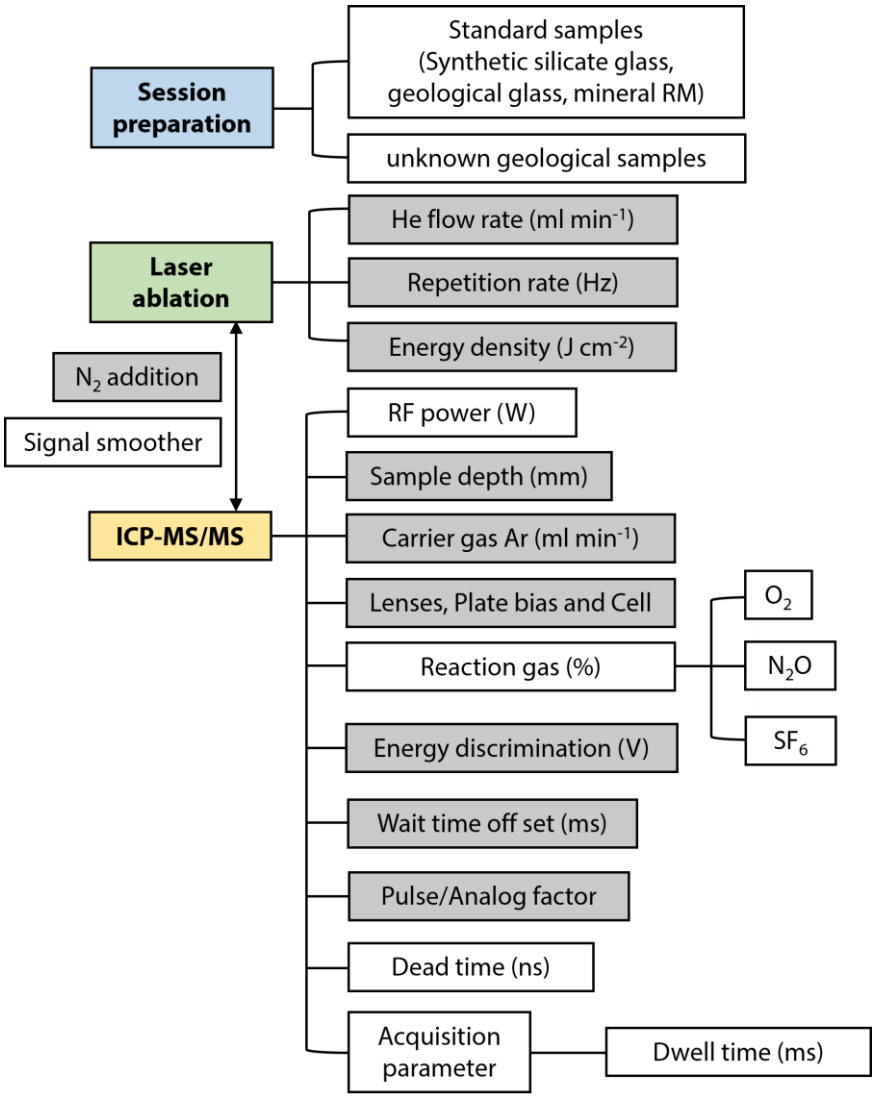

Fig. 3. A flow chart of operating conditions of LA-ICP-MS/MS to set up for in-situ Rb-Sr isotopic analysis during the analytical sessions at GeoRessources. The parameters monitored and optimized during the tuning process are indicated by grey color. The various parameters in white boxes were tested by analyzing the different types of the RMs.

Before the instrument was warm-up, argon (Ar) plasma gas and helium carrier gas were flowed at 1L min^{-1} for about 3 min and at 800 mL min^{-1} for about 5 min, respectively, for conditioning the gas valves. Then, the gases were set up to 0 mL min^{-1} prior to turning the plasma on. NIST 610 was used in line scan mode (60 μm) for tuning the instruments. In SQ mode, plasma conditions, the carrier gas flow rates and ion lens were optimized by monitoring oxide production rate ($^{232}Th^{16}O^{+}/^{232}Th^{+}$ ratios), $^{238}U/^{232}Th$ ratios and the sensitivities of ^{7}Li, ^{89}Y and ^{238}U on NIST 610. The conditions of the LA and the introduction system of ICP-MS/MS were optimized during this tuning process in SQ mode to obtain higher elemental sensitivity of ^{7}Li, ^{89}Y and ^{238}U with ^{85}Rb and ^{88}Sr and lower RSD (≤3-4 %), more efficient ionization ($^{238}U/^{232}Th \approx 0.98$-1.0) and lower oxide production ($^{232}Th^{16}O+/^{232}Th+$ ratios <0.2 %) (**Fig. 3**). Lenses and plate bias in ICP-MS/MS were tuned by ablating NIST 610 in line scan mode with the frequency of 5 Hz and ca. 6-7 J cm^{-2} of fluence.

Next, small amount of nitrogen (N_2) was added to the central gas flow of He and Ar between laser ablation cell and the introduction part of ICP-MS by using a Y-connector. Previous studies have added trace gases such as H_2 and N_2 for the enhancement of signal sensitivity (Guillong & Heinrich, 2007; Hu et al., 2008). In this experiment, we tested the effect of the addition of N_2 by increasing the flow rate from 0 mL min^{-1} to 5 mL min^{-1}. When N_2 was added at the rate of 4 mL min^{-1}, ^{7}Li signal intensity was increased by 30% with increasing Rb and Sr masses on NIST 610, which was maximum intensity with maintaining the RSD of ≤3-4%. The rate of 4 mL min^{-1} N_2 was maintained in all analyses in this study. Sample depth, the distance between the end of the load coil and the sampler orifice, was optimized decreasing by 1 from 7 mm to 4 mm. The sample depth of 4 mm produced highest signal intensity and reduced RSD (%) of signals among the variation during the tuning.

Before SQ mode was shifted to MS/MS mode while the instrument is in standby mode, N_2O reaction gas was flowed at the rate of 0.15-0.19 mL min^{-1} for overnight in the reaction cell. In MS/MS mode, the conditions of the LA system and the introduction system of ICP-MS/MS (plasma, torch positions) optimized in SQ mode were maintained in MS/MS mode. Lenses and cells in ICP-MS/MS were checked again in MS/MS mode by ablating NIST 610 in line scan mode (60 μm) to verify the signal sensitivity and stability. Then, the reaction gas flow rate was optimized in each session by increasing the flow rate, monitoring the intensities of reaction products in mass-shifted mode (e.g., 102 m/z for $^{86}Sr^{16}O^{+}$, 103 m/z for $^{87}Sr^{16}O^{+}$, 104

m/z for $^{88}Sr^{16}O^{+}$) and non-reacted product (85 m/z for ^{85}Rb) in MS/MS mode.

The variations in energy discrimination and wait time offset (WTO) were tested during the tuning in MS/MS mode. The energy discrimination (KED; kinetic energy discrimination) is used as a tuning parameter to discriminate the analyte ion of interest from interfering ions (Agilent Handbook 5991-2802EN). The WTO is an additional time on the settling time of the quadrupole that allows to stabilize the condition and compensate stagnant ions in the reaction cell (Bolea-Fernandez et al., 2016a). By varying the parameters of KED and WTO, no effect on the RSD (%) and signal sensitivity was observed in this work. Therefore, the values for KED (-7 V) and WTO (2 ms) initially set for the instrument were maintained. Finally, the influence of the variable parameters (**Fig. 3)** on the accuracy and precision of the Rb-Sr isotopic analyses was assessed and described in the following **section 1.4**.

1.4. Optimization of operating parameters

In order to optimize and set up the conditions for Rb-Sr isotopic analyses by LA-ICP-MS/MS and its application to geological samples, the effects of various operating parameters on precision and accuracy were tested and evaluated by using the different RMs such as NIST 610, BCR-2G or Mica-Mg (**Fig. 3**). For the evaluation, precision of RSD% or 2 RSD% was obtained on mean raw or measured ratios, defined as 100 × (SD or 2 SD of R_m)/R_m, where R_m is raw or measured Rb-Sr isotopic ratio. Accuracy was defined as the difference between the measured ratios (R_m) and the published values (R_p), expressed in % as ($R_m - R_p$)/R_p × 100. Here, 'raw' ratios indicate the ratios of Rb and SrO intensities after blank correction, and 'measured' ratios are calibrated data after calibration using a primary RM. These measurements were performed in different analytical sessions with different series of RMs and samples over three years. The analytical conditions of the LA systems (650-750 mL min^{-1} of He, 5 Hz of frequency, ca. 6-7 J cm^{-2} of fluence, 4 mL min^{-1} of additional N_2) were optimized as described in **Section 1.3**. The spot size of 50 μm was used for all LA-ICP-MS/MS analytical sessions in this work by following the methods of Hogmalm et al. (2017).

Reaction gases: The reactivity of the three gases O_2, N_2O and 10% SF_6 in He was tested to select the reaction gases for in-situ Rb-Sr isotopic analysis by LA-ICP-MS/MS. The reaction gas was introduced in the reaction cell via 4th inlet of ICP-MS/MS. The analysis of NIST 610

was performed for this test. The sensitivities of N_2O and SF_6 for Sr reaction products were higher ca. 20 and 10 times, respectively, compared to that of O_2 gas. It has been shown that N_2O gas yielded the highest reactivity among the gases in good agreement with the results from the previous studies by Hogmalm et al. (2017) and Cheng et al. (2008). Thus, N_2O gas was selected as a reaction gas in this study. The flow rate of N_2O gas was optimized daily during the tuning process in MS/MS mode in all analytical sessions.

RF (radio frequency) power: One of the factors that affects the instrumental mass bias is RF power related to the plasma temperature (Pearson et al., 2008). In the study of Pearson et al. (2008), they optimized the RF power by monitoring signal intensity to provide the maximum intensity. It has been documented that hot plasma enhances ionization efficiency and buffer the difference in particle size distribution. Hot plasma conditions of 1350 W, 1450 W and 1550 W were tested on the precision and accuracy of the mean raw $^{87}Sr/^{86}Sr$ and $^{87}Rb/^{86}Sr$ ratios of NIST 610, BCR-2G and Mica-Mg. The results under different RF power conditions show that their precision and accuracy were improved at RF power of 1550 W. This value of 1550 W was set at a fixed value for the LA-ICP-MS/MS measurements in **Chapter 3** and **4**.

Signal smoothing devices: Two types of signal smoothing devices, including 'wire' and 'squid' smoothers, were evaluated in order to enhance signal stability as reported by previous LA-ICP-MS studies of Hu et al. (2012) and Muller et al. (2009). It has been documented that these devices can provide smoother signals and better signal stability and reduce elemental fractionation (Hu et al., 2012; Müller et al., 2009). The 'wire' smoothing device was designed by following the procedure described by Hu et al. (2012) and Rösel and Zack (2022). The 'squid' smoother was produced from Teledyne CETAC technologies. To assess the effects of using different types of the smoothing devices, the internal precisions (2 RSE%) of the signals of SrO^+ and Rb^+ and the raw ratios of $^{87}Rb/^{86}Sr$ and $^{87}Sr/^{86}Sr$ ratios in the identical integration time were assessed. We observed similar internal precisions (2 RSE%) of the signals and ratios for both NIST 610 and BCR-2G between the analyses using the two devices, displaying 2 RSE% as ≤4% for SrO^+ and Rb^+ and ≤1% for raw $^{87}Sr/^{86}Sr$ ratios and ≤1.5% for raw $^{87}Rb/^{86}Sr$ ratios. External precisions (2 RSD%) of the mean ratios (n = 5) are similar for all RMs investigated (NIST 610, BCR-2G, Mica-Mg, FK-N) between the two methods with a better precision for raw mean $^{87}Sr/^{86}Sr$ ratios of NIST 610 by a factor of 2.2 when using a wire smoothing device. Therefore, we adapted the wire smoother for LA-ICP-MS/MS measurements in **chapter 3** and

4.

Detector dead time: Detector dead time is defined as '*the time for which the ion counting system is unable to count incoming ions after the impact of a previous ion, which is a feature of both the detector and ion counting electronics*' (Nelms et al., 2001). The importance of detector deadtime determination has been reported for precise isotope measurements by previous ICP-MS studies (Nelms et al., 2001; Vanhaecke et al., 1998). According to Nelms et al. (2001), the inconsistency in isotopic abundance ratios that are independent of mass discrimination effects can be caused by the correction of detector dead time, which depends on the pulse amplifiers in ICP-MS instruments. It has been indicated that the detector dead time is required to be corrected prior to mass discrimination correction in order to acquire accurate isotopic ratio. From the LA-ICP-MS/MS previous studies for Sr isotopic analysis (Bolea-Fernandez, 2016a; Bolea-Fernandez et al., 2016b), the detector dead time was determined experimentally by following the method of Russ (1989).

For the correction of the dead time for our ICP-MS/MS instrument, variation of dead time was tested from 10 to 60 ns by analyzing Sr isotopic ratios of NIST 610, BCR-2G and Mica-Mg with a spot size of 50, 100 and 120 µm. Prior to varying the dead time, P/A factor calibration was conducted in SQ mode by ablating NIST 610 for a wide range of masses and palladium metal for 102, 104, 105, 106 masses in line scan mode (60 µm) for each dead time. The raw ratios of $^{84}Sr/^{86}Sr$ and $^{88}Sr/^{86}Sr$ of the RMs were plotted as a function of dead time in **Fig. 4a** and **4b**. The different lines in **Fig. 4a** and **4b** correspond to the raw ratios of each RM with variable spot sizes. This method was followed by the method (1) reported in Nelms et al. (2001) and based on the method of Russ (1989). The method (1) from Nelms et al. (2001) determined the optimum deadtime by plotting the isotope ratios at different concentrations versus different dead time values and find the point at which the lines of different concentrations intercept each other. Our results show that the interception points of the different lines corresponding to various spot sizes are displayed in the wide range of dead time, and these points are variable dependent on the RMs and different stable isotopic ratios of $^{84}Sr/^{86}Sr$ and $^{88}Sr/^{86}Sr$ (**Fig. 4a** and **4b**). More intercepting points for the RMs were observed in the range of 30-40 ns. The range of dead time from 34 ns to 40 ns were tested for the accuracy of the data compared to natural abundance of $^{88}Sr/^{86}Sr$ for NIST 610 (**Fig. 4c**). The results show that better accuracy of raw $^{88}Sr/^{86}Sr$ for NIST 610 was yielded at dead time ranging from 34 ns to 35.5 ns. Therefore, the

deadtime of 35 ns was set as an optimum deadtime for the Rb-Sr isotopic measurements in **section 1.5**, **chapter 3** and **4**.

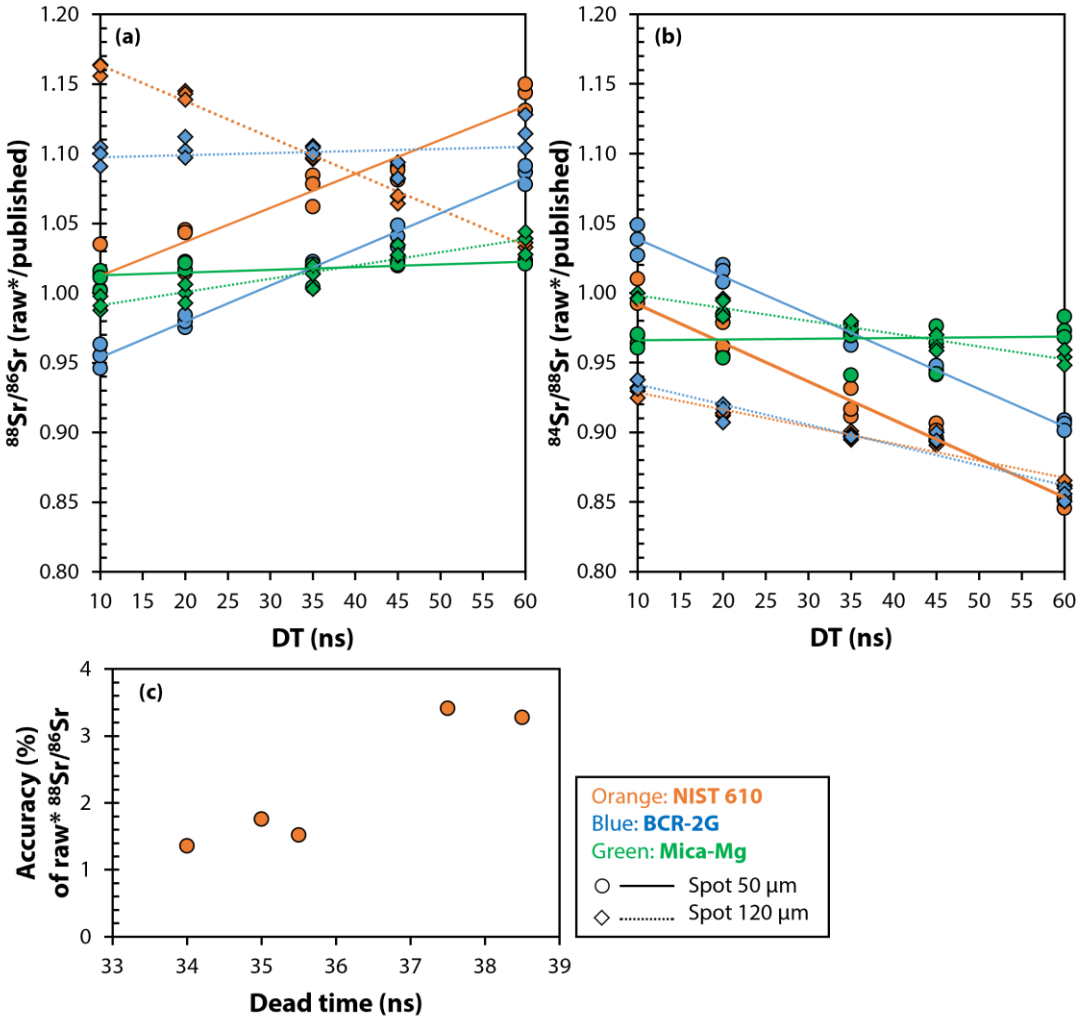

Fig. 4. (a) $^{88}Sr/^{86}Sr$ and **(b)** $^{84}Sr/^{86}Sr$ ratios (raw/published values) of NIST 610, BCR-2G and Mica-Mg and **(c)** accuracy (%) of raw $^{88}Sr/^{86}Sr$ of NIST 610 versus dead time. *Raw ratios indicate the ratios of SrO intensities after blank correction.

Dwell times: Previous LA-ICP-MS/MS studies of Rb-Sr isotopic analysis (Gorojovsky & Alard, 2020) and Sr isotopic analysis (Bolea-Fernandez et al., 2016b) have been reported that the precision can be enhanced by optimizing dwell times. They showed that better counting statistics with lower RSD (%) could be obtained by increasing in dwell time. In this thesis work, dwell times of 50 and 120 ms were compared while measuring NIST 610, BCR-2G and Mica-

Mg. The RSD (%) of NIST 610 with the dwell time of 120 ms are 0.74% for raw $^{87}Rb/^{86}Sr$ and 0.49% for raw $^{87}Sr/^{86}Sr$ (**Fig. 5**). The RSD (%) obtained in this study is as good as those reported in the previous studies (Hogmalm et al., 2017). Therefore, optimum parameter for dwell time in this study was set with a 120 ms dwell time.

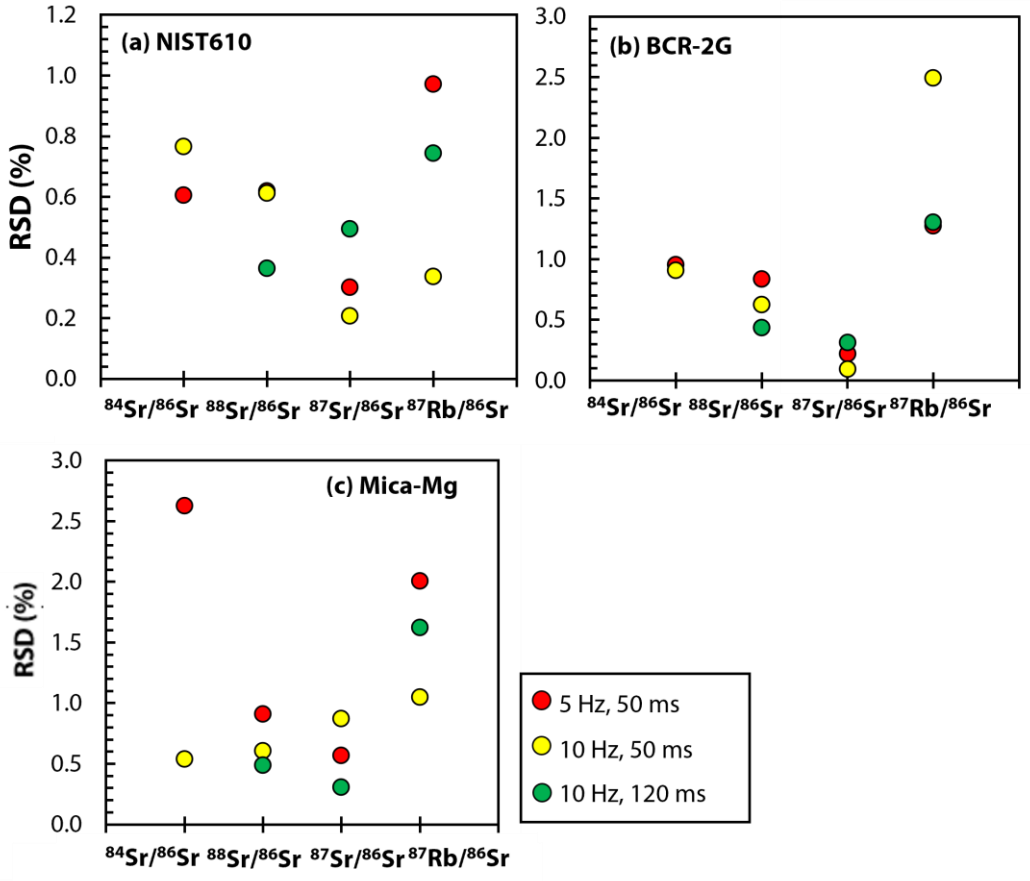

Fig. 5. RSD (%) of raw Sr isotopic ratios and $^{87}Rb/^{86}Sr$ ratios as a function of the dwell time.

In the **section 1.4**, the analyses were performed to optimize analytical conditions and parameters for in-situ Rb-Sr isotope measurement by LA-ICP-MS/MS. **Table 1** summarizes the operating conditions optimized in this study and references that addressed the importance of each parameter or adjusted those parameters in their studies. The LA-ICP-MS/MS measurements described in **chapter 3** and **4** were performed using the optimized conditions in this **chapter 1**. Some parameters such as the flow rates of Ar plasma gas and N_2O reaction gas and the parameters of lenses and cell in ICP-MS/MS were needed to be monitored and

optimized daily or for each analytical session. The details of operating parameters and analytical procedures of the LA-ICP-MS/MS analyses for in-situ Rb-Sr isotope measurements of samples and RMs are described in **chapter 3** and **4**.

►

Table 1. Operating conditions optimized in this work and list of previous studies that explained each parameter and/or used or tested those parameters.

Parameters		Description	Reference
LA system	Ablation conditions	• Spot sizes are adjusted considering the size of targeted minerals and sensitivity of signals. The size of spots for samples and primary and secondary standards should be same. • External precision (RSD%) of $^{87}Sr/^{86}Sr$ can be affected by spot sizes. • Laser ablation duration time are same for the samples and standards. Fractionation behavior and internal precision of $^{87}Rb/^{86}Sr$ ratios should be taken into account to determine the times as disucssed in **section 4.3** of **Chapter 3**.	• LA-ICP-MS: Kroslakova & Günther (2007) • LA-ICP-MS/MS: Bolea-Fernandez et al. (2016b); Redaa et al. (2021)
	Tuning	• Rates of frequency (laser pulse duration), fluence (laser energy per area) and ablation cell gas are optimized to produce sufficient and stable sensitivity. • These factors can affect on the external precision of Rb-Sr isotopic ratios.	• LA-ICP-MS: Günther & Hattendorf (2005) • LA-ICP-MS/MS: Redaa et al. (2021); Gorojovsky & Alard (2021)
	Signal smoother	• Stablilty of ablation signals can be improved by using wire and squid smoothing devices	• LA-ICP-MS: Hu et al. (2012); Müller et al. (2009) • LA-ICP-MS/MS: Rösel & Zack (2022)
	Addition of carrier gases	• Combination of a trace gas such as He and N_2 into the carrier gas enchances the signal sensitivity and reduceds elemental fractionation (Th/U). • Sensitivity of Rb and Sr masses and external precision (RSD%) of $^{87}Rb/^{86}Sr$ are improved by using a small amount of He and/or N_2.	• LA-ICP-MS: Eggins et al. (2005); Guillong & Heinrich (2007); Hu et al. (2008) • LA-ICP-MS/MS: Gorojovsky & Alard (2021)
ICP-MS/MS	Tuning	• Plasma conditions and sample depth (distance between torch and cone) are adjusted in SQ mode.	• LA-ICP-MS: Günther & Hattendorf (2005)
	Reaction gas	• Suitable reaction gases such as O_2, N_2O, SF_6 or CH_3F are selected to improve the reactivity of SrO.	• Reactivity: Moens et al. (2001); Cheng et al. (2008) • LA-ICP-MS/MS: Hogmalm et al. (2017)
	RF power	• Signal intensity can be enhanced by adjsuting RF power.	• LA-ICP-MS: Pearson et al. (2008)
	Detector dead time	• Dead time determination is important for precise isotope measurements.	• ICP-MS: Nelms et al. (2001); Vanhaecke et al. (1998) • (LA)-ICP-MS/MS: Bolea-Fernandez (2016a; 2016b)
	Dwell times	• Better external precision (RSD%) of Rb-Sr isotopic ratios can be obtained by adjusting dwell time.	• (LA)-ICP-MS/MS: Bolea-Fernandez et al. (2016b); Gorojovsky & Alard (2021)

1.5. Mass bias correction of Sr isotopic ratios

Agilent triple quadrupole ICP-MS has two detector modes, pulse and analog (P/A). When the number of ions is too high, ions cannot be measured separately and lead to one pulse count. In this study, P/A conversion factors for ^{104}Pd (same m/z with $^{88}Sr^{16}O$) and ^{85}Rb were determined in single quadrupole (SQ) mode on NIST 610 in line scan mode with a spot size of 60 µm at the optimized dead time of 35 ns.

According to the study of Gorojovsky & Alard (2020), P/A factor calibration in time resolved analysis in MS/MS mode is currently available in the software of Agilent 8900. However, in the software of the instrument used in this thesis work, the P/A factor calibration in MS/MS mode by purging a reaction gas (N_2O) was impossible. The reaction gas was blocked and decreased to zero during P/A factor calibration process in MS/MS mode. Thus, P/A factors were calibrated in SQ mode, and the analyses were performed in MS/MS mode by using N2O gas as a reaction gas. The RMs with a wide range of Sr concentrations (27.1-1650 µg g^{-1}) were analyzed, including NIST 610, BCR-2G, Mica-Mg and MAD apatite used either as primary or secondary standards with a spot size of 50 µm. The operating parameters in this analytical session are reported in **Table 2**.

It has been reported by LA-ICP-MS/MS studies that observed/experimental isotopic ratio is deviated to the true value, defined as mass discrimination or mass fractionation (Jarvis & Williams, 1993) and various calibration methods have been carried out in the previous studies (Jackson & Sylvester, 2008; Lin et al., 2016). Here, three different strategies were assessed to correct for mass discrimination of $^{87}Sr/^{86}Sr$ ratios and to define if the P/A factor was well calibrated in SQ mode: internal (Equation (1)), external (Equation (2)), the combination of internal and external correction (Equation (3)). Equation (1) and (3) were used as following the approaches of Bolea-Fernandez et al. (2016a). Next, the raw ratios were externally corrected by the methods following the correction approach of Zack & Hogmalm et al. (2016). The external correction by Zack & Hogmalm et al. (2016) can be described as equation (3), using the average of correction factors (CF) from the repeated analyses of the RMs. Final approach of equation (3) was the combination of internal and external corrections.

Table 2. LA-ICP-MS/MS parameters.

Laser ablation system		
Model		ESI NWR 193
Ablation cell		Two Volume ablation chamber (TwoVol1)
Laser wavelength	nm	193
Fluence	J cm^{-2}	ca. 6
Repetition rate	Hz	5
Ablation duration	s	50
background and washout	s	30-45
Spot diameter	µm	50
Sampling mode/pattern		Static spot ablation
Carrier gas		He
Cell carrier gas flow	ml min^{-1}	650
N_2 addition	ml min^{-1}	4
ICP-MS Instrument		
Model		Agilent 8900
Scan type		MS/MS
Sample introduction		Wire smoothing device
RF power	W	1550
Sample depth	mm	4
Carrier gas flow Ar	L min^{-1}	0.70-0.75 (optimised daily)
Detection system		dynamic range electron multiplier detector
N_2O gas flow rate	mL min^{-1}	ca. 0.20 (optimised daily)
Q1 → Q2 masses	amu	85 → 85 86 → 102 87 → 103 88 → 104
Energy discrimitation	V	-7
Wait time offset	s	2
Integration time per mass (dwell times)	ms	120 (except 85: 50 ms)
Dead time	ns	35
Typical oxide rate (^{248}ThO / ^{232}Th)	%	0.12-0.19
^{232}Th/^{238}U	%	98-99

Raw isotopic ratios: The raw $^{87}Sr/^{86}Sr$ mean ratios of all RMs investigated here are shown that the ratios are biased to higher ratios compared to reference (published) values (**Fig. 6a-6d**). The accuracy (%) of the mean NIST 610, BCR-2G, Mica-Mg and MAD are 1.4, 1.4, 0.66 and 1.5, respectively (**Table 3**). Vanhaecke et al. (2003) demonstrated that the considerable bias of raw data from reference values were derived from 'space charge effects', 'collisional losses' and 'kinetic effects' in the behavior of ion-molecules reactions. According to the experimental

results of Vanhaecke et al. (2003), these effects can be brought at various operation conditions including collision gas flow rate, reaction gas flow rate and RF frequency.

Internal mass bias correction (Equation (1)): The raw ratios were internally corrected using $^{88}Sr/^{86}Sr$ and $^{84}Sr/^{86}Sr$ ratios by assuming that the ratios are naturally constant as 0.0565 and 8.3752, respectively (Rosman & Taylor, 1998). The calibration is described by Equation (1) adapted from Bolea-Fernandez et al. (2016a).

$$(^{87}Sr/^{86}Sr)_{smpl,\ corrected} = (^{87}Sr\sim/^{86}Sr\sim)_{smpl,\ raw} \times (m_{87Sr}/m_{86Sr})^{f};$$
$$f = \ln[(^{88}Sr/^{86}Sr)_{true}/(^{88}Sr\sim/^{86}Sr\sim)_{raw}] / \ln [m_{88Sr}/m_{86Sr}] \quad (1)$$

where the notation X~ is reaction product of Sr isotopes in mass-shifted mode; f is the mass bias factor by the method of the exponential law of the Russell law; m is the absolute atomic masses of the analyte isotopes; true is the ratios from natural abundances for $^{84}Sr/^{86}Sr$ and $^{88}Sr/^{86}Sr$ ratios; smpl indicates secondary standards.

The results display that internal corrections for the RMs using $^{84}Sr/^{86}Sr$ and $^{88}Sr/^{86}Sr$ ratios lead to corresponding ratios to the published values for NIST 610, BCR-2G and Mica-Mg, yielding the accuracy of 0.025%-1.06% with improvement in the external precision compared to the raw ratios (**Fig. 6a-6c** and **Table 3**). Better external precision (RSD %) is obtained by internal correction using $^{88}Sr/^{86}Sr$ compared to using $^{84}Sr/^{86}Sr$ ratios due to the lowest abundance of ^{84}Sr (0.56%), resulting in lower CPS of $^{84}Sr^{16}O$.

On the other hands, internally corrected $^{87}Sr/^{86}Sr$ ratio of MAD using $^{88}Sr/^{86}Sr$ is highly biased (accuracy of 5.4 %) while internal correction using $^{84}Sr/^{86}Sr$ improve its accuracy to 0.72%, compared to its raw ratio (**Fig. 6d** and **Table 3**). We observed that the raw ratios of $^{88}Sr/^{86}Sr$ ratios of MAD were more than 9.0, which resulted in significant bias of the internally corrected $^{87}Sr/^{86}Sr$ ratios when using its $^{88}Sr/^{86}Sr$. In the software of Agilent 8900, the P/A detector mode can be verified for each analyte as reported in **Table 3**. 'P' indicates pulse mode, and 'M' specifies mixed mode in the threshold of pulse and analog modes. In this analysis, $^{88}Sr^{16}O$ was detected in pulse or mixed mode for NIST 610 as nine-point analyses were detected in M and six-point analyses were in P. For MAD, all analyses of $^{88}Sr^{16}O$ were detected in M. It seems that the highly biased result for MAD by internal correction using $^{88}Sr/^{86}Sr$ is derived

from the counting time on $^{88}Sr^{16}O$ by P/A transition due to its high concentration of Sr content (1650 µg g^{-1}) compared to that of other RMs (**Table 3**). These high CPS could possibly derive the inconsistencies in isotopic abundance ratios of $^{88}Sr/^{86}Sr$.

External mass bias correction (Equation (2)): The raw ratios were externally corrected by the correction approaches of Zack and Hogmalm et al. (2016) described as Equation (2). NIST 610 was selected as a primary standard to correct the raw data of BCR-2G, Mica-Mg and MAD. For the calibration of NIST 610, BCR-2G was used as a primary standard to avoid self-normalization.

$$(^{87}Sr/^{86}Sr)_{smpl,\ corrected} = (^{87}Sr\sim/^{86}Sr\sim)_{smpl,\ raw} / CF\ ;$$
$$CF = (^{87}Sr\sim/^{86}Sr\sim)_{std,\ raw} / (^{87}Sr/^{86}Sr)_{std,\ true} \quad (2)$$

where the notation X~ is reaction product of Sr isotopes in mass-shifted mode; CF is the average of correction factors (CF) from the repeated analyses of primary standards; smpl and std indicate secondary and primary standards, respectively.

The external correction of $^{87}Sr/^{86}Sr$ for all RMs investigated produces corresponding results to the published values with the accuracy ranging from 0.026% for NIST 610 to 0.65% for Mica-Mg (**Fig. 6** and **Table 3**). For samples which have high Sr concentration such as MAD in this study, the external correction leads to better precision and accuracy compared to the internal correction approaches using $^{84}Sr/^{86}Sr$ and $^{88}Sr/^{86}Sr$ ratios in this study.

Combination of external and internal mass bias correction (double correction): Final approach adapted from Bolea-Fernandez et al. (2016a) is to correct by using the combination of internal and external corrections. The raw ratios are firstly corrected internally using $^{84}Sr/^{86}Sr$ or $^{88}Sr/^{86}Sr$ ratios (Equation (1)), followed by sample-standard-sample bracketing using the equation (2). The accuracy of NIST 610, BCR-2G and Mica-Mg is generally improved (0.034-1.18%) by using this method, compared to their raw ratios and internally corrected ratios. Highly biased corrected $^{87}Sr/^{86}Sr$ ratio of MAD with the accuracy of 5.3% is derived its internally corrected ratios related to P/A factor issue. This double correction could produce better precision and accuracy compared to the raw ratios, but this method is not suitable for high Sr samples in this study due to P/A factor issue.

The Rb-Sr dating methods by LA-ICP-MS/MS of Hogmalm et al. (2017), which used ICP-MS/MS of Agilent 8800, suggested that P/A factors could be determined by measurement in single quadrupole mode and using standards with similar concentration to the target samples. They used the external calibration method for mass bias correction of $^{87}Sr/^{86}Sr$ ratios to prioritize ^{87}Sr and ^{86}Sr, and to avoid the issues such as P/A transition (Hogmlam et al., 2017). In this study, we also adapted the external calibration method to produce better precision and accuracy and to avoid P/A factor problems, derived from large concentration contrast between the RMs and samples. The LA-ICP-MS/MS results in **chapter 3** and **4** were calibrated using the external correction for $^{87}Sr/^{86}Sr$ ratios of targeted RMs and samples.

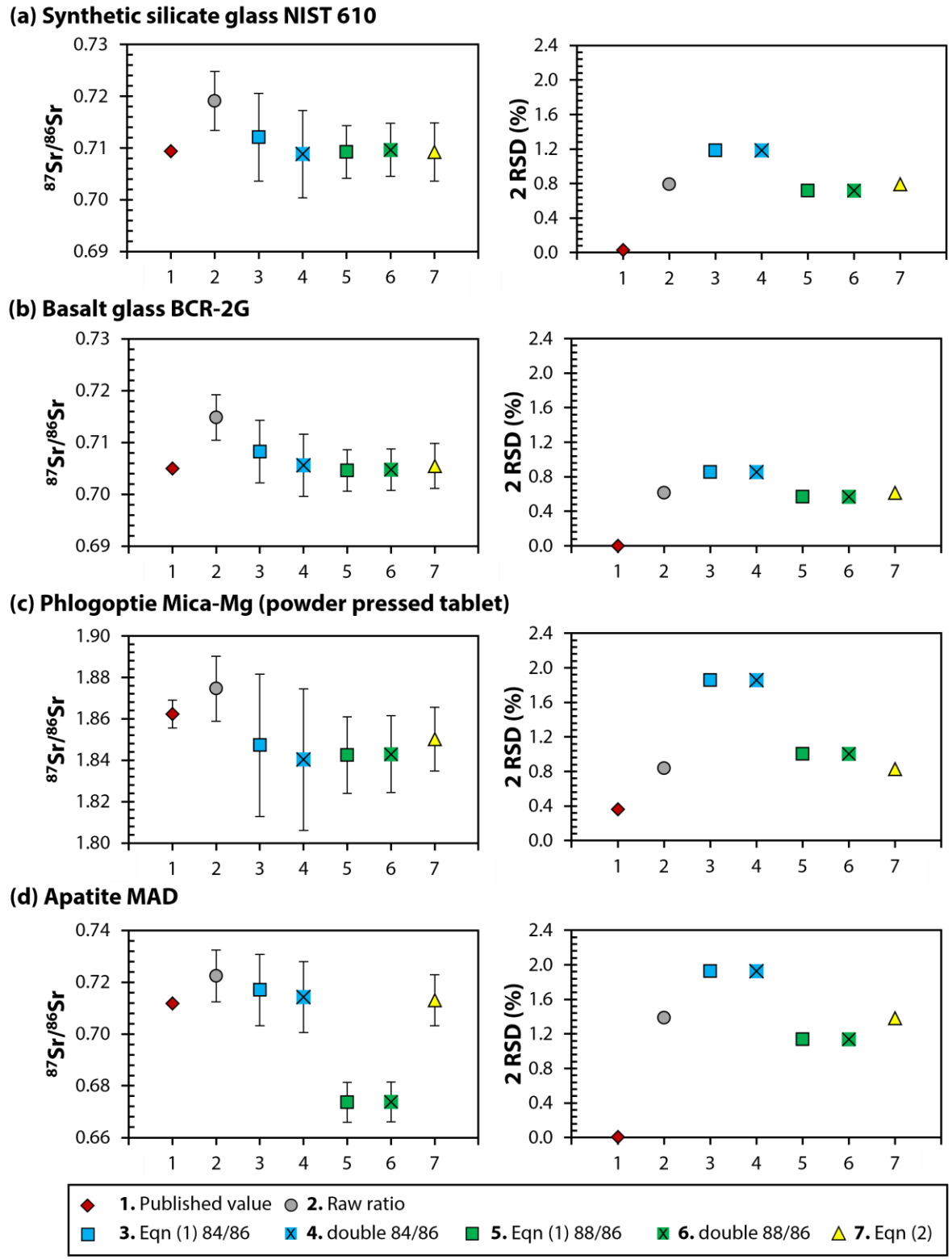

Fig. 6. Raw and corrected $^{87}Sr/^{86}Sr$ mean ratios of (a) NIST 610, (b) BCR-2G, (c) Mica-Mg and (d) MAD, compared with their published (preferred) values. 2 RSD (%) of the mean ratios and the uncertainty of published values are on the right.

Table 3. Results of $^{87}Sr/^{86}Sr$ ratios and CPS of SrO^+ by LA-ICP-MS/MS for NIST 610, BCR-2G, Mica-Mg and MAD with their published values. Calibration methods of #2-#7 correspond to the numbers in **Fig. 6**. n indicates the number of individual analyses.

	Published values			
Sample	Sr (μg g^{-1})	2 RSD%	$^{87}Sr/^{86}Sr$	2 RSD%
NIST 610	515.5	0.1	0.7094	0.028
BCR-2G	323.7	1.5	0.7050	0.0011
Mica-Mg	27.1	5.6	1.8622	0.36
MAD	1650	0.0	0.7118	0.0042

		Mean of Cps (blank corrected)												**Accuracy (%) of $^{87}Sr/^{86}Sr$**					
Sample	n	$^{84}Sr^{16}O$	2 RSD%	P/A	$^{86}Sr^{16}O$	2 RSD%	P/A	$^{87}Sr^{16}O$	2 RSD%	P/A	$^{88}Sr^{16}O$	2 RSD%	P/A	#2	#3	#4	#5	#6	#7
NIST 610	16	3.1E+04	3.4	P	5.61E+05	3.2	P	4.03E+05	3.2	P	4.83E+06	3.4	P/M	1.37	0.38	0.082	0.025	0.034	0.026
BCR-2G	16	1.5E+04	13	P	2.67E+05	13	P	1.91E+05	13	P	2.30E+06	13	P	1.39	0.46	0.082	0.059	0.034	0.066
Mica-Mg	16	1.1E+03	8.6	P	2.00E+04	8.5	P	3.74E+04	8.5	P	1.73E+05	8.4	P	0.66	0.81	1.18	1.06	1.04	0.65
MAD	6	1.4E+05	2.8	P	2.48E+06	3.1	P	1.79E+06	2.6	P	2.39E+07	2.6	M	1.50	0.72	0.35	5.36	5.34	0.18

Published values of NIST 610 from GeoRem and Wise and Watters (2012), BCR-2G from Georem and Elburg et al. (2005), Mica-Mg from Jegal et al. (2022) and MAD from Yang et al. (2014).

2. Secondary Ion Mass Spectrometry (SIMS)

2.1 Principle of SIMS

Secondary Ion Mass Spectrometry (SIMS) is one of the most sensitive elemental and isotopic surface analysis techniques, measuring elements from hydrogen to uranium at a micro scale. SIMS consists of bombardment of a sample surface by a beam of primary ions followed by mass spectrometer of the emitted secondary ions (Reed, 1989). SIMS provides high sensitivity with detection limit down to ppb level, allowing to measure not only localized elemental composition but also precise isotopic values (Dynamic Secondary Ion Mass Spectrometry, 1st edition, 2019).

The interior of sample surface is bombarded by a beam of primary ions of few KV energy from a Hyperion RF Plasma source under the ultra-high vacuum, focused by a set of electrostatic lenses. The Hyperion RF Plasma source is used for dense and stable primary ions beam (O^-), allowing smaller spot analysis and higher stability. The bombardment causes the destruction of lattice structure, displacing of atoms in the sample and ejection of single atoms and clusters (**Fig. 7**). Most of atoms and molecules are neutral, but a small fraction of them is ionized with variable kinetic energies and angles and accelerated by electrostatic field, followed by the extraction of secondary ions.

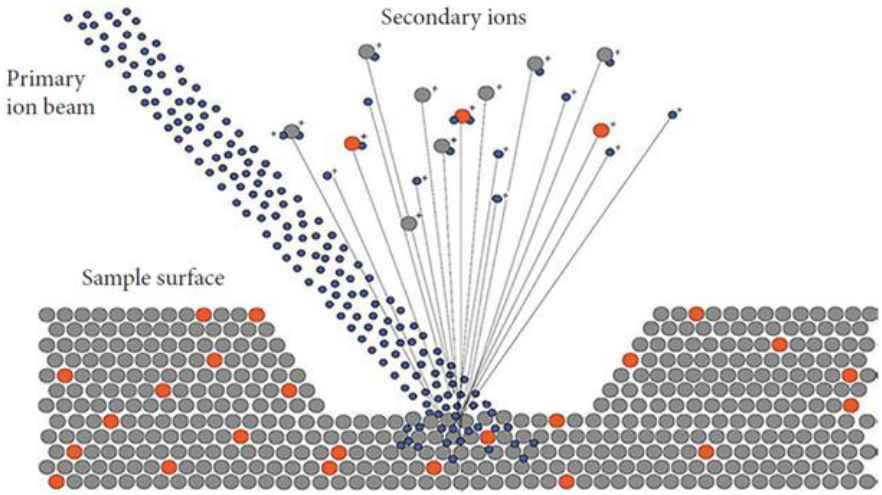

Fig. 7. A schematic diagram displaying sputtering and ionization process in SIMS analysis adapted from Dynamic Secondary Ion Mass Spectrometry, 1st edition, 2019.

Most of elements (H to U) can be ionized except noble gases with ionization efficiency of 0.1% to 10%, expressed by number of secondary ions divided by number of sputtered atoms (John Wiley & Sons Ltd 2019). For electropositive elements (e.g., Mg^+, K^+, Ca^+, Rb^+, Sr^+, Pb^+), a O^- primary beam is used, and secondary ions are measured as positive M^+ species. For electronegative elements (e.g., O^-, C^-, S^-, Si^-), a primary beam of cesium ion (Cs^+) is used, and secondary ions are collected as form of negative M^- species. In this mode, the ejection of electrons from the sample surface causes charging of samples, leading to unstable secondary emission. Charging by sputtering can be prevented by using an electron gun for the charge compensation.

The Cameca IMS 1280 HR2 ion microprobe (CRPG, Nancy, France) used in this study is double focusing magnetic sector coupled with an electrostatic sector, allowing wide energy pass band and high mass resolution power (MRP = M/ΔM) by large radius detector magnet. The IMS 1280 HR2 is an advanced generation of large geometry SIMS with MRP of ca. 40,000.

SIMS analysis undergoes matrix effect and instrumental fractionation, which can cause the analytical precision of isotope data (Fitzsimons et al., 2000). The degree of these effects can vary with analytical conditions, instrument and chemical composition of the matrix or during retuning instrumental parameters (Fitzsimons et al., 2000; Reed, 1989). To minimize this effect, standard samples with same matrix is required.

2.2. Analytical conditions for Rb-Sr isotope measurements by SIMS

Decrée et al. (2020) used the CRPG Cameca IMS 1280 HR2 for in-situ Sr isotope analyses on apatites from the Phalaborwa complex, South Africa. A mass resolution of 20,000 was used, being sufficient to separate Sr isotopes from Ca_2^+ overlapping masses, considering Rb and FeO (<0.09 wt.%) as a minor species. No application study has been conducted using Rb-Sr isotope measurements by SIMS on high Rb/Sr micas and feldspars yet. Therefore, SIMS Rb-Sr isotopic analyses were performed on mineral fragments on epoxy resin (Mica-Mg, Mica-Fe) and powder pressed tablets (Mica-Mg, Mica-Fe, FK-N) to determine suitable analytical conditions and test their isotopic homogeneity by measuring the surface of the reference materials randomly, using the CRPG Cameca IMS 1280-HR instrument.

The pressure in the chamber was maintained in the range of 8.30E-09 and 1.96E-08. The primary ion beam of $^{16}O^-$ was accelerated at 13 kV from a Hyperion RF Plasma source with intensities of about 30 nA and 50 nA to sputter 12 µm diameter spot size. The mass spectrometer entrance and exit slits were set for a MRP of ca. 22,000 (20,000-22,000) to remove the isobaric interference on the Sr isotopes. The energy window was opened at 30 eV and 50 eV. The measurements were performed in monocollection by peak switching on Faraday cup (FC2) and Electron multiplier (EM) ion counting. Each cycle includes the measurement of the EM background on 83.7 (measurement time of 4 s), ^{84}Sr (2.96 s, EM), $^{40}Ca^{44}Ca$ (2.96 s, EM), FC Background on 84.9 (4 s, FC2), ^{85}Rb (6 s, FC2), ^{86}Sr (16 s, EM), ^{87}Sr (12 s, FC2) and ^{88}Sr (8 s, EM). A waiting time of 0.96, 2 and 4 was used between the masses. Pre-sputtering time was 60 s with a 10 x 5 raster μm^2. At the beginning of each analysis, the magnetic field position, the beam centering in the field aperture and the energy offset were checked. Each analysis consists of 24 successive cycles The instrumental mass fractionation of Sr isotopes was corrected using $^{86}Sr/^{88}Sr$ ratio of 0.1194. The isobaric interference of ^{87}Rb on ^{87}Sr was corrected using the measured ^{85}Rb count rates and $^{87}Rb/^{85}Rb$ ratio of 0.3825.

2.3. In-situ Rb-Sr isotope measurements of CRPG mineral RMs by SIMS: Preliminary results

Three CRPG RMs, phlogopite Mica-Mg, biotite Mica-Fe and potash feldspar FK-N were selected based on their broad compositional range of Rb and Sr and major element compositions (**Table 4**). The mineral separates of Mica-Mg and Mica-Fe were embedded with epoxy resin in rings. Powder pressed tablets of Mica-Mg, Mica-Fe and FK-N were produced and provided by myStandards GmbH. NIST 610 glass was used as a secondary standard in order to monitor the stability of the analysis, showing constant measured ratios.

Table 4. Chemical compositions of RMs used in this study.

Sample	Type	Sr ($\mu g\ g^{-1}$)	2 s	Rb ($\mu g\ g^{-1}$)	2 s	Rb/Sr	$^{87}Rb/^{86}Sr$	2 s	$^{87}Sr/^{86}Sr$	2s	FeO (wt.%)	2s
Mica-Mg	Phlogopite	27.1	1.5	1327	41	49	155.6	7.3	1.8622	0.0067	8.5	0.2
Mica-Fe	Biotite	6.2	0.6	2293	142	369	1815.3	246.3	7.994	1.021	23.1	0.4
FK-N	Potash feldspar	37.1	1.0	853	69	23	69.9	4.1	1.2114	0.0021	0.08	0.04

Rb-Sr compositions from Jegal et al. (2022), FeO contents from Govidnaraju (1995).

Table 5. Isotope abundances at 84, 85, 86, 87 and 88 and the possible interference in the SIMS analysis. MRP: Mass resolving power required to resolve the interferences.

	m 84	m 85	m 86	m 87	m 88
Abundance (%)					
Sr	0.56		9.86	7.02	82.56
Rb		72.15		27.85	
Ca_2	3.98	0.002	0.033	0.006	0.405
FeSi	84.70	6.327	3.240	0.083	0.010
MRP ($M/\Delta M$)					
Ca_2 to Sr	18,000		18,000	14,000	14,000
FeSi to Sr	60,000		33,800	77,000	35,608

During the session, the signal of raw data display that the intensity with time after pre-sputtering and centering of the powder pressed tablet was more constant and stable compared to the mineral fragments. Major interferences on naturally occurring isotopes of Sr include $^{87}Rb^{+}$, $FeSi^{+}$ and Ca_2^{+} (**Table 5**). ^{87}Sr is interfered by ^{87}Rb and required high mass resolving power (MRP; 280,000). By monitoring the ^{85}Rb count rate, the ^{87}Rb isobaric interference on ^{87}Sr was corrected using the natural abundance ratio of $^{87}Rb/^{85}Rb$ (0.3825). Ca dimers also affect the Sr isotopes, however, the MRP of ca. 22,000 was enough to resolve all the Ca_2^{+} overlapping masses on Sr isotopes. The major difficulty of Sr isotopic analysis of mica by SIMS is the large contribution of $FeSi^{+}$ on $^{87}Sr/^{86}Sr$ ratios and stable isotope ratios such as $^{88}Sr/^{86}Sr$ and $^{84}Sr/^{86}Sr$ (**Fig. 8**). The interference of $FeSi^{+}$ on Sr isotopes was detected in Mica-Mg and Mica-Fe for both forms of powder pellets and mineral grains due to their high FeO and low Sr contents (**Table 4**). The $FeSi^{+}$ interference problem cannot be solved by the MRP in this study (**Table 5**). Therefore, the measured counting ratios of $^{84}Sr/^{86}Sr$ were monitored and compared with the natural abundance of $^{84}Sr/^{86}Sr$ (0.0568) to correct ^{84}Sr. The results show that the measured $^{84}Sr/^{86}Sr$ ratios of Mica-Mg-P and Mica-Fe-P (P; powder pressed tablets) were highly biased from the natural abundance and the measured $^{84}Sr/^{86}Sr$ ratios of NIST 610 (**Fig. 8a and 8b**). The measured $^{88}Sr/^{86}Sr$ ratios also show that the ratios of Mica-Mg-P and Mica-Fe-P were ca. 9.0 and >25, respectively, highly biased from the natural abundance of $^{88}Sr/^{86}Sr$ (8.375) and the measured ratios of NIST 610 (8.15-8.24). On the other hands, little contribution of $FeSi^{+}$ on Sr isotopes was detected for FK-N-P, which contain low FeO of 0.1 wt.% and higher Sr contents of 39 ppm compared to Mica-Fe and Mica-Mg (**Fig. 8c**).

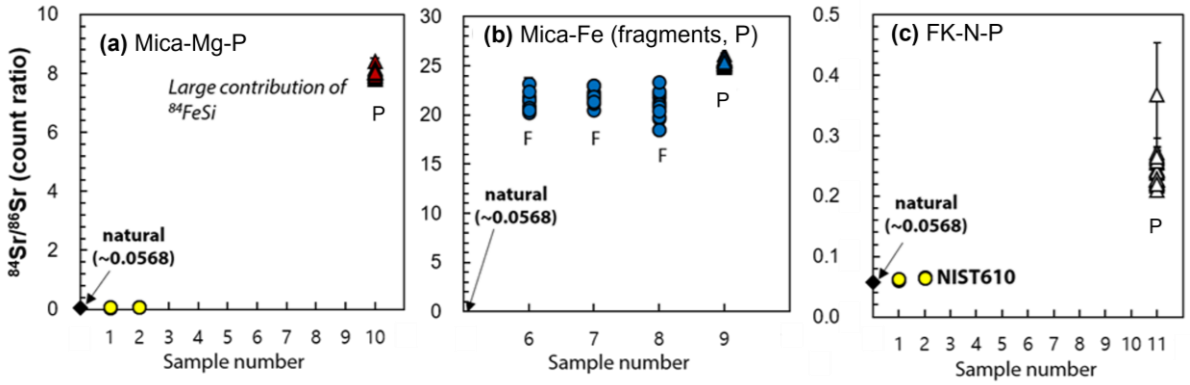

Fig. 8. Count ratios of $^{84}Sr/^{86}Sr$ of the SIMS analyses for (a) Mica-Mg, (b) Mica-Fe and (c) FK-N during 1-week session. Natural abundance of $^{84}Sr/^{86}Sr$ (0.0568) is indicated by black

diamond. F: mineral fragments (circles), P: power pressed tablet (triangles). The count ratios of $^{84}Sr/^{86}Sr$ of NIST 610 with a sample number 1 and 2 indicate five replicate analyses with an energy slit of 30 eV and 50 eV, respectively. Each sample number of the samples represents the replicate analyses of each mineral fragment or power pressed tablet.

Internal precisions (2 SE) of individual $^{88}Sr/^{86}Sr$ ratios are 0.09-0.35% for of NIST 610 and 0.35-0.66% for FK-N-P, respectively, which are better than those of 0.62-0.93% for NIST 610 and 0.90-1.6% for FK-N-P by LA-ICP-MS/MS from one-day session. External precision (2 RSD, n = 5) of measured $^{88}Sr/^{86}Sr$ mean ratios is better for homogeneous NIST 610 by SIMS (0.07% and 0.53% at 30 eV and 50 eV of energy slits, respectively), compared to that of 0.52-2.1% (2 RSD, n = 6-16 from five analytical sessions in one month) by LA-ICP-MS/MS. External precision (2 RSD) of measured $^{88}Sr/^{86}Sr$ mean ratios for FK-N-P via SIMS is 0.85% (n = 25) and its precision via LA-ICP-MS/MS varies from 0.74 to 1.32% (n = 6-16 from five analytical sessions in one month). Variability of external precisions for NIST 610 and FK-N by LA-ICP-MS/MS is considered to be the effect of variability of analytical conditions and heterogeneity of geological samples such as FK-N (Jegal et al., 2022). Although the results of present study indicate that FeSi interferences limit proper measurements of Rb-Sr isotope measurements by SIMS for micas and K-feldspars which contain high Fe and/or high Rb contents, the results show that better analytical precision of Sr isotopic ratios can be obtained via SIMS compared to LA-ICP-MS/MS analysis. SIMS analysis has been conducted for Sr isotope measurements by previous studies for calcite (Exley, 1983), otolith (Weber et al., 2005; Sano et al., 2008), plagioclase (Sas et al., 2019) and apatite (Decrée et al., 2020), documenting successful measured $^{87}Sr/^{86}Sr$ ratios of the samples. Therefore, Sr isotopic analysis by SIMS allows accurate and precise in-situ analysis for mineral phases which contain high Sr and low Fe and Rb contents such as plagioclase, carbonate or apatite as reported studies.

References

Agilent 7500 Series ICP-MS HW Manual, Agilent publication, G3270-90106

Balcaen, L. (2015). Inductively coupled plasma - Tandem mass spectrometry (ICP-MS/MS): A powerful and universal tool for the interference-free determination of (ultra)trace elements - A tutorial review. *Analytica Chimica Acta*, 13.

Bolea-Fernandez, E., Van Malderen, S. J. M., Balcaen, L., Resano, M., & Vanhaecke, F. (2016b). Laser ablation-tandem ICP-mass spectrometry (LA-ICP-MS/MS) for direct Sr isotopic analysis of solid samples with high Rb/Sr ratios. *Journal of Analytical Atomic Spectrometry*, *31*(2), 464–472. https://doi.org/10.1039/C5JA00404G

Bolea-Fernandez, E., Balcaen, L., Resano, M., & Vanhaecke, F. (2016a). Tandem ICP-mass spectrometry for Sr isotopic analysis without prior Rb/Sr separation. *Journal of Analytical Atomic Spectrometry*, *31*(1), 303–310. https://doi.org/10.1039/C5JA00157A

Cheng, P., Koyanagi, G. K., & Bohme, D. K. (2008). On the chemical resolution of the 87Rb+ (s0)/87Sr+ (s1) isobaric interference: A kinetic search for an optimum reagent. *Analytica Chimica Acta*, *627*(1), 148–153. https://doi.org/10.1016/j.aca.2008.03.057

Decrée, S., Cawthorn, G., Deloule, E., Mercadier, J., Frimmel, H., & Baele, J.-M. (2020). Unravelling the processes controlling apatite formation in the Phalaborwa Complex (South Africa) based on combined cathodoluminescence, LA-ICPMS and in-situ O and Sr isotope analyses. *Contributions to Mineralogy and Petrology*, *175*(4), 34. https://doi.org/10.1007/s00410-020-1671-6

Dynamic Secondary Ion Mass Spectrometry, first edition (2019) Essential Knowledge Briefings, John Wiley & Sons Ltd 2019

Elburg, M., Vroon, P., van der Wagt, B., & Tchalikian, A. (2005). Sr and Pb isotopic composition of five USGS glasses (BHVO-2G, BIR-1G, BCR-2G, TB-1G, NKT-1G). *Chemical Geology*, *223*(4), 196–207. https://doi.org/10.1016/j.chemgeo.2005.07.001

Eggins, S. M., Grün, R., McCulloch, M. T., Pike, A. W. G., Chappell, J., Kinsley, L., et al. (2005). In situ U-series dating by laser-ablation multi-collector ICPMS: new prospects for Quaternary geochronology. *Quaternary Science Reviews*, *24*(23–24), 2523–2538. https://doi.org/10.1016/j.quascirev.2005.07.006

Exley, R.A. (1983). Evaluation and application of the ion microprobe in the strontium isotope geochemistry of carbonates. *Earth Planet. Sci. Lett. 65,* 303–310.

Fitzsimons, I. C. W., Harte, B., & Clark, R. M. (2000). SIMS stable isotope measurement: counting statistics and analytical precision. *Mineralogical Magazine*, *64*(1), 59–83. https://doi.org/10.1180/002646100549139

Gorojovsky, L., & Alard, O. (2020). Optimisation of laser and mass spectrometer parameters for the *in situ* analysis of Rb/Sr ratios by LA-ICP-MS/MS. *Journal of Analytical Atomic Spectrometry*, 10.1039.D0JA00308E. https://doi.org/10.1039/D0JA00308E

Guillong, M., & Heinrich, C. A. (2007). Sensitivity enhancement in laser ablation ICP-MS using small amounts of hydrogen in the carrier gas. *Journal of Analytical Atomic Spectrometry*, *22*(12), 1488. https://doi.org/10.1039/b709489b

Günther, D., & Hattendorf, B. (2005). Solid sample analysis using laser ablation inductively coupled plasma mass spectrometry. *TrAC Trends in Analytical Chemistry*, *24*(3), 255–265. https://doi.org/10.1016/j.trac.2004.11.017

Handbook of ICP-QQQ Applications using the Agilent 8800 and 8900, Agilent publication, 2020, 5991-2802EN

Hogmalm, K. J., Zack, T., Karlsson, A. K.-O., Sjöqvist, A. S. L., & Garbe-Schönberg, D. (2017). In situ Rb–Sr and K–Ca dating by LA-ICP-MS/MS: an evaluation of N_2O and SF_6 as reaction gases. *Journal of Analytical Atomic Spectrometry*, *32*(2), 305–313. https://doi.org/10.1039/C6JA00362A

Hu, Z., Gao, S., Liu, Y., Hu, S., Chen, H., & Yuan, H. (2008). Signal enhancement in laser ablation ICP-MS by addition of nitrogen in the central channel gas. *Journal of Analytical Atomic Spectrometry*, *23*(8), 1093. https://doi.org/10.1039/b804760j

Hu, Z., Liu, Y., Gao, S., Xiao, S., Zhao, L., Günther, D., et al. (2012). A "wire" signal smoothing device for laser ablation inductively coupled plasma mass spectrometry analysis. *Spectrochimica Acta Part B: Atomic Spectroscopy*, *78*, 50–57. https://doi.org/10.1016/j.sab.2012.09.007

Jackson, S. E., & Sylvester, P. (2008). Calibration strategies for elemental analysis by LA-ICP-MS. *SIGNAL*, *10*(1,000), 100.

Jarvis, K. E., & Williams, J. G. (1993). Laser ablation inductively coupled plasma mass spectrometry (LA-ICP-MS): a rapid technique for the direct, quantitative determination of major, trace and rare-earth elements in geological samples. *Chemical Geology*, *106*(3), 251–262. https://doi.org/10.1016/0009-2541(93)90030-M

Jegal, Y., Zimmermann, C., Reisberg, L., Yeghicheyan, D., Cloquet, C., Peiffert, C., et al. (2022). Characterisation of Reference Materials for In Situ Rb-Sr Dating by LA-ICP-MS/MS. *Geostandards and Geoanalytical Research*, *n/a*(n/a). https://doi.org/10.1111/ggr.12456

Kroslakova, I., & Günther, D. (2007). Elemental fractionation in laser ablation-inductively coupled plasma-mass spectrometry: evidence for mass load induced matrix effects in the ICP during ablation of a silicate glass. *J. Anal. At. Spectrom.*, *22*(1), 51–62. https://doi.org/10.1039/B606522H

Li, S.-S., Santosh, M., Farkaš, J., Redaa, A., Ganguly, S., Kim, S. W., et al. (2020). Coupled U-Pb and Rb-Sr laser ablation geochronology trace Archean to Proterozoic crustal evolution in the Dharwar Craton, India. *Precambrian Research*, *343*, 105709. https://doi.org/10.1016/j.precamres.2020.105709

Lin, J., Liu, Y., Yang, Y., & Hu, Z. (2016). Calibration and correction of LA-ICP-MS and LA-MC-ICP-MS analyses for element contents and isotopic ratios. *Solid Earth Sciences*, *1*(1), 5–27. https://doi.org/10.1016/j.sesci.2016.04.002

Liu, X., Dong, S., Yue, Y., Guan, Q., Sun, Y., Chen, S., et al. (2020). $^{87}Sr/^{86}Sr$ isotope ratios in rocks determined using inductively coupled plasma tandem mass spectrometry in O_2 mode without prior Sr purification. *Rapid Communications in Mass Spectrometry*, *34*(8). https://doi.org/10.1002/rcm.8690

Moens, L. J., Vanhaecke, F. F., Bandura, D. R., Baranov, V. I., & Tanner, S. D. (2001). Elimination of isobaric interferences in ICP-MS, using ion–molecule reaction chemistry: Rb/Sr age determination of magmatic rocks, a case study. *J. Anal. At. Spectrom.*, *16*(9), 991–994. https://doi.org/10.1039/B103707M

Müller, W., Shelley, M., Miller, P., & Broude, S. (2009). Initial performance metrics of a new custom-designed ArF excimer LA-ICPMS system coupled to a two-volume laser-ablation cell. *J. Anal. At. Spectrom.*, *24*(2), 209–214. https://doi.org/10.1039/B805995K

Nelms, S. M., Quétel, C. R., Prohaska, T., Vogl, J., & Taylor, P. D. P. (2001). Evaluation of detector dead time calculation models for ICP-MS. *J. Anal. At. Spectrom.*, *16*(4), 333–338. https://doi.org/10.1039/B007913H

Olierook, H. K. H., Rankenburg, K., Ulrich, S., Kirkland, C. L., Evans, N. J., Brown, S., et al. (2020). Resolving multiple geological events using in situ Rb–Sr geochronology: implications for metallogenesis at Tropicana, Western Australia. *Geochronology*, *2*(2), 283–303. https://doi.org/10.5194/gchron-2-283-2020

Pearson N.J., W.L. Griffin & Suzanne Y. O'Reilly. (2008). Mass fractionation correction in laser ablation multiple-collector ICP–MS: implications for overlap corrections and precise and accurate in situ isotope ratio measurement. *Mineralogical Association of Canada Short Course*. Volume 40. 93-116

Redaa, A., Farkaš, J., Gilbert, S., Collins, A. S., Wade, B., Löhr, S., et al. (2021). Assessment of elemental fractionation and matrix effects during *in situ* Rb–Sr dating of phlogopite by LA-ICP-MS/MS: implications for the accuracy and precision of mineral ages. *Journal of Analytical Atomic Spectrometry*, *36*(2), 322–344. https://doi.org/10.1039/D0JA00299B

Reed, S. J. B. (1989). Ion microprobe analysis - a review of geological applications. *Mineralogical Magazine*, *53*(369), 3–24. https://doi.org/10.1180/minmag.1989.053.369.02

Rösel, D., & Zack, T. (2022). LA-ICP-MS/MS Single-Spot Rb-Sr Dating. *Geostandards and Geoanalytical Research*, *46*(2), 143–168. https://doi.org/10.1111/ggr.12414

Russ, G.P. III . Gray, A.L. (Ed.)., 1989. Isotope ratio measurements using ICP-MS. United Kingdom: Blackie.

Rosman, K. J. R., & Taylor, P. D. P. (1998). Isotopic Compositions of the Elements 1997. *Journal of Physical and Chemical Reference Data*, *27*(6), 1275–1287. https://doi.org/10.1063/1.556031

Sano, Y., Shirai, K., Takahata, N., Amakawa, H., Otake, T. (2008). Ion microprobe Sr isotope analysis of carbonates with about 5μm spatial resolution: an example from an ayu otolith. *Appl. Geochem. 23,* 2406–2413. https://doi.org/10.1016/j.apgeochem. 2008.02.027.

Sas et al. (2019) The ion microprobe as a tool for obtaining strontium isotopes in magmatic plagioclase: A case study at Okataina Volcanic Centre, New Zealand*, Chemical Geology Volume 513,* 153-166. https://doi.org/10.1016/j.chemgeo.2019.03.016

Şengün, F., Bertrandsson Erlandsson, V., Hogmalm, J., & Zack, T. (2019). In situ Rb-Sr dating of K-bearing minerals from the orogenic Akçaabat gold deposit in the Menderes Massif,

Western Anatolia, Turkey. *Journal of Asian Earth Sciences*, *185*, 104048. https://doi.org/10.1016/j.jseaes.2019.104048

Technical Overview of Agilent 8900 Triple Quadrupole ICP-MS, Agilent publication, 2016, 5991-6942EN

Tillberg, M., Drake, H., Zack, T., Hogmalm, J., & Åström, M. (2017). In Situ Rb-Sr Dating of Fine-grained Vein Mineralizations Using LA-ICP-MS. *Procedia Earth and Planetary Science*, *17*, 464–467. https://doi.org/10.1016/j.proeps.2016.12.117

Tillberg, M., Drake, H., Zack, T., Kooijman, E., Whitehouse, M. J., & Åström, M. E. (2020). In situ Rb-Sr dating of slickenfibres in deep crystalline basement faults. *Scientific Reports*, *10*(1), 562. https://doi.org/10.1038/s41598-019-57262-5

Vanhaecke, F., De Wannemacker, G., Balcaen, L., & Moens, L. (2003). The use of dynamic reaction cell ICP mass spectrometry to facilitate Rb-Sr age determination. *Geological Society, London, Special Publications*, *220*(1), 173–181. https://doi.org/10.1144/GSL.SP.2003.220.01.10

Vanhaecke, Frank, de Wannemacker, G., Moens, L., Dams, R., Latkoczy, C., Prohaska, T., & Stingeder, G. (1998). Dependence of detector dead time on analyte mass number in inductively coupled plasma mass spectrometry. *Journal of Analytical Atomic Spectrometry*, *13*(6), 567–571. https://doi.org/10.1039/a709001c

Weber, P.K., Bacon, C.R., Hutcheon, I.D., Ingram, B.L., Wooden, J.L., 2005. Ion microprobe measurement of strontium isotopes in calcium carbonate with application to salmon otoliths. *Geochim. Cosmochim. Acta 69,* 1225–1239. https://doi.org/10.1016/j.gca.2004.05.051.

Yang, Y.-H., Wu, F.-Y., Yang, J.-H., Chew, D. M., Xie, L.-W., Chu, Z.-Y., et al. (2014). Sr and Nd isotopic compositions of apatite reference materials used in U–Th–Pb geochronology. *Chemical Geology*, *385*, 35–55. https://doi.org/10.1016/j.chemgeo.2014.07.012

Zack, T., & Hogmalm, K. J. (2016). Laser ablation Rb/Sr dating by online chemical separation of Rb and Sr in an oxygen-filled reaction cell. *Chemical Geology*, *437*, 120–133. https://doi.org/10.1016/j.chemgeo.2016.05.027

Chapter II.
Characterization of Reference Materials for in-situ Rb-Sr dating by LA-ICP-MS/MS

Article published in *Geostandards and Geoanalytical Research* (2022)

https://doi.org/10.1111/ggr.12456

Chapter II. Characterization of Reference Materials for in-situ Rb-Sr dating by LA-ICP-MS/MS

Résumé

Nous rapportons les concentrations en Rb et Sr et les rapports $^{87}Sr/^{86}Sr$ pour quatre matériaux de référence (RM) du Service d'Analyse des Roches et des Minéraux (SARM) à Nancy, France : Mica-Mg, Mica-Fe, GL-O et FK-N. Ces 4 RMs ont des compositions chimiques différentes qui couvrent la gamme de celles des feldspaths et micas riches en K, ce qui en fait des matériaux de calibration potentiels pour la datation Rb-Sr in situ par LA-ICP-MS/MS. Des grains sélectionnés dans les 4 RMs présentent des degrés variables d'hétérogénéité observable par imagerie MEB et par cartographie chimique en microsonde électronique. Cette hétérogénéité est principalement liée aux inclusions de minéraux dans les grains, et aux substitutions chimiques lors de la croissance cristalline et/ou lors des processus d'altération. Les poudres disponibles ont été analysées par ID-TIMS ($^{87}Sr/^{86}Sr$ et concentrations Sr) et ID-MC-ICP-MS (Rb) après digestion et séparation chimique. Les rapports moyens $^{87}Rb/^{86}Sr$ sont 155.6 ± 4.7% (2 SD) pour Mica-Mg, 1815 ± 14% pour Mica-Fe, 36.2 ± 11% pour GL-O et 69.9 ± 5.9% pour FK-N. Les rapports moyens $^{87}Sr/^{86}Sr$ sont de 1.8622 ± 0.36% (2 SD) pour Mica-Mg, 7.99 ± 13% pour Mica-Fe, 0.75305 ± 0.12% pour GL-O, et 1.2114 ± 0.17% pour FK-N. Les 4 RMs présentent chacun une dispersion du rapport $^{87}Sr/^{86}Sr$ et des concentrations de Rb et Sr, à des degrés qui diffèrent entre les RMs et qui reflètent l'hétérogénéité de leurs cristaux d'origine. Les RMs les plus hétérogènes sont GL-O et Mica-Fe, les plus homogènes étant Mica-Mg et FK-N. Les âges isotopiques Rb-Sr moyens calculés sont 521 ± 24 Ma pour Mica-Mg, 287 ± 55 Ma pour Mica-Fe, 89.2 ± 9.9 Ma pour GL-O et 512 ± 30 Ma pour FK-N. L'âge proposé pour Mica-Fe est incertain en raison de la dispersion élevée des analyses individuelles, liée à la composition hautement radiogénique de la biotite et à la présence de nombreuses inclusions minérales. Nous recommandons l'utilisation des valeurs $^{87}Sr/^{86}Sr$ et $^{87}Rb/^{86}Sr$ proposées et des incertitudes associées lors de l'utilisation des 4 RMs pour la datation Rb-Sr in situ par LA-ICP-MS/MS. La disponibilité de ces 4 échantillons bien caractérisés permettra de progresser dans le développement et l'application des datations Rb-Sr par LA-ICP-MS/MS.

Mots-clés : datation Rb-Sr, LA-ICP-MS/MS, matériaux de référence, in-situ, mica, feldspath

Characterisation of Reference Materials for *In Situ* Rb-Sr Dating by LA-ICP-MS/MS

Yujin **Jegal** (1, 2)*, Catherine **Zimmermann** (1), Laurie **Reisberg** (1), Delphine **Yeghicheyan** (1), Christophe **Cloquet** (1), Chantal **Peiffert** (2), Marie **Gerardin** (2), Etienne **Deloule** (1) and Julien **Mercadier** (2)

(1) Université de Lorraine, CNRS, CRPG, Vandoeuvre-lès-Nancy 54500, France
(2) Université de Lorraine, CNRS, GeoRessources, Vandoeuvre-lès-Nancy 54506, France
* Corresponding author. e-mail: yujin.jegal@univ-lorraine.fr

We present Rb and Sr mass fraction and $^{87}Sr/^{86}Sr$ isotope ratio measurement results for four reference materials (RMs) obtained from the Service d'Analyse des Roches et des Minéraux (SARM), Nancy, France: Mica-Mg, Mica-Fe, GL-O and FK-N. These four RMs have different chemical compositions spanning the range of those of most K-bearing feldspars and micas, making them potential calibration materials for *in situ* Rb-Sr dating of natural minerals by LA-ICP-MS/MS. Selected grains and flakes from the four RMs present variable degrees of heterogeneity observable by SEM-EDS and EPMA imaging, and chemical mapping. This heterogeneity is mainly related to inclusions of minerals within flakes and grains and to chemical substitutions linked to crystallographic control and alteration processes. The Mica-Mg RM is the least affected. The powders available at the SARM were analysed by ID-TIMS ($^{87}Sr/^{86}Sr$ and Sr) and ID-MC-ICP-MS (Rb) after digestion and separation. The mean $^{87}Rb/^{86}Sr$ ratios are 155.6 ± 4.7% (2*s*, as for other RMs) for Mica-Mg, 1815 ± 14% for Mica-Fe, 36.2 ± 11% for GL-O and 69.9 ± 5.9% for FK-N. The mean $^{87}Sr/^{86}Sr$ ratios are 1.8622 ± 0.36% (2*s*, as for other RMs) for Mica-Mg, 7.99 ± 13% for Mica-Fe, 0.75305 ± 0.12% for GL-O, and 1.2114 ± 0.17% for FK-N. The four RMs each show dispersion in $^{87}Sr/^{86}Sr$ and Rb and Sr mass fractions, to degrees that differ between RMs and that reflect the heterogeneity of their original crystals. The most heterogeneous RMs are GL-O and Mica-Fe. The calculated mean Rb-Sr isotopic ages are 521 ± 24 Ma for Mica-Mg, 287 ± 55 Ma for Mica-Fe, 89.2 ± 9.9 Ma for GL-O and 512 ± 30 Ma for FK-N. The proposed age for Mica-Fe may be unreliable due to the elevated dispersion of individual analysis linked to the highly radiogenic composition of the biotite and to the presence of numerous mineral inclusions. We recommend use of these proposed working values of $^{87}Sr/^{86}Sr$ and $^{87}Rb/^{86}Sr$ ratios and associated uncertainties when using the four RMs for *in situ* Rb-Sr dating by LA-ICP-MS/MS. The availability of these four well-characterised RMs will allow progress in the development and application of the Rb-Sr dating approach by LA-ICP-MS/MS.

Keywords: Rb-Sr dating, LA-ICP-MS/MS, reference material, *in situ*, mica, feldspar.

Received 27 Feb 22 – Accepted 23 Jul 22

The Rb-Sr geochronometer (see summary in Nebel 2014) has been widely used for decades to date and constrain the cooling history of geological events based on the Rb-Sr decay system. In this system ^{87}Rb undergoes β- decay to ^{87}Sr with a constant of 1.3972 ± 0.0045 × 10^{-11} a^{-1} (Villa *et al.* 2015), corresponding to a half-life of ~ 49.6 Ga. Rubidium is a common element in numerous minerals, such as K-rich phases in which Rb^{1+} substitutes for K^{1+}. The Rb-Sr dating method is particularly useful for rocks that lack minerals such as zircon or monazite that are datable using the U-Pb radiometric couple. To define Rb-Sr isochrons, $^{87}Rb/^{86}Sr$ and $^{87}Sr/^{86}Sr$ ratios have been traditionally measured in co-genetic minerals and/or whole rock powders (Armstrong *et al.* 1966, Walawender *et al.* 1990, Freeman *et al.* 1997, Glodny *et al.* 2002, 2008) by conventional isotope dilution thermal ionisation mass spectrometry (TIMS) or multi-collector inductively coupled plasma-mass spectrometry (MC-ICP-MS) with a precision (2*s*) of *ca.* 0.1–0.2% for Rb/Sr measurements (Waight

doi: 10.1111/ggr.12456

et al. 2002, Willigers *et al.* 2004, Nebel *et al.* 2005, Nebel and Mezger 2006). Quadrupole based ICP-MS (ICP-QMS) has also been used for $^{87}Sr/^{86}Sr$ isotope ratio measurement when high precision is not required (Vanhaecke *et al.* 1999). To measure $^{87}Rb/^{86}Sr$ and $^{87}Sr/^{86}Sr$ ratios in co-genetic pure mineral separates by these analytical approaches, samples need to be initially prepared by crushing followed by extraction of minerals by hand-picking or mineral separation (Chen *et al.* 1996, Fletcher *et al.* 1997, Li *et al.* 2005, Farina *et al.* 2014, Eberlei *et al.* 2015). The dissolution of mineral separates and/or powders is followed by the chemical separation of Rb from Sr using extraction chromatography, which is required to remove isobaric interference of ^{87}Rb on ^{87}Sr. Conventional Rb-Sr dating using digestion and wet chemistry methods is consequently analytically time-consuming, and could moreover be affected by geological and mineralogical limitations that perturb the isotopic systems of target minerals, such as inclusions, alteration and/or complex age zonation.

Recently, the use of tandem ICP mass spectrometers (ICP-MS/MS) associated with suitable reaction gases (O_2, N_2O, SF_6 or CH_3F) has been demonstrated to be a promising approach for resolving the ^{87}Rb-^{87}Sr isobaric overlap without prior Rb-Sr chemical separation (Bolea-Fernandez *et al.* 2016a, Liu *et al.* 2020). These results are based on initial work by Moens *et al.* (2001) that demonstrated that Sr^+ selectively reacts with CH_3F in an ICP-MS equipped with a dynamic reaction cell (DRS) by forming SrF^+ ions. The experimental study of Cheng *et al.* (2008) reported that Sr^+ is much more reactive than Rb^+ with CH_3F or SF_6, forming SrF^+ by F-atom transfer, and with N_2O or O_2, forming SrO^+ by O-atom transfer. The coupling of a laser ablation (LA) system with such ICP-MS/MS associated with appropriately selected reaction gases now allows *in situ* Rb-Sr dating of geological samples with short sample preparation and analytical times, and precisions of *ca.* 1.0–2.5% for Rb-Sr dating (Zack and Hogmalm 2016, Hogmalm *et al.* 2017, Gorojovsky and Alard 2020, Redaa *et al.* 2021). This new approach avoids the drawbacks of the bulk Rb-Sr method and is revolutionising the application of Rb-Sr age dating in geosciences. Its use has increased over the past few years for geochronological analyses of K-bearing mica and/or feldspar minerals in various case studies: in hydrothermal vein and fault systems (Tillberg *et al.* 2017, Tillberg *et al.* 2020), in ore (Şengün *et al.* 2019, Olierook *et al.* 2020) and mineral deposits (Redaa *et al.* 2021), for kimberlites (Gorojovsky and Alard 2020), and for the characterisation of Archaean to Proterozoic crustal rocks (Li *et al.* 2020).

The *in situ* Rb-Sr dating method by LA-ICP-MS/MS, however, currently faces some challenges that limit the accuracy and precision of the measured ^{87}Sr-^{86}Sr and ^{87}Rb-^{86}Sr ratios and related Rb-Sr ages. Among these limitations, the main ones are elemental and isotopic fractionation and matrix effects. Such effects during LA-ICP-MS analysis of other elemental and isotope systems have been investigated by many studies (e.g., Rodushkin *et al.* 2002, Jackson and Günther 2003, Jackson and Sylvester 2008, Claverie *et al.* 2009, Liu *et al.* 2013, Zhang *et al.* 2016 among others) and recently have been documented for LA-ICP-MS/MS analysis applied to Rb-Sr dating (Gorojovsky and Alard 2020, Redaa *et al.* 2021). Gorojovsky and Alard (2020) showed that the use of reference materials (RMs) with diverse matrices using different laser systems and conditions can significantly affect the accuracy of $^{87}Sr/^{86}Sr$ and $^{87}Rb/^{86}Sr$ ratios of selected minerals and thus their calculated Rb-Sr ages. Redaa *et al.* (2021) also reported that different ablation parameters and contrasts between the physical properties of nano-powder pellet and glass RMs and phlogopites can influence the accuracy of the obtained Rb-Sr ages. Measurements of $^{87}Sr/^{86}Sr$ and $^{87}Rb/^{86}Sr$ ratios by LA-ICP-MS/MS consequently require use of the same analytical conditions and "external" calibration using RMs with physical and chemical properties similar to those of the unknown natural samples (Zack and Hogmalm 2016, Hogmalm *et al.* 2017). Thus, homogeneous RMs with well-characterised Rb/Sr ratios and Sr isotopic compositions are crucial for accurate calibration of LA-ICP-MS/MS systems when used for *in situ* Rb-Sr geochronology. Unfortunately, the availability of suitable RMs is limited. As a result, synthetic reference glasses such as NIST SRM 610 or 612 have been widely used as primary calibration materials for *in situ* measurements of $^{87}Sr/^{86}Sr$ values of geological reference glasses and natural minerals (Zack and Hogmalm 2016, Bolea-Fernandez *et al.* 2016b, Hogmalm *et al.* 2017, Şengün *et al.* 2019, Gorojovsky and Alard 2020, Li *et al.* 2020, Olierook *et al.* 2020, Redaa *et al.* 2021). NIST SRM 612 and USGS BCR-2G or USGS BHVO-2G, although subject to matrix effects, have also been used to calibrate $^{87}Rb/^{86}Sr$ ratios of natural minerals such as feldspars (Zack and Hogmalm 2016, Gorojovsky and Alard 2020, Tillberg *et al.* 2020). The CRPG phlogopite Mica-Mg (Govindaraju 1979) is currently used as a RM to calibrate $^{87}Rb/^{86}Sr$ ratios of micas (Hogmalm *et al.* 2017, Şengün *et al.* 2019, Gorojovsky and Alard 2020, Li *et al.* 2020, Olierook *et al.* 2020, Redaa *et al.* 2021, Rösel and Zack 2021), using the $^{87}Rb/^{86}Sr$ values for Mica-Mg proposed by Hogmalm *et al.* (2017). While this alleviates concerns about matrix effects, it raises the issue of possible Rb/Sr heterogeneity in this natural material. In the study of Hogmalm *et al.* (2017), the $^{87}Sr/^{86}Sr$ ratio of Mica-Mg was measured and calibrated relative to NIST SRM 610 by

LA-ICP-MS/MS, and the $^{87}Rb/^{86}Sr$ ratio was calculated using the mean of the reported ages (519.4 ± 6.5 Ma) in the Bekily area of Madagascar where the Mica-Mg phlogopite was collected, coupled with an initial ratio of 0.72607 ± 0.00070 from Morteani *et al.* (2013). The homogeneity of Mica-Mg is currently unknown, and true $^{87}Sr/^{86}Sr$ and $^{87}Rb/^{86}Sr$ values are not yet characterised. More broadly, the development and distribution of matrix-matched RMs are critical to expanding the application of *in situ* Rb-Sr dating to minerals, such as micas and feldspars, covering various matrices and a wide range of $^{87}Sr/^{86}Sr$ and $^{87}Rb/^{86}Sr$.

Therefore, the aim of this work is to characterise and establish RMs suitable for *in situ* Rb-Sr geochronology of micas and feldspars by LA-ICP-MS/MS. Four RMs, phlogopite Mica-Mg, biotite Mica-Fe, glauconite GL-O and potassium feldspar FK-N, were obtained from the Service d'Analyse des Roches et des Minéraux (SARM) of the CRPG laboratory in Nancy, France. The nature and homogeneity of the RMs were first investigated by imaging and elemental mapping of the mineral grains before powdering. Isotope dilution MC-ICP-MS and TIMS were performed to determine $^{87}Sr/^{86}Sr$ and $^{87}Rb/^{86}Sr$ ratios for these four RMs using different powder batches. Based on the results, recommended values of these parameters and related absolute ages are proposed.

Sample selection

The RMs in this study were selected based on their compositional variation which spans a large range in Rb/Sr ratios (12–440), covering the global chemical compositions of micas and feldspars from different locations compiled in the Georoc database (Figure 1). They include a phlogopite (Mica-Mg), a biotite (Mica-Fe), a glauconite (GL-O) and a potassium feldspar (FK-N), which are certified for their chemical compositions and distributed by the SARM (Service d'Analyse des Roches et des Minéraux, CNRS National facility; https://sarm.cnrs.fr/), located at the Centre de Recherches Pétrographiques et Géochimiques (CRPG, Nancy, France). Details of the sample collection, preparation, and working values of the RMs were reported by Govindaraju (1979, 1984, 1995) and Odin *et al.* (1982) and the RMs are available on request. Phlogopite Mica-Mg originates from a phlogopite deposit of the Bekily area, southern Madagascar (Govindaraju 1979). Biotite Mica-Fe is extracted from biotitite emplaced in magmatic shear zones within the Saint-Sylvestre two mica leucogranitic complex near Razès, France (Govindaraju 1979, Friedrich 1983). Glauconite GL-O was sampled from a calcareous and glauconitic sand in the basal Cenomanian section in the Cauville cliff, Normandy, France (Odin *et al.* 1982). Potassium feldspar FK-N is from Tamil Nadu, India (Govindaraju 1984). Brief descriptions of reported geochronological data for the four RMs are presented in Table 1. The reported ages range from 503 ± 15 to 528 ± 9 Ma for Mica-Mg, from 307.6 ± 0.4 to 321 ± 10 Ma for Mica-Fe, and from 80.9 to 98.2 Ma for GL-O. Precise sample location and age data for the FK-N RM have not been reported (Govindaraju 1984), but a Rb-Sr age based on samples from leucogranites and pegmatites from Tamil Nadu considered to be co-genetic with FK-N was proposed (521 ± 9 Ma; Pandey *et al.* 1993).

In this work, all four RMs were investigated in powder form and as mineral grains for GL-O and FK-N and flakes for Mica-Mg and Mica-Fe (Table S1). The powdered RMs were provided by the SARM in the form of three bags (10 g each) for Mica-Mg and Mica-Fe and as aliquots of less than 5 g for GL-O and FK-N. A 10 g bag is the conventional form of distribution of RM by the SARM. Multiple powder batches (50–110 mg for each batch) from the different bags and aliquots were analysed by isotope dilution TIMS and MC-ICP-MS. Multiple powder batches (200 mg) of the RMs were also analysed by alkali fusion ICP-MS. The powder batches for alkali fusion ICP-MS analyses were from three bags (10–20 g) for each of the RM, which are different from the bags and aliquots used for ID-TIMS and MC-ICP-MS analyses. Additionally, several grains (GL-O and FK-N) and flakes (Mica-Mg and Mica-Fe) were randomly selected and investigated by SEM-EDS and EPMA. For simplicity, the form of the four RMs analysed by SEM-EDS and EPMA is indicated as "grains" in the rest of this work.

Analytical methods

SEM-EDS and EPMA

Several grains from the four RMs were randomly selected, and embedded in epoxy resin, abraded and polished. Polished sections were carbon coated for scanning electron microscopy (SEM) and electron probe microanalysis (EPMA). A TESCAN VEGA3 SEM equipped with an EDS (Bruker Xflash6 30 mm^2) was used for mineralogical observations at the Service Commun de Microscopie Electronique et de Microanalyses (SCMEM) of the GeoRessources laboratory (Vandoeuvre-lès-Nancy, France). Backscattered electron (BSE) images were obtained with an accelerating voltage of 15 kV, a beam current of 10 nA and a working distance of 15 mm. Major element compositions were determined by EPMA (CAMECA SX100) equipped with wavelength dispersive spectrometers (WDS) at the SCMEM of the GeoRessources laboratory. An accelerating of voltage of 15 kV and a beam current of

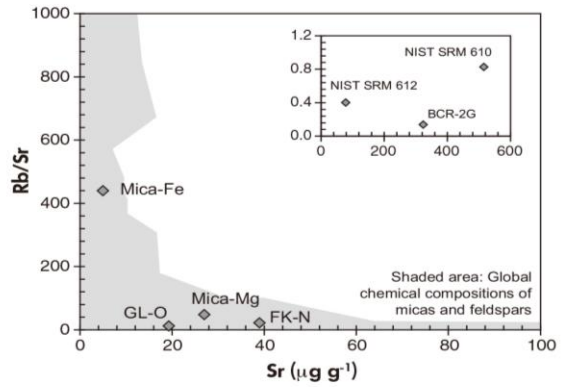

Figure 1. Rb/Sr and Sr (μg g^{-1}) diagram showing the accepted working values (Govindaraju 1995) for the four reference materials (Mica-Mg, Mica-Fe, GL-O and FK-N) used in this study. Inset shows these values for the certified reference materials NIST SRM 610, NIST SRM 612 and BCR-2G (Woodhead and Hergt 2001, Elburg *et al.* 2005, Wise and Watters 2012) used in previous LA-ICP-MS/MS studies of Rb-Sr dating of natural minerals. Note the difference in Sr and Rb/Sr scales relative to the main figure. Grey shaded area indicates the chemical composition of micas and feldspars from different locations compiled in the Georoc database (http://www.georoc.mpch-mainz.gwdg.de/).

12 nA were used with a counting time of 10 s per element. X-ray element distribution maps by SEM-EDS were acquired with a dwell time of 16.384 ms per pixel and an image resolution of 512 × 512 pixels. X-ray maps by EPMA were obtained using a step size of 5–9 μm, dwell time of 200 ms, accelerating voltage of 15 kV, current at 100 nA and a beam diameter of 1 μm.

Alkali fusion ICP-MS

The four RMs powders were analysed by ICP-MS measurements using the alkali fusion technique applied routinely at the SARM adapted from the procedure of Carignan *et al.* (2001). Briefly, 200 mg were weighted in a Pt crucible and mixed with 600 mg of ultrapure $LiBO_2$. Ultrapure $LiBO_2$ is produced from pure lithium carbonate and boric acid at the SARM, allowing much lower blank levels to be attained than with commercially available $LiBO_2$. The samples were progressively heated to 980 °C and maintained for about 40 min at this temperature. The resulting fused beads were cooled at room temperature before dissolution of the glass in a solution containing 0.5 mol l^{-1} HNO_3 and distilled glycerol, which serves as a wetting agent. Dilution of the resultant solution by a factor of 10 was done in PTFE vials before analysis using an iCAP Q ICP-MS (Thermo Fisher Scientific). Lithium, Rh and Re were used as internal standard elements for the measurements. Each RM was sampled from three different 10 g bags and two powder aliquots were digested from each bag (Table S1). Each digestion was measured three times to give a total of eighteen measurements for each material. The Sr and Rb contents (μg g^{-1}) in batches of $LiBO_2$ ranged from 0.005 to 0.065 and from 0.010 to 0.050, respectively, which would thus contribute < ~ 3.3% (Mica-Fe) and < ~ 1% (other RMs) of the total Sr and < ~ 0.3% (BE-N) and < ~ 0.1% (other RMs) of the total Rb present in the samples.

Isotope dilution TIMS and MC-ICP-MS

Spike calibration: The ^{84}Sr-enriched (99.64%) and ^{85}Rb-enriched (99.77%) isotope tracers (spikes) from Oak Ridge Laboratory (ORNL, Tennessee, USA) were prepared separately. The isotopic compositions of the Sr spike reported in assays provided by ORNL in 1999 was used in this work. The Rb isotopic compositions of the Rb spikes were measured in this study using a Neptune Plus MC-ICP-MS at CRPG. For calibration of the Rb spike concentration, the ASTASOL® standard solution (Analytica®, spol. s.r.o.) of 1000 ± 2 mg l^{-1} Rb was diluted to 10 μg ml^{-1} solution in 2% HNO_3 then mixed with the spike solution in spike/standard mass ratios ranging from *ca.* 0.22 to 0.30. The Sr spikes were calibrated using NIST SRM 987 powder dissolved and diluted to 10 μg g^{-1} solution in 2% HNO_3 using spike/standard weight ratios of 1.6 to 8.2. Isotope measurements of the mixtures were performed using a Neptune Plus MC-ICP-MS for Rb and a TRITON Plus thermal ionisation instrument (TIMS) for Sr at CRPG. Replicate calibrations yield values for ^{84}Sr (M/g) of 3.53 × 10^{-8} ± 0.66% for Spk-3 and 7.03 × 10^{-9} ± 0.47% for Spk-4 and values for ^{85}Rb (M/g) of 9.36 × 10^{-6} ± 1.9% for Spk-1 and 1.98 × 10^{-7} ± 1.7% for Spk-2 (all total uncertainties 2*s* %, Table 2). The total uncertainties (2*s*%) of the Rb spikes presented in Table 2 are dominated by the uncertainties associated with the replicate calibrations but also include the uncertainties on the ASTASOL solution.

Chemistry and analyses: Digestion, chemical separation and purification were performed in laminar flow hoods in a clean laboratory with filtered air at CRPG. To determine the Rb-Sr isotopic compositions of the powdered RMs, multiple batches from aliquots of SARM sample bags (Table S1) were analysed using 50 to 110 mg for each analysis. The sample powders were doped with calibrated ^{85}Rb-enriched and ^{84}Sr-enriched spikes, with the amount of

Table 1.
Previously reported ages for the samples and for their host rocks or associated deposits with Rb-Sr model ages of the samples in this study

Sample	Age (Ma)	Reference	Method
Mica-Mg	524.7 ± 2.7	Zimmermann *et al.* (1985)	K-Ar of Mica-Mg flakes
	503 ± 15[a]	Govindaraju (1979)	Rb-Sr of Mica-Mg
	522 ± 12	Govindaraju (1979)	K-Ar of Mica-Mg flakes
	528 ± 9.37	Laureijs *et al.* (2021)	Rb-Sr of Mica-Mg powder
	526 ± 34	Kröner *et al.* (1996)	U-Pb of zircon lower interception from K-feldspar gneiss from Ihosy quarry, southern Madagascar
	518 ± 8[a]	Morteani *et al.* (2013)	Rb-Sr of phlogopites from the pegmatites, Ampandrandrava, southern Madagascar
	499 ± 10[a]	Martin *et al.* (2014)	Rb-Sr of calcite-phlogopite from the Sakamasy deposit, southern Madagascar
	500 ± 10[a]	Martin *et al.* (2014)	Rb-Sr of calcite-phlogopite from the Sakaravy deposit, southern Madagascar
	521 ± 24[b]	this study	Rb-Sr of Mica-Mg by ID-TIMS and MC-ICP-MS[b]
GL-O	80.9–98.2[a]	Odin *et al.* (1982)	Rb-Sr of GL-O powder
	87.5–95.6[a]	Odin *et al.* (1982)	Rb-Sr of GL-O grains
	93.1–96.7[a]	Odin *et al.* (1982)	K-Ar of GL-O grains
	88.3–95.8[a]	Smith *et al.* (1998)	Ar-Ar of GL-O grains
	89.2 ± 9.9[b]	this study	Rb-Sr of GL-O by ID-TIMS and MC-ICP-MS[b]
Mica-Fe	315.9 ± 8.5	Zimmermann *et al.* (1985)	K-Ar of Mica-Fe flakes
	321 ± 10[a]	Govindaraju (1979)	Rb-Sr of Mica-Fe
	310 ± 10	Govindaraju (1979)	K-Ar of Mica-Fe
	307.6 ± 0.4	Grove and Harrison (1996)	Ar-Ar of Mica-Fe flakes
	324 ± 4	Holliger *et al.* (1986)	U-Pb upper intercept age of monazite and zircon from the western part of the Saint-Sylvestre Massif
	320.1 ± 18.3[a]	Duthou (1977)	Rb-Sr of whole-rock, Saint-Sylvestre leucogranite
	302.10 ± 0.87	Scaillet *et al.* (1996)	Ar-Ar plateau age obtained on muscovites from the Saint-Sylvestre granite
	302.44 ± 063	Scaillet *et al.* (1996)	Ar-Ar plateau age obtained on biotites from the Saint-Sylvestre granite
	301.44 ± 0.65	Scaillet *et al.* (1996)	
	287 ± 55[b]	this study	Rb-Sr of Mica-Fe by ID-TIMS and MC-ICP-MS[b]
FK-N	521 ± 9[a]	Pandey *et al.* (1993)	Rb-Sr of leucogranite and alkali feldspar pegmatite granite in Tamil Nadu, India
	512 ± 30[b]	this study	Rb-Sr of FK-N by ID-TIMS and MC-ICP-MS[b]

[a] Recalculated using revised ^{87}Rb decay constant of Villa *et al.* (2015)
[b] Rb-Sr model ages calculated from the mean Rb-Sr isotopic values and total uncertainties by ID-TIMS and MC-ICP-MS and assumed initial Sr ratio. Details of the calculation are described in section 'Model ages of the RMs'.

each spike dependent on the sample compositions (Table 2). The samples were then dissolved in a mixture of 1.5 ml ultra-pure HF (Seastar Chemicals) and 1.5 ml concentrated HNO_3 (67–69%, PlasmaPURE Plus Acids) on a hot plate (120 °C) for about 48 h. Samples were dried at 110 °C and refluxed with 3 ml of ultra-pure 6 mol l^{-1} HCl (Seastar Chemicals) at 120 °C for more than 48 h to dissolve fluorides precipitated during the first dissolution. After drying, 1 ml of 2.5 mol l^{-1} HCl was added to each beaker, and the samples were centrifuged in 1-ml plastic centrifuge tubes. Next, 0.5 ml of the resulting solution was loaded on cation exchange resin (AG-50X8) columns for Rb and Sr separation and removal of the matrix. The Sr fractions were purified by loading again on the same columns after cleaning the resin with 6 mol l^{-1} HCl and purified water. This procedure resulted in Rb and Sr fractions with only small isobaric interferences ($^{85}Rb/^{86}Sr < 0.0001$ for Sr determinations by TIMS; $^{88}Sr/^{85}Rb < 0.0002$ ($^{86}Sr/^{85}Rb < 0.00001$) for Rb determinations by MC-ICP-MS).

Strontium isotopic compositions were measured using a TRITON Plus TIMS at CRPG. Mass fractionation was corrected using an exponential law and assuming a natural $^{86}Sr/^{88}Sr$ ratio of 0.1194 for normalisation. However, the spike contains trace amounts of Sr isotopes other than ^{84}Sr, which have a minor effect on the measured ratios of both $^{87}Sr/^{86}Sr$ and $^{86}Sr/^{88}Sr$, and thus on the fractionation correction. For this reason, the corrections for fractionation and for the spike contribution to $^{87}Sr/^{86}Sr$ were done offline, using an iterative routine that allows the appropriate fractionation factor for the spike-sample mixture to be calculated. As the approximate Sr mass fractions were known in advance, it was possible to avoid overspiking and the large corrections and associated uncertainties on the $^{87}Sr/^{86}Sr$ ratios that would result. The mean $^{87}Sr/^{86}Sr$ for NIST SRM 987 obtained from fifty-three replicate analyses during the TIMS session of this study was 0.710242 ± 20 (2*s*). Within-run errors (2SE) of $^{87}Sr/^{86}Sr$ were generally better than 0.00001, except for Mica-Fe (0.00005–0.0003)

Table 2.
^{85}Rb and ^{84}Sr (M/g) of the ^{85}Rb and ^{84}Sr spikes, respectively, and uncertainties (2*s*%). The uncertainties of the Rb spikes are total values that include both the variation of replicate spike calibration measurements and uncertainties on the concentrations of the solutions used for calibration. The ^{85}Rb and ^{84}Sr spikes were added separately in differing amounts depending on the sample compositions

Spike	M/g	2*s*%	Spiked samples
Rb Spike			
Spk-1	9.36×10^{-6}	1.9	Mica-Mg, Mica-Fe, GL-O, FK-N, NIST SRM 607, GA
Spk-2	1.98×10^{-7}	1.7	BE-N
Sr Spike			
Spk-3	3.53×10^{-8}	0.66	Mica-Mg, GA, BE-N
Spk-4	7.03×10^{-9}	0.47	Mica-Fe, GL-O, FK-N, NIST SRM 607

Spike calibration uncertainties of the Rb spikes include both two standard deviation (2*s*) variation of replicate analyses and uncertainties of the mass fraction of the reference material used for calibration.

due to its low Sr content resulting in low intensity of the ^{86}Sr signal (≤ 0.6 V).

Rubidium measurements were performed on a Thermo Fisher Scientific Neptune Plus MC-ICP-MS at CRPG. The ^{85}Rb, ^{87}Rb and ^{88}Sr ion beams were collected on L4, L2 and L1 Faraday cups, respectively. The signal of ^{88}Sr was monitored for correction of the interference of ^{87}Sr on ^{87}Rb by assuming a constant ^{87}Sr/^{88}Sr ratio of 0.085. The signal of ^{88}Sr was always less than 1 mV with a ^{88}Sr/^{85}Rb ratio $< 2 \times 10^{-4}$. For the most radiogenic Sr sample in this study, Mica-Fe, use of the interference correction obtained assuming a ^{87}Sr/^{88}Sr ratio of 0.085 compared with that obtained using the measured ratio (~ 1.0 for Mica-Fe) resulted in calculated Rb contents that differed by less than 0.04%. Thus, a constant ^{87}Sr/^{88}Sr ratio of 0.085 was used for the interference correction for the studied samples. Each block of Rb isotope analyses consisted of fifty cycles of data with an integration time of 4.194 s per cycle. The mass bias drift was corrected by sample-standard bracketing using a 50 or 100 ng ml^{-1} Rb standard solution (Plasma CAL or ASTASOL®). During the individual measurement sessions, the reproducibility of ^{87}Rb/^{85}Rb for the standard solutions ranged from 0.05 to 0.08% (2*s*).

Procedural blank contribution and correction: Rubidium and Sr blanks were determined by isotope dilution using the most diluted ^{85}Rb-enriched and ^{84}Sr-enriched spikes. A total of fifteen total chemistry blank analyses were done for nine sample digestion series, with one or two blank measurements per series. Twelve of the Sr blanks obtained were < 2000 pg, with most being < 500 pg, but three exceptionally high blanks were found, with values of 4351 pg, 4886 pg, and 9078 pg (Figure 2). Because of the highly skewed blank distribution, use of the mean value (1641 pg) for blank correction would lead to a small but systematic bias in Sr mass fractions and isotopic ratios. For this reason, the median value of the Sr blanks (294 pg) was used. A ^{87}Sr/^{86}Sr ratio of 0.708 was assumed for Sr blank correction because the low ^{86}Sr signals of the blanks (always ≤ 0.16 V, with most runs < 0.01 V, Figure S1), prevented reliable analysis of their isotopic compositions. The Rb-Sr data of samples associated with the high blank with 4886 pg of Sr were rejected and are not presented here, while those run with the two other high blanks with values of 4351 pg and 9078 pg were accepted and yielded results in good agreement with those from other sessions. A second blank from the same digestion series as the 4351 pg blank was much lower (1784 pg).

The potential influence of rare high Sr blanks was evaluated by comparing the amount of Sr in the highest measured blank (9078 pg) with the Sr contents of each of the sample digestions. In the worst case, an aliquot of RM Mica-Fe containing 573 ng of Sr (Table S3), this high blank would represent 1.6% of the measured Sr. For all other reference materials, the blank contribution would be less than 1%. The effects of such contributions are shown in Table S4. For each RM, this table shows the mean Sr mass fraction, ^{87}Sr/^{86}Sr, ^{87}Rb/^{86}Sr, and the resulting age calculated assuming: (1) no blank correction; (2) the median Sr blank of 294 pg; (3) the maximum Sr blank of 9078 pg. For Mica-Fe, use of the maximum rather than the median blank would change the calculated Sr concentration by -1.4% and the ^{87}Sr/^{86}Sr ratio by 2.2%. For Mica-Mg, the changes would be -0.3% and 0.21%, respectively, while the effects on GL-O and FK-N would be similarly small (Table S4). These effects are smaller than the uncertainties on the mean Sr mass fractions and Sr isotopic compositions representing the means of the analyses of individual digestions (Tables 3a–3c). Furthermore, as the Sr blank effects on ^{87}Sr/^{86}Sr and ^{87}Rb/^{86}Sr are strongly correlated, the influence of the blank on the calculated age is negligible, ranging from 0.00% for GL-O and FK-N to 0.02% for Mica-Mg and 0.03% for Mica-Fe. We therefore conclude that the occasional high Sr blanks obtained during our measurements had no significant effect on the results.

The total chemistry blanks for Rb were negligible. By this we mean that, after correction for the instrumental blank preceding each analysis, the ^{87}Rb/^{85}Rb ratios of the blanks were smaller than the ^{87}Rb/^{85}Rb ratios of the spikes, resulting in

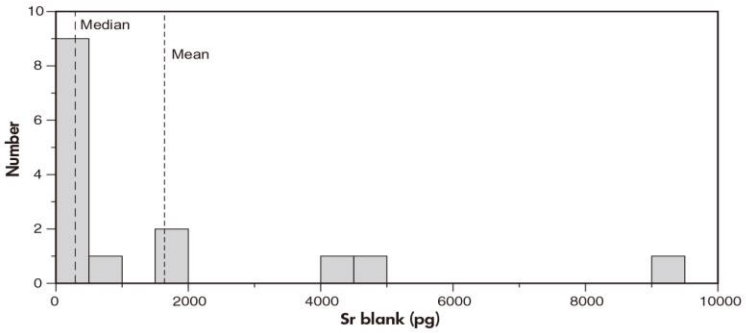

Figure 2. Frequency (number) of Sr procedural blanks during the course of this work for nine sample digestion series. Each series included one to two blanks, for a total of fifteen blanks. The difference between the median and mean values reflects the highly skewed blank distribution. Details concerning the Sr procedural blanks and their potential effects on the results are given in section 'Procedural blank contribution and correction'.

nonsensical calculated blank values. To place some constraints on the maximum potential Rb blank contribution, we calculated the Rb blanks using the measured $^{87}Rb/^{85}Rb$ ratios uncorrected for the instrumental contributions to ^{87}Rb and ^{85}Rb. The resulting apparent blanks, which overestimate the true total chemistry blanks, range from 526 to 1207 pg. This represents < 0.05% of the total quantity of Rb present in each sample (≥ 2495 ng Rb). Therefore, Rb blanks were negligible relative to the amounts of Rb in the samples.

Uncertainties on Rb-Sr ratios and mass fractions: Uncertainties for individual Sr and Rb isotope measurements are within-run uncertainties expressed as 2SE in Table 3, and thus represent minimum errors on the individual measurements. The 2SE values of $^{87}Rb/^{86}Sr$ for individual sample digestions (Table 3) were calculated using the in-run Rb and Sr mass fraction uncertainties. Additional random error sources affecting the individual analyses would include blank variability for Rb and Sr mass fractions and Sr isotopic compositions, and weighing errors for the mass fractions. The latter would also affect $^{87}Rb/^{86}Sr$ ratios, as Rb and Sr spikes were added separately. Weighing uncertainties were approximately ±0.00020 g, which would correspond to uncertainties on the individual $^{87}Rb/^{86}Sr$ ratios ranging from 0.57 to 0.92%, given the quantities of spike added. As discussed in section 'Procedural blank contribution and correction', the uncertainty related to Sr blank variability is somewhat difficult to characterise, given the highly skewed blank distribution shown in Figure 2. Nevertheless, even in the worst case (Mica-Fe and highest blank) the maximum effect on the $^{87}Sr/^{86}Sr$ ratio would be ~ 2%, while the effect on the $^{87}Sr/^{86}Sr$ of the other RMs would be ≤ ~ 0.2%. Adding all of these uncertainty sources together, the total maximum random errors on the individual analyses for Mica-Mg, GL-O, Mica-Fe and FK-N respectively would be <0.75%, < 1.1%, < 2.5%, and < 0.75% for $^{87}Rb/^{86}Sr$ and < 0.21%, < 0.04%, < 2.2% and < 0.20% for $^{87}Sr/^{86}Sr$.

For each RM, the mean uncertainties on Rb and Sr mass fractions and $^{87}Rb/^{86}Sr$ and $^{87}Sr/^{86}Sr$ ratios in Table 3 represent the 2*s* and 2SE values of the means of the individual measurements. The uncertainties on the mean values automatically incorporate all of the random error components affecting each individual analysis. It is evident that the random uncertainties on the mean values for all RMs in this work are much larger than the uncertainties on the individual analyses, even if blank variability and weighing errors are included in the uncertainty on each measurement. Finally, we note that the total uncertainties (2*s*) on the mean values for each RM listed in Table 3 include not only the random components reflected in the 2*s* values, but also a systematic component reflecting the uncertainties on the spike calibration (Table 2).

Reproducibilities of the reference materials: For Mica-Mg and Mica-Fe, duplicate dissolutions (of 100–110 mg powder) and Rb and Sr separations were done on three individual powder batches (Mica-Mg-10, 11, 12 in Table 3a and Mica-Fe-7, 8, 9 in Table 3c), yielding agreement within ≤ 0.27% for Rb in Mica-Mg and Mica-Fe, ≤ 0.42% for Sr in Mica-Mg and Mica-Fe, ≤ 0.16% for $^{87}Sr/^{86}Sr$ in Mica-Mg and ≤ 1.42% for $^{87}Sr/^{86}Sr$ in Mica-Fe. The mean of the duplicates was used when calculating the mean values for each RM.

Rubidium and Sr compositions of NIST SRM 607 K-feldspar, CRPG GA granite and CRPG BE-N basalt were determined in the same sample digestion series and

Table 3a.
Rb-Sr mass fractions and $^{87}Sr/^{86}Sr$ ratios of Mica-Mg for repeat analyses of the studied RMs compared with literature values

Sample/comments	Rb (µg g^{-1})	2SE	2*s*	*n*	Sr (µg g^{-1})	2SE	2*s*	*n*	Rb/Sr
CRPG Phlogopite Mica-Mg									
ID-TIMS and MC-ICP-MS									
(This study)									
Mica-Mg-1					27.057	0.011			
Mica-Mg-2					25.845	0.007			
Mica-Mg-3					26.334	0.009			
Mica-Mg-4					27.173	0.003			
Mica-Mg-5					26.001	0.007			
Mica-Mg-6	1336.8	0.1			27.528	0.003			48.6
Mica-Mg-7	1329.8	0.2			27.011	0.010			49.2
Mica-Mg-8	1324.4	0.2			26.451	0.002			50.1
Mica-Mg-9	1302.5	0.1			27.597	0.004			47.2
Mica-Mg-10[a]	1333.3	0.2			27.849	0.013			47.9
Mica-Mg-10r[a]	1332.0	0.1			27.860	0.009			47.8
Mica-Mg-10[a]	*1332.7*		*1.7*		*27.855*		*0.015*		*47.8*
Mica-Mg-11[a]	1312.8	0.1			27.505	0.005			47.7
Mica-Mg-11r[a]	1312.0	0.1			27.571	0.009			47.6
Mica-Mg-11[a]	*1312.4*		*1.1*		*27.538*		*0.092*		*47.7*
Mica-Mg-12[a]	1352.7	0.2			28.205	0.011			48.0
Mica-Mg-12r[a]	1349.1	0.1			28.224	0.010			47.8
Mica-Mg-12[a]	*1350.9*		*5.2*		*28.215*		*0.026*		*47.9*
Mean[b]	**1327**	12	32	7	**27.05**	0.43	1.50	12	**49.1**
Total uncertainty[c]			**41**				**1.51**		
ICP-MS (this study)									
Mica-Mg	1269	28	63	18	27.19	0.75	1.68	18	47.0
Working value									
Govindaraju (1995)	1300		229		27		14		48.1
Reported value by									
(LA)-ICP-MS/MS									
Hogmlam *et al.* (2017)[d]									
Laureijs *et al.* (2021)[e]	1320		33		27		1		48.1

SE: standard error, s: standard deviation, *n*: the number of values included in a total mean
Each sample name by ID-TIMS and MC-ICP-MS (this study) indicates individual powder batches (50–110 mg) from different sample packets or aliquots as presented in Table S1. Mean values and their total uncertainties **in bold** are displayed in Figure 7 and 8. 2SE values for Rb and Sr mass fractions are based on in-run 2SE uncertainties. 2SE of $^{87}Rb/^{86}Sr$ for individual batches was calculated by error propagation of Rb and Sr mass fraction uncertainties. $^{87}Sr/^{86}Sr$ uncertainties are 2SE in-run values. See text for discussion of other potential sources of uncertainties.
[a] Duplicate analyses of each individual powder batch. The mean of the duplicate values (*italic*) are included in total means.
[b] Total mean value from the replicate measurements of individual powder batches.
[c] Total uncertainty combines the random uncertainty (2*s*) of the mean of the individual analyses with the systematic uncertainty related to spike calibration (Table 2).
[d] Data by LA-ICP-MS/MS (nineteen analytical runs, Hogmalm *et al.* 2017). $^{87}Sr/^{86}Sr$ calibrated relative to NIST SRM 610. $^{87}Rb/^{86}Sr$ was calculated based on the calibrated $^{87}Sr/^{86}Sr$, the mean of reported ages (519.4 ± 6.5 Ma) with an assumed initial ratio (0.72607 ± 0.0007).
[e] Data by ICP-MS/MS for $^{87}Sr/^{86}Sr$ and standard addition ICP-MS for Rb and Sr mass fractions of Mica-Mg powder (Laureijs *et al.* 2021).

measurement sessions as the other RMs for quality control (Table S2). In almost all cases, the measured Rb/Sr and $^{87}Sr/^{86}Sr$ values of these secondary reference materials agree well within uncertainties with the literature values compiled in Table S2. For NIST SRM 607, a difference of 2.3% was observed between our measured values and the NIST certified values for the absolute mass fractions of both Rb and Sr. However, the Rb/Sr ratio differs by only 0.01% suggesting that a minor error in the sample mass may explain the small discrepancies in absolute Rb and Sr mass fractions for this RM. This variation could also be real, as Nebel and Mezger (2006) have documented substantial heterogeneity in this material. In addition, $^{87}Rb/^{86}Sr$ and $^{87}Sr/^{86}Sr$ ratios of NIST SRM 607 obtained in this work are in excellent agreement with previous MC-ICP-MS results (Waight *et al.* 2002, Nebel and Mezger 2006).

Results

Imaging and chemical mapping of RM mineral grains

BSE images and elemental maps obtained by both SEM-EDS and EPMA of selected grains from Mica-Mg,

2*s*	$^{87}Rb/^{86}Sr$	2SE	2*s*	*n*	$^{87}Sr/^{86}Sr$	2SE	2*s*	*n*
					1.86435	0.00001		
					1.86493	0.00001		
					1.86430	0.00001		
					1.86477	0.00002		
					1.86464	0.00003		
	156.34	0.02			1.86192	0.00001		
	158.52	0.06			1.86389	0.00001		
	161.22	0.03			1.86358	0.00001		
	151.92	0.02			1.85976	0.00001		
	154.04	0.08			1.85558	0.00002		
	153.84	0.05			1.85525	0.00001		
	153.94		*0.29*		*1.85542*		*0.00047*	
	153.60	0.03			1.85759	0.00001		
	153.10	0.05			1.85468	0.00001		
	153.35		*0.70*		*1.85614*		*0.00411*	
	154.42	0.06			1.86329	0.00001		
	153.89	0.06			1.86260	0.00002		
	154.16		*0.75*		*1.86295*		*0.00097*	
2.5	**155.6**	2.5	6.5	7	**1.8622**	0.0019	**0.0067**	12
2.7			**7.3**					
3.7								
	154.6		1.9		1.8525		0.0024	
	154.3		6.9		1.8628		0.0049	

GL-O, Mica-Fe and FK-N RMs are shown in Figures 3-6 and Figures S2-S5 (use of SEM-EDS or EPMA is indicated in caption to each panel). Chemical determination of major elements by EPMA for these grains was carried out on zones devoid of impurities, inclusions or alteration to compare with the working values of bulk major element compositions proposed for the four RMs (Table S5-S8).

Phlogopite Mica-Mg: All investigated Mica-Mg grains display darker zones in BSE images that correspond to lower Fe and greater Mg contents relative to the brighter zones, as shown in the grain of Mica-Mg-j (Figure S2h). Nevertheless, Fe and Mg contents measured by EPMA in darker and brighter zones in the grain Mica-Mg-j agree within analytical error, and both agree with the working values of Govindaraju (1995) (Table S5). Compositional variability also appears in EPMA elemental maps (Figures S2a, S2c, S2d, S2f). The intra-grain variability of Mica-Mg grains is relatively limited for major elements (SiO_2, Al_2O_3, FeO, MgO and K_2O), as shown by the low 1*s* values of the means of the analysed EPMA points for each grain (Table S5). In the SEM-EDS elemental maps, the grains appear to have

Table 3b.
Rb-Sr mass fractions and $^{87}Sr/^{86}Sr$ ratios of GL-O and FK-N for repeat analyses of the studied RMs compared with literature values

Sample/comments	Rb (µg g^{-1})	2SE	2*s*	*n*	Sr (µg g^{-1})	2SE	2*s*	*n*	Rb/Sr
CRPG Glauconite GL-O									
ID-TIMS and MC-ICP-MS									
(This study)									
GL-O-1	236.18	0.03			17.676	0.002			13.4
GL-O-2	224.59	0.04			18.797	0.004			11.9
GL-O-3	217.29	0.03			18.244	0.002			11.9
GL-O-4	234.01	0.02			18.614	0.010			12.6
Mean[b]	**228**	9	17	4	**18.33**	0.49	1.0	4	**12.4**
Total uncertainty[c]			**18**				**1.0**		
ICP-MS (this study)									
GL-O	237	5	11	18	19.11	1.02	2.3	18	12.4
Working value									
Govindaraju (1995)	238	5			19.3	0.5			12.3
Compiled value of									
different laboratories from									
Odin et al. (1982)									
GL-O powder[f]	239		11	5	19.2		2.2	5	
GL-O grains[f]	239		12	15	19.3		2.1	15	
CRPG Potassium Feldspar FK-N									
ID-TIMS and MC-ICP-MS (this study)									
FK-N-1	814.5	0.2			36.522	0.004			22.3
FK-N-2	873.9	0.1			37.149	0.023			23.5
FK-N-3	870.5	0.1			37.490	0.014			23.2
Mean[b]	**853**	39	67	3	**37.05**	0.57	1.0	3	**23.0**
Total uncertainty[c]			**69**				**1.0**		
ICP-MS (this study)									
FK-N	836	21	46	18	36.67	0.83	1.9	18	22.8
Working value									
Govindaraju (1995)	860		112		39		17		22.1

SE: standard error, *s*: standard deviation, *n*: the number of values included in a total mean
Each sample name by ID-TIMS and MC-ICP-MS (this study) indicates individual powder batches (50–110 mg) from different sample packets or aliquots as presented in Table S1. Mean values and their total uncertainties **in bold** are displayed in Figures 7 and 8. 2SE values for Rb and Sr mass fractions are based on in-run 2SE uncertainties. 2SE of $^{87}Rb/^{86}Sr$ for individual batches was calculated by error propagation of Rb and Sr mass fraction uncertainties. $^{87}Sr/^{86}Sr$ uncertainties are 2SE in-run values. See text for discussion of other potential sources of uncertainties.
[b] Total mean value from the replicate measurements of individual powder batches.
[c] Total uncertainty combines the random uncertainty (2*s*) of the mean of the individual analyses with the systematic uncertainty related to spike calibration (Table 2).
[f] Calculated mean value using the reported values compiled from the different laboratories by Odin *et al.* (1982).

homogeneous compositions (Figures 3, S2b, S2e, S2g) due to the lower beam current (10 nA) of this technique, limiting detection of subtle compositional variations, relative to the higher beam current of 100 nA used for EPMA. The grain Mica-Mg-f display small inclusion (< 50 µm in diameter) with higher Fe mass fractions (Figure 3). The mean Al_2O_3, FeO and MgO contents of the investigated grains and 1*s* uncertainties (% *m/m*, *n* = 22) are 14.9 ± 0.7, 7.6 ± 1.3 and 20.2 ± 1.1 respectively. One grain (Mica-Mg-a) displays FeO and MgO contents of 5.0 and 22.2 (% *m/m*), lower by 42% and higher by 9% than the working values of bulk Mica-Mg from Govindaraju (1995) (Table S5 and Figure S2a). The mean SiO_2 and K_2O contents are relatively homogenous between grains, with the mean value of each grain agreeing within uncertainty with the mean of all grains. The mean contents of Mica-Mg grains by EPMA are generally comparable to the working values of Govindaraju (1995) with a difference of less than 2% for all measured elements, except FeO, which shows a difference of 10%. If the grain Mica-Mg-a is excluded, the mean measured FeO content also agrees within error with the working value of Govindaraju (1995) (Table S5).

Glauconite GL-O: Heterogeneity in grains was observed by BSE image analysis (Figures 4a, 4b and S3). The results are consistent with a previous study by Boulesteix *et al.* (2020) who noted the presence of apatite and carbonate in GL-O grains. These authors described phosphate phases in GL-O grains as massive or disseminated apatite, as observed in the present work. Our EPMA measurement results for apatite-free sections of GL-O grains (*n* = 12; Table S6) agree with those of Boulesteix

2*s*	$^{87}Rb/^{86}Sr$	2SE	2*s*	*n*	$^{87}Sr/^{86}Sr$	2SE	2*s*	*n*
	38.822	0.007			0.752872	0.00001		
	34.715	0.009			0.752536	0.00001		
	34.607	0.006			0.753228	0.00001		
	36.531	0.019			0.753566	0.00001		
1.2	**36.2**	2.0	4.0	4	**0.75305**	0.00044	**0.00089**	4
1.2			**4.0**					
1.6								
					0.7535	0.0010		
	36.4		5.2	5	0.7532		0.0026	5
	36.1		4.1	15	0.7539		0.0053	15
	67.69	0.01			1.21066	0.00002		
	71.41	0.05			1.21255	0.00001		
	70.47	0.03			1.21089	0.00001		
1.9	**69.9**	2.2	3.9	3	**1.2114**	0.0012	**0.0021**	3
2.0			**4.1**					
1.7								

et al. (2020) within their 1*s* uncertainties, but are higher for SiO_2 by 5%, FeO by 17% and K_2O by 12% and lower for MgO by 2% and Al_2O_3 by 13%, compared with the working values of bulk GL-O from Govindaraju (1995).

Biotite Mica-Fe: BSE images and elemental maps of Mica-Fe grains show that grains include variable types of mineral inclusions such as apatite, monazite, K-feldspar, zircon and ilmenite (Figures 4c, 4d, 5, S4d and S4e). Mica-Fe grains display compositional variation at the intra-grain scale with relative uncertainties (1*s*) up to 1.7% for SiO_2, 3.8% for Al_2O_3, 4.5% for FeO, 3.2% for MgO and 2.5% for K_2O, respectively (Table S7). Compositional variability of Mica-Fe in randomly selected grains was relatively low compared with that of Mica-Mg grains, with the mean and *s* (% *m/m*, $n = 17$) of 34.6 ± 0.4 for SiO_2, 18.9 ± 0.4 for Al_2O_3, 22.9 ± 0.6 for FeO, 4.7 ± 0.2 for MgO, 9.0 ± 0.1 for K_2O and 2.4 ± 0.1 for TiO_2. The mean values of EPMA results are in good agreement with the working values of bulk Mica-Fe from Govindaraju (1995) within its uncertainty limits (1*s*).

Potassium feldspar FK-N: BSE images and elemental maps show that all investigated FK-N grains do not occur as pure single varieties but as a perthite containing sodium feldspar in various proportions with small inclusions of quartz (Figures 6 and S5), consistent with the reported sample description in Govindaraju (1984). EPMA analyses were done on the perthite and the anti-perthite phases of the grains resulting in a high deviation of the EPMA results of the FK-N grains compared with the working values of Govindaraju (1995) for bulk FK-N. The mean Na_2O and K_2O

Table 3c.
Rb-Sr mass fractions and $^{87}Sr/^{86}Sr$ ratios of Mica-Fe for repeat analyses of the studied RMs compared with literature values

Sample/comments	Rb (µg g^{-1})	2SE	2*s*	*n*[c]	Sr (µg g^{-1})	2SE	2*s*	*n*[c]
CRPG Biotite Mica-Fe								
ID-TIMS and MC-ICP-MS								
(This study)								
Mica-Fe-1					6.153	0.012		
Mica-Fe-2					5.980	0.005		
Mica-Fe-3	2253.2	0.4			5.997	0.002		
Mica-Fe-4	2219.2	0.5			5.896	0.005		
Mica-Fe-5	2251.6	0.3			5.536	0.006		
Mica-Fe-6	2240.2	0.1			6.384	0.002		
Mica-Fe-7[a]	2330.4	0.6			6.491	0.004		
Mica-Fe-7r[a]	2336.8	0.1			6.463	0.004		
Mica-Fe-7[a]	*2333.6*		*9.0*		*6.477*		*0.039*	
Mica-Fe-8[a]	2376.8	0.1						
Mica-Fe-8r[a]	2377.7	0.2			7.001	0.007		
Mica-Fe-8[a]	*2377.2*		*1.3*					
Mica-Fe-9[a]	2373.0	0.2						
Mica-Fe-9r[a]	2379.0	0.2			6.550	0.006		
Mica-Fe-9[a]	*2376.0*		*8.5*					
Mean[b]	**2293**	51	135	7	**6.22**	0.29	0.87	9
Total uncertainty[c]			**142**				**0.63**	
ICP-MS (this study)								
Mica-Fe	2174	63	141	18	5.95	0.15	0.34	18
Working value								
Govindaraju (1995)	2200		538		5		19	

SE: standard error, *s*: standard deviation, *n*: the number of values included in a total mean
Each sample name by ID-TIMS and MC-ICP-MS (this study) indicates individual powder batches (50–110 mg) from different sample packets or aliquots as presented in Table S1. Mean values and their total uncertainties **in bold** are displayed in Figures 7 and 8. 2SE values for Rb and Sr mass fractions are based on in-run 2SE uncertainties. 2SE of $^{87}Rb/^{86}Sr$ for individual batches was calculated by error propagation of Rb and Sr mass fraction uncertainties. $^{87}Sr/^{86}Sr$ uncertainties are 2SE in-run values. See text for discussion of other potential sources of uncertainties.
[a] Duplicate analyses of each individual powder batch. The mean of the duplicate values (*italic*) are included in total means.
[b] Total mean value from the replicate measurements of individual powder batches.
[c] Total uncertainty combines the random uncertainty (2*s*) of the mean of the individual analyses with the systematic uncertainty related to spike calibration (Table 2).

contents (n = 19) are 1.7 times higher in Na_2O and 0.8 times lower in K_2O than the working values of Govindaraju (1995) (Table S8). The mean orthoclase (Or) contents of potassium feldspar sections (n = 13) in FK-N grains measured by EPMA is 88 mol.% and the reported Or content of bulk FK-N from Govindaraju (1984) is 77 mol %. The difference of 13% in the Or contents between the bulk FK-N from of Govindaraju (1984) and potassium feldspar sections in FK-N grains in our study indicates that the Or content is highly variable at the intra-grain scale, and that a small number of grains will not be representative of the bulk FK-N RM.

Bulk powder Rb and Sr mass fractions and isotopic compositions of the four RMs

Rubidium and Sr and Rb-Sr isotopic compositions obtained for the four RMs are given in Tables 3a–3c and 4 and shown in Figures 7 and 8. Multiple measurements of individual powder batches from different bags or aliquots were performed for the four RMs (Table S1). The means of the multiple analyses and their standard error (2SE) and standard deviation (2*s*) are presented in Tables 3a–3c and were used to evaluate the compositional homogeneity of the bulk samples. As discussed in section 'Uncertainties on Rb-Sr ratios and mass fractions', the uncertainties of the total mean values indicate random errors from multiple measurements of different powder batches, which include the uncertainties from the Sr blank contribution.

Rubidium and Sr contents obtained by the isotope dilution method using TIMS and MC-ICP-MS and by the alkali fusion method using ICP-MS are presented in Figure 7, Table 3 (TIMS and MC-ICP-MS) and Table S9 (ICP-Q-MS). The mean Rb and Sr mass fractions of the four RMs measured by the two methods were within uncertainty of the working values of Govindaraju (1995). This is also true of the Rb and Sr contents of the individual batches (Figure 7). Differences $<$1.0% were observed in the mean Rb/Sr ratios of Mica-Fe, GL-O and FK-N between the two

Rb/Sr	2*s*	$^{87}Rb/^{86}Sr$	2SE	2*s*	*n*[c]	$^{87}Sr/^{86}Sr$	2SE	2*s*	*n*[c]
						8.35640	0.00007		
						8.03423	0.00008		
376		1859.9	0.8			7.97738	0.00009		
376		1831.0	1.7			7.67401	0.00006		
407		1987.5	2.1			7.75431	0.00005		
351		1792.3	0.7			8.53462	0.00034		
		1828.8	1.2			8.48485	0.00010		
		1854.0	1.1			8.60622	0.00008		
360		*1841.4*		*36*		*8.54553*		*0.17164*	
340		1578.8	1.6			6.91305	0.00016		
363		1816.6	1.6			8.15958	0.00005		
369	52	**1815**	92	244	7	**7.99**	0.34	**1.02**	9
	52			**246**					
366	32								
440									

methods (Table 3). A difference of 4.8% in the mean Rb/Sr ratios for Mica-Mg between the two methods was obtained, but they overlap well within 2*s* uncertainties. The means from eighteen analyses of different powder aliquots for the Rb/Sr mass fraction ratios by alkali fusion ICP-MS have uncertainties (2*s*, *n* = 18) of 7.9% for Mica-Mg, 13% for GL-O, 8.7% for Mica-Fe and 7.5% for FK-N. The mean Rb/Sr mass fraction ratios of multiple measurements by ID-TIMS and ID-MC-ICP-MS yield mean and total uncertainties (2*s*) of 5.1% and 5.5% for Mica-Mg (*n* = 7), 9.4% and 9.6% for GL-O (*n* = 4), 14.1% and 14.2% for Mica-Fe (*n* = 7) and 8.3% and 8.5% for FK- N (*n* = 3), respectively.

The Rb/Sr and Sr isotopic compositions obtained for the four RMs are given in Table 3a–3c and 4 and shown in Figure 8. The mean $^{87}Rb/^{86}Sr$ ratio for Mica-Mg (*n* = 7) is 155.6 with mean and total errors (2*s*) of 4.2% and 4.7%, respectively. The mean $^{87}Sr/^{86}Sr$ ratio for Mica-Mg (*n* = 12) is 1.8622 with a mean error (2*s*) of 0.36%. The measured Rb/Sr and Sr isotopic values agree with the literature data within their reported uncertainties (Hogmalm *et al.* 2017, Laureijs *et al.* 2021). GL-O was measured on four different batches, yielding a mean $^{87}Rb/^{86}Sr$ ratio of 36.2 with mean and total uncertainties (2*s*) of 10.9% and 11.1%, respectively. The mean of $^{87}Sr/^{86}Sr$ ratios is 0.75305 with a mean uncertainty (2*s*) of 0.12%. The compositional variability of Rb/Sr and Sr isotopic compositions of GL-O is very similar to the variation of the literature values on GL-O grains and powder from Odin *et al.* (1982). To our knowledge, there are no literature data for Sr isotopic compositions for Mica-Fe and FK-N. The mean $^{87}Rb/^{86}Sr$ ratio for Mica-Fe (*n* = 7) is 1815 with an mean and total uncertainties (2*s*) of 13.4% and 13.6%, respectively. The mean $^{87}Sr/^{86}Sr$ ratio for Mica-Fe (*n* = 9) is 7.99 with a mean uncertainty of 13%. The mean $^{87}Rb/^{86}Sr$ ratio for FK-N (*n* = 3) is 69.9 with 2*s* of 5.6% and 5.9% for mean and total uncertainties, respectively. The mean $^{87}Sr/^{86}Sr$ ratio for FK-N (*n* = 3) is 1.2114 with a mean uncertainty (2*s*) of 0.17%.

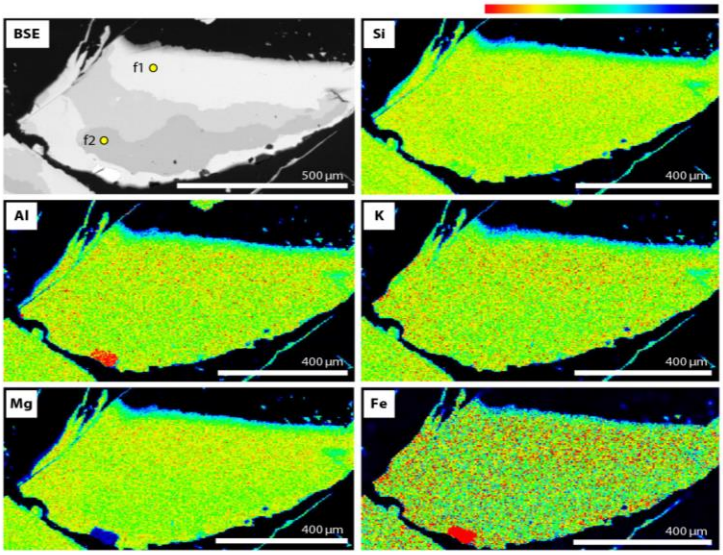

Figure 3. BSE image and SEM-EDS elemental maps of a grain of Mica-Mg phlogopite (Mica-Mg-f). The coloured scale bar on the top shows the relative abundance of the mapped major element scaled between 0 (dark blue) and 100 (red). The elemental maps show a small area with higher Fe and lower Mg within the grain. Yellow circles indicate spot locations of EPMA in Table S5.

Discussion

Three different aspects are considered to evaluate the suitability of Mica-Mg, Mica-Fe, GL-O and FK-N as potential reference materials for *in situ* Rb-Sr dating by LA-ICP-MS/MS. The first is the possible effect of chemical and mineralogical heterogeneities, both within individual mineral grains and between grains, on the bulk Rb/Sr and Sr isotopic values of the RMs. The second is the precision of the determined Rb/Sr and Sr isotopic compositions and their uncertainties. The third is the comparison between the absolute ages for the four RMs that can be inferred from our data with previously suggested ages for these RMs.

Homogeneity of the RMs at the scale of mineral grains

At the grain scale, BSE images, elemental maps and EPMA (Figures 3–6, Tables S5–S8, Figures S2–S5) of the four RMs show varying degrees of heterogeneity in their major element compositions. The geological contexts of the RMs are considered in order to better understand the origin of this heterogeneity.

Phlogopite Mica-Mg was separated from a pyroxenite in the Bekily area, southern Madagascar (Govindaraju 1979). The location of the pyroxenite and name of the sampled zone are not given and a recent search of the available documentation at the SARM unfortunately did not provide additional information. In BSE images and SEM-EDS and EPMA elemental maps of selected grains, the intra-grain compositions of Mica-Mg show only limited heterogeneity evident as small areas with high Fe contents in a few grains (Figures 3 and S2). As noted above, only one grain (Mica-Mg-a, Table S5) displays significantly lower FeO and higher MgO contents than other grains and the working value of Govindaraju (1979). Govindaraju (1979) reported that the initial form of Mica-Mg was large sheets without any visible impurities. This may explain our observation that the compositional variation is small. The limited extent of heterogeneity is confirmed by the consistency of the measured Rb and Sr contents by alkali fusion ICP-MS and ID-TIMS and MC-ICP-MS and their agreement with the working values of bulk Mica-Mg from Govindaraju (1979). Phlogopites from Ampandarandava and nearby deposits in southern Madagascar, occurring in a matrix of calcite, anhydrite and diopside, have been reported to have homogeneous major element compositions (Morteani *et al.* 2013, Martin *et al.* 2014). Nevertheless, the presence of micro-inclusions of titanite and rutile, inclusions of calcite or anhydrite was documented in

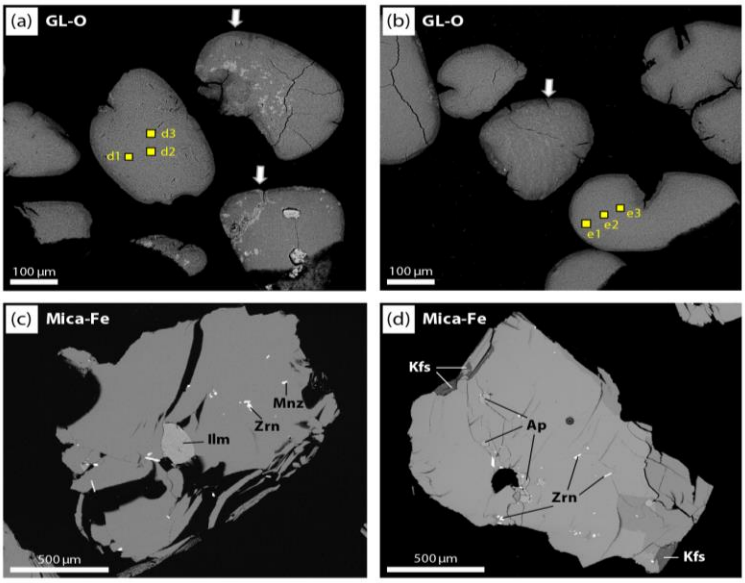

Figure 4. BSE images displaying heterogeneity of (a, b) GL-O glauconite grains and (c, d) Mica-Fe biotite grains. Heterogeneous grains in (a) and (b) are indicated by arrows. Lighter sections in the grains correspond to phosphate minerals (apatite) as previously observed by Boulesteix *et al.* (2019). Yellow square points represent locations of 10 µm × 10 µm defocused analyses by EPMA of the GL-O grains (Table S6). (c) and (d) show various mineral phases including ilmenite (Ilm), zircon (Zrn), monazite (Mnz), apatite (Ap) and K-feldspar (Kfs) within Mica-Fe grains.

these phlogopites (Martin *et al.* 2014). Such inclusions were not observed within the tested Mica-Mg grains in our study.

For glauconite GL-O, no impurities were detected under microscopic observation in early work (Odin *et al.* 1982), but the recent study of Boulesteix *et al.* (2020) revealed the presence of included microphases such as apatite and calcite. Their observation is in good agreement with our BSE imaging results (Figures 4a, 4b and S3). EPMA results on GL-O grains show a high discrepancy of the major element contents compared with the working values of Govindaraju (1995), consistent with the findings of Boulesteix *et al.* (2020). These authors suggested that the discrepancy between the major element compositions of GL-O powder and the grains analysed *in situ* reflected the contribution of the phosphate inclusions in GL-O. If the bulk compositions of GL-O are highly impacted by impurities such as apatite, the Rb/Sr ratios could also be biased compared with phosphate-free GL-O grains.

Biotite Mica-Fe was separated from a biotitite emplaced in a magmatic shear zone within the Saint-Sylvestre two mica leucogranitic complex near Razès, France (Govindaraju 1979, Friedrich 1983). This complex is dominated by a two-mica granite (granite de Saint-Sylvestre) composed of quartz ± Fe biotite ± muscovite ± plagioclase ± K-feldspar ± sillimanite (Cuney *et al.* 1990, Turpin *et al.* 1990, Villaros and Pichavant 2019). The sampled biotitite corresponds to the latest phase of crystallisation of magma expelled from the Fanay fine grained peraluminous leucogranite intrusion in the Saint-Sylvestre leucogranitic complex (Friedrich 1983, Friedrich *et al.* 1987). This magma was very rich in incompatible elements (e.g., U, Th, REE, K, Zr, Rb), explaining the high proportion of minerals bearing these elements (monazite, zircon, apatite) included within biotite grains (Figures 4c, 4d, 5 and S4), as well as the high Rb/Sr ratio and highly radiogenic Sr composition measured for Mica-Fe. Inclusions of apatite, monazite, K-feldspar, zircon and ilmenite in Mica-Fe are depleted in Rb and/or Sr compared with biotite and therefore could affect the bulk Rb-Sr isotopic compositions of the Mica-Fe bulk sample if their proportion varies between aliquots. Such impurities in Mica-Fe grains were reported during separation of Mica-Fe by Govindaraju (1979), with 13 kg of minerals including muscovite, quartz and feldspars being eliminated. Reported Rb and Sr mass fractions in biotite flakes extracted from the Saint-

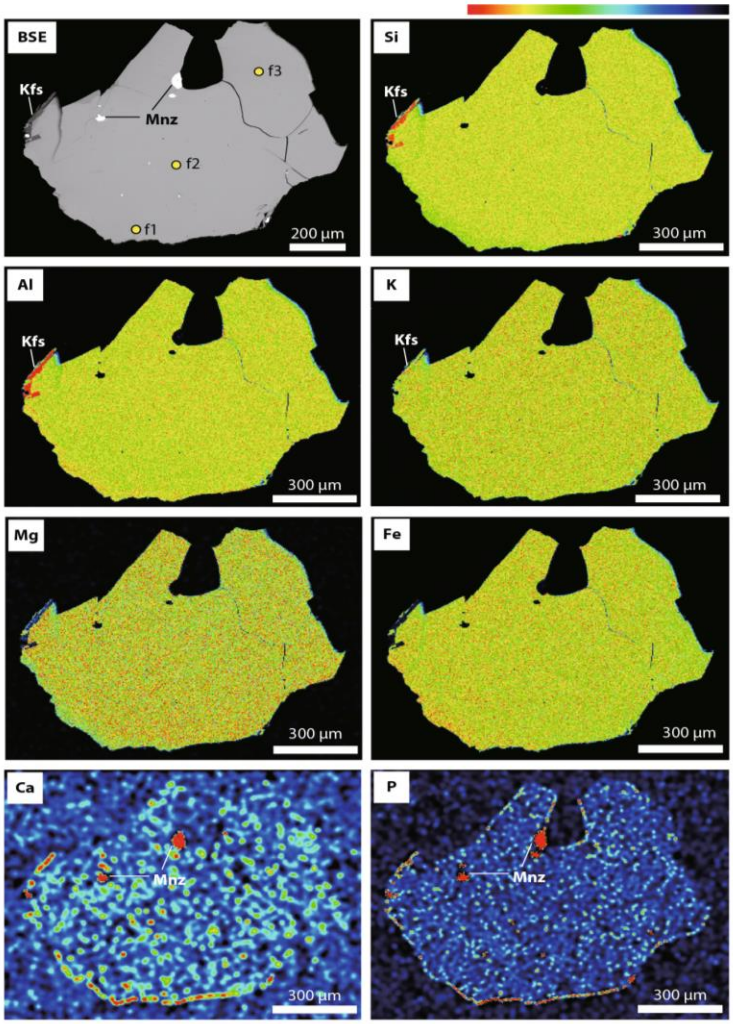

Figure 5. BSE image and SEM-EDS elemental maps for a grain of Mica-Fe biotite (Mica-Fe-f), showing heterogeneities including K-feldspar (Kfs) and monazite (Mnz). Explanation of the coloured scale bar is given in the caption for Figure 3. Yellow circles indicate spot locations of EPMA in Table S7.

Sylvestre granite by Duthou (1977) are 2660 µg g^{-1} and 4.1 µg g^{-1} (sample B1354) and 1335 µg g^{-1} and 5.2 µg g^{-1} (sample B1355), respectively, and the reported values for $^{87}Rb/^{86}Sr$ and $^{87}Sr/^{86}Sr$ isotopic ratios are 1884 ± 54 and 8.69 ± 0.09 (sample B1354) and 739 ± 22 and 3.94 ± 0.04 (sample B1355), respectively. The latter value is significantly less radiogenic than those we measured for Mica-Fe. Together, the Duthou (1977) values define two-point isochrons of 303 ± 9 Ma for sample B1354 and 312 ± 10 Ma for sample B1355 using the initial $^{87}Sr/^{86}Sr$ ratio from Duthou (1977) (see Figure S6 for further details). These previous results are consistent with the highly radiogenic and quite variable composition of Mica-Fe obtained in the present study (7.99 ± 13% (2s) for $^{87}Sr/^{86}Sr$ and 1815 ± 14% (2s) for $^{87}Rb/^{86}Sr$). Newly reported Rb/Sr mass fraction ratios of biotite from a sample from the Saint-Sylvestre granite range from 59 to 640 (Villaros and Pichavant 2019), further supporting the variability observed in our Mica-Fe samples.

Potassium feldspar FK-N originates from Tamil Nadu, India (Govindaraju 1984), where orthoclase-rich and

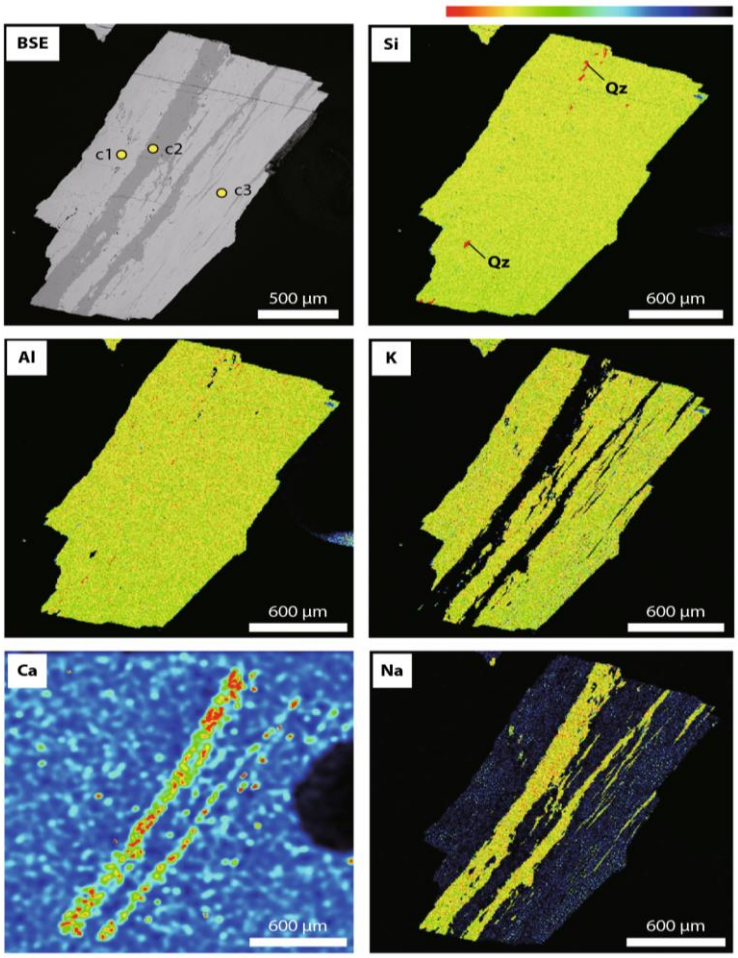

Figure 6. BSE image and SEM-EDS elemental maps for a grain of FK-N potassium feldspar (FK-N-c), displaying the coexistence of orthoclase and albite (Ca- and Na-rich zones) and small inclusions of quartz (Qz). Explanation of the coloured scale bar is given in the caption for Figure 3. Yellow circles indicate spot location of EPMA in Table S8.

Table 4.
Working values and uncertainties for the RMs in this study

Sample	$^{87}Rb/^{86}Sr$	2*s*	$^{87}Sr/^{86}Sr$	2*s*
Phlogopite Mica-Mg	155.6	7.3 (4.7% RSD)	1.8622	0.0067 (0.36% RSD)
Glauconite GL-O	36.2	4.0 (11% RSD)	0.75305	0.00089 (0.12% RSD)
Biotite Mica-Fe	1815	246 (14% RSD)	7.99	1.02 (13% RSD)
Potassium Feldspar FK-N	69.9	4.1 (5.9% RSD)	1.2114	0.0021 (0.17% RSD)

Uncertainties of the $^{87}Rb/^{86}Sr$ values include both a random component from replicate analyses and a systematic component related to spike calibration.

quartz-rich leucocratic medium grained to pegmatitic granites and pink coarse to pegmatitic granites occur (Roy and Raju 1999). Feldspars from pegmatitic rocks in the Tamil Nadu area occur as K-feldspar composed of microcline mixed with various proportions of sodic plagioclase intergrown as perthite (Roy and Raju 1999). The reported mineralogy of feldspars from pegmatitic rocks in Tamil Nadu is consistent with our EPMA results and elemental maps

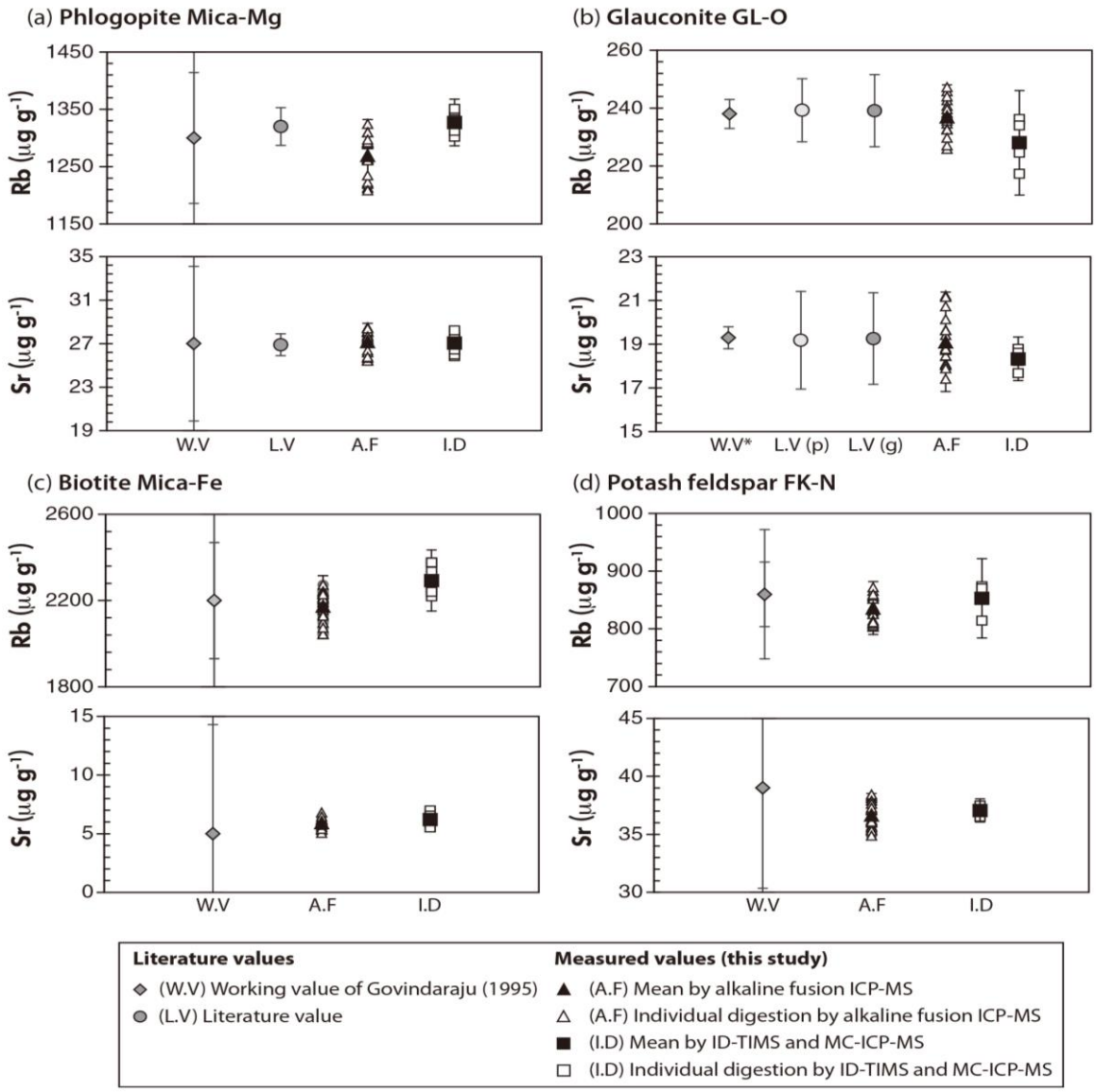

Figure 7. Comparison of Rb and Sr mass fractions determined by alkali fusion ICP-MS and ID-TIMS and ID-MC-ICP-MS, and with literature values. Uncertainties (2*s*) for the measurements by alkali fusion ICP-MS are shown for the mean values. Bars associated with the mean values by ID-TIMS and ID-MC-ICP-MS correspond to the total uncertainties (2*s*) in Tables 3a-3c and are smaller than the spread of the symbols for the individual Sr contents of Mica-Mg and Mica-Fe. Range bars from working values (W.V) of Govindaraju (1995) indicate ±1*s* and 2*s*, except for GL-O for which the bars indicate 95% confidence limits (W.V*) given by Govindaraju (1995). Literature values (L.V) are from (a) Laureijs *et al.* (2021) and (b) compiled data of different laboratories from Odin *et al.* (1982) for powder (p) and grains (g) of GL-O. Details of the literature data are provided in Tables 3a–3c.

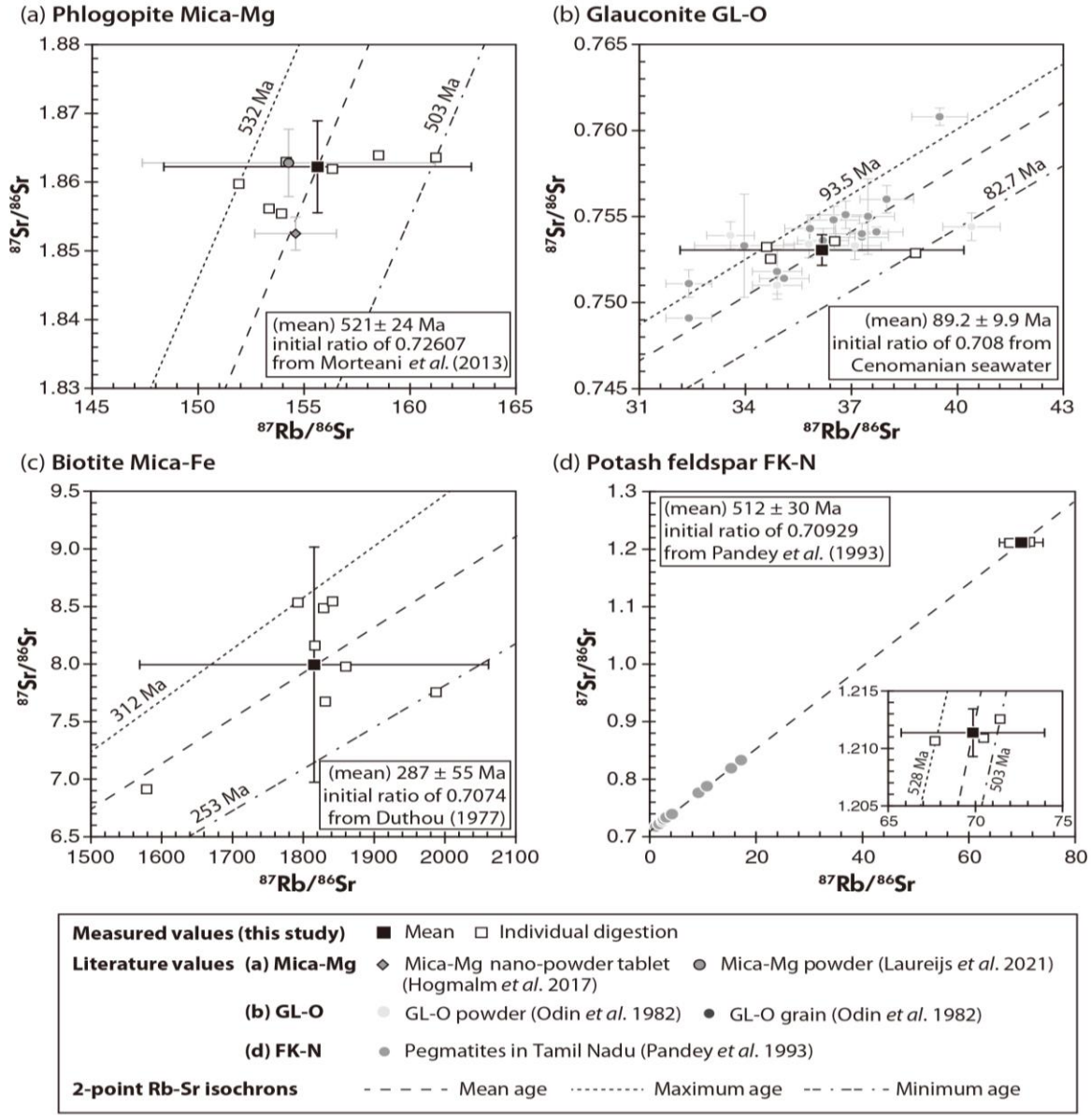

Figure 8. Measured $^{87}Rb/^{86}Sr$ and $^{87}Sr/^{86}Sr$ isotopic compositions, compiled with literature data, for (a) Mica-Mg, (b) GL-O, (c) Mica-Fe and (d) FK-N. Errors in the mean $^{87}Rb/^{86}Sr$ and $^{87}Sr/^{86}Sr$ ratios are total uncertainties (2*s*) in Table 3. Uncertainties (2SE) for the individual digestions are smaller than the symbols for $^{87}Sr/^{86}Sr$ and $^{87}Rb/^{86}Sr$. Dotted lines in (a), (b), (c) and (d) indicate two-point isochrons using the mean and individual values analysed in this study and assumed initial ratios (see text for details). Isochron age uncertainties were calculated using maximum likelihood regressions implemented in the online version of IsoplotR (Vermeesch 2018, http://isoplotr.es.ucl.ac.uk/). (d) Uncertainties in $^{87}Rb/^{86}Sr$ and $^{87}Sr/^{86}Sr$ ratios from Pandey *et al.* (1993) are 2% and 0.05%, respectively. Literature data and their uncertainties are given in Tables 3a–3c.

(Figures 6 and S4, Table S8) and the sample description of FK-N given in Govindaraju (1984). Highly variable Rb/Sr mass fraction ratios with ranges of 7.5% (2*s*, *n* = 18) and 8.5% (2*s*, *n* = 3) were measured by alkali fusion ICP-MS and ID-TIMS and MC-ICP-MS, respectively. The heterogeneity of FK-N grains, observed from our microscopic and SEM-EDS observations and EPMA results, potentially affects the bulk composition of FK-N, likely explaining the high variability of trace element characteristics such as Rb/Sr ratios.

Our study of the four RMs at the grain scale combined with previous work shows that these RMs display differing degrees of chemical and mineralogical heterogeneities. GL-O, Mica-Fe and FK-N present the most heterogeneity, as observed in the variability of the chemical analyses, whereas Mica-Mg is somewhat more homogeneous.

$^{87}Sr/^{86}Sr$ and Rb/Sr ratio determinations and homogeneity of the RMs

Rb-Sr determinations for each RM, obtained from separate aliquots of multiple powder batches provided by the SARM, show a variable spread in $^{87}Sr/^{86}Sr$ compositions and Rb/Sr mass fraction ratios as shown in Figures 7 and 8, implying heterogeneity in the bulk powder samples. The degree of heterogeneity is not equivalent between the RMs, as can be seen by comparing the uncertainties on their mean Rb-Sr mass fractions and isotopic ratios obtained by ID-TIMS and ID-MC-ICP-MS (Table 3). These uncertainties reflect both random measurement errors, including variable Sr blank contributions (Table S4) and potential powder heterogeneity both within and between different batches of each RM, and systematic uncertainties related to the spike calibration (Table 2).

Measurements of Rb and Sr mass fractions were done using two methods (Alkali fusion ICP-MS and ID-TIMS + MC-ICP-MS) to test the validity of the analytical protocols and the homogeneity of the RMs. The coherent and reproducible results of Rb/Sr ratios acquired using the two methods on multiple batches of the RMs taken from different bags argues for the reliability of both methods. The large ranges in the Rb/Sr mass fraction ratios measured for the four RMs, with mean uncertainties (2*s*) of 7.5–13% and 5.1–14% determined respectively by the alkali fusion and the isotope dilution methods, imply sample heterogeneity in Rb-Sr compositions exceeding the analytical errors.

The analyses of seven individual digestions for Mica-Mg yielded a mean $^{87}Rb/^{86}Sr$ ratio of 155.6 ± 7.3 (4.7%, 2*s*) (Table 3a). This value is identical within error to the calculated $^{87}Rb/^{86}Sr$ ratio of 154.6 ± 1.2% for nano-powder pellet Mica-Mg obtained by Hogmalm *et al.* (2017) and the measured $^{87}Rb/^{86}Sr$ ratio value of 154.3 ± 4.5% for powder Mica-Mg given by Laureijs *et al.* (2021). In addition to random measurement related uncertainties, the uncertainties of our measured and literature data for Rb/Sr mass fraction and isotopic ratios of Mica-Mg are considered to reflect minor compositional heterogeneities between different aliquots of the Mica-Mg bulk sample. Our data on Mica-Mg do not reflect the high variability of Rb/Sr ratios on intra-grain and grain-to-grain scales previously reported for phlogopite minerals from deposits in the Bekily area (Morteani *et al.* 2013).

The mean $^{87}Rb/^{86}Sr$ value from analyses (Table 3b) of four individual digestions of GL-O is 36.2 ± 4.0 (11%, 2*s*). Odin *et al.* (1982) reported results of an interlaboratory comparison of Rb-Sr isotopic analyses of GL-O powder, showing large scatter in both Rb/Sr mass fraction ratios and $^{87}Sr/^{86}Sr$ (Figures 7b and 8b). The mean $^{87}Rb/^{86}Sr$ value of the GL-O powder from the Odin *et al.* (1982) compilation is 36.4 ± 14% (2*s*, *n* = 5) in excellent agreement with our results (Table 3b). Their study also presented compiled interlaboratory results for GL-O grains, which yielded a mean $^{87}Rb/^{86}Sr$ value of 36.1 ± 11% (2*s*, *n* = 15). These large uncertainties could reflect procedural differences between laboratories and/or heterogeneity between the different GL-O powder batches. The latter possibility is supported by BSE imaging and EPMA results for GL-O grains showing phosphate inclusions and within grain major element variations. The mean major element contents of inclusion-free sections of GL-O grains in our study differed from the working values of bulk GL-O given by Govindaraju (1995). These results indicate that GL-O is affected by impurities and chemical variations on both an inter and intra-grain scale, which affect Rb and Sr mass fractions and isotopic compositions of the bulk sample powder.

The mean of $^{87}Rb/^{86}Sr$ ratios from seven individual digestions of Mica-Fe is 1815 ± 246 (14%, 2*s*) (Table 3c). We consider that bulk Mica-Fe is heterogeneous, so different powder aliquots may have contained different proportions of mineral inclusions with $^{87}Sr/^{86}Sr$ and Rb/Sr ratios distinct from those of the biotite. In addition to Rb/Sr isotopic heterogeneity introduced from inclusions, the large spread in Rb/Sr and Sr isotopic compositions of Mica-Fe may be due to high and variable Rb/Sr ratios within biotite (Villaros and Pichavant 2019), which over time produced highly radiogenic and variable $^{87}Sr/^{86}Sr$ compositions in the biotitite from which Mica-Fe was extracted (Friedrich 1983). Interaction with post-crystallisation fluids in the Saint-Sylvestre complex associated with the formation of uranium deposits (Turpin *et al.* 1990), may have led to a heterogeneous

distribution of the Rb/Sr isotopic ratios at the grain and/or the bulk sample scale (discussed below).

Three analyses of $^{87}Rb/^{86}Sr$ ratios for FK-N yielded a mean value of 69.9 ± 4.1 (5.9%, 2*s*) (Table 3b). Chemical heterogeneity within and between grains of FK-N was observed in EPMA measurements with varying major element contents and discrepancies relative to the working value of bulk FK-N from Govindaraju (1995). This variability within and between FK-N grains suggests that Rb/Sr isotopic heterogeneity of the bulk powder could be derived from variable amounts of potassium feldspar and sodium plagioclase in different aliquots.

To summarise, the analyses done on multiple powder digestions of the four tested RMs show variable degrees of dispersion in Rb and Sr mass fractions and $^{87}Rb/^{86}Sr$ ratios. Such dispersion is consistent with observations done by SEM and EPMA and with the findings of previous studies. The most heterogeneous RMs are Mica-Fe and GL-O for Rb/Sr values with total uncertainties of 14% and 11% (2*s*), respectively, and the most reproducible Rb/Sr values were obtained for Mica-Mg with a total uncertainty of 4.7% (2*s*) followed by FK-N with an uncertainty of 5.9% (2*s*). We consider that the $^{87}Rb/^{86}Sr$ heterogeneity measured in the bulk RMs is derived mainly from the initial heterogeneity of their original crystals. The addition of the spike to the sample resulted in additional uncertainties linked to the spike calibration. Based on these considerations, we propose our working values of $^{87}Rb/^{86}Sr$ and $^{87}Sr/^{86}Sr$ ratios for the RMs with their total uncertainties in Table 4.

Model ages of the RMs

Rb-Sr model ages of the RMs calculated from the mean Rb-Sr isotopic values obtained by ID-TIMS and ID-MC-ICP-MS and the total uncertainties (2*s*) are presented in Table 1 and the associated two-point isochrons are shown in Figure 8. All model ages were calculated using maximum likelihood regressions in Isoplot R (Vermeesch 2018, http://isoplotr.es.ucl.ac.uk/) with $\lambda^{87}Rb = 1.3972 \pm 0.0045 \times 10^{-11}$ a, an estimate of initial $^{87}Sr/^{86}Sr$ ratio and uncertainties are reported at 95% confidence.

A two-point isochron age of 521 ± 24 Ma of Mica-Mg using the mean $^{87}Rb/^{86}Sr$ and $^{87}Sr/^{86}Sr$ ratios (Figure 8a) is obtained assuming an initial $^{87}Sr/^{86}Sr$ of 0.72607, also assumed by Hogmalm *et al.* (2017). This value was constrained by Morteani *et al.* (2013) from two diopside samples paired with two phlogopite samples from the Ampandrandava deposit. This calculated age is in agreement with previous age determinations on Mica-Mg within reported uncertainties (Govindaraju 1979, Zimmermann *et al.* 1985, Laureijs *et al.* 2021). The individual two-point isochron ages range from 503 to 532 Ma using the measured Rb-Sr isotopic ratios of individual digestions of Mica-Mg (Figure 8a). This result is also coherent with other local geochronological dates from the Bekily area of southern Madagascar, such as Rb-Sr phlogopite ages of 518 ± 8 Ma (Morteani *et al.* 2013) and 500 ± 10 Ma (Martin *et al.* 2014), re-calculated using the ^{87}Rb decay constant of Villa *et al.* (2015), and a U-Pb zircon age of 526 ± 34 Ma (Kröner *et al.* 1996).

The mean $^{87}Rb/^{86}Sr$ and $^{87}Sr/^{86}Sr$ ratios for GL-O yield a two-point isochron age of 89.2 ± 9.9 Ma with a range of 82.7 to 93.5 Ma for the individual digestions (Figure 8b) using the estimated initial $^{87}Sr/^{86}Sr$ ratio of 0.708 for Cenomanian seawater, reported in Odin *et al.* (1982). This calculated age is within the range of the reported Rb-Sr and K-Ar ages for original GL-O powder and grains compiled in Table 1 (Odin *et al.* 1982, Smith *et al.* 1998). The large variation in reported ages and our calculated ages and uncertainties reflect sample heterogeneity in the bulk sample of GL-O, as GL-O grains show compositional zones and have mineral impurities including apatite and calcite.

A two-point isochron age of 287 ± 55 Ma for Mica-Fe was calculated using the mean Rb/Sr and Sr isotopic compositions of Mica-Fe, with a range of 253 to 312 Ma for the individual digestions (Figure 8c). Individual $^{87}Sr/^{86}Sr$ ratios are scattered and not linearly correlated with $^{87}Rb/^{86}Sr$, resulting in the high uncertainty on the age. Though there is some overlap within uncertainty, our calculated ages for Mica-Fe are younger than previously determined ages for this RM obtained by Rb-Sr, K-Ar and Ar-Ar dating (Govindaraju 1979, Zimmermann *et al.* 1985, Grove and Harrison 1996). They are also younger than ages for the Saint-Sylvestre leucogranite that encloses the biotitites, which include Ar-Ar plateau ages obtained on muscovites (302.1 ± 0.87 Ma) and biotite (302.44 ± 0.63 Ma and 301.44 ± 0.65 Ma) (Scaillet *et al.* 1996), U-Pb zircon and monazite ages of 324 ± 4 Ma (Holliger *et al.* 1986) and a whole-rock Rb-Sr isochron age of 320 ± 18 Ma (Duthou 1977, age recalculated using the revised ^{87}Rb decay constant of Villa *et al.* 2015). In our calculations, an initial $^{87}Sr/^{86}Sr$ ratio of 0.7074 was used, derived from the whole-rock Rb-Sr isochron of the Saint-Sylvestre leucogranite reported in Duthou (1977). To test whether the variability of our calculated ages and the bias relative to previous ages could be caused by the choice of initial ratio, we recalculated our ages assuming initial $^{87}Sr/^{86}Sr$ between 0.7039 and 0.7130 corresponding to the range of initial ratios of individual granite samples from

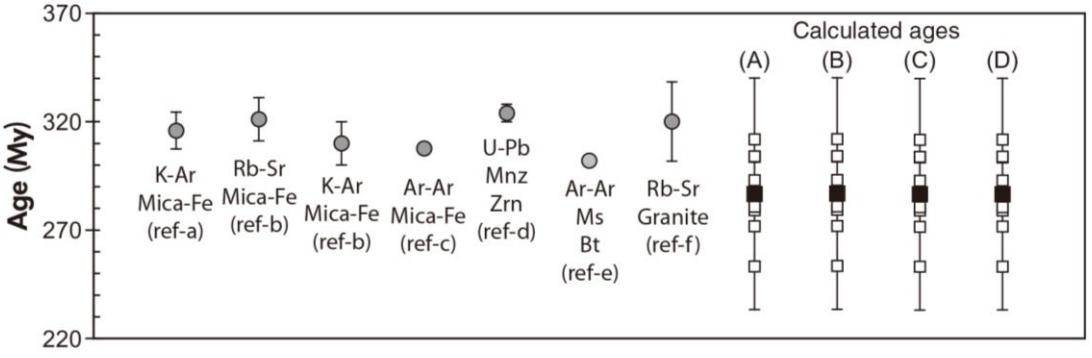

Figure 9. Two-point isochron Rb-Sr ages calculated using the measured Rb/Sr values of the mean (black squares) and individual powder aliquots (white squares) for Mica-Fe compared with previously reported ages and their uncertainties as compiled in Table 1. Two assumed initial ratios of (A) 0.7074 (Duthou 1977) and (D) 0.71067 (Turpin *et al.* 1990) are used for calculated ages of Mica-Fe. Minimum and maximum initial ratios of (B) 0.7039 and (C) 0.7130 are calculated using the reported Rb-Sr isotopic data of each granite sample from Duthou (1977) and the U-Pb zircon and monazite ages of 324 ± 4 Ma (Holliger *et al.* 1986) from the Saint-Sylvestre leucogranitic complex. It is apparent that within these limits, the choice of the initial ratio has an insignificant effect on the calculated age. References presented are (a) Zimmermann *et al.* (1985), (b) Govindaraju (1979), (c) Grove and Harrison (1996), (d) Holliger *et al.* (1986), (e) Scaillet *et al.* (1996) and (f) Duthou (1977). (d) Zircon (Zrn) and monazite (Mnz), (e) muscovite (Ms) and biotite (Bt) and (f) granite are from the Saint-Sylvestre massif. The Ar-Ar plateau age from Scalillet *et al.* (1996) presented here is the mean age calculated from muscovite (302.1 ± 0.87 Ma) and biotite (302.44 ± 0.63 Ma and 301.44 ± 0.65 Ma) from the Saint-Sylvestre granite (Scaillet *et al.* 1996).

Duthou (1977) calculated using the U-Pb zircon and monazite ages of 324 ± 4 Ma (Holliger *et al.* 1986). This variation of initial ratios modifies the calculated ages by only 0.04–0.09% (Figure 9), implying that other factors are responsible for the large variation and bias in our results. Mica-Fe has an exceptionally high Rb/Sr ratio (2293 μg g^{-1} of Rb for only 6.2 μg g^{-1} of Sr), coupled with an extremely radiogenic Sr composition (Govindaraju 1979, Friedrich *et al.* 1987). This implies that even minor changes in Rb or Sr abundances occurring since the biotite formed could inordinately affect the calculated age. Mica-Fe grains are quite heterogeneous, with abundant inclusions of apatite, monazite, zircon, K-feldspar and ilmenite with different Rb/Sr ratios. While such grains should in theory not affect the calculated age if they were included within and equilibrated with the biotite at the time it formed, they could instead provide evidence of alteration of the system. Turpin *et al.* (1990) reported that alteration of the Saint-Sylvestre complex by oxidised hydrothermal fluids continued for 25 Ma after granite emplacement, as dated from barren episyenites at 306 ± 2 Ma (recalculated using the ^{87}Rb decay constant of Villa *et al.* 2015), followed by the influx of a sedimentary fluid related to U ore deposition that produced mineralised episyenites at ~ 270 Ma. As these authors documented, the interaction of granites with hydrothermal fluids, resulted in radiogenic ^{87}Sr-loss and Rb-gain, which would be consistent with the younger than expected Rb/Sr ages and the high degree of dispersion in the data. Although causes of the wide dispersion of Rb-Sr ages of individual powder batches of Mica-Fe remain unclear, we suggest that it may result from the highly evolved and radiogenic composition of the magmas in the Saint-Sylvestre massif, the variable contents of inclusions between measured batches (~ 110 mg), especially of Sr-rich apatite and Rb-rich K-feldspar and/or ^{87}Sr-loss during the hydrothermal alteration that affected the Saint-Sylvestre granite.

The calculated two-point isochron Rb-Sr age of FK-N using the mean $^{87}Rb/^{86}Sr$ and $^{87}Sr/^{86}Sr$ ratios is 512 ± 30 Ma (Figure 8d). An estimated initial $^{87}Sr/^{86}Sr$ of 0.70929 was assumed, based on a whole-rock Rb-Sr isochron for pegmatite from the Kullampatti area in Tamil Nadu, southern India (Pandey *et al.* 1993). The two-point isochron ages calculated for the individual digestions of FK-N range from 503 to 528 Ma using the same assumed $^{87}Sr/^{86}Sr$ initial ratio. No previous age information or Rb-Sr isotopic data exist for FK-N, and while this sample is known to originate in Tamil Nadu, the precise sample location is unknown. Nevertheless, our calculated age for this RM closely matches the age of 521 ± 9 Ma of the Rb-Sr pegmatite isochron used to estimate the initial ratio (Pandey *et al.* 1993), suggesting that FK-N may also be derived from the Kullampatti area.

Conclusions: characterisation of the RMs for *in situ* Rb-Sr dating

This study provides working values of Rb and Sr mass fractions and Rb/Sr and Sr isotopic compositions for four RMs: Mica-Mg, Mica-Fe, GL-O and FK-N. The mean $^{87}Sr/^{86}Sr$ and $^{87}Rb/^{86}Sr$ ratios are given in Table 4, along with the uncertainties that must be propagated into the total uncertainties of Rb-Sr isotopic measurements by LA-ICP-MS/MS that use these RMs for calibration. The uncertainties (2*s*) of measured $^{87}Rb/^{86}Sr$ ratios are 4.7% for Mica-Mg, 11% for GL-O, 14% for Mica-Fe and 5.9% for FK-N, reflecting mostly the inhomogeneity of the powdered RMs. Smaller contributions to the total uncertainties come from random (in-run uncertainties, Sr blank variability, weighing errors) and systematic (spike calibration) analytical errors.

The use of appropriate matrix-matched and isotopically homogeneous RMs plays a key role in all applications of *in situ* instrumentation in geosciences. Rb-Sr dating by LA-ICP-MS/MS is one of these applications. Calibration materials of variable Rb/Sr compositions allowing matrix-matched correction for precise Rb-Sr age determination were lacking before our work. The present study provides controlled Rb and Sr mass fractions and Sr/Sr and Rb/Sr isotopic values for four natural RMs, which are chemically representative of micas and feldspars. These four RMs are available for the scientific community and can be used to calibrate LA-ICP-MS/MS data after a simple preparation stage. The availability of the RMs with various chemical compositions (phlogopite, biotite, glauconite and potassium feldspar) will permit for example detailed studies of matrix effects. It will also facilitate matching pulse/analogue settings with unknown samples and calculation and propagation of analytically robust uncertainties when dating feldspars and micas by LA-ICP-MS/MS.

Among the four RMs, Mica-Fe has limitations related to its exceptionally high and heterogeneous $^{87}Rb/^{86}Sr$ and $^{87}Sr/^{86}Sr$ values, which have uncertainties (2*s*) of 14%. Mica-Fe cannot be considered as an ideal RM for calibration of biotites with less extreme Rb-Sr compositions. Development of Fe-rich mica RMs with less radiogenic values is still needed with two potential candidates: (i) biotite from the La Posta granodiorite, California (Walawender *et al.* 1990) used as a primary reference material by Zack and Hogmalm (2016) for Rb-Sr dating by LA-ICP-MS/MS and (ii) GA-1550 biotite from monazite in Mt. Dromedary (McDougall and Roksandic 1974) which was dated by several isotope systems, presenting identical ages within uncertainties (e.g., K-Ar age by Spell and McDougall 2003 and McDougall and Wellman 2011 and Rb/Sr age by Li *et al.* 2008). These two biotites were successfully tested and used in the LA-ICP-MS/MS study of Rösel and Zack (2021).

Potential Rb/Sr isotopic heterogeneity of the RMs in powder form can affect the nano-powder pellet, which is currently the best sample preparation method for Rb-Sr dating by LA-ICP-MS/MS (Hogmalm *et al.* 2017, Redaa *et al.* 2021). Sample heterogeneity of Rb/Sr ratios in the RMs is large relative to the uncertainty (2*s*) for homogenous glass reference materials including 0.21% for NIST SRM 610 (Wise and Watters 2012), 1.3% for NIST SRM 612 (Woodhead and Hergt 2001) and 0.23% for BCR-2G (Elburg *et al.* 2005), widely used for Rb/Sr calibration for minerals with low to medium Rb/Sr ratios. We suggest that ID-TIMS and MC-ICP-MS measurement of $^{87}Sr/^{86}Sr$ and Rb/Sr compositions should be done directly on nano-powders to define whether the procedure of producing nano-powders reduces analytical uncertainties by producing greater homogenisation of the material before isotopic measurement. Until such results become available, we recommend use of our $^{87}Sr/^{86}Sr$ and $^{87}Rb/^{86}Sr$ values and related uncertainties for the four tested RMs for *in situ* Rb-Sr dating by LA-ICP-MS/MS.

Acknowledgements

This work was supported by the French National Research Agency through the national programme "Investissements d'avenir" (reference ANR-10-LABX-21-RESSOURCES21), the LUE Graduate programme of Lorraine University of Excellence (reference R01PKUFX-DREAM-JEGAL-GEO) and the Ministère de l'Enseignement supérieur de la Recherche et de l'Innovation (MESRI) for PhD funding to Yujin Jegal. Michel Cuney is thanked for geological information concerning the Saint-Sylvestre massif and related isotopic data. We thank Gaston Giuliani for discussion of the geological context of phlogopite deposits in southern Madagascar. Thomas Zack is thanked for providing aliquots of NIST SRM 607 K-feldspar. We thank Andreï Lecomte and Olivier Rouer (SCMEM) for their help during SEM and EPMA analyses, and Aimeryc Schumacher, Christiane Parmentier, Damien Cividini (CRPG) for their assistance with MC-ICP-MS analyses and clean lab experiments, and for fruitful discussions. We also thank Camille Kieffer, Élise Guérin and Hélène Pastel Gény (SARM-CRPG) for the ICP-MS analyses and the alkali fusion experiments. Alexandre Flammang and John Moine (Lithopreparation platforme, GeoRessources) are thanked for their help with sample preparation for SEM and EPMA work.

[Correction added on 28 October 2022, after first online publication: the acknowledgement section has been revised]

Data availability statement

The data that support the findings of this study are available in the supplementary material of this article.

References

Armstrong R.L., Jäger E. and Eberhardt P. (1966)
A comparison of K-Ar and Rb-Sr ages on Alpine biotites. Earth and Planetary Science Letters, 1, 13–19.

Bolea-Fernandez E., Balcaen L., Resano M. and Vanhaecke F. (2016a)
Tandem ICP-mass spectrometry for Sr isotopic analysis without prior Rb/Sr separation. Journal of Analytical Atomic Spectrometry, 31, 303–310.

Bolea-Fernandez E., Van Malderen S.J., Balcaen L., Resano M. and Vanhaecke F. (2016b)
Laser ablation-tandem ICP-mass spectrometry (LA-ICP-MS/MS) for direct Sr isotopic analysis of solid samples with high Rb/Sr ratios. Journal of Analytical Atomic Spectrometry, 31, 464–472.

Boulesteix T., Solé J., Pi T. and Cathelineau M. (2020)
Reappraisal of the GL-O reference material for K-Ar dating: New insight from microanalysis, single-grain and milligram Ar measurements. Geostandards and Geoanalytical Research, 44, 287–306.

Carignan J., Hild P., Mevelle G., Morel J. and Yeghicheyan D. (2001)
Routine analyses of trace elements in geological samples using flow injection and low pressure on-line liquid chromatography coupled to ICP-MS: A study of geochemical reference materials BR, DR-N, UB-N, AN-G and GH. Geostandards Newsletter: The Journal of Geostandards and Geoanalysis, 25, 187–198.

Chauvel C., Bureau S. and Poggi C. (2011)
Comprehensive chemical and isotopic analyses of basalt and sediment reference materials. Geostandards and Geoanalytical Research, 35, 125–143

Chen C.-H., DePaolo D.J. and Lan C.-Y. (1996)
Rb-Sr microchrons in the Manaslu granite: Implications for Himalayan thermochronology. Earth and Planetary Science Letters, 143, 125–135.

Cheng P., Koyanagi G.K. and Bohme D.K. (2008)
On the chemical resolution of the $^{87}Rb^{+}$ (s^{0})/$^{87}Sr^{+}$ (s^{1}) isobaric interference: A kinetic search for an optimum reagent. Analytica Chimica Acta, 627, 148–153.

Claverie F., Fernández B., Pécheyran C., Alexis J. and Donard O.F. (2009)
Elemental fractionation effects in high repetition rate IR femtosecond laser ablation ICP-MS analysis of glasses. Journal of Analytical Atomic Spectrometry, 24, 891–902.

Cuney M., Friedrich M., Blumenfeld P., Bourguignon A., Boiron M.C., Vigneresse J.L. and Poty B. (1990)
Metallogenesis in the French part of the Variscan orogen. Part I: U preconcentrations in pre-Variscan and Variscan formations – A comparison with Sn, W and Au. Tectonophysics, 177, 39–57.

Duthou J.L. (1977)
Chronologie Rb-Sr et geochimie des granitoides d'un segment de la chaine varisque, relations avec le metamorphisme: le Nord limousin, Massif Central Francais. Universite de Clermont, Unite d'enseignement et de recherche de sciences

Eberlei T., Habler G., Wegner W., Schuster R., Körner W., Thöni M. and Abart R. (2015)
Rb/Sr isotopic and compositional retentivity of muscovite during deformation. Lithos, 227, 161–178.

Elburg M., Vroon P., van der Wagt B. and Tchalikian A. (2005)
Sr and Pb isotopic composition of five USGS glasses (BHVO-2G, BIR-1G, BCR-2G, TB-1G, NKT-1G). Chemical Geology, 223, 196–207.

Farina F., Dini A., Rocchi S. and Stevens G. (2014)
Extreme mineral-scale Sr isotope heterogeneity in granites by disequilibrium melting of the crust. Earth and Planetary Science Letters, 399, 103–115.

Fletcher I., McNaughton N., Pidgeon R. and Rosman K. (1997)
Sequential closure of K–Ca and Rb–Sr isotopic systems in Archaean micas. Chemical Geology, 138, 289–301.

Freeman S., Inger S., Butler R. and Cliff R. (1997)
Dating deformation using Rb-Sr in white mica: Greenschist facies deformation ages from the Entrelor shear zone, Italian Alps. Tectonics, 16, 57–76.

Friedrich M. (1983)
Le complexe granitique hyperalumineux de Saint Sylvestre, nord-ouest du Massif central français: évolution de la cristallochimie des phases minérales et de la géochimie des éléments en trace et majeurs; caractérisation du polygénisme dans les granites hyperalumineux; implications sur la métallogénie de l'uranium. Thèse de doctorat de troisième cycle. Université de Nancy I.

Friedrich M., Cuney M. and Poty B. (1987)
Uranium geochemistry in peraluminous leucogranites. Uranium, 3, 353–385.

Glodny J., Bingen B., Austrheim H., Molina J.F. and Rusin A. (2002)
Precise eclogitization ages deduced from Rb/Sr mineral systematics: The Maksyutov complex, southern Urals, Russia. Geochimica et Cosmochimica Acta, 66, 1221–1235.

Glodny J., Kühn A. and Austrheim H. (2008)
Diffusion versus recrystallization processes in Rb–Sr geochronology: Isotopic relics in eclogite facies rocks, Western Gneiss Region, Norway. Geochimica et Cosmochimica Acta, 72, 506–525.

Gorojovsky L. and Alard O. (2020)
Optimisation of laser and mass spectrometer parameters for the *in situ* analysis of Rb/Sr ratios by LA-ICP-MS/MS. Journal of Analytical Atomic Spectrometry, 35, 2322–2336.

Govindaraju K. (1979)
Report (1968–1978) on two mica reference samples: Biotite Mica-Fe and Phlogopite Mica-Mg. Geostandards Newsletter, 3, 3–24.

references

Govindaraju K. (1984)
Report (1973–1984) on two ANRT geochemical reference samples: Granite GS-N and Potash Feldspar FK-N. **Geostandards Newsletter, 8**, 173–206.

Govindaraju K. (1995)
1995 Working values with confidence limits for twenty-six CRPG, ANRT and IWG-GIT geostandards. **Geostandards Newsletter, 19 (Special Issue)**, 32pp.

Grove M. and Harrison T.M. (1996)
Diffusion in $^{40}Ar^*$ Fe-rich biotite. **American Mineralalogist, 81**, 940–951.

Hogmalm K.J., Zack T., Karlsson A.K.-O., Sjöqvist A.S. and Garbe-Schönberg D. (2017)
In situ Rb–Sr and K–Ca dating by LA-ICP-MS/MS: An evaluation of N_2O and SF_6 as reaction gasses. **Journal of Analytical Atomic Spectrometry, 32**, 305–313.

Holliger P., Cuney M., Friedrich M. and Turpin L. (1986)
U-Pb carboniferous age on zircons and monazites from the Brame unit of the Saint-Sylvestre peraluminous granitic complex (NW Massif Central, France). **Comptes Rendus des Seances de l'Academie des Sciences. Serie 2, 303**, 1309–1314.

Jackson S.E. and Günther D. (2003)
The nature and sources of laser induced isotopic fractionation in laser ablation-multicollector-inductively coupled plasma-mass spectrometry. **Journal of Analytical Atomic Spectrometry, 18**, 205–212.

Jackson S.E. and Sylvester P. (2008)
Calibration strategies for elemental analysis by LA-ICP-MS. **Signal, 10**, 100.

Kröner A., Braun I. and Jaeckel P. (1996)
Zircon geochronology of anatectic melts and residues from a high grade pelitic assemblage at Ihosy, southern Madagascar: Evidence for Pan-African granulite metamorphism. **Geological Magazine, 133**, 311–323.

Laureijs C.T., Coogan L.A. and Spence J. (2021)
A high throughput Rb-Sr dating method using solution tandem ICP-MS/MS ($^{87}Sr/^{86}Sr$) and standard addition calibration ICP-MS (Rb/Sr). **MethodsX, 8**, 101309.

Li Q.-L., Chen F., Li X.-H., Wang F. and He H.-Y. (2008)
Single grain Rb-Sr isotopic analysis of GA-1550 biotite, LP-6 biotite and Bern-4M muscovite ^{40}Ar-^{39}Ar dating standards. **Geochemical Journal, 42**, 263–271.

Li Q., Chen F., Wang X., Li X. and Li C. (2005)
Ultra-low procedural blank and the single-grain mica Rb-Sr isochron dating. **Chinese Science Bulletin, 50**, 2861–2865.

Li S.-S., Santosh M., Farkaš J., Redaa A., Ganguly S., Kim S.W., Zhang C., Gilbert S. and Zack T. (2020)
Coupled U-Pb and Rb-Sr laser ablation geochronology trace Archean to Proterozoic crustal evolution in the Dharwar Craton, India. **Precambrian Research, 343**, 105709.

Liu X., Dong S., Yue Y., Guan Q., Sun Y., Chen S., Zhang J. and Yang Y. (2020)
$^{87}Sr/^{86}Sr$ isotope ratios in rocks determined using inductively coupled plasma tandem mass spectrometry in O_2 mode without prior Sr purification. **Rapid Communications in Mass Spectrometry, 34**, e8690.

Liu Y., Hu Z., Li M. and Gao S. (2013)
Applications of LA-ICP-MS in the elemental analyses of geological samples. **Chinese Science Bulletin, 58**, 3863–3878.

Martin R.F., Randrianandraisana A. and Boulvais P. (2014)
Ampandrandava and similar phlogopite deposits in southern Madagascar: Derivation from a silicocarbonatitic melt of crustal origin. **Journal of African Earth Sciences, 94**, 111–118.

McDougall I. and Roksandic Z. (1974)
Total fusion $^{40}Ar/^{39}Ar$ ages using HIFAR reactor. **Journal of the Geological Society of Australia, 21**, 81-89.

McDougall I. and Wellman P. (2011)
Calibration of GA1550 biotite standard for K/Ar and $^{40}Ar/^{39}Ar$ dating. **Chemical Geology, 280**, 19–25.

Moens L., Vanhaecke F., Bandura D., Baranov V. and Tanner S. (2001)
Elimination of isobaric interferences in ICP-MS, using ion–molecule reaction chemistry: Rb/Sr age determination of magmatic rocks, a case study. **Journal of Analytical Atomic Spectrometry, 16**, 991–994.

Morteani G., Kostitsyn Y., Gilg H., Preinfalk C. and Razakamanana T. (2013)
Geochemistry of phlogopite, diopside, calcite, anhydrite and apatite pegmatites and syenites of southern Madagascar: Evidence for crustal silicocarbonatitic (CSC) melt formation in a Panafrican collisional tectonic setting. **International Journal of Earth Sciences, 102**, 627–645.

Nebel O. (2014)
Rb–Sr dating. **In: Rink W.J. and Thompson J. (eds), Encyclopedia of scientific dating methods. Springer Netherlands (Dordrecht)**, 1–19.

Nebel O. and Mezger K. (2006)
Reassessment of the NBS SRM-607 K-feldspar as a high precision Rb/Sr and Sr isotope reference. **Chemical Geology, 233**, 337–345.

Nebel O., Mezger K., Scherer E. and Münker C. (2005)
High precision determinations of $^{87}Rb/^{85}Rb$ in geologic materials by MC-ICP-MS. **International Journal of Mass Spectrometry, 246**, 10–18.

references

Odin G.S. A.C.J., Armstrong R.L., Bagdasaryan G.P., Baksi A.K., Balogh K., Barnes N.A., Boelrijk I.M., Bonadonna F.P., Bonhomme M.G., Cassignol C., Chanin L., Gillot P.Y., Gledhill A., Govindaraju K., Harakal R., Harre W., Hebeda E.H., Hunziker J.C., Ingamells C.O., Kawashita K., Kiss E., Kreuzer H., Long L.E., McDougall I., McDowell F., Mehnert H., Montigny R., Pasteels P., Radicati F., Rex D.C., Rundle C.C., Savelli C., Sonet J., Welin E. and Zimmermann J.L. (1982)
Intel-laboratory standards for dating purposes. In: Odin G.S. (ed.), Numerical dating in stratigraphy, 123–149.

Olierook H.K., Rankenburg K., Ulrich S., Kirkland C.L., Evans N.J., Brown S., McInnes B.I., Prent A., Gillespie J. and McDonald B. (2020)
Resolving multiple geological events using *in situ* Rb–Sr geochronology: Implications for metallogenesis at Tropicana, Western Australia. **Geochronology, 2**, 283–303.

Pandey B., Krishna V., Sastry D., Chabria T., Mary K. and Dhanaraju R. (1993)
Pan-African wholerock Rb–Sr isochron ages for the granites and pegmatites of Kullampatti–Suriyamalai area, Salem District, Tamil Nadu, India. **Mass Spectrometry/IIP, Dehra Dun**, 480–482.

Redaa A., Farkaš J., Gilbert S., Collins A.S., Wade B., Löhr S., Zack T. and Garbe-Schönberg D. (2021)
Assessment of elemental fractionation and matrix effects during *in situ* Rb–Sr dating of phlogopite by LA-ICP-MS/MS: Implications for the accuracy and precision of mineral ages. **Journal of Analytical Atomic Spectrometry, 36**, 322–344.

Rodushkin I., Axelsson M.D., Malinovsky D. and Baxter D.C. (2002)
Analyte- and matrix-dependent elemental response variations in laser ablation inductively coupled plasma-mass spectrometry. **Journal of Analytical Atomic Spectrometry, 17**, 1223–1230.

Rösel D. and Zack T. (2021)
LA-ICP-MS/MS single spot Rb-Sr dating. **Geostandards and Geoanalytical Research, 46**, 143–168.

Roy M. and Raju R.D. (1999)
Petrogenetic model of A-type granitoids of the Kullampatti area, Salem district, Tamil Nadu, India. **Gondwana Research, 2**, 127–135.

Scaillet S., Cheilletz A., Cuney M., Farrar E. and Archibald D. (1996)
Cooling pattern and mineralization history of the Saint Sylvestre and western Marche leucogranite pluton, French Massif Central: I. $^{40}Ar/^{39}Ar$ isotopic constraints. **Geochimica et Cosmochimica Acta, 60,** 4653–4671.

Şengün F., Bertrandsson Erlandsson V., Hogmalm J. and Zack T. (2019)
In situ Rb-Sr dating of K-bearing minerals from the orogenic Akçaabat gold deposit in the Menderes Massif, western Anatolia, **Turkey Journal of Asian Earth Sciences, 185**, 104048.

Smith P.E., Evensen N.M., York D. and Odin G.S. (1998)
Single-Grain ^{40}Ar- ^{39}Ar ages of glauconies: Implications for the geologic time scale and global sea level variations. **Science, 279**, 1517–1519.

Spell T.L. and McDougall I. (2003)
Characterization and calibration of $^{40}Ar/^{39}Ar$ dating standards. **Chemical Geology, 198**, 189–211.

Tillberg M., Drake H., Zack T., Hogmalm J. and Åström M. (2017)
In situ Rb-Sr dating of fine-grained vein mineralizations using LA-ICP-MS **Procedia Earth and Planetary Science, 17**, 464–467.

Tillberg M., Drake H., Zack T., Kooijman E., Whitehouse M.J. and Ström M.E. (2020)
In situ Rb-Sr dating of slickenfibres in deep crystalline basement faults. **Scientific Reports, 10**, 1–13.

Turpin L., Leroy J.L. and Sheppard S.M. (1990)
Isotopic systematics (O, H, C, Sr, Nd) of superimposed barren and U-bearing hydrothermal systems in a Hercynian granite, Massif Central, France. **Chemical Geology, 88**, 85–98.

Uhlig D., Amelung W. and Von Blanckenburg F. (2020)
Mineral nutrients sourced in deep regolith sustain long-term nutrition of mountainous temperate forest ecosystems. **Global Biogeochemical Cycles, 34**, e2019GB006513.

Vanhaecke F., De Wannemacker G., Moens L. and Hertogen J. (1999)
The determination of strontium isotope ratios by means of quadrupole-based ICP-mass spectrometry: A geochronological case study. **Journal of Analytical Atomic Spectrometry, 14**, 1691–1696.

Vermeesch P. (2018)
IsoplotR: A free and open toolbox for geochronology. **Geoscience Frontiers, 9**, 1479–1493.

Villa I.M., De Bièvre P., Holden N.E. and Renne P.R. (2015)
IUPAC-IUGS recommendation on the half life of ^{87}Rb. **Geochimica et Cosmochimica Acta, 164**, 382–385.

Villaros A. and Pichavant M. (2019)
Mica-liquid trace elements partitioning and the granite-pegmatite connection: The St-Sylvestre complex (western French Massif Central). **Chemical Geology, 528**, 119265.

Waight T., Baker J. and Willigers B. (2002)
Rb isotope dilution analyses by MC-ICP-MS using Zr to correct for mass fractionation: Towards improved Rb–Sr geochronology? **Chemical Geology, 186**, 99–116.

Walawender M., Gastil R., Clinkenbeard J., McCormick W., Eastman B., Wemicke R., Wardlaw M., Gunn S. and Smith B. (1990)
Origin and evolution of the zoned La Posta-type plutons, eastern Peninsular. **The nature and origin of Cordilleran Magmatism, 174**, 1.

Willigers B., Mezger K. and Baker J. (2004)
Development of high precision Rb–Sr phlogopite and biotite geochronology: An alternative to $^{40}Ar/^{39}Ar$ tri-octahedral mica dating. **Chemical Geology, 213**, 339–358.

Wise S.A. and Watters R.L. (2012)
Certificate of analysis: Standard Reference Material 610. **National Institute of Standards and Technology (Gaithersburg, USA)**.

references

Woodhead J.D. and Hergt J.M. (2001)
Strontium, neodymium and lead isotope analyses of NIST glass certified reference materials: SRM 610, 612, 614. **Geostandards Newsletter: The Journal of Geostandards and Geoanalysis, 25**, 261–266.

Zack T. and Hogmalm K.J. (2016)
Laser ablation Rb/Sr dating by online chemical separation of Rb and Sr in an oxygen-filled reaction cell. **Chemical Geology, 437**, 120–133.

Zhang S., He M., Yin Z., Zhu E., Hang W. and Huang B. (2016)
Elemental fractionation and matrix effects in laser sampling based spectrometry. **Journal of Analytical Atomic Spectrometry, 31**, 358–382.

Zimmermann J., Vernet M., Guyetand G. and Dautel D. (1985)
Données sur potassium et argon (de 1976 à 1984) dans quelques échantillons géochimiques de référence. **Geostandards Newsletter, 9**, 205–208.

Supporting information

The following supporting information may be found in the online version of this article:

Figure S1. $^{87}Sr/^{86}Sr$ compositions of Sr blanks.

Figure S2. BSE images and SEM-EDS (Figures S2b, S2e, S2g), and EPMA (Figures S2a, S2c, S2d, S2f) elemental maps for Mica-Mg phlogopite grains (grain# a, b, c, e, g, h, i, h).

Figure S3. BSE images of GL-O glauconite grains. Yellow squares represent locations of 10 μm × 10 μm defocused analyses by EPMA (Table S6).

Figure S4. BSE image and SEM-EDS (Figures S4c, S4d, S4e), and EPMA (Figures S4a, S4b) elemental maps for Mica-Fe biotite grains (grain# a, b, c, d, g).

Figure S5. BSE image and SEM-EDS (Figures S5a, S5b, S5c, S5d, S5e) elemental maps for FK-N potassium feldspar grains (grain# a, b, d, e, f).

Figure S6. $^{87}Rb/^{86}Sr$ and $^{87}Sr/^{86}Sr$ isotopic compositions of Mica-Fe in this study and the Rb-Sr isotopic data of biotites (sample B1355 and B1354) from Duthou (1977). The two-point isochron Rb-Sr ages for sample B1355 and B1354 were calculated using an assumed initial ratio of 0.7074 from Duthou (1977).

Table S1. Powdered and solid reference materials used in this study.

Table S2. Rb-Sr mass fractions and $^{87}Sr/^{86}Sr$ ratios for the secondary reference materials compared with literature values.

Table S3. Absolute quantities (ng) of Rb and Sr in the samples analysed by ID-TIMS and MC-ICP-MS (this study) in Table 3.

Table S4. Mean Sr, Rb/Sr, $^{87}Rb/^{86}Sr$, and $^{87}Sr/^{86}Sr$ values and corresponding ages for each RM calculated using different assumptions for the Sr blank contribution.

Table S5. EPMA measurement results for Mica-Mg grains.

Table S6. EPMA measurement results for GL-O grains.

Table S7. EPMA measurement results for Mica-Fe flakes.

Table S8. EPMA measurement results for FK-N grains.

Table S9. Rubidium and Sr mass fractions of the RMs determined by alkali fusion followed by ICP-MS analysis.

This material is available from: http://onlinelibrary.wiley.com/doi/10.1111/ggr.12456/abstract (This link will take you to the article abstract).

Chapter III.
In-Situ Rb-Sr dating by LA-ICP-MS/MS on different matrices

Chapter III. In-Situ Rb-Sr dating by LA-ICP-MS/MS on different matrices

1. Introduction

Rb-Sr isotope measurements are used widely in the earth sciences, as dating tools to constrain the crystallization and cooling ages in silicate magmatic systems, and traces of alteration processes (Glodny et al., 2002; Page, 1978; Willigers et al., 2004). The introduction of inductively coupled plasma-mass spectrometry (ICP-MS) with the incorporation of collision/reaction cell coupled to a laser system (LA-ICP-MS/MS) has led to improvements in measurements of Rb-Sr isotopic ratios in minerals to small scale levels by overcoming the isobaric overlap of ^{87}Rb on ^{87}Sr in recent years (Bolea-Fernandez et al., 2016; Hogmalm et al., 2017; Zack & Hogmalm, 2016).

Despite this advancement, the accurate and precise data of Rb-Sr isotopes remains one of the challenges due to matrix effects in the in-situ Rb-Sr isotope measurements. Raw Rb-Sr isotopic ratios measured by LA-ICP-MS/MS generally differ from preferred values due to elemental and isotopic fractionation during the measurements. Fractionation between Rb and Sr occurs and affects more on the bias of ^{87}Rb/^{86}Sr ratios than ^{87}Sr/^{86}Sr, derived from different energy distributions and ionization potentials between Rb and Sr (Jackson, 2008). During ablation, signal intensities of Rb which is a more volatile element, are less decreased with a relative fractionation factor of ca. 1.4 compared to Sr, which is a refractory element (Eggins et al., 1998; Jackson, 2008.). Thus, the external calibration method with standard-sample-standard bracketing has been applied by using different types of reference materials depending on the type of targeted minerals in the previous LA-ICP-MS/MS studies for Rb-Sr dating (Hogmalm et al., 2017; Zack & Hogmalm, 2016). These corrections were made for natural geological samples by using reference materials (RMs) with similar matrices or Rb-Sr compositions such as phlogopite Mica-Mg for mica samples, basalt glass BCR-2G for feldspars or synthetic silicate glass NIST 610 for apatite in the previous LA-ICP-MS/MS studies (Gorojovsky & Alard, 2020; Hogmalm et al., 2017; Li et al., 2020; Olierook et al., 2020; Redaa et al., 2021; Rösel & Zack, 2022; Tillberg et al., 2020).

An external calibration method with standard-sample-standard bracketing can be used to correct for mass bias if there is no difference in mass discrimination between the standard matrix relative to the sample matrix, and their fractionation trends are similar over the course of an analytical session (Pearson et al., 2008). It has been investigated by previous studies that the different behavior during the process of laser analysis between various matrices influence elemental and isotopic fractionation effects (Pearson et al., 2008; Sylvester, 2008; Zhang et al., 2016). Mass discrimination during the LA-ICP-MS analysis and matrix effects are the main source of error that affects isotope ratio measurements and their accuracy. To have better precision and accuracy of the LA-ICP-MS isotopic data, the importance of using matrix-matched standards has been highlighted for mass bias correction (Jackson, 2008; Lin et al., 2016).

The recent studies of in-situ Rb-Sr isotopic analysis by LA-ICP-MS/MS documented that instrument operating parameters of ICP-MS/MS and LA system as well as differences in chemical and physical properties between standards and samples can influence Rb-Sr isotopic fractionation and the accuracy and precision of the Rb-Sr isotopic data (Gorojovsky & Alard, 2020; Redaa et al., 2021). Gorojovsky & Alard (2021) reported that Rb-Sr ages of the Monastery phlogopite (Kaapvaal Craton, South Africa) measured by LA-ICP-MS/MS with mass bias correction of $^{87}Rb/^{86}Sr$ made using glass RMs of NIST 610 and BCR-2G and mineral RM of Mica-Mg gave the range of the ages from 73.29 ± 1.94 Ma by NIST 610 to 90.04 ± 3.64 Ma by Mica-Mg. The obtained age with the external calibration by using Mica-Mg agree better with known age of 90.26 ± 0.56 Ma for the Monastery phlogopite, compiled by Gorojovsky & Alard (2021). Redaa et al. (2021) measured Rb-Sr isotopic ratios for the MDC phlogopite (Madagascar) by LA-ICP-MS/MS with external calibration of $^{87}Rb/^{86}Sr$ against NIST 610 and Mica-Mg. Compared to the known age of 519.4 ± 6.5 Ma for the phlogopite from Hogmalm et al. (2017), the calibration using NIST 610 and Mica-Mg yielded the age of 455 ± 6 Ma and 601 ± 8 Ma, respectively, in the same laser conditions of 193 nm laser wavelengths. This study proposed that the discrepancy of the measured two ages relative to the known age of the MDC phlogopite are related to the matrix effects, resulting in various fractionation and ablation characteristics between the RMs and the sample. In the study of Rösel & Zack (2022), they also observed the discrepancy of measured $^{87}Rb/^{86}Sr$ ratios of BCR-2G and NIST 610 calibrated using Mica-Mg gave the agreement within 0.9-15.4% and 0.6-8.5% between the

measured and preferred values, respectively, which are variable depending on the analytical sessions. These studies suggested that the matrix effects related to standard selection and operating conditions could limit the accuracy and precision of Rb-Sr ages acquired by LA-ICP-MS/MS. Comparison with reference ages by Gorojovsky & Alard (2021) shows systematic age offsets in Rb-Sr ages up to ca. 18% in the studied sample by non-matrix-matched calibration using NIST 610. Influences of matrix effects on the measurements and potential parameters giving rise to the matrix effects have been investigated from the existing works. However, the extent to which matrix is appropriate and what causes can lead to the matrix effects for external calibration of Rb-Sr isotopic analyses of natural geological samples by LA-ICP-MS/MS is still unclear for better accuracy and precision of Rb-Sr isotope measurements.

In this study, our investigation focuses on examining possible correlations of the accuracy and precision for Rb-Sr isotopic values and age offsets in mica and feldspar samples with chemical compositions and ablation characteristics of the RMs and samples. Various types of RMs and geological samples with wide compositional variations were conducted including synthetic glass (NIST 610, NIST 612), geological glass RMs (BCR-2G, BHVO-2G and KL2-G basalt glasses, ATHO-G rhyolite and T1-G diorite glasses) and mineral RMs (Mica-Mg phlogopite, Mica-Fe biotite, FK-N potash feldspar and GL-O glauconite) with natural mica and feldspar samples. We discuss factors that could contribute to the matrix effects between difference matrices and the precision and accuracy of the measurements. Finally, we suggest the recommended procedures using matrix-matched and matrix-mismatched external calibrations for in-situ Rb-Sr dating method by LA-ICP-MS/MS.

2. Samples

The selection of the RMs in this work was carried out to investigate and compare matrix effects, ablation properties and fractionation between different types of materials and their effect on the in-situ Rb-Sr dating of natural samples. The RMs cover a wide range of Rb-Sr isotopic ratios, Rb-Sr concentrations and major element compositions (**Fig. 9**) and display different physical properties as glass, powder and natural mineral. The RMs were used either as primary calibration standards for mass bias correction or as secondary standards. The list of samples with their number of individual analyses is presented in **Table 6**. The published and

measured chemical compositions of the RMs used in this work are summarized in **Table 7**. Based on the published data of the RMs in **Table 7**, the expected Rb-Sr isotopic ratios and corresponding Rb-Sr ages were compared to the results in this work in order to evaluate the accuracy and precision of the LA-ICP-MS/MS analyses.

Table 6. Sample list and number of single analyses in the LA-ICP-MS/MS sessions.

Sample name	Analysis name	Sample type	Session 1	2	3	4	5
Glass RMs							
NIST SRM 610	NIST 610	Synthetic silicate glass	16*	14*	6*	16*	16*
NIST SRM 612	NIST 612	Synthetic silicate glass		14*		16*	16*
USGS BCR-2G	BCR-2G	Basalt glass	16*	14*	6*	16*	16*
USGS BHVO-2G	BHVO-2G	Basalt glass		14*		16*	16*
MPI-DING KL2-G	KL2-G	Basalt glass				16*	16*
MPI-DING ATHO-G	ATHO-G	Rhyolite glass				16*	16*
MPI-DING T1-G	T1-G	Diortie glass				16*	16*
Mineral powder RMs							
CRPG Mica-Mg	Mica-Mg-P-1	Phlogopite	16*	14*			
	Mica-Mg-P-2	Phlogopite	12	14*	6*	16*	16*
	Mica-Mg-P-3	Phlogopite	12		6*	16*	16*
	Mica-Mg-P-4	Phlogopite	12				
CRPG Mica-Fe	Mica-Fe-P	Biotite	16*	14*			
CRPG GL-O	GL-O-P	Glauconite	16*	14*	6*	16*	16*
CRPG FK-N	FK-N-P	Potash feldspar	16*	14*	6*	16*	16*
Mineral and whole-rock samples							
CRPG Mica-Mg	Mica-Mg-G	Phlogopite				24	
CRPG Mica-Fe	Mica-Fe-G	Biotite	12	15			
CRPG FK-N	FK-N-G	Potash feldspar	12				24
CRPG GL-O	GL-O-G	Glauconite		12	6		24
Ampandarandava Phologopite	Apd-Phl	Phlogopite					
La Posta granodiorite	LP	Granodiorite	12		9	20	
Mt. Dromedary biotite	MD	Biotite flakes		3			
Mt. Dromedary monzonite	MD	Biotite in monzonite		9			

*RMs used either as primary or secondary standards

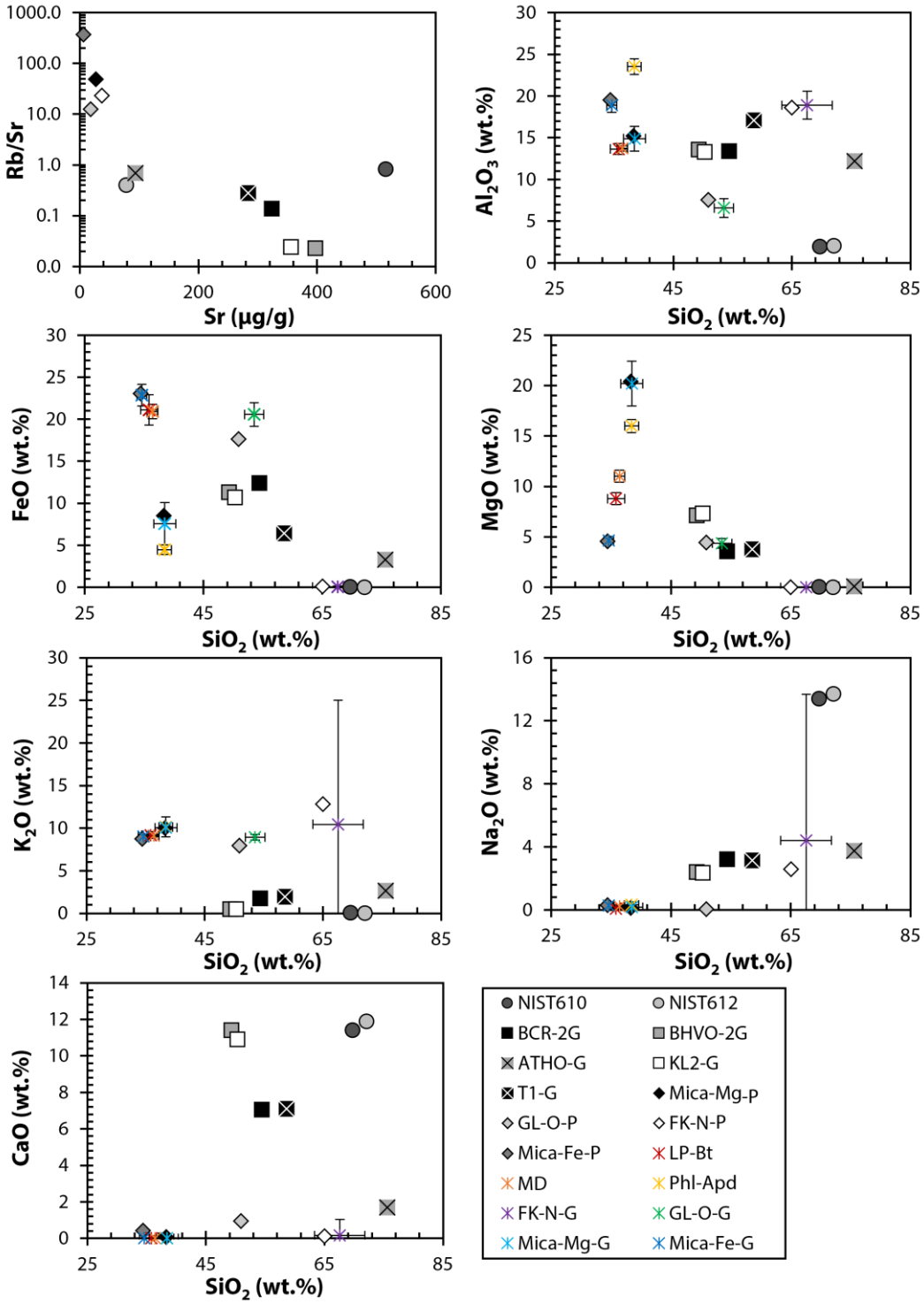

Fig. 9. Rb-Sr and major element compositions of the RMs and samples. Error bars are measured or published uncertainties (2 SD) in **Table 7**. Circles, squares, diamonds and stars represent synthetic silicate glasses (NIST 610, 612), geological glasses (BCR-2G, BHVO-2G, ATHO-G, KL2-G, T1-G), mineral powder pressed pellets (Mica-Mg-P, GL-O-P, FK-N-P, Mica-Fe-P) and mineral grain RMs and samples (LP-Bt, MD, Phl-Apd, FK-N-G, GL-O-G, Mica-Mg-G, Mica-Fe-G).

Table 7. Chemical compositions of RMs and samples used in this study.

Sample	Type	SiO_2 (wt.%)	2 SD	Al_2O_3 (wt.%)	2 SD	FeO (wt.%)	2 SD	MgO (wt.%)	2 SD	CaO (wt.%)	2 SD	Na_2O (wt.%)	2 SD	K_2O (wt.%)	2 SD
NIST 610[a]	Silicate	69.7	0.5	1.95	0.04	0.06	0.02	0.07	0.00	11.4	0.2	13.4	0.3	0.06	0.00
NIST 612[b]	Silicate	72.1	0.6	2.03	0.04	0.02		0.01		11.9	0.1	13.7	0.3	0.01	0.00
BCR-2G[c]	Basalt	54.4	0.8	13.40	0.80	12.4	0.6	3.6	0.2	7.1	0.2	3.2	0.1	1.7	0.1
BHVO-2G[d]	Basalt	49.3	0.2	13.60	0.20	11.3	0.2	7.1	0.0	11.4	0.2	2.4	0.2	0.51	0.04
KL2-G[e]	Basalt	50.3	0.3	13.30	0.20	10.7	0.1	7.3	0.1	10.9	0.2	2.4	0.1	0.48	0.01
ATHO-G[f]	Rhyolite	75.6	0.7	12.20	0.20	3.3	0.1	0.10	0.01	1.7	0.0	3.8	0.3	2.6	0.1
T1-G[g]	Diorite	58.6	0.4	17.10	0.20	6.4	0.1	3.75	0.04	7.1	0.1	3.1	0.1	2.0	0.0
Mica-Mg[h]	Phlogopite	38.3	0.4	15.20	0.44	8.5	0.2	20.4	0.7	0.08	0.04	0.12	0.21	10.0	0.3
Mica-Mg-G[i]	Phlogopite	38.5	1.8	14.90	1.48	7.6	2.5	20.2	2.2			0.17	0.09	10.1	0.4
Mica-Fe[j]	Biotite	34.4	0.7	19.50	0.65	23.1	0.4	4.6	0.4	0.43	0.11	0.30	0.12	8.8	0.4
Mica-Fe-G[k]	Biotite	34.6	0.8	18.89	0.88	22.9	1.3	4.7	0.4			0.27	0.08	9.0	0.2
GL-O[l]	Glauconite	50.9	0.7	7.55	0.37	17.6	0.2	4.5	0.3	0.96	0.15	0.04	0.02	7.9	0.3
GL-O-G[m]	Glauconite	53.5	1.6	6.57	1.11	20.6	1.4	4.4	0.5					8.9	0.3
FK-N[o]	Potash feldspar	65.0	0.7	18.61	0.55	0.08	0.04	0.01	0.06	0.11	0.08	2.6	0.2	12.8	0.5
FK-N-G[p]	Potash feldspar	67.6	4.2	18.90	1.68	0.04	0.09	0.00	0.02	0.16	0.87	4.4	9.3	10.4	14.6
LP[q]	Biotite	35.8	1.4	13.64	0.66	21.1	1.8	8.8	0.6	0.00	0.03	0.08	0.06	9.2	0.4
MD-Bt[r]	Biotite	36.4	0.9	13.71	0.33	20.9	0.9	11.0	0.6	0.00	0.00	0.22	0.08	9.1	0.2
Apd-Phl[s]	Phlogopite	38.4	1.2	23.52	0.95	4.5	0.6	16.0	0.7	0.01	0.02	0.32	0.20	10.1	1.2

Table 7. (continued).

Sample	Type	Rb (µg g^{-1})	2 SD	Sr (µg g^{-1})	2 SD	Rb/Sr	$^{87}Rb/^{86}Sr$	2 SD	$^{87}Sr/^{86}Sr$	2 SD
NIST 610[a]	Silicate	425.7	0.8	515.5	0.5	0.83	2.3308	0.0049	0.709699	0.000018
NIST 612[b]	Silicate	31.4	0.4	78.4	0.2	0.40	1.130	0.015	0.709063	0.000020
BCR-2G[c]	Basalt	44.75	7.38	323.7	5	0.14	0.3901	0.0009	0.705003	0.000008
BHVO-2G[d]	Basalt	9.2	0.2	397	5	0.02	0.0652	0.0003	0.703469	0.000014
KL2-G[e]	Basalt	8.7	0.4	356	8	0.02	0.0690	0.0035	0.703565	0.000022
ATHO-G[f]	Rhyolite	65.3	3	94.1	2.7	0.69	1.96	0.11	0.703271	0.000015
T1-G[g]	Diorite	79.7	3.5	284	6	0.28	0.792	0.039	0.710137	
Mica-Mg[h]	Phlogopite	1327	41	27.1	1.5	49	155.6	7.3	1.8622	0.0067
Mica-Mg-G[i]	Phlogopite									
Mica-Fe[j]	Biotite	2293	142	6.2	0.6	369	1815.3	246.3	7.994	1.021
Mica-Fe-G[k]	Biotite									
GL-O[l]	Glauconite	228	18	18.3	1.0	12	36.2	4.0	0.7531	0.0009
GL-O-G[m]	Glauconite									
FK-N[o]	Potash feldspar	853	69	37.1	1.0	23	69.9	4.1	1.2114	0.0021

[a, b, c, d, e, f, g] Major element compositions from GeoRem, $^{87}Rb/^{86}Sr$ calculated using (total Rb ∗ 0.2782) / (total Sr ∗ 0.0986).

[a] Rb and Sr concentration from Wide and Watters (2012), $^{87}Sr/^{86}Sr$ from Woodhead and Hergt (2001)

[b] Rb and Sr concentrations from GeoRem, $^{87}Sr/^{86}Sr$ from Woodhead and Hergt (2001)

[c, d] Rb and Sr concentrations and $^{87}Sr/^{86}Sr$ from Elburg et al. (2005)

[e, f, g] Rb and Sr concentrations and $^{87}Sr/^{86}Sr$ from GeoRem

[h, j, l, o] Rb-Sr concentration and Rb-Sr isotopic values from Jegal et al. (2022), major element compositions from Govidnaraju (1995)

[i, K, m, p] major element elements from Jegal et al. (2022)

[q, s] major element elements are mean values analyzed by EPMA in this study (n = 16 for LP-Bt, 25 for Apd-Phl)

[r] Mean (n = 10) of GA-1550 from Li et al. (2008)

2.1. Glass RMs

The synthetic and geological reference glasses were mounted into resin and analyzed for their Rb-Sr isotopic compositions: SRM 610 and 612 silicate glasses available from NIST (National Institute of Standards and Technology, MD, USA), BCR-2G and BHVO-2G basalt glasses from USGS (United States Geological Survey, VA, USA), KL2-G basalt glass, ATHO-G rhyolite glass and T1-G diorite glass from MPI-DING (Max-Planck-Institut für Chemie, Germany). Details of sample information were published for NIST glasses (Jochum et al., 2011), USGS RMs (Wilson 1997a, b; Raczek et al., 2001) and the MPI-DING RMs (Jochum et al., 2000).

The Rb/Sr ratios in the RMs range from 0.02 to 0.83 (**Table 7**). NIST 610 or 612 have been widely used as primary standards for mass discrimination correction in in-situ measurements of $^{87}Sr/^{86}Sr$ values of geological reference glasses and natural minerals (Bolea-Fernandez et al., 2016; Gorojovsky & Alard, 2020; Hogmalm et al., 2017; Li et al., 2020; Olierook et al., 2020; Redaa et al., 2021; Şengün et al., 2019; Zack & Hogmalm, 2016). NIST 612 and USGS BCR-2G or USGS BHVO-2G have also been used to calibrate $^{87}Rb/^{86}Sr$ ratios of natural minerals such as feldspars (Gorojovsky & Alard, 2020; Tillberg et al., 2020; Zack & Hogmalm, 2016). In this study, the glass RMs were used either as primary or secondary standards and compared to the published reference values in **Table 7**.

2.2. Mineral RMs

The four mineral RMs, including a phlogopite (Mica-Mg), a biotite (Mica-Fe), a glauconite (GL-O) and a potassium feldspar (FK-N), are certified and available from SARM (Service d'Analyse des Roches et des Minéraux, CNRS National facility; https://sarm.cnrs.fr/), CRPG, Nancy, France. Details of the sample collection, preparation, and working values were reported by Govindaraju, (1979, 1995, 1984) and Odin et al. (1982). They were selected based on a variety of mineral types and Rb-Sr compositions with Rb/Sr ratios ranging from 12 to 369 (**Table 7**). Mica-Mg has been widely used as a primary standard to calibrate $^{87}Rb/^{86}Sr$ ratios of micas by LA-ICP-MS community for Rb-Sr geochronology studies (Gorojovsky & Alard, 2020; Hogmalm et al., 2017; Li et al., 2020; Olierook et al., 2020; Redaa et al., 2021; Şengün et al., 2019; Rösel & Zack, 2022), using the $^{87}Rb/^{86}Sr$ values for Mica-Mg proposed by Hogmalm et

al. (2017). The nature and homogeneity of the four CRPG RMs were characterized as potential RMs for in-situ Rb-Sr isotopic analysis by LA-ICP-MS/MS by Jegal et al. (2022). The published ages of the RMs range from 499 to 528 Ma for Mica-Mg, from 287 to 324 Ma for Mica-Fe, from 80.9 to 98.2 Ma for GL-O and from 512 to 521 Ma for FK-N (**Table 8**).

In this work, the four CRPG RMs were investigated in the form of powder pressed tablets and as mineral grains. Four powder pressed tablets of Mica-Mg (Mica-Mg-P1, P2, P3, P4 in **Table 6**) from different powder aliquots were used in this work. The original powdered Mica-Mg RM from SARM were processed into pressed powder pellet from BRGM (France): Mica-Mg-P1 and P2. The Mica-Mg-P3 and Mica-Mg-P4 were supplied from Gothenburg University (Sweden) and myStandards GmbH (Germany), respectively. The pressed powder tablets of GL-O-P was produced from BRGM (France) by using the original powdered GL-O RM provided from SARM. The powder pressed tablets of Mica-Fe and FK-N were from myStandards GmbH. These powder pressed tablets of the RMs were used either as primary calibration standards or secondary standards for the in-situ Rb-Sr isotopic measurement and compared to the published ID-TIMS and MC-ICP-MS Rb-Sr isotopic values. The mineral grains of Mica-Mg, GL-O, Mica-Fe and FK-N provided from SARM were randomly selected and mounted into resin. The cleavage planes of large Mica-Mg flakes were mounted with perpendicular to the polished surface. These mineral grains were treated as unknown samples for in-situ LA-ICP-MS/MS Rb-Sr dating to compared with their published ages. A summary of reported geochronological data for the four RMs are presented in **Table 8**.

2.3. Mineral and whole-rock samples

To test the in-situ Rb-Sr analysis by LA-ICP-MS/MS method on natural geological materials, we analyzed minerals from different location, composition and age ranging from Cambrian to Tertiary. They were selected based on the availability of precise age data determined from other geochronologic systems and/or by other methods. The brief descriptions of the previous age determinations and chemical compositions are reported in **Table 8** and **Table 7**, respectively.

La Posta granodiorite (analysis name: LP) sourced from the small-biotite facies of the La Posta intrusion, California, consists of mm-sized euhedral to subhedral biotites in a matrix

of plagioclase-quartz-K-feldspar (Clinkenbeard & Walawender, 1989). Previously reported ages of La Posta granodiorite were compiled by Zack & Hogmalm (2016) with a weighted mean age of 91.6 ± 1.2 Ma. Rb-Sr ages ranging from 88.6 ± 1.7 to 92.1 ± 3.5 Ma were reported for La Posta biotite by Rösel & Zack (2022) using in-situ Rb-Sr dating method by LA-ICP-MS/MS and Mica-Mg as a primary standard. Biotite, K-feldspars and plagioclase from La Posta granodiorite analyzed in this work were prepared in the form of whole-rock, provided from Gothenburg University (Sweden), polished section mounted in epoxy resin.

The Mount Dromedary biotite (analysis name: MD) were collected from a monzonite of the Mount Dromedary igneous complex, Central Tilba, New South Wales, Australia. A K-Ar age of 98.5 ± 0.5 Ma was reported for the biotite (also known as GA-1550) by McDougall &Wellman (2011), and many studies have confirmed this age (e.g., Li et al., 2008; Phillips et al., 2017.; Wang et al., 2006 among others). The in-situ Rb-Sr dating study of Rösel & Zack (2022) reported Rb-Sr isochron ages for the Mount Dromedary biotite of 98.7 ± 4.2 Ma and 100.2 ± 2.9 Ma when using Mica-Mg as a primary calibrator. The Mt. Dromedary biotites in this study were provided from Gothenburg University (Sweden) and analyzed in the form of biotite grains lying on their cleavage along the copper tape and as a whole-rock of monzonite mounted in epoxy mounts.

Ampandarandava Phlogopite (analysis name: Apd-Phl) originated from the pegmatite of Ampandrandava phlogopite quarry, southern Madagascar. Morteani et al. (2013) reported a Rb-Sr age of 518 ± 8 Ma for the Ampandarandava phlogopites, recalculated using the revised ^{87}Rb decay constant of Villa et al. (2015). The published ages of phlogopites from southern Madagascar range from 500 ± 10 Ma for Rb-Sr phlogopite from Sakaravy deposit (Martin et al., 2014), recalculated using the revised ^{87}Rb decay constant of Villa et al. (2015), to 528 ± 9.37 Ma for Mica-Mg powder from Bekily area (Laureijs et al., 2021). For recent in-situ Rb-Sr dating by LA-ICP-MS/MS (Li et al., 2020; Redaa et al., 2021), phlogopites from southern Madagascar have been used as a secondary standard, calibrated using Mica-Mg powder tablet. The reported Rb-Sr ages range from 503 ± 7 Ma to 559 ± 7 Ma by Redaa et al. (2021) and 543 ± 7 Ma by Li et al. (2020). The phlogopite grains in this study, provided from BRGM (France), were mounted into resin with the cleavage plans perpendicular to the polished surface.

Table 8. Compilation of reported ages of RMs and samples in this study.

Sample name	Type	Age (Ma)
CRPG Mica-Mg	Phlogopite	499-528 (compiled)[a]
		521 ± 24 Ma (Rb-Sr)[a,*]
CRPG GL-O	Glauconite	80.9-98.2 (compiled)[a]
		89.2 ± 9.9 Ma (Rb-Sr)[a,*]
CRPG Mica-Fe	Biotite	287-324 (compiled)[a]
		307.6 ± 0.4 (Ar-Ar)[g,*]
CRPG FK-N	Potash feldspar	512-521 (compiled)[a]
		512 ± 30 Ma (Rb-Sr)[g,*]
Ampandarandava Phologopite	Phlogopite	518 ± 8 (Rb-Sr)[b,*]
La Posta granodiorite	Granodiorite	91.6 ± 1.2 (compiled)[c,*]
		93.8 ± 2.5 (Rb-Sr)[d]
Mt. Dromedary biotite	Biotite	100.3 ± 1.9 (Rb-Sr)[e,*]
		98.5 ± 0.5 (K-Ar)[f]

* used to evaluate the accuracy of the different approaches in **section 5.2.**

[a] reported and calculated ID-TIMS and MC-ICP-MS ages compiled by Jegal et al. (2022)

[b] Rb-Sr of phlogopites from the pegmatite, Amandarndava deposit (Morteani et al. 2013)

[c] Weighted mean age compiled by Zack and Hogmalm (2010)

[d] Rb-Sr ages of La Posta bitotie, apatite and whole rock from Walawender et al. (1990), recalculated using the decay constants from Villa et al. (2015)

[e] Rb-Sr ages of GA1550 from Li et al. (2008), recalculated using the decay constants from Villa et al. (2015)

[f] McDougall and Wellman (2011)

[g] Ar-Ar Mica-Fe age of Grove and Harrison (1996)

3. Analytical Methods

3.1. LA-ICP-MS/MS

3.1.1. Instrumentation

In-situ Rb-Sr isotopic analyses were conducted at the GeoRessources laboratory, Nancy, France. An Agilent 8900 ICP-MS/MS instrument, coupled to an ESI 193 nm, ArF excimer laser ablation (LA) system with a two-volume 'TwoVol2' ablation chamber, was used to determine $^{87}Rb/^{86}Sr$ and $^{87}Sr/^{86}Sr$ ratios of the studied RMs and samples. The instrumental setup and tuning parameters of the LA-ICP-MS/MS are summarized in **Table 9.** In the main chamber (100 mm × 100 mm) of the LA system, the targets were ablated in a helium (He) environment. He was used as carrier gas with a flow rate of 650 mL min^{-1}, then mixed with N_2 via a Y-connector at a flow rate of 4 mL min^{-1}. The glass cylinder filled with steel wool (wire smoothing device described in **chapter 1**), installed prior to the entering the ICP, was created following the procedure described by Rösel & Zack (2022). N_2O was used as a reaction gas in the reaction cell of ICP-MS/MS to separate ^{87}Sr from ^{87}Rb. The carrier gas flow rates and plasma conditions were tuned in SQ mode (single quadrupole; no gas in the reaction cell) to provide (i) to high elemental sensitivity (ii) to minimize the fractionation of Th/U for efficient ionization of the aerosol in the plasma and (iii) to maintain a low oxide production (ThO/Th). By using NIST 610 glass in line scan mode (60 µm), the ThO/Th ratio was below 0.2%, and a Th/U ratio was typically from 0.98 to 1.0. After shifting to MS/MS mode (reaction gas in the cell), the parameters of lenses and cells were checked, and then the reaction gas N_2O was optimized by monitoring the sensitivity for both on-mass Rb (85 m/z) and mass-shifted Sr reaction products (102 m/z for $^{86}Sr^{16}O^+$, 103 m/z for $^{87}Sr^{16}O^+$, 104 m/z for $^{88}Sr^{16}O^+$).

Five analytical sessions were conducted on the RMs and samples with a same laser spot size of 50 µm, repetition rate of 5 Hz, and laser energy density of ca. 6 (6.0-6.5) J cm^{-2}. The following isotopes were measured (integration time in parentheses): $^{28}Si \rightarrow {}^{28}Si$ (2 ms), $^{84}Sr \rightarrow {}^{84}Sr$ (5 ms), $^{84}Sr \rightarrow {}^{100}SrO$ (120 ms), $^{85}Rb \rightarrow {}^{85}Rb$ (20 ms), $^{85}Rb \rightarrow {}^{101}Rb$ (5 ms), $^{86}Sr \rightarrow {}^{86}Sr$ (5 ms), $^{86}Sr \rightarrow {}^{102}SrO$ (120 ms), $^{87}Sr \rightarrow {}^{87}Sr$ (5 ms), $^{87}Sr \rightarrow {}^{103}SrO$ (120 ms), $^{88}Sr \rightarrow {}^{88}Sr$ (5 ms), $^{88}Sr \rightarrow {}^{104}SrO$ (120 ms). A sweep of all isotopes (sampling period) took about 500 ms. Each measurement consists of 50 s of ablation and 30 s and 45 s of background and washout time, respectively. The sensitivity on the measurements of ^{85}Rb and $^{88}Sr^{16}O^+$ from the five

sessions were quantified with the NIST 610 glass ranging from 6838 to 7395 and from 8677 to 9522 cps/ppm, respectively. The reported sensitivity of $^{88}Sr^{16}O^{+}$ for NIST 610 by LA-ICP-MS/MS from the previous study of Gorojovsky & Alard (2021) is 330 cps/ppm (170,000 cps; LA conditions of 85 µm spot size, 5 Hz and 193 nm).

Table 9. LA-ICP-MS/MS parameters.

Laboratory and sample preparation		
Laboratory		GeoRessources, Nancy, France
Sample type		Glass and mineral RMs and natural geolgocial samples
Sample preparation		powder pressed tablet or chips/grains mounted in epoxy
Laser ablation system		
Model		ESI NWR 193
Ablation cell		Two Volume ablation chamber (TwoVol1)
Laser wavelength	nm	193
Fluence	J cm^{-2}	ca. 6
Repetition rate	Hz	5
Ablation duration	s	50
background and washout	s	30-45
Spot diameter	µm	50
Sampling mode/pattern		Static spot ablation
Carrier gas		He
Cell carrier gas flow	ml min^{-1}	650
N_2 addition	ml min^{-1}	4
ICP-MS Instrument		
Model		Agilent 8900
Scan type		MS/MS
Sample introduction		Wire smoothing device
RF power	W	1550
Sample depth	mm	4
Ar carrier gas flow	L min^{-1}	0.70-0.75 (optimised daily)
Detection system		dynamic range electron multiplier detector
N_2O gas flow rate	mL min^{-1}	ca. 0.20 (optimised daily)
Q1 → Q2 masses	amu	85 → 85 86 → 102 87 → 103 88 → 104
Energy discrimitation	V	-7
Wait time offset	s	2
Integration time per mass (dwell times)	ms	120 (except 85: 50 ms)
Dead time	ns	35
Typical oxide rate (^{248}ThO / ^{232}Th)	%	0.12-0.19
$^{232}Th/^{238}U$	%	98-99
Sensitivity of ^{85}Rb	cps/ppm	6838-7395
Sensitivity of $^{88}Sr^{16}O$	cps/ppm	8677-9522

Table 9. (continued).

Data processing in Iolite 3	
Gas blank	30s
Reference material	NIST, MPDI-ING, USGS, CRPG RMs
Mass discrimination	Sample standard bracketing, normalized to selected primary RMs
Data processing package	Iolite 3 for interval selection, gas blank and mass discrimination correction (DRS of Iolite 3 from Rösel & Zack 2022)
Calibration strategy	(1) Calculation of the average background-subtracted ^{85}Rb, ^{86}Sr and ^{87}Sr count per second (cps) from signals collected on masses 85, 102, and 103 amu, respectively (2) Conversion of ^{85}Rb cps signal to ^{87}Rb cps based on the natural abundance of Rb isotopes where $^{87}Rb = {}^{85}Rb \times 0.38562$ (3) Calculation of raw $^{87}Sr^{16}O/^{86}Sr^{16}O$ and $^{87}Rb/^{86}Sr^{16}O$ ratios using 'mean of the ratios approach' of Fisher et al. (2010) (4) Correction of drift and mass bias using correction factors obtained by dividing the measured $^{87}Sr/^{86}Sr$ and $^{87}Rb/^{86}Sr$ ratios of reference materials, by their
Uncertianty	Propogation in quadrature. 2 SE of the mean ratio of the integration period and the session-based excess variance of the repeated analyses of the selected primary RMs.

3.1.2. Analytical sequence and data calibration

In our experiments, each sample was analyzed in RMs-samples-RMs sequence. The RMs were measured after every 12-16 sample measurements. The list and number of analyses for each sample in the analytical sessions are reported in **Table 6**. LA-ICP-MS/MS data were processed using the Iolite 3 software (Paton et al., 2011). The data reduction scheme (DRS) used in this study was customized for in-situ Rb-Sr dating by Rösel & Zack (2022). The data processing steps are summarized in **Table 9**. An identical integration period of 25 s was chosen for RM and sample analyses to ensure an interval of stable ablation signal for the different analyses of mineral samples and powder RMs. The processed and calibrated data for $^{87}Sr/^{86}Sr$ and $^{87}Rb/^{86}Sr$ ratios were plotted in conventional isochron plots and calculated for Rb-Sr isochron ages and the Sr isotope initial ratios by using IsoplotR v. 5.0 (Vermeesch, 2018).

The 'raw' $^{87}Sr/^{86}Sr$ and $^{87}Rb/^{86}Sr$ ratios indicate the ratios of raw Rb and SrO intensities after blank correction. The calibrated data are indicated as 'measured' $^{87}Sr/^{86}Sr_{RM}$ and $^{87}Rb/^{86}Sr_{RM}$ ratios, where RM indicates external RM calibrants (**Fig. 10**). In the **section 4**, the 'measured' Rb-Sr ratios were normalized to the published values (**Table 7**) as measured/published ratios, and these ratios are indicated as $^{87}Sr/^{86}Sr_N$ and $^{87}Rb/^{86}Sr_N$.

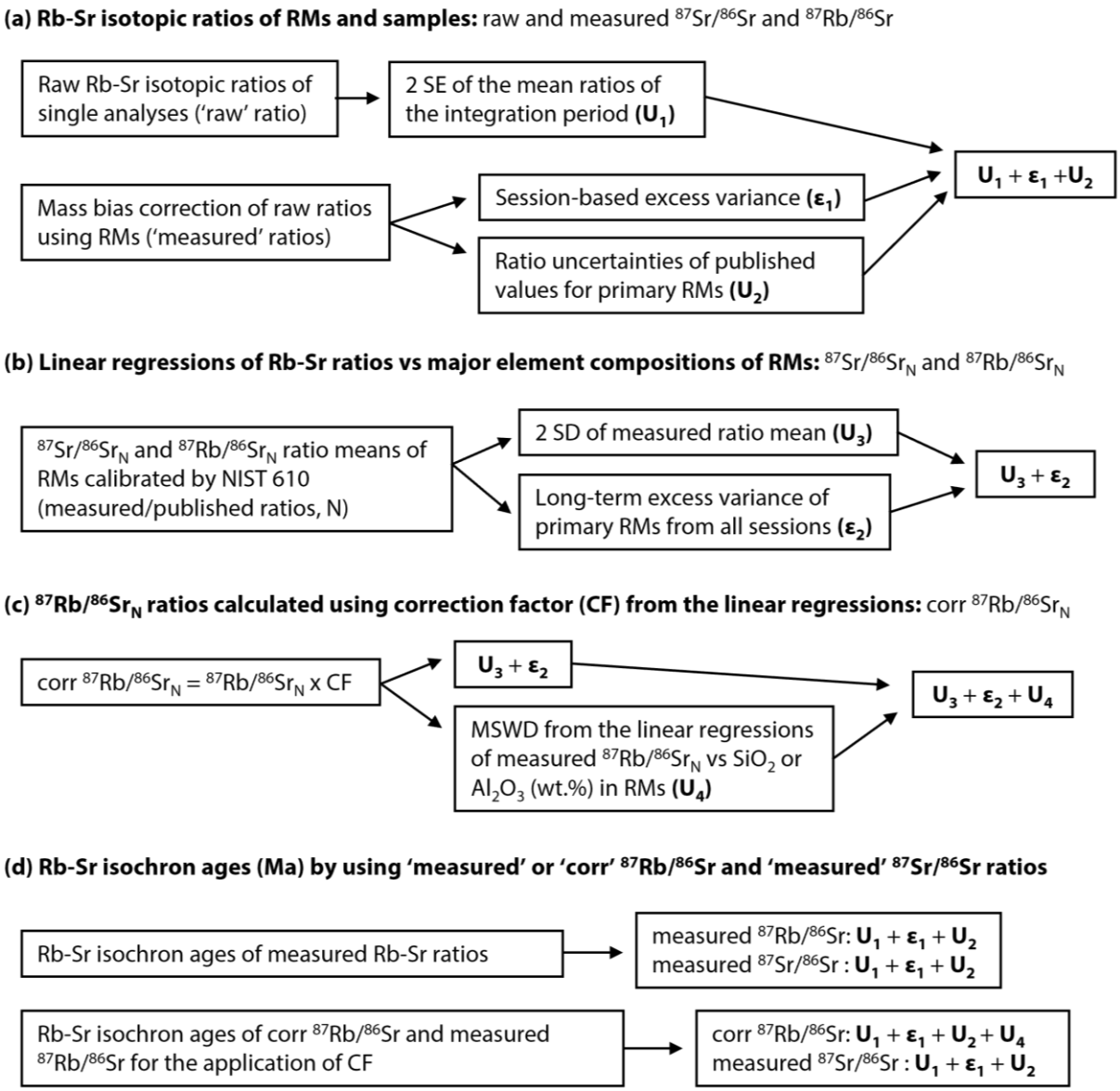

Fig. 10. Schematic illustration of the defined uncertainty propagation workflow.

3.1.3. Uncertainty

A schematic overview of the calculation for the uncertainty is illustrated in **Fig. 10**. Uncertainties for raw $^{87}Rb/^{86}Sr$ and $^{87}Sr/^{86}Sr$ ratios (U_1) were calculated from the mean ratio of the selected integration periods and corrected for background signals. The uncertainties of measured $^{87}Rb/^{86}Sr$ and $^{87}Sr/^{86}Sr$ ratios corrected for mass bias using primary calibration RMs were calculated in the Iolite 3 software by adding U_1 and session-based excess variance for the primary standards (ε_1) in quadrature. The excess variance (ε) represents excess scatter using

RM to produce MSWD = 1 to be added to each data point (Horstwood et al., 2016), which could reflect the inhomogeneities of the RMs and variance between measurements. With these random uncertainties (U_1 and ε_1), the ratio uncertainties of the published values for the primary standards (U_2, see **Table 7**) were added for the final measured $^{87}Rb/^{86}Sr$ and $^{87}Sr/^{86}Sr$ ratios to plot in Rb-Sr isochrons and calculate Rb-Sr isochron ages.

For the measured $^{87}Sr/^{86}Sr_N$ and $^{87}Rb/^{86}Sr_N$ mean ratios in **section 4**, the 2 SD uncertainties of the mean ratios (U_3) were calculated by averaging the measured $^{87}Sr/^{86}Sr_N$ and $^{87}Rb/^{86}Sr_N$ ratios from all measurement sessions. The uncertainties of $^{87}Sr/^{86}Sr_N$ and $^{87}Rb/^{86}Sr_N$ ratios for linear regressions in **section 4.5** include the U_3 and long-term excess variance of primary RMs (ε_2) calculated using all individual data from all analytical sessions for each RM. The following long-term excess variance of each RM was determined by calculating a weighted mean from the repeated analyses of the RMs among all measurement sessions using Isoplot (v. 4.14, Ludwig 2012) displayed as 'External 2s err req'd (each point)' term for $^{87}Rb/^{86}Sr$ and $^{87}Sr/^{86}Sr$, respectively: 0.46% and 0.49% for NIST 610 (n = 68), 1.2% and 0.0% for NIST 612 (n = 46), 4.2% and 0.36% for BCR-2G (n = 68), 5.5% and 0.0% for BHVO-2G (n = 46), 2.0% and 0.0% for ATHO-G (n = 32), 4.6% and 0.0% for KL2-G (n = 32), 4.5% and 0.0% for T1-G (n = 32), 5.5% and 0.74% for Mica-Mg-P (P1 and P2, n = 68), 3.5% and 0.0% for GL-O-P (n = 68), 6.0% and 0.76% for FK-N-P (n = 68), and 4.3% and 5.5% for Mica-Fe-P (n = 30).

For the measured $^{87}Rb/^{86}Sr_N$ ratios corrected using a correction factor (CF), indicated as 'corr $^{87}Rb/^{86}Sr_N$', in **section 5.1**, the uncertainties of U_3 and ε_2 were included with the addition of MSWD from the linear regressions (U_4). The details of calculations for the CF and the MSWD from the linear regressions (U_4) are described in **section 5.1**.

3.2. Laser pit measurement

The ablation pits of the glass and mineral RMs were measured in using an optical profilometer based on coherence correlation interferometry (Zygo Zescope™ optical profilometer) and analyzed using ZYGO's Mx™ software at CRPG, Nancy, France. The images and measurements were acquired with the use of a 50 × objective lens. The volume values were determined over the entire 3D surface using the following data processing protocol of ZYGO's Mx™ software: (1) a circular mask to the target sample and remove the unwanted

background by selecting the ablation area and as test region and non-ablated area as the reference region and (2) all voids are data filled to account for any dropped pixels during image collection. Three different ablation pits per sample (except for NIST 610, n = 2) were acquired for the pit measurements and the average, and standard deviation (SD) for each RM were calculated (**Fig. 13**). The laser pits of each spot were ablated in the same laser ablation conditions with the same laser spot size of 50 μm, repetition rate of 5 Hz, and laser energy density of ca. 6 J cm^{-2}.

3.3. EPMA

Major element compositions of the samples LP and Apd-Phl in the form of grains were determined by EPMA with a CAMECA SX100 at the Service Commun de Microscopie Electronique et de Microanalyses (SCMEM) of the GeoRessources laboratory (Vandoeuvre-lès-Nancy, France). The data were calibrated using natural and synthetic oxides (Albi, wollastonite, Al_2O_3, forsterite, apatite, arthose, $MnTiO_3$, Andradite, Topaz, Vanadinite). Analyses were performed using a beam current of 12 nA, an accelerating of voltage of 15 kV and a counting time of 10 s per element.

4. Results

4.1. Chemical compositions of the RMs and samples

Table 7 lists the Rb-Sr and major element compositions of the RMs and samples used in this study. It contains published data for the glass and powder RMs, and measured data for other grain RMs and samples obtained by the EPMA. The chemical compositions in **Table 7** are plotted in **Fig. 9** to display the compositional variations and differences between the RMs and samples.

The major element compositions of **NIST 610** and **612** are nearly identical with similar Rb/Sr ratios, but with Rb and Sr concentrations ca. 10 times higher for NIST 610. Their major element contents (e.g. ca. 2 wt.% of Al_2O_3, ca. 11 wt.% of CaO, ca. 13 wt.% of N_2O, ca. 0.0 wt.% of K_2O) are different from those of the mineral RMs and grain samples, except for SiO_2 contents (69.7 ± 0.5 wt.% for NIST 610 and 72.1 ± 0.6 wt.% for NIST 612) similar with those

of FK-N-G (65.0 ± 0.7 wt.% SiO_2) and FK-N-P (67.6 ± 4.2 wt.% SiO_2). FeO and MgO contents of NIST 610 and 612 (<0.1 wt.%) are similar to those of FK-N-G and FK-N-P (<0.1 wt.%), which are lower than those of mica RMs and mica samples in this study. Rb/Sr ratios of NIST 610 and 612 (<1) are much lower than those in the mineral RMs between 12.4 and 369 (**Table 7** and **Fig. 9**).

Three basalt RMs (**BCR-2G, BHVO-2G** and **KL2-G**) have similar major element contents of SiO_2 (49-50 wt.%), Al_2O_3 (13.3-13.6 wt.%), FeO (11-12 wt.%), Na_2O (2.4-3.2 wt.%) and K_2O (0.5-1.7 wt.%) and variable MgO and CaO contents which are lower by ca. 50% and ca. 35% in BCR-2G, respectively. Their SiO_2 contents are similar to those in bulk GL-O (50.9 ± 0.7 wt.%) and GL-O-G (53.5 ± 1.6 wt.%) other than other major element contents of the basalt RMs are different from those of GL-O RMs. **Rhyolite ATHO-2G** and **diorite T1-G**, which have more fractionated compositions than basalt RMs, higher SiO_2 and lower MgO and FeO contents than those in studied basalt RMs (**Table 7** and **Fig. 9**). The Rb/Sr ratios of the geological glass RMs range from 0.02 to 0.69 and much lower than those in the mineral RMs (12-369, **Table 7** and **Fig. 9**).

Major element contents of the glass RMs cover only a partial range of those in the mineral RMs and samples, with SiO_2 content (49-75 wt.%) higher than those of biotite and phlogopite, (34-39 wt.%). Al_2O_3 contents (2-17 wt.%) lower than those of Mica-Fe, FK-N and Apd-Phl (19-24 wt.%), K_2O contents of the glass RMs (0.01-2.6 wt.%) lower than those in the mineral RMs and samples (7.9-12.8 wt.%). FeO contents of the glass RMs (0.02-6.4 wt.%) cover those in GL-O, FK-N, Apd-Phl, and lower than phlogopite and biotite RMs and samples. MgO contents of FK-N, GL-O and Mica-Fe are in the range of those the glass RMs (0.01-7.3 wt.%), and lower compared to those in Mica-Mg and phlogopite and biotite samples of LP, MD and Apd-Phl.

It has been investigated that most elements including Sr and Rb in NIST 610 and 612 are homogeneous for microanalysis (Eggins & Shelley, 2002). BCR-2G and BHVO-2G show variations (RSD) for major elements of less than 1-2% (Jochum et al., 2005) and for Rb/Sr ratios of 0.22% for BCR-2G and 0.12% for BHVO-2G (Elburg et al., 2005). The homogeneity of MPI-DING glasses for major element was evaluated with RSD of 0.3-2%, and their trace elements including Sr and Rb show RSD variations of 0.1-4.0% within analytical errors

(Jochum et al., 2000).

In contrast with the glass RMs, the mineral RMs (**Mica-Mg, Mica-Fe, GL-O** and **FK-N**) were characterized by larger uncertainties and heterogeneity in the study of Jegal et al. (2022). This variability was found for both some of major element compositions of the RM grains such as FeO and MgO for Mica-Mg-G and SiO_2, Na_2O and K_2O for FK-N-G with the variations (2 RSD) of 5.1-14.2% in Rb/Sr ratios (Jegal et al. 2022). SiO_2, Al_2O_3, MgO and FeO contents of the bulk Mica-Mg, Mica-Fe and GL-O from Govindaraju (1995) are generally comparable to those in the mean contents for their grain RMs (**Table 7**). The differences of the mean major element compositions between bulk and grain GL-O RMs and FK-N RMs were derived from its variable contents within the grains by inclusion and heterogeneity of the RMs, investigated by Jegal et al. (2022). The range of major element compositions of the mineral RMs fell within the range of values for the studied mineral samples in this study except for higher Al_2O_3 in Apd-Phl (**Table 7** and **Fig. 9**).

4.2. Precision of LA-ICP-MS/MS analyses

Measured $^{87}Rb/^{86}Sr$ and $^{87}Sr/^{86}Sr$ ratios of NIST 610, BCR-2G and Mica-Mg-P during the course of this work are shown in **Table 10** to assess the precision of the LA-ICP-MS/MS measurements. The precision (2 RSD%) is obtained on the mean ratios of spot analysis calibrated using Mica-Mg-P as 2 RSD% (100 × (2 SD of R_m)/R_m) from the mean ratios, where R_m is the measured Rb-Sr isotopic ratios. Note that the Rb-Sr ratios of Mica-Mg-P in each session in **Table 10** were calibrated using different pellets of Mica-Mg-P used in the same analytical session to avoid self-normalization (e.g., Mica-Mg-P2 calibrated using P1 in Session 1). Accuracy was determined as the difference between the measured ratios (R_m) and the published values (R_p), expressed in % as $(R_m - R_p)/R_p \times 100$.

Six to sixteen single spot measurements were obtained for NIST 610, BCR-2G and Mica-Mg-P depending on the length of the sessions. The precision (2 RSD%) of $^{87}Sr/^{86}Sr$ for NIST 610, BCR-2G and Mica-Mg-P ranges from 0.59 to 0.93, 0.61 to 1.1 and 0.80 to 1.3, respectively, as good as those reported in previous studies (Bolea-Fernandez et al., 2016; Gorojovsky & Alard, 2020; Hogmalm et al., 2017; Redaa et al., 2021; Rösel & Zack, 2022; Zack & Hogmalm, 2016). The better precision of $^{87}Rb/^{86}Sr$ was observed for NIST 610 (0.49-1.2%) than that for

BCR-2G (2.3-4.4%) and Mica-Mg (2.1-5.0%). The lower precision of $^{87}Rb/^{86}Sr$ observed for BCR-2G and Mica-Mg-P was derived from the variability of raw $^{87}Rb/^{86}Sr$ ratios by decreasing and increasing trend over the course of an individual analytical session for BCR-2G and Mica-Mg-P, respectively (**Fig. 11a**). 2 RSD% of raw $^{87}Rb/^{86}Sr$ ratios for basalt glasses BCR-2G and BHVO-2G are more than 10 times higher than the published uncertainties of bulk BCR-2G and BHVO-2G due to larger fractionation over the analytical courses relative to those of NIST glasses (**Fig. 11**). For Mica-Mg-P and other powder mineral RMs, the uncertainties of $^{87}Rb/^{86}Sr$ ratios by ID-TIMS and MC-ICP-MS were higher than the point analyses by LA-ICP-MS/MS (**Fig. 11b, 11c** and **11d**) due to their potential heterogeneity reported by Jegal et al. (2022).

The mean $^{87}Sr/^{86}Sr$ ratios of NIST 610, BCR-2G and Mica-Mg-P agree well with the published data falling within the range of accuracy (%) from -1.1 to 0.72, whereas $^{87}Rb/^{86}Sr$ ratios showed less accurate results with the accuracy from -15% to -10% for NIST 610, from -8.1% to -2.4% for BCR-2G and from 1.8% to 3.3% for Mica-Mg-P. We first address that these results are calibrated in using Mica-Mg-P, which has different matrix and physical properties relative to those of BCR-2G and NIST 610. These discrepancies between glass RMs and Mica-Mg-P have been also observed by previous studies (Gorojovsky & Alard, 2020; Redaa et al., 2021; Rösel & Zack, 2022). $^{87}Rb/^{86}Sr$ obtained for Mica-Mg-P calibrated using other Mica-Mg powder tablets overlap within the uncertainty of the reported value of 155.6 ± 4.7% (2 RSD) for bulk Mica-Mg RM by Jegal et al. (2022). In addition, all Mica-Mg-P used in this study were produced from different powder aliquots of Mica-Mg RM, which could be heterogeneous as indicated by Jegal et al. (2022).

Table 10. Precision and accuracy of LA-ICP-MS/MS analyses of NIST 610, BCR-2G and Mica-Mg calibrated using Mica-Mg-P.

Reference material	NIST SRM 610					BCR-2G					Mica-Mg				
Session	S1	S2	S3	S4	S5	S1	S2	S3	S4	S5	S1	S2	S3	S4	S5
n	16	14	6	16	16	16	14	6	16	16	12	11	6	16	16
measured $^{87}Rb/^{86}Sr$	2.109	2.092	2.041	2.054	1.990	0.3712	0.3807	0.3637	0.3735	0.3586	158.4	160.2	158.5	160.7	160.6
Precision (2 RSD%)	1.1	1.0	0.49	0.89	1.2	3.8	3.8	2.3	3.6	4.4	2.8	5.0	2.1	3.0	3.3
Accuracy (Difference %)	-10	-10	-12	-12	-15	-4.8	-2.4	-6.8	-4.3	-8.1	1.8	2.9	1.8	3.3	3.2
measured $^{87}Sr/^{86}Sr$	0.7143	0.7111	0.7113	0.7098	0.7096	0.7101	0.7064	0.7053	0.7041	0.7066	1.873	1.855	1.843	1.846	1.842
Precision (2 RSD%)	0.80	0.70	0.59	0.77	0.93	0.61	0.75	1.1	1.1	0.85	1.2	1.3	0.97	0.80	1.0
Accuracy (Difference %)	0.70	0.24	0.26	0.06	0.03	0.72	0.20	0.04	-0.13	0.23	0.58	-0.41	-1.05	-0.85	-1.10
Primary standard of Mica-Mg-P	P1	P2	P2	P2	P2	P1	P2	P2	P2	P2	P1	P2	P2	P2	P2
Sample	NIST SRM 610					BCR-2G					P2	P1	P3	P3	P3

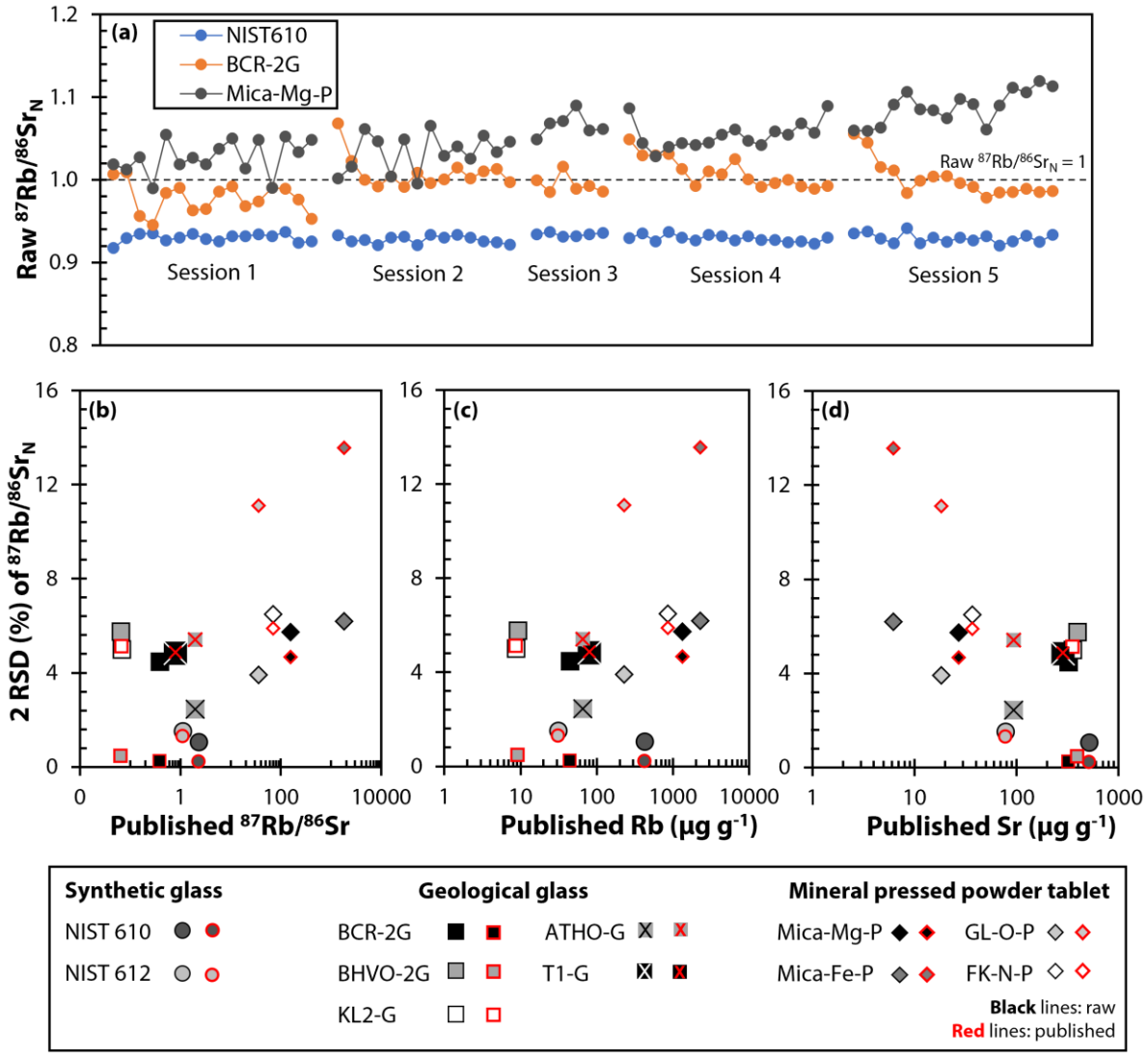

Fig. 11. (a) Raw $^{87}Rb/^{86}Sr_N$ (raw/published) ratios of individual point analyses in each session for NIST 610, BCR-2G and Mica-Mg-P1 and P2. Dotted line indicates raw $^{87}Rb/^{86}Sr_N$ ratios to be 1. **(b, c, d)** 2 RSD% of raw $^{87}Rb/^{86}Sr_N$ (raw/published) mean ratios and published $^{87}Rb/^{86}Sr$ ratios of the RMs as a function of published Rb-Sr compositions, indicated by black and red solid lines, respectively. Raw $^{87}Rb/^{86}Sr_N$ mean ratios of the RMs were averaged from all analytical sessions. Published data are presented in **Table 7**.

4.3. Fractionation of Rb-Sr isotopic ratios during LA-ICP-MS/MS analyses

The down-hole fractionation patterns of raw $^{87}Rb/^{86}Sr_N$ and $^{87}Sr/^{86}Sr_N$ ratios for the glass and mineral RMs are shown in **Fig. 12a** and **12b**. The spot analyses were obtained over a period of ca. 50 s ablation for 16 spot analyses in each material from the analytical session 5. Then, the raw data were averaged and normalized to published values for each RM (raw/published ratios, N).

The results shown in **Fig. 12a** and **12b** indicate that the fractionation for $^{87}Rb/^{86}Sr_N$ varies with time during ablation and by sample types, whereas the fractionation effect on $^{87}Sr/^{86}Sr_N$ of the RMs was not detectable. This higher variability in $^{87}Rb/^{86}Sr_N$ ratios compared to that in $^{87}Sr/^{86}Sr_N$ indicates that elemental fractionation occurs between Rb and Sr during the LA-ICP-MS/MS analysis. BCR-2G, BHVO-2G, KL-2G and T1-G display a progressive increase of $^{87}Rb/^{86}Sr$ ratios whereas ATHO-G displays a decrease during the ablation. Compared to the geological RMs, the pattern for both NIST 610 and 612 was relatively stable.

The evolutions of $^{87}Rb/^{86}Sr_N$ for mineral powder RMs vary between the RMs (**Fig. 12a**). GL-O-P displays gradually increasing trend during the first ca. 20 s then stabilized after 30 s. Mica-Mg-P has a more complex pattern, where the ratios decrease over the first ca. 10 s and flatten over the next ca. 20 s, then decreased and flatten again during the last ca. 10 s. For FK-N-P, the ratios right after the ablation starts are highly biased from the published value, decreased gradually during an interval from 5 s to 30 s, then stabilized over the last ca. 20 s. These variability of the patterns in Rb/Sr ratios between the different RMs has been documented by Redaa et al. (2021). Note that the profiles of $^{87}Rb/^{86}Sr_N$ and $^{87}Sr/^{86}Sr_N$ for Mica-Fe are not evaluated here due to the high uncertainty on its ratios of 14% and 13% (2RSD), respectively (Jegal et al., 2022).

The down-hole fractionation patterns impact on the single-spot precision for the $^{87}Rb/^{86}Sr$ ratios depending on the selected integration time of ca. 25 s, 35 s and 45s from the end of the ablation as shown in **Fig. 12c**. The uncertainties of the raw $^{87}Rb/^{86}Sr$ ratios in each ablation interval, averaged and normalized to published values of the RMs in each ablation interval were calculated as two relative standard error (2 RSE%). The 2 RSE% values were ca. 1.5 and 1.3 times higher for FK-N-P using ca. 35 s and 45s of integration time, respectively, compared to the interval of ca. 25 s. In contrast, the 2 SE of other RMs were lower than 0.12 % using the

ca. 25s, 35s and 45s of integration time. The calculated 2 RSE% for NIST RMs and mineral RMs and ATHO-G decreased whereas those for basalt glass RMs increased by using the longer integration time. Based on the 2 RSE and down-hole fraction effects between the different RMs, integration period of ca. 25s before ablation ends was used for all the analyses of the RMs and samples in this study.

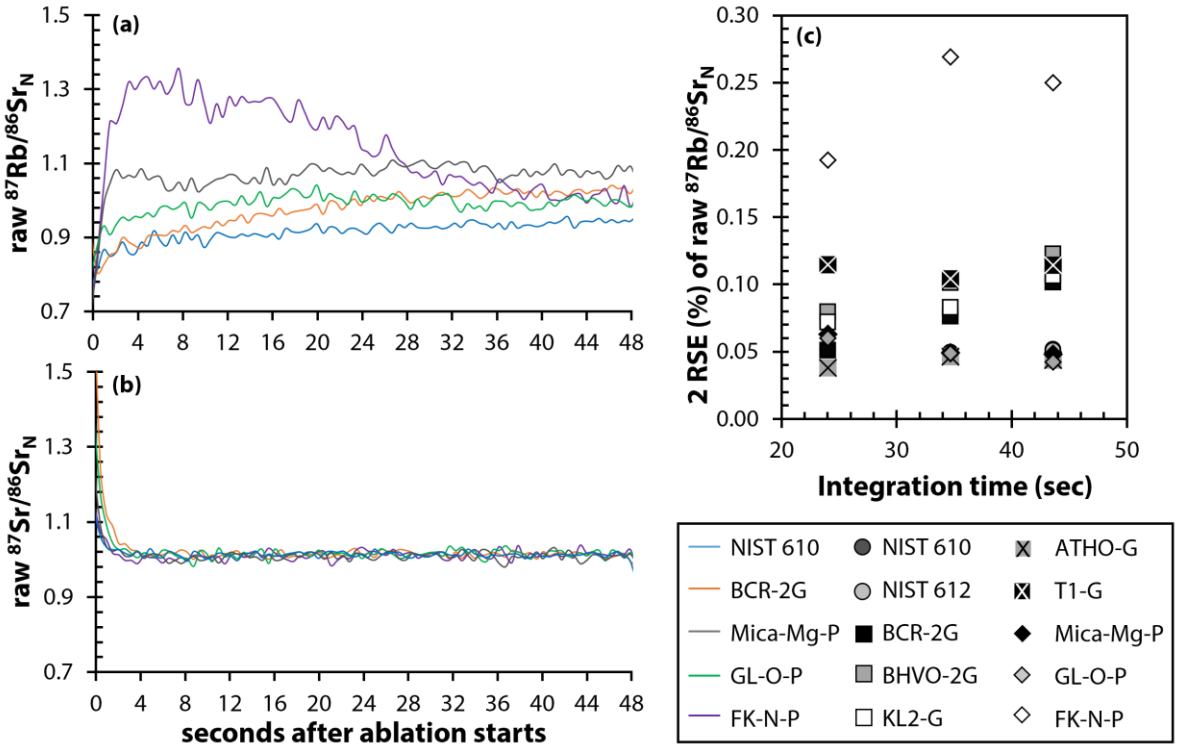

Fig. 12. (a) Raw $^{87}Rb/^{86}Sr_N$ and **(b)** $^{87}Sr/^{86}Sr_N$ (raw/published) fractionation for NIST 610, BCR-2G, Mica-Mg-P, GL-O-P and FK-N-P by averaging 16 individual spot analyses from a single session (session 5). **(c)** 2 RSE% of raw $^{87}Rb/^{86}Sr_N$ mean ratios averaged in the integration times of ca. 25 s, 35 s and 45 s for the studied RMs.

4.4. Pit morphology and volume

The pit morphology and volumes of laser pits for the RMs under the same laser ablation conditions (50 μm, ca. 6 J cm^{-1}, 5 Hz) were imaged and measured to examine their effects on $^{87}Rb/^{86}Sr$ ratio offsets and $^{87}Sr/^{86}Sr$ ratios in the studied RMs calibrated using NIST 610 (**Fig. 13**). The measured $^{87}Rb/^{86}Sr$ and $^{87}Sr/^{86}Sr$ of the RMs calibrated using NIST 610 are normalized to their published ratios (measured/published ratios) in **Fig. 13a**.

As shown in **Fig. 13b**, the glass RMs exhibit smooth and convex base with constant and reproducible volumes from spot to spot with the variation (SD%) from 0.24% in NIST 610 to 1.0% in BCR-2G. The ablation pits in the Mica-Mg-P show an elevated rim and a very uneven and irregular base. The similar morphology with Mica-Mg-P was shown in Mica-Fe-P. The LA pits in La Posta (LP) biotite and Apd-Phl display similar morphology of high rims to the two mica RMs. The pits of GL-O-P and FK-N-P display more even base and flat rims, which are different relative to Mica-Mg-P and Mica-Fe-P. The mean volumes (μm^3) of the mineral RMs in the form of pressed powder tablet ranged from ca. 53757 for Mica-Mg-P to ca. 70406 for GL-O-P with larger variations (RSD%, n = 3) from spot to spots (5.0%-11%) compared to those of the glass RMs (≤1%). There is no obvious correlation between the measured $^{87}Rb/^{86}Sr$ ratio offsets and the volume of pits as shown in **Fig. 13a**. It seems that the physical properties of ablated materials are unlikely produce the $^{87}Rb/^{86}Sr$ and $^{87}Sr/^{86}Sr$ ratio offsets when using non-matrix matched RM such as NIST 610.

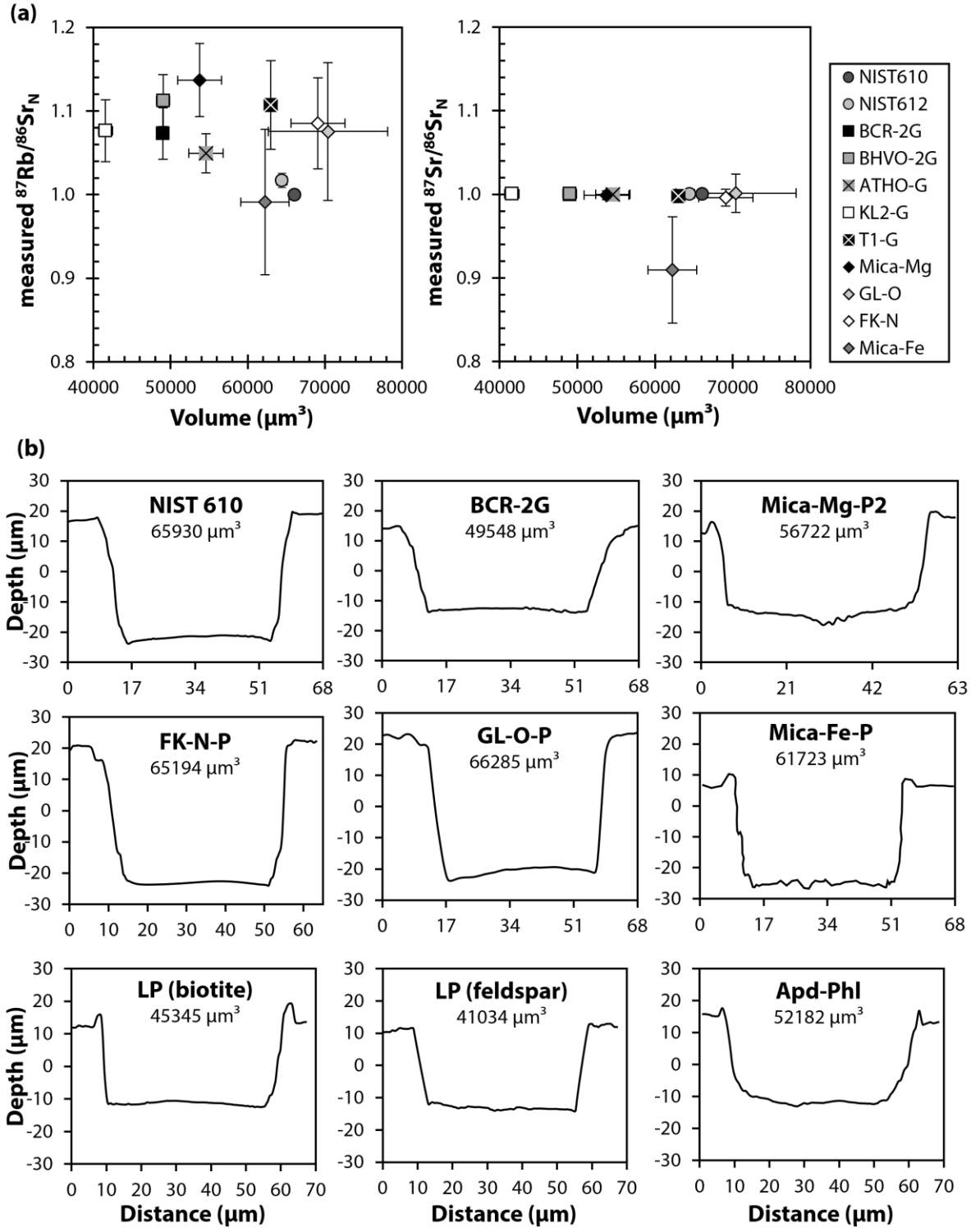

Fig. 13. (a) Measured $^{87}Rb/^{86}Sr_N$ and $^{87}Sr/^{86}Sr_N$ (measured/published) calibrated using NIST 610 vs mean volumes (µm³) of ablation pits from three different ablation for the RMs under the same laser conditions. Error bars of $^{87}Rb/^{86}Sr_N$ and volumes are 2 SD and 1 SD, respectively. The bars not displayed are smaller than the symbols. **(b)** 2D morphologies of ablation pits of glass and mineral RMs and biotite and feldspar samples under the same laser fluence and

frequency. Volumes displayed in **(b)** were measured on the individual ablation pits for each RM.

4.5. Comparison of bulk and in-situ Rb-Sr isotopic ratios

Mean and individual analysis values of Rb-Sr isotope ratio measurements by LA-ICP-MS/MS are plotted for NIST 610, BCR-2G, Mica-Mg-P (P2, P3, P4), GL-O-P and FK-NP together with their reported bulk compositions in **Fig. 14**. In order to assess the uncertainties from LA-ICP-MS/MS measurements and published values by bulk analyses, the results for each individual analysis from the same analytical session in the same analytical conditions (Session 1), and Mica-Mg-P1 was used as an external calibrant. The individual analysis of each RM was averaged, and error bars of the mean values indicate 2 SD of the mean ratios.

There is general agreement between measured $^{87}Sr/^{86}Sr$ ratios of the RMs by LA-ICP-MS/MS and the reported bulk values with the accuracy of 0.70% (NIST 610)-0.96% (GL-O-P). The scatter in the published bulk $^{87}Sr/^{86}Sr$ ratios for the RMs are less than those measured by LA-ICP-MS/MS analysis. The scatter in the published bulk values of the $^{87}Rb/^{86}Sr$ is much less than that by LA-ICP-MS/MS for NIST 610 and BCR-2G. Strong heterogeneity in $^{87}Rb/^{86}Sr$ ratios in the mineral powder RMs of bulk Mica-Mg, FK-N and GL-O is observed by the isotope dilution analyses (Jegal et al., 2022) relative to the in-situ $^{87}Rb/^{86}Sr$ ratios by LA-ICP-MS/MS (**Fig. 14b-14e**). In addition, Mica-Mg-P produced using different powder aliquots of Mica-Mg RM as P2, P3 and P4 show the discrepancies between the in-situ RMs for both measured $^{87}Sr/^{86}Sr$ and $^{87}Rb/^{86}Sr$ ratios, yielding the accuracy of 0.29-0.78% and 1.7-3.0%, respectively. The measured $^{87}Rb/^{86}Sr$ ratios of Mica-Mg-P2, P3 and P4 were within the uncertainty of the published bulk Mica-Mg value. The accuracy of the measured $^{87}Rb/^{86}Sr$ ratios of other glass RMs and mineral RMs calibrated using Mica-Mg-P1 range from 1.5% (GL-O-P) to 9.5% (NIST 610). The results of this comparison between bulk and in-situ Rb-Sr values suggest that the precision and accuracy of Rb-Sr isotopic data can be affected by non-matrix matched calibration for mass discrimination and the variability of the individual LA-ICP-MS/MS analyses derived from intrinsic heterogeneity in the mineral RMs.

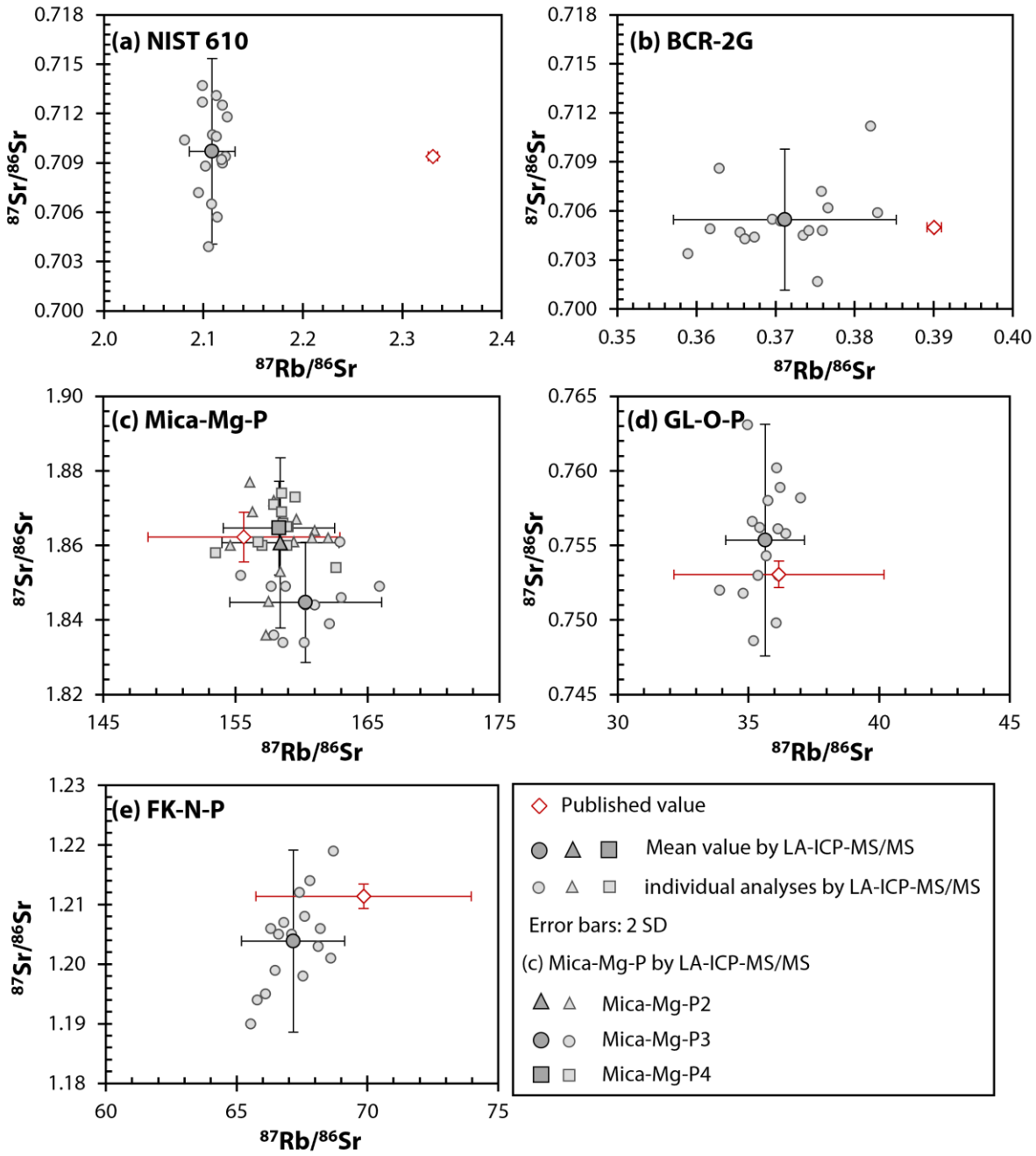

Fig. 14. (a) Measured $^{87}Rb/^{86}Sr$ and $^{87}Sr/^{86}Sr$ mean and individual values calibrated using Mica-Mg-P1 for (a) NIST 610, (b) BCR-2G, (c) Mica-Mg-P2, P3, P4, (d) GL-O-P and (e) FK-N-P from the same analytical session (session 1). Published Rb-Sr data and references are reported in **Table 7**.

4.6. Effects of chemical compositions on measured Rb-Sr isotopic ratios of RMs

The RMs studied here display a wide range of Rb-Sr and major element compositions (**Fig. 9**) with different types of matrices as synthetic silicate glasses (NIST 610 and 612), geological glasses (BCR-2G, BHVO-2G, KL2-G, ATHO-G and T1-G) and mineral powder pressed tablets (Mica-Mg-P, Mica-Fe-P, GL-O-P and FK-N-P). These variabilities could affect the ablation characteristics and produce matrix effects by their different hardness, density and/or interaction behavior between laser and samples. Numerous papers have highlighted ablation difference between various matrices leading to elemental and isotopic fractionation (Jackson & Günther, 2003; Sylvester, 2008; Zhang et al., 2016). NIST 610 and 612 have a very different matrix composition from the mineral RMs and natural samples with different ablation properties as explained in **section 4.1, 4.3** and **4.4**. Significant matrix effects between NIST 610, geological glass RMs, Mica-Mg and natural geological samples on $^{87}Rb/^{86}Sr$ ratios and Rb-Sr ages have been investigated by previous LA-ICP-MS/MS studies (Gorojovsky & Alard, 2020; Redaa et al., 2021). These matrix effects were observed in this study with the accuracy of 10-15% for $^{87}Rb/^{86}Sr$ ratios of NIST 610 calibrated using Mica-Mg-P (**Table 10**). The results also show that the accuracy of the $^{87}Sr/^{86}Sr$ ratios (0.04-1.1%) calibrated between non-matrix matched RMs were overall much better than that for $^{87}Rb/^{87}Sr$ (**Table 10**). In addition, **Fig. 13** shows that the volumes and different morphology of the ablation pits for the RMs does not have clear correlation with the measured $^{87}Rb/^{86}Sr$ ratios of the RMs calibrated using NIST 610.

In order to assess the effect of non-matrix-matched external calibration on the accuracy of $^{87}Sr/^{86}Sr$ and $^{87}Rb/^{86}Sr$ for the RMs, NIST 610 was used as an external calibrant (**Fig. 15** and **Fig. 16**) because NIST 610 has most homogeneous Rb-Sr compositions (Eggins & Shelley, 2002; Jochum & Stoll, 2008; Woodhead & Hergt, 2001) and very different chemical and physical matrix from the other mineral samples and RMs (**Fig. 9** and **Fig. 13**). Furthermore, NIST 610 is one of the most widely used RM for calibration purposes by LA-ICP-MS (/MS) analyses (Jochum & Stoll, 2008). The measured $^{87}Sr/^{86}Sr_N$ and $^{87}Rb/^{86}Sr_N$ ratios calibrated using NIST 610 in each session were averaged from all analytical sessions, then divided by the published Rb-Sr isotopic ratios for each RM, reported in **Table 7**. The measured $^{87}Sr/^{86}Sr_N$ and $^{87}Rb/^{86}Sr_N$ ratios are plotted as a function of Rb-Sr and major element compositions of the RMs in **Fig. 15** and **Fig. 16**, respectively. The error bars in **Fig. 15** and **Fig. 16** are the total uncertainties including 2 SD of the $^{87}Sr/^{86}Sr_N$ and $^{87}Rb/^{86}Sr_N$ mean ratios and long-term excess

variance (ε_2) as described in **Fig. 10**.

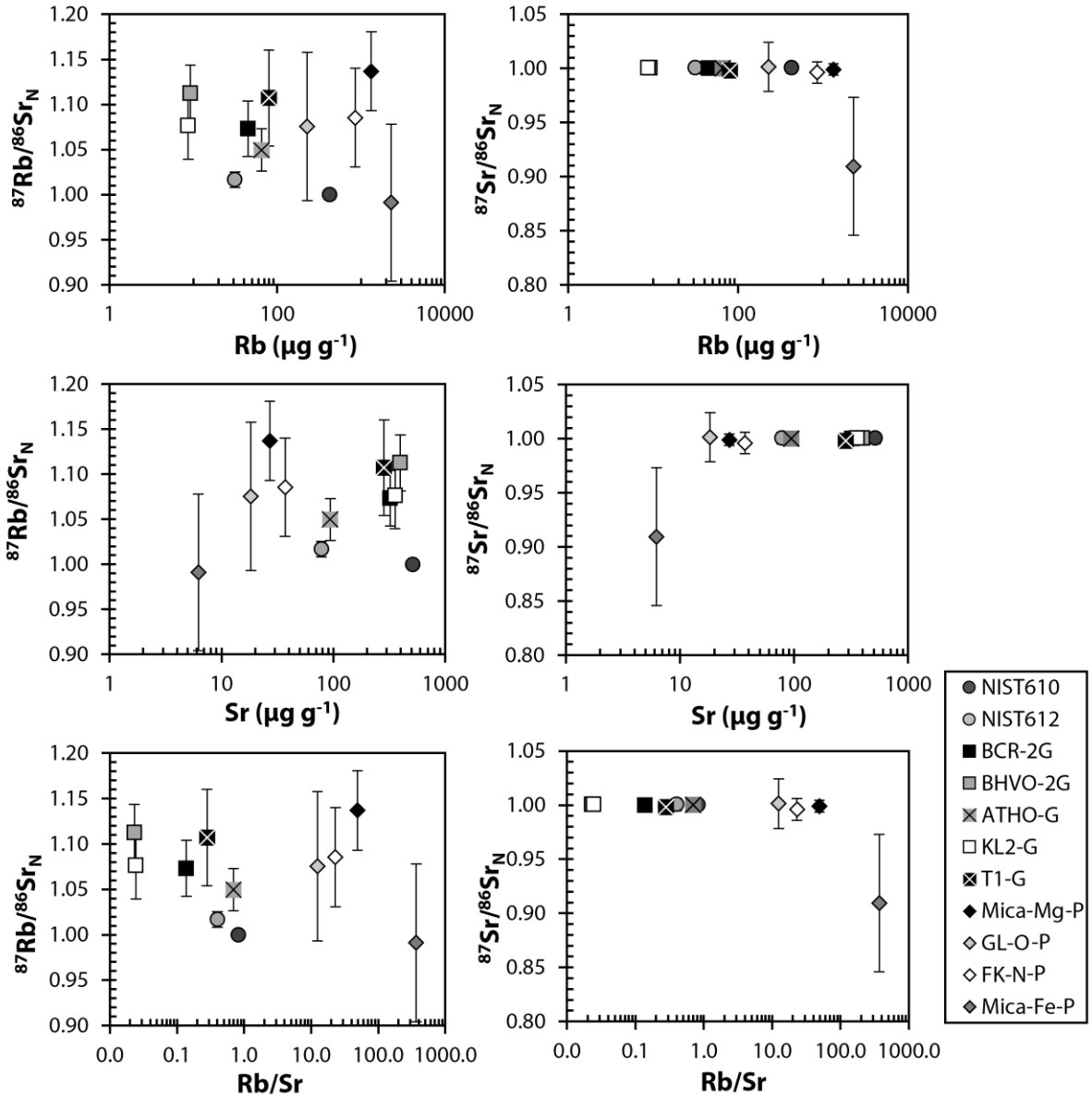

Fig. 15. Measured $^{87}Rb/^{86}Sr_N$ and $^{87}Sr/^{86}Sr_N$ (measured/published) ratios calibrated using NIST 610 for the RMs as a function of Rb-Sr compositions of the RMs. The ratios are mean values of measured $^{87}Rb/^{86}Sr_N$ and $^{87}Sr/^{86}Sr_N$ from all analytical sessions. Bars associated with the mean values correspond to the total uncertainties including U_3 and ε_2, described in **Fig. 10** and **section 3.1.3**.

Furthermore, to account for the effect of chemical compositions on the measured $^{87}Sr/^{86}Sr_N$ and $^{87}Rb/^{86}Sr_N$ ratios of the RMs (except for Mica-Fe-P due to its reported high uncertainties), linear regressions through the data with the total uncertainties on the plots were computed by

using Maximum likelihood regression model in IsoplotR (v. 5.0, Vermeesch 2018). The linear regression lines are displayed on **Fig. 16**, and the slopes and their uncertainties are given in **Table 11**. Mica-Fe-P is not included in the linear regressions due to its large compositional heterogeneity and the high uncertainties for its $^{87}Sr/^{86}Sr$ and $^{87}Rb/^{86}Sr$, respectively (Jegal et al., 2022).

The results show that the measured $^{87}Sr/^{86}Sr_N$ of the studied RMs (NIST, USGS, MPI-DING and CRPG RMs) are close to 1 with the range from 0.996 for FK-N-P to 1.001 for GL-O-P, except for Mica-Fe-P with the $^{87}Sr/^{86}Sr_N$ of 0.91. There is no obvious correlation between the $^{87}Sr/^{86}Sr_N$ ratios and chemical compositions of the RMs, including Rb-Sr and major element compositions (**Fig. 15** and **Fig. 16**), yielding the slope close to 0 (**Table 11**).

In contrast, discrepancies relative to the published values were observed for the measured $^{87}Rb/^{86}Sr$ ratios as $^{87}Rb/^{86}Sr_N$ ratios range from 1.14 for Mica-Mg-P to 1.02 for NIST 612 (**Fig. 15** and **Fig. 16**). The measured Rb-Sr ratios of NIST 610 were self-normalized by using NIST 610, so the $^{87}Rb/^{86}Sr_N$ and $^{87}Sr/^{86}Sr_N$ ratios of NIST 610 are 1.00. The much more discrepancies for the $^{87}Rb/^{86}Sr$ relative to the published values than for the $^{87}Sr/^{86}Sr$, calibrated using matrix-mismatched RMs such as NIST 610, have been reported by previous LA-ICP-MS/MS studies, with various degree of the accuracy by varying analytical conditions and types of the RMs (Gorojovsky & Alard, 2020; Redaa et al., 2021). While Rb-Sr compositions are variable between the RMs, we did not observe a correlation with the measured $^{87}Rb/^{86}Sr_N$ of the studied RMs (**Fig. 15**) with the slopes close to 0 with large uncertainties (2 RSE%) of 130-247% (**Table 11**). On the other hand, the major element contents of the RMs show weak to relatively strong correlations with the $^{87}Rb/^{86}Sr_N$ ratios of the studied RMs, yielding the slopes ranging from -0.007 to 0.012 (**Table 11** and **Fig. 8**). The results of $^{87}Rb/^{86}Sr_N$ for the RMs show linear anti-correlations with SiO_2, Na_2O_3 and CaO contents and linear correlations with Al_2O_3, FeO, MgO and K_2O contents, suggesting potential matrix effects related to the major element compositions of the RMs on the calibration of $^{87}Rb/^{86}Sr$ ratios measured by LA-ICP-MS/MS.

►

Fig. 16. Measured $^{87}Rb/^{86}Sr_N$ (measured/published) ratios calibrated using NIST 610 for the RMs as a function of major element compositions of the RMs. The ratios and their error bars are identical to those in **Fig. 13**. The linear regressions through the data on plots of $^{87}Rb/^{86}Sr_N$ versus major element compositions of the RMs (except for Mica-Fe-P) and their associated

uncertainties are computed using Maximum likelihood regression model in IsoplotR v5.0 (Vermeesch 2018), represented by dotted lines and shade area, respectively.

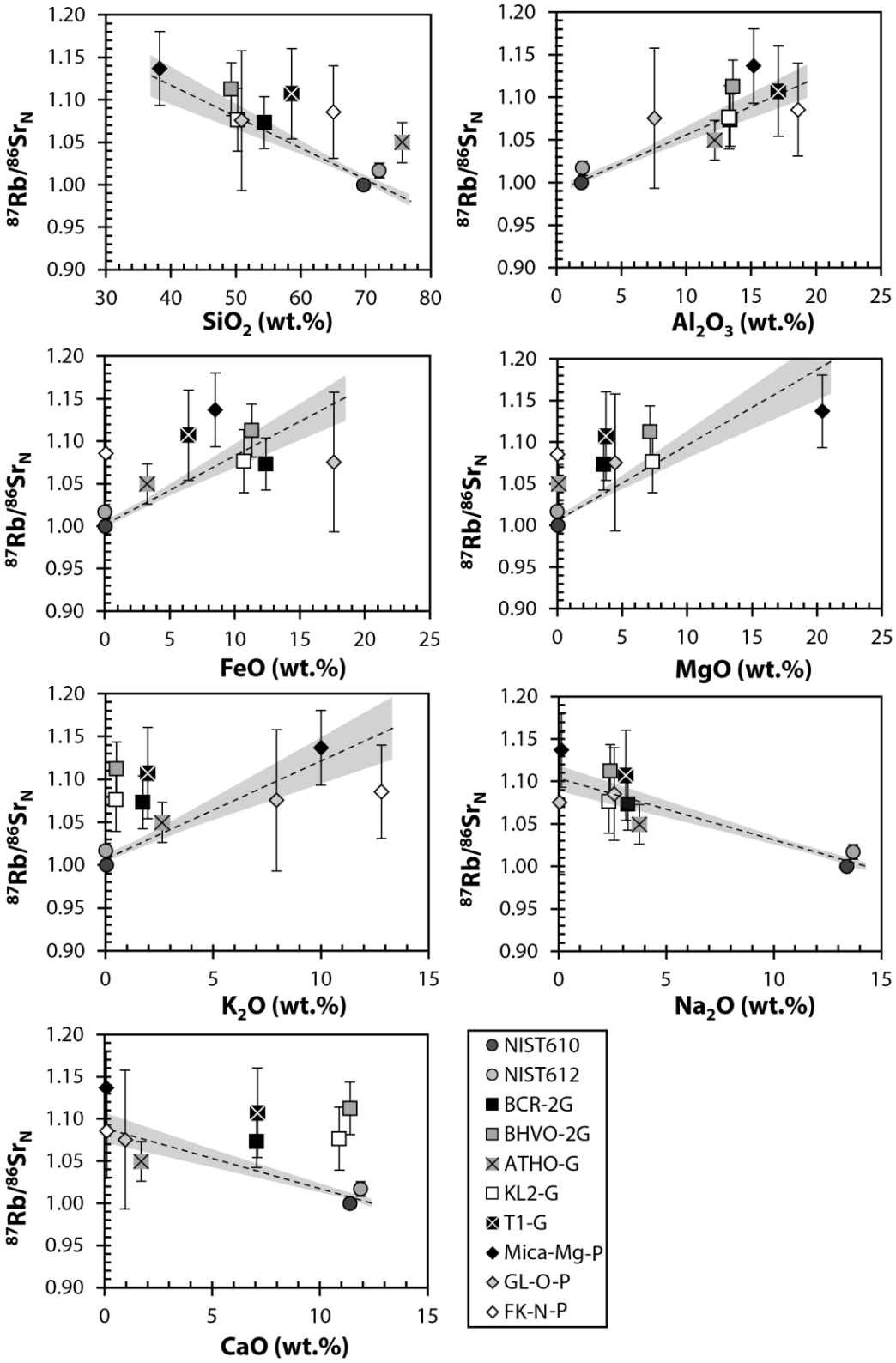

Table 11. Linear regression results of measured $^{87}Rb/^{86}Sr_N$ and $^{87}Sr/^{86}Sr_N$ of the RMs calibrated using NIST610.

	Rb	**Sr**	**Rb/Sr**	**SiO_2**	**Al_2O_3**	**FeO**	**MgO**	**CaO**	**Na_2O**	**K_2O**
$^{87}Rb/^{86}Sr_N$										
Slope	-3.40E-05	-6.70E-05	0.0026	-0.0037	0.0068	0.0081	0.0090	-0.0071	-0.0073	0.0116
2 SE	8.40E-05	8.10E-05	0.0034	0.0023	0.0020	0.0035	0.0050	0.0063	0.0023	0.0097
2 RSE (%)*	247	121	130	63	29	43	56	89	32	84
$^{87}Sr/^{86}Sr$										
Slope	-1.10E-06	0.000002	-2.80E-05	0.000011	-0.000110	0.000030	-2.70E-05	0.000140	0.000076	-2.0E-04
2 SE	4.20E-06	0.000011	0.000114	0.000152	0.000330	0.000382	0.000290	0.000400	0.000372	5.0E-04
2 RSE (%)*	382	450	407	1382	300	1273	1074	286	489	250

*absolute values

5. Discussion

5.1. Matrix effects and correction factor (CF)

The Rb-Sr isotope measurement by LA-ICP-MS/MS requires mass bias corrections for different fractionation factors for Sr and Rb that have different energy distributions and ionization potentials (Jackson, 2008), which affects measured $^{87}Rb/^{86}Sr$ ratios. These corrections have been made for natural geological samples by using RMs with similar matrices or Rb-Sr compositions such as Mica-Mg for mica samples or BCR-2G for feldspars in the previous LA-ICP-MS/MS studies (Gorojovsky & Alard, 2020; Hogmalm et al., 2017; Li et al., 2020; Olierook et al., 2020; Redaa et al., 2021; Rösel & Zack, 2022; Şengün et al., 2019; Zack & Hogmalm, 2016).

In this study, we observed much higher variability and offsets in the measured $^{87}Rb/^{86}Sr$ ratios of the studied RMs with various types of matrices depending on the external calibrants, compared to their measured $^{87}Sr/^{86}Sr$ ratios (**section 4.2-4.6**). The measured $^{87}Rb/^{86}Sr_{N610}$ and $^{87}Sr/^{86}Sr_{N610}$ ratios calibrated using NIST 610 for different types of the RMs were compared relative to their published Rb-Sr isotopic values in **Table 7** by indicating as $^{87}Rb/^{86}Sr_N$ and $^{87}Sr/^{86}Sr_N$. The results indicate that large differences in the physical and chemical properties between the studied RMs produce larger differences in the measured $^{87}Rb/^{86}Sr_N$ ratios ranging from 1.14 (Mica-Mg-P) to 1.02 (NIST 612). Evaluated by comparing pit morphology and volumes of the ablation pits between the different RMs, there is no correlation between the ablation characteristics and the measured $^{87}Rb/^{86}Sr_N$ ratios of the RMs (**Fig. 12** and **Fig. 13**). Another potential cause of matrix effects in LA-ICP-MS analysis is matrix compositions that requires careful external calibration approaches (Jackson, 2008; Lin et al., 2016). In this study, there is no obvious correlation between the measured $^{87}Rb/^{86}Sr_N$ ratios and Rb-Sr compositions of the RMs (**Fig. 16**), nor does there appear to be any correlation between their uncertainties (2 RSD) of raw $^{87}Rb/^{86}Sr_N$ ratios and Rb-Sr compositions (**Fig. 11b-11d**). On the other hand, the comparison between the measured $^{87}Rb/^{86}Sr_N$ ratios and major element compositions obtained for the RMs defines linear relations with varying degree of correlations with the slopes ranging from -0.007 to 0.012 (**Fig. 16** and **Table 11**). These results suggest that the matrix effects on the measured $^{87}Rb/^{86}Sr_N$ are predominantly linked to the major element compositions. The effects become more significant in case of larger differences in the major element contents

between samples and matrix-mismatched external calibrants (e.g., Mica-Mg vs NIST 610).

To calculate a corrected $^{87}Rb/^{86}Sr$ ratio for the mineral RMs from the biased ratios based on their NIST 610-calibrated values (measured $^{87}Rb/^{86}Sr$), a correction factor (CF) is determined for each mineral by using its major element composition and the slopes and intercepts from the linear regressions. The calculation procedure is described in **Fig. 17**. The uncertainty of the corrected $^{87}Rb/^{86}Sr$ ratios using CF where subscript 'corr $^{87}Rb/^{86}Sr_{N610}$' is calculated by adding in quadrature the uncertainties of 2 SD from measured $^{87}Rb/^{86}Sr$ ratio mean (U_3), long-term excess variance (ε_2) and MSWD from the linear regressions (U_4) as described in **Fig. 10**. For the application of CF on the measured $^{87}Rb/^{86}Sr$ ratios of the mineral RMs, the linear regression results through the plots on their measured $^{87}Rb/^{86}Sr_N$ ratios with SiO_2 and Al_2O_3 (wt.%) in **Fig. 16** are used for the following reasons: (i) the relatively higher slopes with lower uncertainties for SiO_2 and Al_2O_3 compared to other elements (**Table 11**), (ii) the heterogeneous within grains or at intra-grain scales such as 4.4 ± 9.3 wt.% (2 SD) of Na_2O and 10.4 ± 14.6 wt.% (2 SD) of K_2O in FK-N-G and (iii) the low concentrations in some minerals (e.g., Na_2O or CaO ≤0.1 wt.% in mica samples, MgO and FeO <0.1 wt.% in FK-N-G and P) as reported in **Table 7**. The results of measured $^{87}Rb/^{86}Sr_{N610}$ calibrated using NIST 610 and corr $^{87}Rb/^{86}Sr_{N610}$ mean ratios for Mica-Mg-P, GL-O-P and FK-N-P in each analytical session are given in **Table 12**. The CF determined in each mineral RM varies ranging from 0.90 for FK-N-P to 0.96 for GL-O-P and from 0.89 for Mica-Mg-P to 0.97 for FK-N-P, depending on Al_2O_3 and SiO_2 contents in the RMs (**Table 12**).

There are large discrepancies in the measured $^{87}Rb/^{86}Sr_{N610}$ ratios relative to the published ID-TIMS and MC-ICP-MS values for the three RMs. These discrepancies decrease by applying the CF_{Al2O3} and CF_{SiO2} to correct the measured ratios (**Table 12**), where CF_{Al2O3} and CF_{SiO2} are the CF calculated from Al_2O_3 or SiO_2 contents in the samples and their regressions, respectively. The correction for Mica-Mg-P2 overall improve the accuracy from 11-17% of the measured $^{87}Rb/^{86}Sr_{N610}$ ratios to 1.8-7.1% for the corr $^{87}Rb/^{86}Sr_{N610}$ ratios by using CF_{Al2O3} and to 0.02-1.5% by using CF_{SiO2}. This improvement can also be seen for the $^{87}Rb/^{86}Sr$ ratios of GL-O-P from 6.7-8.9% to 2.5-4.5% and 0.03-0.99% for the corr $^{87}Rb/^{86}Sr_{N610}$ ratios corrected using CF_{Al2O3} and CF_{SiO2}, respectively, and for FK-N-P from 5.4-12% to 0.31-5.6% using CF_{Al2O3} and to 2.7-9.1% using CF_{SiO2}. For, the accuracy increases from 5.4 to 5.6% by using the CF_{Al2O3} but improves to 2.7% by using the CF_{SiO2}.

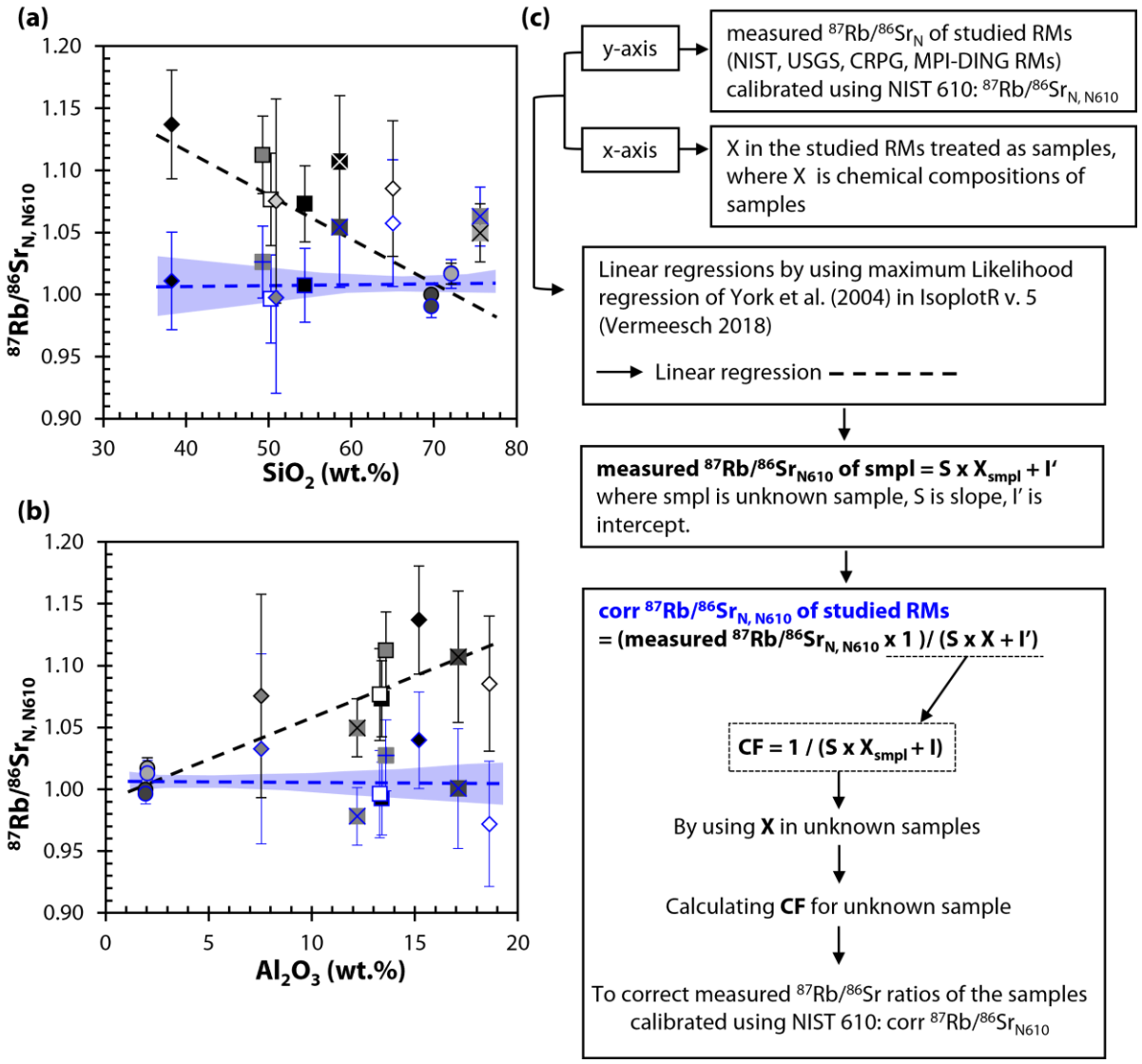

Fig. 17. Measured $^{87}Rb/^{86}Sr_N$ calibrated using NIST 610 and corr $^{87}Rb/^{86}Sr_N$ ratios indicated by the symbols with black and blue solid lines, respectively as a function of **(a)** SiO_2 and **(b)** Al_2O_3 of the RMs. **(c)** Determination of the correction factor (CF) workflow from linear regressions through the data on plots of $^{87}Rb/^{86}Sr_N$ vs major element compositions of the studied RMs. Linear regressions through the data for corrected ratios ($^{87}Rb/^{86}Sr_N$) and their uncertainties are displayed in blue dotted line and blue shade area in **(a)** and **(b)**. The symbols are identical to those in **Fig. 15** and **Fig. 16**.

Table 12. CF_{Al2O3}, CF_{SiO2}, precision (2 RSD%) and accuracy (%) of non-corrected (measured) and corrected $^{87}Rb/^{86}Sr$ mean ratios for the mineral RMs (powder pressed tablet) in each analytical session.

Sample	CF_{Al2O3}	CF_{SiO2}	Session	n		$^{87}Rb/^{86}Sr_{N610}$ Measured	$^{87}Rb/^{86}Sr_{N610,\ Al2O3}$ Corrected	$^{87}Rb/^{86}Sr_{N610,\ SiO2}$ Corrected
Mica-Mg-P2	0.91	0.89	S1	12	Precision%	2.8	2.8	2.8
					Accuracy%	12	2.8	0.02
			S2	14	Precision%	4.3	4.3	4.3
					Accuracy%	11	1.8	-0.99
			S3	6	Precision%	2.6	2.6	2.6
					Accuracy%	14	4.4	1.5
			S4	16	Precision%	3.1	3.1	3.1
					Accuracy%	13	3.7	0.86
			S5	16	Precision%	3.7	3.7	3.7
					Accuracy%	17	7.1	4.1
GL-O-P	0.96	0.93	S1	16	Precision%	4.2	4.2	4.2
					Accuracy%	8.9	4.5	0.98
			S2	14	Precision%	4.6	4.6	4.6
					Accuracy%	7.9	3.6	0.03
			S3	6	Precision%	3.0	3.0	3.0
					Accuracy%	6.9	2.6	-0.89
			S4	16	Precision%	3.1	3.1	3.1
					Accuracy%	6.7	2.5	-0.99
			S5	16	Precision%	3.1	3.1	3.1
					Accuracy%	7.4	3.1	-0.40
FK-N-P	0.90	0.97	S1	16	Precision%	2.9	2.9	2.9
					Accuracy%	6.2	-4.9	3.5
			S2	14	Precision%	5.3	5.3	5.3
					Accuracy%	9.8	-1.7	7.0
			S3	6	Precision%	4.6	4.6	4.6
					Accuracy%	5.4	-5.6	2.7
			S4	16	Precision%	7.5	7.5	7.5
					Accuracy%	9.2	-2.2	6.4
			S5	16	Precision%	4.1	4.1	4.1
					Accuracy%	12	0.31	9.1

Due to the high uncertainties of published $^{87}Rb/^{86}Sr$ ratios for the mineral RMs, most of the corrected and measured ratios calibrated using different RMs remains within the uncertainties of the published values. However, the mean $^{87}Rb/^{86}Sr$ values by ID-TIMS and MC-ICP-MS for the mineral RMs (Jegal et al., 2022) are comparable to the corrected ratios using CF_{Al2O3} and CF_{SiO2} relative to the measured ratios using other RMs such as non-matrix matched glass RMs. In summary, the correction procedure using CF_{Al2O3} and CF_{SiO2} significantly improves the accuracy of $^{87}Rb/^{86}Sr$ ratios of the mineral RMs. Accuracy is effectively better when using CF_{SiO2} for mica RMs such as Mica-Mg and GL-O and better for FK-N when using CF_{Al2O3}. This may suggest that the accuracy of corr $^{87}Rb/^{86}Sr$ ratios calibrated using matrix-mismatched RMs such as NIST 610 is related to the type of mineral samples (mica vs feldspar) and the linear regression results through the data of major element compositions.

5.2. Effects of chemical compositions on in-situ Rb-Sr ages

The correction approach in **section 5.1** shows that accurate $^{87}Rb/^{86}Sr$ ratios of the mineral RMs in the form of powder pressed tablets can be determined by LA-ICP-MS/MS using a synthetic silicate glass NIST 610 as external calibration standards after using the CF. Here, the goal is to test and access this approach with natural samples which may show higher degrees of complexity and heterogeneity than the RMs such as the powder pressed tables of mineral RMs. Rb-Sr isotopic data were calculated for the mineral/whole-rock samples ranging from Cambrian to Tertiary, previously determined for their ages from other isotopic systems or Rb-Sr bulk analyses (**Table 8**).

$^{87}Rb/^{86}Sr_{N610}$ ratios are calculated for the natural minerals by using CF_{Al2O3} and CF_{SiO2} based on NIST 610 glass-calibrated matrix-matched RM values and compare them with their known ages determined from previous studies. Rb-Sr isochron ages from the LA-ICP-MS/MS measurements in this study are calculated using a maximum likelihood regression of York (2004) available in the IsoplotR (v. 5.0, Vermeesch 2018) and Rb-Sr decay constant of $1.3972 \pm 0.0045 \times 10^{-11}$ a^{-1} (Villa et al., 2015). Ages and $^{87}Sr/^{86}Sr$ initial ratios are reported as 95% confidence limits (2s). $^{87}Rb/^{86}Sr$ ratios for the samples and RMs studied here were calculated by external calibration using (i) matrix-mismatched glass RMs (NIST 610, BCR-2G and

ATHO-G), (ii) matrix-matched mineral RMs (Mica-Mg-P, GL-O-P and FK-N-P) and (iii) applying the CF_{Al2O3} and CF_{SiO2} to the measured $^{87}Rb/^{86}Sr$ ratios calibrated using NIST 610 (corr $^{87}Rb/^{86}Sr$) while the measured $^{87}Sr/^{86}Sr$ ratios calibrated using NIST 610 were used for isochron of all studied samples due to the good accuracy and little differences for the measured $^{87}Sr/^{86}Sr$ calibrated using different RMs (**Fig. 14, Fig. 15** and **Table 10**).

The Rb-Sr isochron age results by using the calibration methods are expressed as $^{87}Rb/^{86}Sr_{RM}$ for the method (i) and (ii), where RM is external calibrants (glass and mineral RMs) for $^{87}Rb/^{86}Sr$ ratios, and corr $^{87}Rb/^{86}Sr_{N610,\ SiO2}$ and corr $^{87}Rb/^{86}Sr_{N610,\ Al2O3}$ for the method (iii) calculating by using CF_{SiO2} and CF_{Al2O3}, respectively. The uncertainties of measured and corrected $^{87}Rb/^{86}Sr$ and measured $^{87}Sr/^{86}Sr$ ratios are total uncertainties as described in **Fig. 10**. Their age accuracy is summarized in **Table 13**. The age accuracy by comparing between the calculated Rb-Sr isochron ages and published ages is used to evaluate the accuracy of the different approaches by using the published ages reported in **Table 8**.

Mica-Mg-G (Phlogopite Mica-Mg grains): Spot analyses of Mica-Mg-G (n = 24) by using the different calibration approaches form a Rb-Sr isochron defining ages from 437.8 ± 3.3 Ma for $^{87}Rb/^{86}Sr_{N610}$, 496.3 ± 5.5 Ma for $^{87}Rb/^{86}Sr_{Mica\text{-}Mg}$, and 491.8 ±3.7 Ma for corr $^{87}Rb/^{86}Sr_{N610,\ SiO2}$, assuming an initial $^{87}Sr/^{86}Sr$ of 0.72607 used by Hogmalm et al. (2017) (**Table 13**). Among the different calibration procedure, the best age result was obtained for $^{87}Rb/^{86}Sr_{Mica\text{-}Mg}$ with an accuracy of -4.8% and within the uncertainties of the ID-TIMS and MC-ICP-MS mean age from Jegal et al. (2022) and the range of compiled ages (**Table 8**). Mica-Mg-P has the same chemical matrix with Mica-Mg-G (**Fig. 9**). The age accuracy of $^{87}Rb/^{86}Sr_{N610}$ (-16%) is improved when using CF_{SiO2} to -5.6% for corr $^{87}Rb/^{86}Sr_{N610,\ SiO2}$. A better age precision of 3.7% for Mica-Mg-G is obtained for the corr $^{87}Rb/^{86}Sr_{N610,\ SiO2}$, compared to the precision of 5.5% for $^{87}Rb/^{86}Sr_{Mica\text{-}Mg}$ (**Table 13**), mainly derived from the uncertainties of the published values for the primary RM, reported in **Table 7**.

GL-O-G (Glauconite GL-O grains): Spot analyses yield a Rb-Sr isochron with an age of 87.0 ± 3.3 Ma ($^{87}Rb/^{86}Sr_{N610}$), 94.1 ± 6.0 Ma ($^{87}Rb/^{86}Sr_{GL\text{-}O}$) and 90.1 ± 4.6 Ma (corr $^{87}Rb/^{86}Sr_{N610,\ Al2O3}$) in Session 2 (n = 12), and 87.6 ± 4.4 Ma ($^{87}Rb/^{86}Sr_{N610}$), 94.4 ± 3.3 Ma ($^{87}Rb/^{86}Sr_{GL\text{-}O}$) and 90.7 ±3.4 Ma (corr $^{87}Rb/^{86}Sr_{N610,\ Al2O3}$), in Session 5 (n = 24) by using an assumed initial $^{87}Sr/^{86}Sr$ ratios of 0.708, also assumed by Jegal et al. (2022). Although these

ages overlap within errors of the reported ages in **Table 7**, the best accuracy of 1.0% and 1.6% were obtained for corr $^{87}Rb/^{86}Sr_{N610}$ using CF_{Al2O3}.

Mica-Fe-G (Biotite Mica-Fe grains): Rb-Sr isochron ages of Mica-Fe-G using an assumed initial $^{87}Sr/^{86}Sr$ ratios of 0.7074 from Duthou (1977) range from 264.0 ± 9.4 Ma ($^{87}Rb/^{86}Sr_{N610}$) to 300.4 ± 10.8 Ma (corr $^{87}Rb/^{86}Sr_{N610, SiO2}$) in session 1 and from 271.4 ± 10.1 Ma ($^{87}Rb/^{86}Sr_{N610}$) to 308.8 ± 11.6 Ma (corr $^{87}Rb/^{86}Sr_{N610, SiO2}$) in session 2. The age accuracy is calculated by using the reported Ar-Ar age of 307.6 ± 0.4 for Mica-Fe flakes by Grove & Harrison (1996). The correction of $^{87}Rb/^{86}Sr_{N610}$ using CF_{Al2O3} and CF_{SiO2} enhance the accuracy to -2.3% and -4.0% in session 1 and -1.3 and 0.4% in session 2, respectively, and yield better precision of 3.6%-3.8% relative to that of 4.0-4.1%. from $^{87}Rb/^{86}Sr_{Mica-Mg}$.

FK-N-G (Potash feldspar FK-N grains): The Rb-Sr isochron ages for the spot analyses range from 501.1 ± 10.6 Ma ($^{87}Rb/^{86}Sr_{N610}$), 532.0 ± 15.4 Ma ($^{87}Rb/^{86}Sr_{FK-N}$) and 509.6 ± 10.9 Ma (corr $^{87}Rb/^{86}Sr_{N610, SiO2}$) in session 1 (n = 12) and 450.2 ± 34.6 Ma ($^{87}Rb/^{86}Sr_{N610}$), 510.0 ± 64.3 Ma ($^{87}Rb/^{86}Sr_{FK-N}$) and 503.6 ± 39.0 Ma (corr $^{87}Rb/^{86}Sr_{N610, Al2O3}$) in session 5 (n = 24) (**Table 13, Fig. 18a**). The uncertainties of these LA-ICP-MS/MS ages are overlapped within the errors for FK-N bulk by ID-TIMS and MC-ICP-MS (512 ± 30 Ma, Jegal et al. 2022). Better accuracy (3.9% and -0.4% in session 1 and 5, respectively) was obtained when using the same matrix RM of FK-N-P.

LP (La Posta biotite and feldspar): **Fig. 18b** shows Rb-Sr isochron ages of LP biotite and feldspar (session 4) by calibration using different RMs (NIST 610, BCR-2G and Mica-Mg-P) and correction method. Spot analyses of LP biotite and feldspars yield Rb-Sr ages from 83.1 ± 2.2 Ma ($^{87}Rb/^{86}Sr_{N610}$) to 94.9 ± 3.7 Ma ($^{87}Rb/^{86}Sr_{Mica-Mg}$) in three analytical sessions (S1, S3, S4) (**Table 13**). Rb-Sr isochron age from biotite in session 1 was calculated by assuming the initial $^{87}Sr/^{86}Sr$ of 0.7049 from Walawender et al. (1990) as assumed by Rösel & Zack (2022). The age accuracy of 0.7-3.6% from $^{87}Rb/^{86}Sr_{Mica-Mg}$ in the three sessions is generally better than other approaches. To calculate CF_{SiO2} and CF_{Al2O3} of LP biotite and feldspar, SiO_2 and Al_2O_3 contents of LP biotite are reported in **Table 8**, and averaged SiO_2 (64.9 wt.%) and Al_2O_3 (18.5 wt. %) contents of LP feldspar from Clinkenbeard & Walawender (1989) were used, respectively. The age accuracy of -9.0-9.2% from $^{87}Rb/^{86}Sr_{N610}$ is improved to the accuracy better than 3.2% by using the correction approaches of corr $^{87}Rb/^{86}Sr_{N610, SiO2}$. The precision is

also enhanced by using corr $^{87}Rb/^{86}Sr_{N610,\ SiO2}$ compared to that from $^{87}Rb/^{86}Sr_{Mica\text{-}Mg}$.

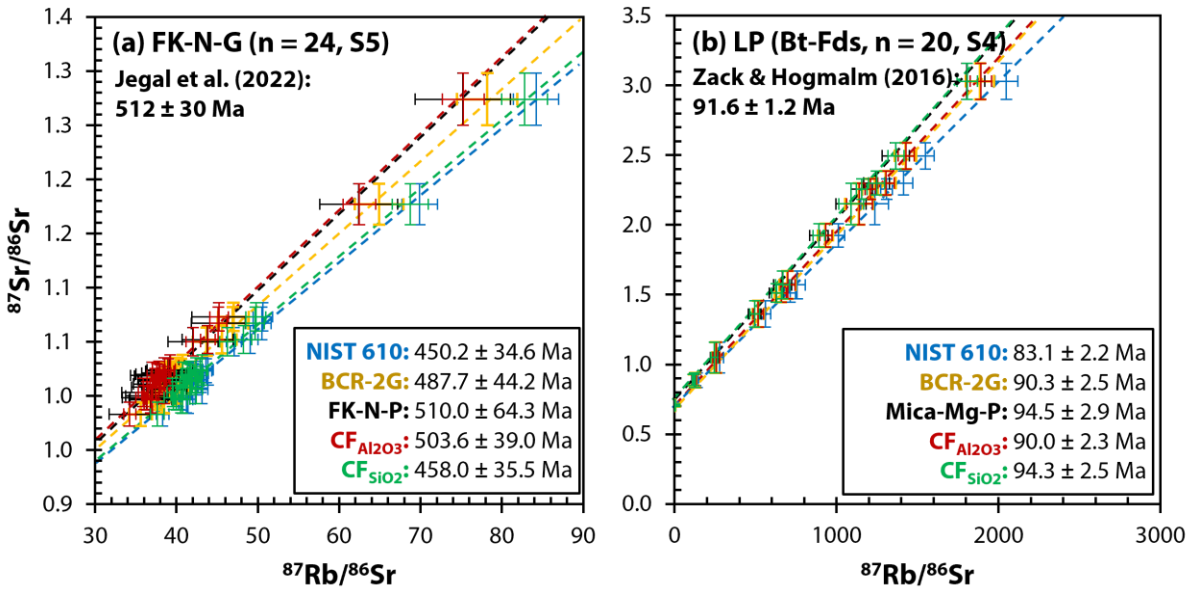

Fig. 18. Rb-Sr isochrons for (a) FK-N-G and (b) LP using different RMs and correction factors (CF) for $^{87}Rb/^{86}Sr$ ratios. NIST 610 is used to calibrate $^{87}Sr/^{86}Sr$ for all isochrons.

Apd-Phl (Ampandarandava phlogopite): The Rb-Sr isochron ages of Apd-Phl range from 463.8 Ma ($^{87}Rb/^{86}Sr_{N610}$) to 533.2 Ma (corr $^{87}Rb/^{86}Sr_{N610,\ Al2O3}$) in session 2 and from 495.9 Ma ($^{87}Rb/^{86}Sr_{N610}$) to 528.7 Ma (corr $^{87}Rb/^{86}Sr_{N610,\ Al2O3}$). The best accuracy is obtained for $^{87}Rb/^{86}Sr_{Mica\text{-}Mg}$, where the similar matrix RM of Mica-Mg was used as an external calibrant. By applying CF_{SiO2} and CF_{Al2O3} on $^{87}Rb/^{86}Sr_{N610}$, the accuracy of the age was improved to -0.2% with similar precision of 1.0-2.7% with that from $^{87}Rb/^{86}Sr_{Mica\text{-}Mg}$.

MD (Mt. Dromedary biotite): The Rb-Sr age of MD range is between 91.1 ± 8.3 Ma ($^{87}Rb/^{86}Sr_{N610}$) to 103.5 ± 9.5 Ma (corr $^{87}Rb/^{86}Sr_{N610,\ SiO2}$). The Rb-Sr age results using mineral RMs ($^{87}Rb/^{86}Sr_{Mica\text{-}Mg}$, $^{87}Rb/^{86}Sr_{GL\text{-}O}$, $^{87}Rb/^{86}Sr_{FK\text{-}N}$) and glass RM of BCR-2G ($^{87}Rb/^{86}Sr_{BCR\text{-}2G}$) yield better accuracy of -1.2-2.0% compared to the accuracy of -9.1% from $^{87}Rb/^{86}Sr_{N610}$. Due to the high uncertainties of the published $^{87}Rb/^{86}Sr$ values for the mineral RMs (4.5-11%, RSD) from Jegal et al. (2022), the better precision of 9.1% was obtained by using BCR-2G which has similar Al_2O_3 content with that of MD (**Fig. 9**). The ages from corr $^{87}Rb/^{86}Sr_{N610,\ Al2O3}$ and corr $^{87}Rb/^{86}Sr_{N610,\ SiO2}$ are also in good agreement with the reported ages with the accuracy of -2.1% and 3.2%, respectively, and the precision of 9.1%.

Table 13. Precision and accuracy of Rb-Sr isochron ages for the samples using measured and corrected $^{87}Rb/^{86}Sr$ ratios. Δ Age (%) indicates the accuracy of the age by LA-ICP-MS/MS compared to the reported age in **Table 8**.

Sample	Session	n	Approach	(i) matrix-mismatched RMs			(ii) matrix-matched RMs			(iii) application of CF on $^{87}Rb/^{86}Sr_{N610}$	
				$^{87}Rb/^{86}Sr_{N610}$	$^{87}Rb/^{86}Sr_{BCR-2G}$	$^{87}Rb/^{86}Sr_{ATHO-G}$	$^{87}Rb/^{86}Sr_{Mica-Mg}$	$^{87}Rb/^{86}Sr_{GL-O}$	$^{87}Rb/^{86}Sr_{FK-N}$	corr $^{87}Rb/^{86}Sr_{N610,\ Al2O3}$	corr $^{87}Rb/^{86}Sr_{N610,\ SiO2}$
Mica-Mg-G*	S4	24	Age (Ma)	437.8	475.2	462.9	496.3	466.7	477.6	477.7	491.8
			± 2s	3.3	3.7	3.4	5.5	11.0	9.8	3.6	3.7
			± 2s%	0.74	0.78	0.74	1.11	2.36	2.06	0.74	0.74
			Δ Age (%)	-16.0	-8.8	-11.1	-4.8	-10.4	-8.3	-8.3	-5.6
			MSWD	2.60	0.92	2.00	0.44	0.10	0.13	2.40	2.30
GL-O-G*	S2	12	Age (Ma)	87.0	94.6		97.1	94.1	95.8	90.1	93.0
			± 2s	4.4	4.8		5.3	6.0	6.5	4.6	4.7
			± 2s%	5.1	5.1		5.5	6.4	6.7	5.1	5.1
			Δ Age (%)	-2.4	6.1		8.8	5.5	7.3	1.0	4.3
			MSWD	0.65	0.64		0.58	0.46	0.54	0.65	0.65
GL-O-G*	S5	24	Age (Ma)	87.6	94.4	91.4	102.8	94.4	98.3	90.7	93.6
			± 2s	3.0	3.3	3.3	3.7	3.3	3.7	3.1	3.2
			± 2s%	3.4	3.5	3.6	3.6	3.5	3.7	3.4	3.4
			Δ Age (%)	-1.8	5.8	2.5	15.2	5.8	10.2	1.6	4.9
			MSWD	0.83	0.80	0.76	0.75	0.80	0.73	0.83	0.83
FK-N-G	S1	12	Age (Ma)	501.1	526.7		553.2	544.8	532.0	560.3	509.6
			± 2s	10.6	10.4		15.6	26.1	15.4	11.9	10.9
			± 2s%	2.1	2.0		2.8	4.8	2.9	2.1	2.1
			Δ Age (%)	-2.1	2.9		8.0	6.4	3.9	9.4	-0.5
			$^{87}Sr/^{86}Sr_i$	0.724	0.724		0.724	0.724	0.724	0.724	0.724
			MSWD	2.20	1.30		0.65	0.23	0.60	2.10	2.10
FK-N-G	S5	24	Age (Ma)	450.2	487.7	473.8	532.8	489.7	510.0	503.6	458.0
			± 2s	34.6	44.2	52.8	60.0	88.6	64.3	39.0	35.5
			± 2s%	7.7	9.1		11.3	18.1	12.6	7.7	7.8
			Δ Age (%)	-12.1	-4.7		4.1	-4.4	-0.4	-1.6	-10.5
			$^{87}Sr/^{86}Sr_i$	0.746	0.744	0.743	0.743	0.742	0.742	0.746	0.746
			MSWD	0.81	0.56	0.35	0.34	0.13	0.27	0.80	0.79

Sample	Session	n	Approach	(i) matrix-mismatched RMs			(ii) matrix-matched RMs			(iii) application of CF on $^{87}Rb/^{86}Sr_{N610}$	
				$^{87}Rb/^{86}Sr_{N610}$	$^{87}Rb/^{86}Sr_{BCR-2G}$	$^{87}Rb/^{86}Sr_{ATHO-G}$	$^{87}Rb/^{86}Sr_{Mica-Mg}$	$^{87}Rb/^{86}Sr_{GL-O}$	$^{87}Rb/^{86}Sr_{FK-N}$	corr $^{87}Rb/^{86}Sr_{N610, Al2O3}$	corr $^{87}Rb/^{86}Sr_{N610, SiO2}$
Mica-Fe-G*	S1	12	Age (Ma)	264.0	277.7		291.8	287.5	280.3	295.3	300.4
			± 2s	9.4	10.4		11.8	14.3	11.4	10.6	10.8
			± 2s%	3.6	3.7		4.0	5.0	4.1	3.6	3.6
			Δ Age (%)	-14.2	-9.7		-5.1	-6.5	-8.9	-4.0	-2.3
			MSWD	0.08	0.07		0.06	0.04	0.07	0.08	0.08
Mica-Fe-G*	S2	15	Age (Ma)	271.4	295.0		302.0	292.2	297.8	303.5	308.8
			± 2s	10.1	11.1		12.4	14.4	12.8	11.4	11.6
			± 2s%	3.7	3.8		4.1	4.9	4.3	3.8	3.8
			Δ Age (%)	-11.8	-4.1		-1.8	-5.0	-3.2	-1.3	0.4
			MSWD	0.15	0.16		0.13	0.09	0.12	0.15	0.15
LP	S1	12	Age (Ma)	83.4	87.7		92.2	90.9	88.6	90.3	94.5
Bt only*			± 2s	1.9	2.2		2.7	3.7	2.6	2.1	2.2
			± 2s%	2.3	2.5		2.9	4.1	3.0	2.3	2.3
			Δ Age (%)	-9.0	-4.2		0.7	-0.8	-3.2	-1.4	3.2
			MSWD	0.64	0.52		0.36	0.18	0.36	0.64	0.63
LP	S3	9	Age (Ma)	83.2	88.6		94.9	88.5	87.4	90.1	94.3
Bt-Fds			± 2s	2.7	2.9		3.7	5.1	3.6	2.9	3.1
			± 2s%	3.2	3.3		3.9	5.8	4.2	3.3	3.3
			Δ Age (%)	-9.1	-3.3		3.6	-3.4	-4.6	-1.6	3.0
			$^{87}Sr/^{86}Sr_i$	0.7029	0.7029		0.7029	0.7029	0.7029	0.7029	0.7029
			± 2s	0.0040	0.0040		0.0040	0.0040	0.0040	0.0040	0.0040
			MSWD	0.29	0.28		0.19	0.08	0.16	0.28	0.28
LP	S4	20	Age (Ma)	83.1	90.3	88.1	94.5	89.2	91.5	90.0	94.3
Bt-Fds			± 2s	2.2	2.5	2.9	2.9	4.2	4.0	2.3	2.5
			± 2s%	2.6	2.8	3.3	3.1	4.7	4.3	2.6	2.6
			Δ Age (%)	-9.2	-1.4	-3.8	3.1	-2.6	-0.1	-1.7	2.9
			$^{87}Sr/^{86}Sr_i$	0.7048	0.7048	0.7048	0.7048	0.7048	0.7048	0.7048	0.7048
			± 2s	0.0020	0.0020	0.0020	0.0020	0.0020	0.0020	0.0020	0.0020
			MSWD	0.65	0.62	0.58	0.59	0.49	0.31	0.65	0.65

*Results using an assumed initial $^{87}Sr/^{86}Sr$ ratio (see **section 5.2**)

Table 13. (continued)

Sample	Session	n	Approach	(i) matrix-mismatched RMs			(ii) matrix-matched RMs			(iii) application of CF on $^{87}Rb/^{86}Sr_{N610}$	
				$^{87}Rb/^{86}Sr_{N610}$	$^{87}Rb/^{86}Sr_{BCR-2G}$	$^{87}Rb/^{86}Sr_{ATHO-G}$	$^{87}Rb/^{86}Sr_{Mica-Mg}$	$^{87}Rb/^{86}Sr_{GL-O}$	$^{87}Rb/^{86}Sr_{FK-N}$	corr $^{87}Rb/^{86}Sr_{N610,\ Al2O3}$	corr $^{87}Rb/^{86}Sr_{N610,\ SiO2}$
Apd-Phl*	S2	15	Age (Ma)	463.8	503.8		514.8	497.9	507.3	533.2	521.1
			± 2s	12.4	13.6		14.6	16.3	11.6	14.3	14.0
			± 2s%	2.7	2.7		2.8	3.3	2.3	2.7	2.7
			Δ Age (%)	-10.5	-2.7		-0.6	-3.9	-2.1	2.9	0.6
			MSWD	8.9	7.40		2.20	0.76	1.50	8.6	8.5
Apd-Phl*	S4	20	Age (Ma)	495.9	499.7	487.0	522.2	491.3	502.7	528.7	516.8
			± 2s	4.8	5.1	7.1	7.0	13.0	11.7	5.5	5.4
			± 2s%	1.0	1.0	1.5	1.3	2.6	2.3	1.0	1.0
			Δ Age (%)	-4.3	-3.5	-6.0	0.8	-5.2	-3.0	2.1	-0.2
			MSWD	1.9	0.98	0.46	0.54	0.14	0.18	1.8	1.8
MD-Bt, Mz	S2	12	Age (Ma)	91.1	99.1		102.3	100.5	101.2	98.2	103.5
			± 2s	8.3	9.1		10.7	13.3	11.3	9.0	9.5
			± 2s%	9.1	9.2		10.5	13.2	11.2	9.1	9.1
			Δ Age (%)	-9.1	-1.2		2.0	0.2	0.9	-2.1	3.2
			$^{87}Sr/^{86}Sr_i$	0.7055	0.7055		0.7051	0.7045	0.7050	0.7055	0.7055
			± 2s	0.0048	0.0048		0.0052	0.0062	0.0055	0.0048	0.0048
			MSWD	0.98	0.97		0.88	0.69	0.83	0.98	0.98

*Results using an assumed initial $^{87}Sr/^{86}Sr$ ratio (see **section 5.2**)

In this work, the results show that the Rb-Sr ages from $^{87}Rb/^{86}Sr_{N610}$ underestimate systematically the ages for all studied samples. NIST 610 is the most different matrix RM compared to the matrices of the samples in this study in terms of chemical compositions and physical properties. This result strengthens the requirement for in-situ Rb-Sr dating by LA-ICP-MS/MS to use matrix-matched RMs such as Mica-Mg for mica samples and FK-N for feldspar samples. However, the precision of the Rb-Sr isochron ages can be affected by the uncertainties of their published Rb-Sr ratio values that needs to be used for the external calibration and to be propagated in the Rb-Sr ratios of single analyses. The precision of the ages strongly depends on their uncertainties. One of the limitations of this approach is high uncertainties of $^{87}Rb/^{86}Sr$ ratios and potential heterogeneity for the mineral RMs. Our approach shows that the highly biased $^{87}Rb/^{86}Sr$ data and Rb-Sr ages by using matrix-mismatched RMs such as NIST 610 can be corrected using the correction factor (CF) defined from the linear regressions through the data plotting measured $^{87}Rb/^{86}SrN$ calibrated using NIST 610 as a function of SiO_2 or Al_2O_3.

6. Conclusions: Suggested procedures for in-situ Rb/Sr geochronology by LA-ICP-MS/MS

With the recent increasing number of applications on in-situ Rb-Sr geochronology by LA-ICP-MS/MS, standardized analysis protocol and calibration approaches for various matrix samples are necessary. In **Fig. 19**, we suggest the recommended procedures for in-situ Rb/Sr dating of various types of samples by LA-ICP-MS/MS.

• **Session preparation:** (i) Well-characterized homogeneous RMs matrix-matched with targeted unknown samples are required to use as primary standards for external calibration of $^{87}Rb/^{86}Sr$ ratios. (ii) If matrix-matched RMs cannot be found, glass RMs that have similar major compositions with unknown samples can be used. (iii) If RMs described in (i) and (ii) are not available, matrix-mismatched homogeneous RMs with a wide range of major element compositional variations are selected to cover the range of major element compositions for targeted unknown minerals based on the EPMA analysis of the samples. (iv) NIST 610 is used for external calibration of $^{87}Sr/^{86}Sr$ ratios for all type of samples. (v) Secondary standards as

natural mineral samples that have similar types with targeted unknown samples and well-defined known ages are prepared to monitor the quality of the measurements.

• **Test for matrix effects and CF:** (i) If well-characterized homogeneous RMs matrix-matched with targeted unknown samples is found, the test for matrix effects is not required. (ii) The selected RMs with secondary standard are tested in the beginning day of analytical sessions by using standard-sample-standard bracketing method to define a linear correlation through the data on the plots of $^{87}Rb/^{86}Sr_{N610}$ and major element compositions. (iii) The results of linear regressions are conducted to calculate the CF by using the major clement compositions of secondary standards.

• **Analysis of targeted unknown samples:** (i) The calculated CF is applied firstly to secondary standards in order to examine if the linear regressions and CF are well defined and if this approach can be applied to unknown samples. (ii) Then, the CF is applied to unknown targeted samples.

• **External mass bias correction:** (i) $^{87}Sr/^{86}Sr$ ratios of all type of unknown samples are calibrated using NIST 610. (ii) If matrix-matched RMs are used, raw $^{87}Rb/^{86}Sr$ of unknown samples are calibrated externally using matrix-matched RMs. (iii) If matrix-mismatched homogeneous RM with similar major element compositions to the samples is available, measured $^{87}Rb/^{86}Sr$ of samples are calculated by external matrix-mismatched calibration. (iv) In case matrix-matched RMs or matrix-mismatched RMs with similar compositions to samples cannot be used, the calculated CF are applied to correct measured $^{87}Rb/^{86}Sr_{N610}$ ratios of the unknown samples.

In this chapter, the analytical procedure and calibration approaches were suggested by using matrix-matched and non-matrix matched RMs for in-situ Rb-Sr dating by LA-ICP-MS/MS, showing that these approaches can be applied to various matrices samples. The results show that Rb/Sr heterogeneity in the mineral RMs such as Mica-Mg, GL-O, FK-N and Mica-Fe affect the uncertainties of measured $^{87}Rb/^{86}Sr$ ratios and Rb/Sr ages of samples by Rb-Sr dating by LA-ICP-MS/MS. From the study of Jegal et al. (2022), the heterogeneity and high uncertainties of Rb-Sr isotopic ratios of the mineral RMs were mainly attributed from natural variability of the RMs including inclusions, alteration and/or compositional variations of the mineral grains. This variability limits the precision of in-situ Rb-Sr dating methods by LA-

ICP-MS/MS. Thus, development of homogeneous matrix-matched mineral RMs for in-situ LA-ICP-MS/MS dating of low to high Rb/Sr ratio samples are still needed for further studies such as mineral RMs in the form of fused glasses or well-homogenized nano-powder RMs produced from mostly pure mineral. Until the appropriate RMs are available, we propose new approach of using the CF derived from regression lines to correct the measured $^{87}Rb/^{86}Sr$ ratios, calibrated using non-matrix matched homogeneous RMs such as NIST 610, that permit more precise Rb-Sr ages by in-situ Rb-Sr LA-ICP-MS/MS analysis.

►

Fig. 19. Flow chart of the suggested procedure for mass bias correction of in-situ Rb/Sr dating by LA-ICP-MS/MS.

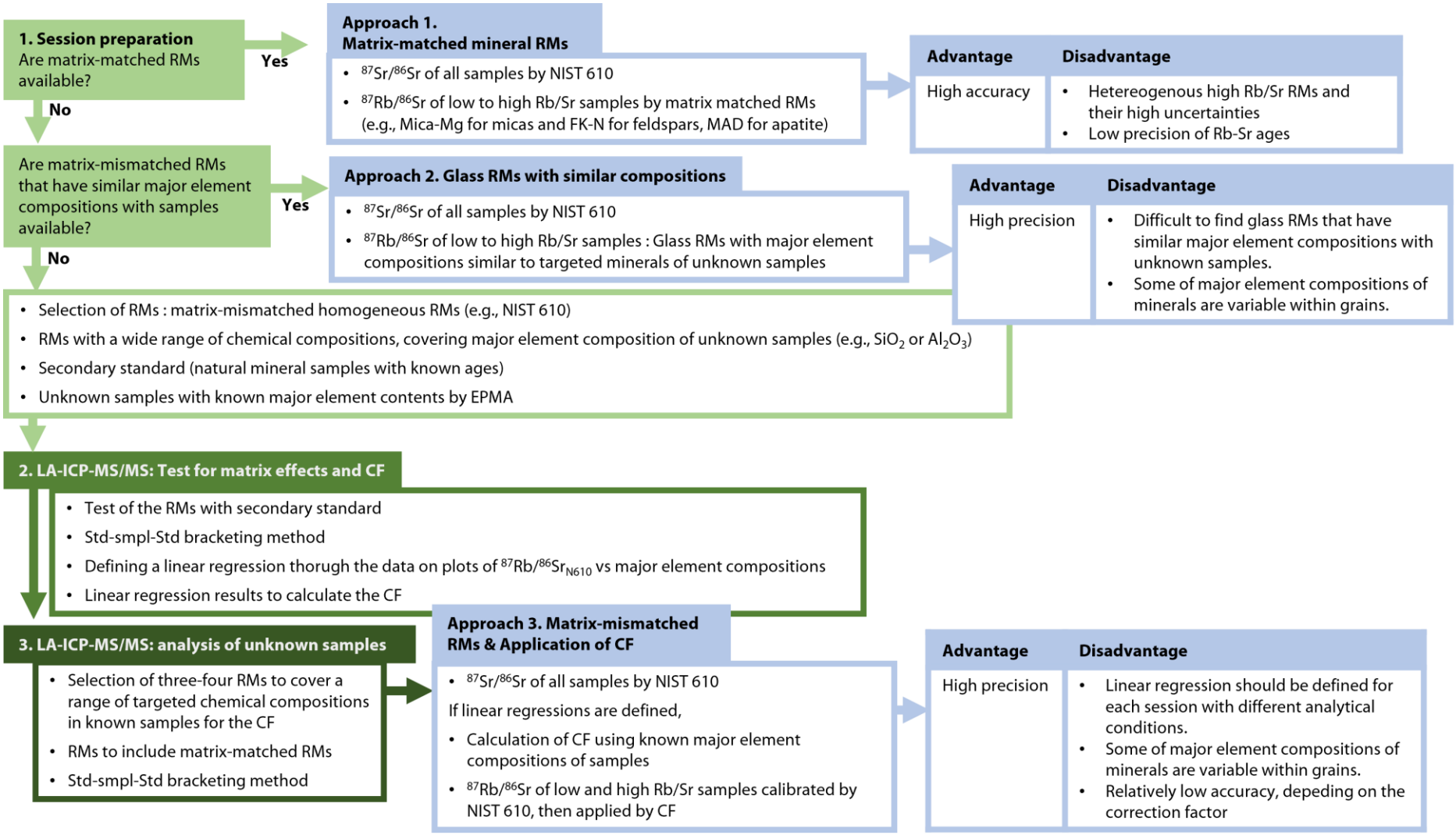
1. Session preparation
Are matrix-matched RMs available?
Yes
No
Approach 1.
Matrix-matched mineral RMs
• 87Sr/86Sr of all samples by NIST 610
• 87Rb/86Sr of low to high Rb/Sr samples by matrix matched RMs (e.g., Mica-Mg for micas and FK-N for feldspars, MAD for apatite)
Advantage
High accuracy
Disadvantage
• Hetereogenous high Rb/Sr RMs and their high uncertainties
• Low precision of Rb-Sr ages
Are matrix-mismatched RMs that have similar major element compositions with samples available?
Yes
No
Approach 2. Glass RMs with similar compositions
• 87Sr/86Sr of all samples by NIST 610
• 87Rb/86Sr of low to high Rb/Sr samples : Glass RMs with major element compositions similar to targeted minerals of unknown samples
Advantage
High precision
Disadvantage
• Difficult to find glass RMs that have similar major element compositions with unknown samples.
• Some of major element compositions of minerals are variable within grains.
• Selection of RMs : matrix-mismatched homogeneous RMs (e.g., NIST 610)
• RMs with a wide range of chemical compositions, covering major element composition of unknown samples (e.g., SiO2 or Al2O3)
• Secondary standard (natural mineral samples with known ages)
• Unknown samples with known major element contents by EPMA
2. LA-ICP-MS/MS: Test for matrix effects and CF
• Test of the RMs with secondary standard
• Std-smpl-Std bracketing method
• Defining a linear regression thorugh the data on plots of 87Rb/86Sr N610 vs major element compositions
• Linear regression results to calculate the CF
3. LA-ICP-MS/MS: analysis of unknown samples
• Selection of three-four RMs to cover a range of targeted chemical compositions in known samples for the CF
• RMs to include matrix-matched RMs
• Std-smpl-Std bracketing method
Approach 3. Matrix-mismatched RMs & Application of CF
• 87Sr/86Sr of all samples by NIST 610
If linear regressions are defined,
• Calculation of CF using known major element compositions of samples
• 87Rb/86Sr of low and high Rb/Sr samples calibrated by NIST 610, then applied by CF
Advantage
High precision
Disadvantage
• Linear regression should be defined for each session with different analytical conditions.
• Some of major element compositions of minerals are variable within grains.
• Relatively low accuracy, depeding on the correction factor

References

Bolea-Fernandez, E., Van Malderen, S. J. M., Balcaen, L., Resano, M., & Vanhaecke, F. (2016). Laser ablation-tandem ICP-mass spectrometry (LA-ICP-MS/MS) for direct Sr isotopic analysis of solid samples with high Rb/Sr ratios. *Journal of Analytical Atomic Spectrometry*, *31*(2), 464–472. https://doi.org/10.1039/C5JA00404G

Clinkenbeard, J. P., & Walawender, M. J. (1989). Mineralogy of the La Posta pluton: Implications for the origin of zoned plutons in the eastern Peninsular Ranges batholith, southern and Baja California. *American Mineralogist*, *74*(11–12), 1258–1269.

Duthou J.L. (1977). Chronologie Rb-Sr et geochimie des granitoides d'un segment de la chaine varisque, relations avec le metamorphisme: le Nord limousin, Massif Central Francais. Universite de Clermont, Unite d'enseignement et de recherche de sciences

Eggins, S.M., Kinsley, L. P. J., & Shelley, J. M. G. (1998). Deposition and element fractionation processes during atmospheric pressure laser sampling for analysis by ICP-MS. *Applied Surface Science*, *127–129*, 278–286. https://doi.org/10.1016/S0169-4332(97)00643-0

Eggins, Stephen M., & Shelley, J. M. G. (2002). Compositional Heterogeneity in NIST SRM 610-617 Glasses. *Geostandards and Geoanalytical Research*, *26*(3), 269–286. https://doi.org/10.1111/j.1751-908X.2002.tb00634.x

Elburg, M., Vroon, P., van der Wagt, B., & Tchalikian, A. (2005). Sr and Pb isotopic composition of five USGS glasses (BHVO-2G, BIR-1G, BCR-2G, TB-1G, NKT-1G). *Chemical Geology*, *223*(4), 196–207. https://doi.org/10.1016/j.chemgeo.2005.07.001

Fisher, C. M., Longerich, H. P., Jackson, S. E., & Hanchar, J. M. (2010) Data acquisition and calculation of U-Pb isotopic analyses using laser ablation (single collector) inductively coupled plasma-mass spectrometry. *Journal of Analytical Atomic Spectrometry, 25,* 1905–1920, https://doi.org/10.1039/C004955G

Glodny, J., Bingen, B., Austrheim, H., Molina, J. F., & Rusin, A. (2002). Precise eclogitization ages deduced from Rb/Sr mineral systematics: The Maksyutov complex, Southern Urals, Russia. *Geochimica et Cosmochimica Acta*, *66*(7), 1221–1235. https://doi.org/10.1016/S0016-7037(01)00842-0

Gorojovsky, L., & Alard, O. (2020). Optimisation of laser and mass spectrometer parameters for the *in situ* analysis of Rb/Sr ratios by LA-ICP-MS/MS. *Journal of Analytical Atomic Spectrometry*, 10.1039.D0JA00308E. https://doi.org/10.1039/D0JA00308E

Govindaraju, K. (1979). Report (1968-1978) on Two Mica Reference Samples: Biotite Mica-Fe and Phlogopite Mica-Mg. *Geostandards and Geoanalytical Research*, *3*(1), 3–24. https://doi.org/10.1111/j.1751-908X.1979.tb00235.x

Govindaraju, K. (1995). 1995 WORKING VALUES WITH CONFIDENCE LIMITS FOR TWENTY-SIX CRPG, ANRT AND IWG-GIT GEOSTANDARDS. *Geostandards and Geoanalytical Research*, *19*, 1–32. https://doi.org/10.1111/j.1751-908X.1995.tb00164.x

Govindaraju, Kuppusami. (1984). Report (1973-1984) on Two ANRT Geochemical Reference Samples: Granite GS-N and Potash Feldspar FK-N. *Geostandards and Geoanalytical Research*, *8*(2), 173–206. https://doi.org/10.1111/j.1751-908X.1984.tb00426.x

Grove, M., & Harrison, T. M. (1996). diffusion in 40∗ Ar Fe-rich phlogopite. *Am. Mineral*, *81*, 940–951.

Hogmalm, K. J., Zack, T., Karlsson, A. K.-O., Sjöqvist, A. S. L., & Garbe-Schönberg, D. (2017). In situ Rb–Sr and K–Ca dating by LA-ICP-MS/MS: an evaluation of N_2O and SF_6 as reaction gases. *Journal of Analytical Atomic Spectrometry*, *32*(2), 305–313. https://doi.org/10.1039/C6JA00362A

Horstwood, M. S. A., Košler, J., Gehrels, G., Jackson, S. E., McLean, N. M., Paton, C., et al. (2016). Community-Derived Standards for LA - ICP - MS U-(Th-)Pb Geochronology – Uncertainty Propagation, Age Interpretation and Data Reporting. *Geostandards and Geoanalytical Research*, *40*(3), 311–332. https://doi.org/10.1111/j.1751-908X.2016.00379.x

Jackson, S. E. (2008). CHAPTER 11: CALIBRATION STRATEGIES FOR ELEMENTAL ANALYSIS BY LA–ICP–MS, 21. *Mineralogical Association of Canada Short Course*. 40.

Jackson, S. E., & Günther, D. (2003). The nature and sources of laser induced isotopic fractionation in laser ablation-multicollector-inductively coupled plasma-mass spectrometry. *Journal of Analytical Atomic Spectrometry*, *18*(3), 205–212. https://doi.org/10.1039/b209620j

Jegal, Y., Zimmermann, C., Reisberg, L., Yeghicheyan, D., Cloquet, C., Peiffert, C., et al. (n.d.). Characterisation of Reference Materials for In Situ Rb-Sr Dating by LA-ICP-MS/MS. *Geostandards and Geoanalytical Research*, *n/a*(n/a). https://doi.org/10.1111/ggr.12456

Jochum, K. P., & Stoll, B. (2008). CHAPTER 10: REFERENCE MATERIALS FOR ELEMENTAL AND ISOTOPIC ANALYSES BY LA–(MC)–ICP–MS: SUCCESSES AND OUTSTANDING NEEDS, 23. *Mineralogical Association of Canada Short Course*. 40.

Jochum, K. P., Dingwell, D. B., Rocholl, A., Stoll, B., Hofmann, A. W., Becker, S., et al. (2000). The Preparation and Preliminary Characterisation of Eight Geological MPI-DING Reference Glasses for In-Situ Microanalysis. *Geostandards and Geoanalytical Research*, *24*(1), 87–133. https://doi.org/10.1111/j.1751-908X.2000.tb00590.x

Jochum, K. P., Willbold, M., Raczek, I., Stoll, B., & Herwig, K. (2005). Chemical Characterisation of the USGS Reference Glasses GSA-1G, GSC-1G, GSD-1G, GSE-1G, BCR-2G, BHVO-2G and BIR-1G Using EPMA, ID-TIMS, ID-ICP-MS and LA-ICP-MS. *Geostandards and Geoanalytical Research*, *29*(3), 285–302. https://doi.org/10.1111/j.1751-908X.2005.tb00901.x

Jochum, K. P., Weis, U., Stoll, B., Kuzmin, D., Yang, Q., Raczek, I., et al. (2011). Determination of Reference Values for NIST SRM 610-617 Glasses Following ISO Guidelines. *Geostandards and Geoanalytical Research*, *35*(4), 397–429. https://doi.org/10.1111/j.1751-908X.2011.00120.x

Laureijs, C. T., Coogan, L. A., & Spence, J. (2021). A high throughput Rb-Sr dating method using solution tandem ICP-MS/MS (87Sr/86Sr) and standard addition calibration ICP-MS (Rb/Sr). *MethodsX*, *8*, 101309. https://doi.org/10.1016/j.mex.2021.101309

Li, Q.-L., Chen, F., Li, X.-H., Wang, F., & He, H.-Y. (2008). Single grain Rb-Sr isotopic analysis of GA-1550 biotite, LP-6 biotite and Bern-4M muscovite 40Ar-39Ar dating standards. *GEOCHEMICAL JOURNAL*, *42*(3), 263–271. https://doi.org/10.2343/geochemj.42.263

Li, S.-S., Santosh, M., Farkaš, J., Redaa, A., Ganguly, S., Kim, S. W., et al. (2020). Coupled U-Pb and Rb-Sr laser ablation geochronology trace Archean to Proterozoic crustal evolution in the Dharwar Craton, India. *Precambrian Research*, *343*, 105709. https://doi.org/10.1016/j.precamres.2020.105709

Lin, J., Liu, Y., Yang, Y., & Hu, Z. (2016). Calibration and correction of LA-ICP-MS and LA-MC-ICP-MS analyses for element contents and isotopic ratios. *Solid Earth Sciences*, *1*(1), 5–27. https://doi.org/10.1016/j.sesci.2016.04.002

Ludwig, K. R. (2012). Berkeley Geochronology Center Special Publication No. 5, 75.

Martin, R. F., Randrianandraisana, A., & Boulvais, P. (2014). Ampandrandava and similar phlogopite deposits in southern Madagascar: Derivation from a silicocarbonatitic melt of crustal origin. *Journal of African Earth Sciences*, *94*, 111–118. https://doi.org/10.1016/j.jafrearsci.2013.08.002

McDougall, I., & Wellman, P. (2011). Calibration of GA1550 biotite standard for K/Ar and 40Ar/39Ar dating. *Chemical Geology*, *280*(1–2), 19–25. https://doi.org/10.1016/j.chemgeo.2010.10.001

Morteani, G., Kostitsyn, Y. A., Gilg, H. A., Preinfalk, C., & Razakamanana, T. (2013). Geochemistry of phlogopite, diopside, calcite, anhydrite and apatite pegmatites and syenites of southern Madagascar: evidence for crustal silicocarbonatitic (CSC) melt formation in a Panafrican collisional tectonic setting. *International Journal of Earth Sciences*, *102*(3), 627–645. https://doi.org/10.1007/s00531-012-0832-x

Odin G.S. A.C.J., Armstrong R.L., Bagdasaryan G.P., Baksi A.K., Balogh K., Barnes N.A., Boelrijk I.M., Bonadonna F.P., Bonhomme M.G., Cassignol C., Chanin L., Gillot P.Y., Gledhill A., Govindaraju K., Harakal R., Harre W., Hebeda E.H., Hunziker J.C., Ingamells C.O., Kawashita K., Kiss E., Kreuzer H., Long L.E., McDougall I., McDowell F., Mehnert H., Montigny R., Pasteels P., Radicati F., Rex D.C., Rundle C.C., Savelli C., Sonet J., Welin E. & Zimmermann J.L. (1982) Intel-laboratory standards for dating purposes. In: Odin G.S. (ed.), Numerical dating in stratigraphy, 123–149.

Olierook, H. K. H., Rankenburg, K., Ulrich, S., Kirkland, C. L., Evans, N. J., Brown, S., et al. (2020). Resolving multiple geological events using in situ Rb–Sr geochronology: implications for metallogenesis at Tropicana, Western Australia. *Geochronology*, *2*(2), 283–303. https://doi.org/10.5194/gchron-2-283-2020

Page, R. W. (1978). Response of U-Pb Zircon and Rb-Sr total-rock and mineral systems to low-grade regional metamorphism in proterozoic igneous rocks, mount Isa, Australia. *Journal of the Geological Society of Australia*, *25*(3–4), 141–164. https://doi.org/10.1080/00167617808729025

Paton, C., Hellstrom, J., Paul, B., Woodhead, J., & Hergt, J. (2011). Iolite: Freeware for the visualisation and processing of mass spectrometric data. *Journal of Analytical Atomic Spectrometry*, *26*(12), 2508. https://doi.org/10.1039/c1ja10172b

Pearson N.J., W.L. Griffin & Suzanne Y. O'Reilly. (2008). Mass fractionation correction in laser ablation multiple-collector ICP–MS: implications for overlap corrections and precise and accurate in situ isotope ratio measurement. *Mineralogical Association of Canada Short Course*. Volume 40. 93-116

Phillips, D., Matchan, E. L., Honda, M., & Kuiper, K. F. (2017). Astronomical calibration of 40Ar/39Ar reference minerals using high-precision, multi-collector (ARGUSVI) mass spectrometry. *Geochimica et Cosmochimica Acta*, *196*, 351–369. https://doi.org/10.1016/j.gca.2016.09.027

Raczek, I., Stoll, B., Hofmann, A. W., & Peter Jochum, K. (2001). High-Precision Trace Element Data for the USGS Reference Materials BCR-1, BCR-2, BHVO-1, BHVO-2, AGV-1, AGV-2, DTS-1, DTS-2, GSP-1 and GSP-2 by ID-TIMS and MIC-SSMS. *Geostandards Newsletter*, *25*(1), 77–86. https://doi.org/10.1111/j.1751-908X.2001.tb00789.x

Redaa, A., Farkaš, J., Gilbert, S., Collins, A. S., Wade, B., Löhr, S., et al. (2021). Assessment of elemental fractionation and matrix effects during *in situ* Rb–Sr dating of phlogopite by LA-ICP-MS/MS: implications for the accuracy and precision of mineral ages. *Journal of Analytical Atomic Spectrometry*, *36*(2), 322–344. https://doi.org/10.1039/D0JA00299B

Rösel, D., & Zack, T. (2022). LA-ICP-MS/MS Single-Spot Rb-Sr Dating. *Geostandards and Geoanalytical Research*, *46*(2), 143–168. https://doi.org/10.1111/ggr.12414

Şengün, F., Bertrandsson Erlandsson, V., Hogmalm, J., & Zack, T. (2019). In situ Rb-Sr dating of K-bearing minerals from the orogenic Akçaabat gold deposit in the Menderes Massif, Western Anatolia, Turkey. *Journal of Asian Earth Sciences*, *185*, 104048. https://doi.org/10.1016/j.jseaes.2019.104048

Sylvester, P. J. (2008). CHAPTER 5: MATRIX EFFECTS IN LASER ABLATION–ICP–MS, 13. *Mineralogical Association of Canada Short Course*. 40.

Tillberg, M., Drake, H., Zack, T., Kooijman, E., Whitehouse, M. J., & Åström, M. E. (2020). In situ Rb-Sr dating of slickenfibres in deep crystalline basement faults. *Scientific Reports*, *10*(1), 562. https://doi.org/10.1038/s41598-019-57262-5

Vermeesch, P. (2018). IsoplotR: A free and open toolbox for geochronology. *Geoscience Frontiers*, *9*(5), 1479–1493. https://doi.org/10.1016/j.gsf.2018.04.001

Villa, I. M., De Bièvre, P., Holden, N. E., & Renne, P. R. (2015). IUPAC-IUGS recommendation on the half life of 87Rb. *Geochimica et Cosmochimica Acta*, *164*, 382–385. https://doi.org/10.1016/j.gca.2015.05.025

Walawender, M. J., Gastil, R. G., Clinkenbeard, J. P., McCormick, W. V., Eastman, B. G., Wernicke, R. S., et al. (1990). Chapter 1: Origin and evolution of the zoned La Posta-type plutons, eastern Peninsular Ranges batholith, southern and Baja California. In *Geological Society of America Memoirs* (Vol. 174, pp. 1–18). Geological Society of America. https://doi.org/10.1130/MEM174-p1

Wang, F., He, H., Zhu, R. et al. (2006) Intercalibration of international and domestic 40Ar/39Ar dating standards. *SCI CHINA SER D* 49, 461–470. https://doi.org/10.1007/s11430-006-0461-y

Willigers, B. J. A., Mezger, K., & Baker, J. A. (2004). Development of high precision Rb–Sr phlogopite and biotite geochronology; an alternative to 40Ar/39Ar tri-octahedral mica dating. *Chemical Geology*, *213*(4), 339–358. https://doi.org/10.1016/j.chemgeo.2004.07.006

Wilson, S.A. (1997a) The collection, preparation and testing of USGS reference material BCR-2, Columbia River, Basalt, U.S. Geological Survey Open-File Report 98-00x.

Wilson, S.A. (1997b) Data compilation for USGS reference material BHVO-2, Hawaiian Basalt, U.S. Geological Survey Open-File Report.

Woodhead, J. D., & Hergt, J. M. (2001). Strontium, Neodymium and Lead Isotope Analyses of NIST Glass Certified Reference Materials: SRM 610, 612, 614. *Geostandards and Geoanalytical Research*, *25*(2–3), 261–266. https://doi.org/10.1111/j.1751-908X.2001.tb00601.x

York, D., Evensen, N. M., Martínez, M. L., & De Basabe Delgado, J. (2004). Unified equations for the slope, intercept, and standard errors of the best straight line. *American Journal of Physics*, *72*(3), 367–375. https://doi.org/10.1119/1.1632486

Zack, T., & Hogmalm, K. J. (2016). Laser ablation Rb/Sr dating by online chemical separation of Rb and Sr in an oxygen-filled reaction cell. *Chemical Geology*, *437*, 120–133. https://doi.org/10.1016/j.chemgeo.2016.05.027

Zhang, S., He, M., Yin, Z., Zhu, E., Hang, W., & Huang, B. (2016). Elemental fractionation and matrix effects in laser sampling based spectrometry. *Journal of Analytical Atomic Spectrometry*, *31*(2), 358–382. https://doi.org/10.1039/C5JA00273G

Chapter IV.
Test and applicability case-study of Rb-Sr dating by LA-ICP-MS/MS in polyphase magmatic-hydrothermal systems: the Quiberon detachment zone (Brittany, France)

Chapter IV. Test and applicability case-study of Rb-Sr dating by LA-ICP-MS/MS in polyphase magmatic-hydrothermal systems: the Quiberon detachment zone (Brittany, France)

1. Introduction

The objective of the present chapter is to test the applicability and contribution of in-situ Rb-Sr isotope measurements by LA-ICP-MS/MS on a geological case study, following the analytical developments achieved within the three previous chapters of this PhD thesis manuscript. The selected case study is the Quiberon detachment zone, located in the Southern Domain of the Armorican Massif, French Variscan belt. This particular zone was selected as previous scientific works have been done to understand the evolution of this part of the Armorican Massif mainly structured during the Variscan Orogeny from 360 to 300 Ma (Ballèvre et al., 2009; 2013; Gapais et al., 2015). Several publications have indeed coupled petrographic observations to state-of-the-art geochronological approaches with different isotopic systems (U-Pb, Ar-Ar, Rb-Sr) applied on different minerals (zircon, monazite, apatite, micas) and to isotopic tracers (O, H, Sr) to decipher as precisely as possible the P-T-t-x evolution of this zone (Le Hébel, 2002; Tartèse & Boulvais, 2010; Tartèse et al., 2011a, 2011b, 2012; Lemarchand et al., 2012; Ballouard et al., 2015, 2017a, 2017b, 2018; Dusséaux et al., 2019, 2022). These recent studies have been mainly done by researchers from Geosciences Rennes (France), with recent important contributions from M. Poujol, P. Boulvais and Y. Branquet and related PhD students (R. Tartèse, C. Ballouard), associated to researchers from other institutions (C. Dusséaux and A. Gebelin among others).

The South Armorican Domain (SAD), that belongs to the internal zones of the Variscan belt, is characterized by the occurrence of high-grade metamorphic rocks and intense deformation (**Fig. 20**). From 320 to 300 Ma, this domain underwent extensional tectonics marked by the exhumation of anatectic domes, cored by migmatites and coated by syntectonic leucogranites, along extensional shear zones such as the Quiberon Detachment (Gapais et al., 1993, 2015; Cagnard et al., 2004; Ballouard et al., 2015). The SAD is delimited to the north by the South Armorican Shear Zone (SASZ), a lithospheric scale dextral transcurrent fault that

also localized voluminous syntectonic leucogranite magmatism from 320 to 310 Ma (Berthé et al., 1979; Jégouzo, 1980; Gumiaux et al., 2004a, 2004b; Tartèse et al., 2011a, 2011b, 2012; Ballouard et al., 2017a). During Late-Carboniferous, the SASZ accommodated extension in the high-grade South Armorican Domain and acted as a transfer zone toward the Central Armorican Domain to the north that was weakly deformed and thickened during the Variscan orogeny (Gapais et al., 2015). From Late-carboniferous to Early-Permian (320-275 Ma), ductile to brittle deformations along the SASZ and detachments from the SAD promoted the circulations of deep crustal and surface-derived hydrothermal fluids (Tartèse & Boulvais, 2010; Lemarchand et al., 2012; Tartèse et al., 2012; Ballouard et al., 2017b; Dusséaux et al., 2019). The magmatic and hydrothermal events along those shear zones had major impacts and controlled the developments of successive paragenetic associations, some of which linked with the formation of economic mineralizations such as rare-metals, cassiterite or uranium (Chauris, 1977; Cathelineau, 1981; Cathelineau et al., 1990; Cuney et al., 1990; Tartèse et al., 2013; Ballouard et al., 2017b, 2018) (**Fig. 20**).

In this framework, recent specific studies have been conducted on one locality of the Quiberon Peninsula, i.e., the outcropping zone of the Vivier. This locality was subjected to detailed petrographic, geochemical and geochronological characterizations and is known to be representative of the diversity of geological processes active in the Armorican Massif during the 320-275 Ma period. Considering this exceptional knowledge and framework, discussions with P. Boulvais were done and a collaborative project was defined to apply the in-situ Rb-Sr dating approach developed during the present PhD on a selection of samples representative of the different geological phases and processes that affected the zone. A field mission to the Quiberon peninsula and to the laboratory of Geosciences Rennes was done in October 2021 to visit the zone, learn about the geological context and recent scientific acquisitions, and select samples to be analyzed at Nancy. Applying Rb-Sr in-situ measurements on this selection of samples will allow testing in the best conditions the capabilities of the method and the potential gain of its application to polyphased geological case studies.

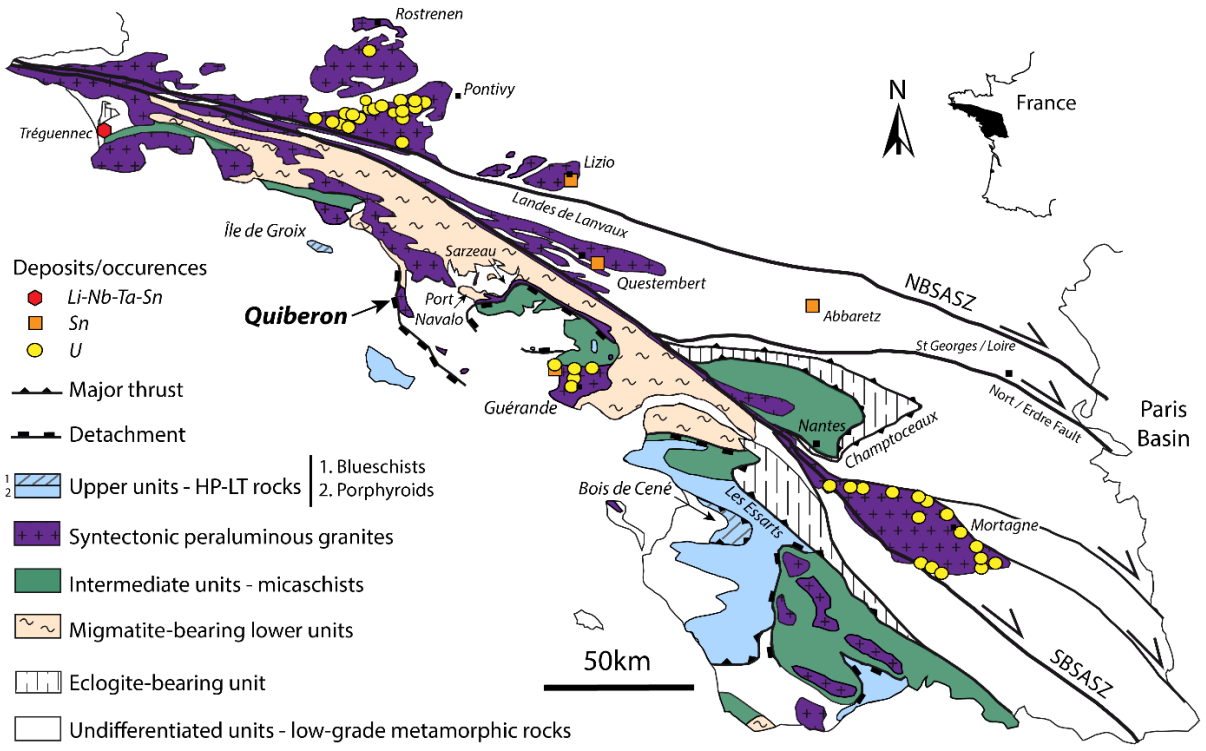

Fig. 20. Structural map of the southern part of the Armorican Massif showing the localization of the uranium (U), tin (Sn) and rare-metal occurrences as well as Late-Carboniferous peraluminous leucogranites. Modified from Gapais et al. (1993, 2015) and Ballouard et al. (2015, 2017b). SBSASZ: southern branch of the South Armorican Shear Zone. NBSASZ: northern branch of the South Armorican Shear Zone.

2. Geological framework of the South Armorican Domain

Three main tectonic-metamorphic units can be distinguished in the South Armorican Domain, from top to bottom (e.g., Gapais et al., 2015) (**Fig. 20**):

(i) Upper high pressure-low temperature metamorphic units that were deformed and exhumed in relation with early Variscan tectonics around 360 Ma and belonged to the upper brittle crust during Late-Carboniferous. Those units include the blueschist klippe from the Ile de Groix recording peak conditions of 1.4-1.8 GPa and 500-550°C (Bosse et al., 2002, 2005), as well as the Vendée porphyroid nappe mostly consisting of Ordovician metavolcanics (0.8 Gpa, 350-400°C; Le Hébel et al., 2002; Ballèvre et al., 2012).

(ii) Intermediate units mostly consisting of Neoproterozoic to Paleozoic micaschists that

record Barrovian-type medium pressure-medium temperature metamorphism from greenschist- to amphibolite-facies conditions (Bossière, 1988; Triboulet & Audren, 1988).

(iii) Lower high-temperature units made of mostly para-derived migmatites and gneisses as well as granites, reaching 800°C at 0.8 Gpa (Jones & Brown 1990). Partial melting up to biotite-dehydration conditions occur in the Port Navalo migmatites, located below the Quiberon detachment (**Fig. 20**), between 320 and 290 Ma (monazite U/Th-Pb, Dusséaux et al., 2022).

Barrovian-type metamorphism affecting the deepest units relates to continental collision with nappe emplacement around 360 Ma (Ballèvre et al., 2009, 2013). East-west dominated crustal extension accommodated by dextral shearing along the SASZ mostly occurred from 320 to 300 Ma and led to the exhumation of migmatite domes and syntectonic leucogranites along low-dipping shear zones such as the Quiberon detachment (Gapais et al., 1993, 2015; Gumiaux et al., 2004a; Tartèse et al., 2012).

The leucogranite sheets from the SAD (e.g., Guérande and Quiberon leucogranites) were emplaced, above the migmatites, within the micaschists units and below the HP-LT units, from 320 to 310 Ma (U-Pb zircon, Ballouard et al., 2015; Dusséaux et al., 2022) (**Fig. 21**). They commonly bear S/C fabrics characteristic of syn-cooling shearing (Gapais, 1989). Moreover, numerous syntectonic leucogranites, locally bearing S/C structures, were also emplaced along the SASZ from 320 to 315 Ma such as the Pontivy, Lizio and Questembert leucogranites (U-Pb zircon; Tartèse et al., 2011a, 2011b, Ballouard et al., 2017a). This main pulse of crustal peraluminous leucogranite magmatism was contemporaneous with mantle-derived mafic-intermediate magmatism in the Pontivy-Rostrenen complex at 316 ± 2 Ma (Ballouard et al., 2017a).

A later event of peraluminous leucogranite magmatism occur from ca. 306 to 302 Ma. It is marked by the intrusion of granitic dykes within the Guérande area and the emplacement of the Langonnet leucogranite body within the Pontivy-Rostrenen complex (U-Pb zircon and monazite, Ballouard et al., 2015, 2017a). This late-magmatic event was synchronous with hydrothermalism as well as ductile deformation along the SASZ and the extensional shear-zones as suggested by ^{40}Ar-^{39}Ar dates on muscovite from variably deformed leucogranites and

quartz veins from ca. 319 to 300 Ma (Le Hébel, 2002; Tartèse et al., 2011b; Gapais et al., 2015; Dusséaux et al., 2022). In the Guérande area, late leucogranite magmatism was also sub-contemporaneous with intra-granitic vein-type Sn mineralization at 306 ± 6 Ma (U-Pb on cassiterite, Ballouard, personal communication) but preceded peri- to intra-granitic vein-type U mineralization that occurred by pulse from 297 ± 3 to 275 ± 1 Ma (U-Pb on uranium oxide, Ballouard et al., 2017b). Similar uraninite U-Pb ages from 300 to 275 Ma were obtained for intra- to peri-granitic hydrothermal U deposits from the Pontivy and Mortagne district emplaced along or to the north of the SASZ (Cathelineau et al., 1990; Ballouard et al., 2018).

Oxygen isotope analyses of whole-rock, feldspar and quartz as well as hydrogen isotope compositions of muscovite from S/C and mylonitic leucogranites emplaced along the SASZ and detachments indicate that ductile deformation from 320 to 300 Ma was associated with sub-solidus alteration via surface-derived low $\delta^{18}O$ and δD fluids (Tartèse et al., 2010, 2012; 2013; Ballouard et al., 2017b; Dusséaux et al., 2019). It was suggested that surface-derived oxidized fluid circulations (meteoric and possibly connate waters), enhanced by brittle dominated deformation, has continued from 300 to 275 Ma and promoted the leaching of magmatic uranium oxides in the deformed leucogranites (Tartèse et al., 2013; Ballouard et al., 2017b, 2018). This is supported by the presence of altered apatite with U-Pb dates from 290 to 270 Ma in the U-mineralized Pontivy leucogranite (Ballouard et al., 2018). The leached-out U was then eventually precipitated in the surrounding reducing sedimentary formations to form U deposits (Cathelineau, 1981; Tartèse et al., 2013; Ballouard et al., 2017b, 2018).

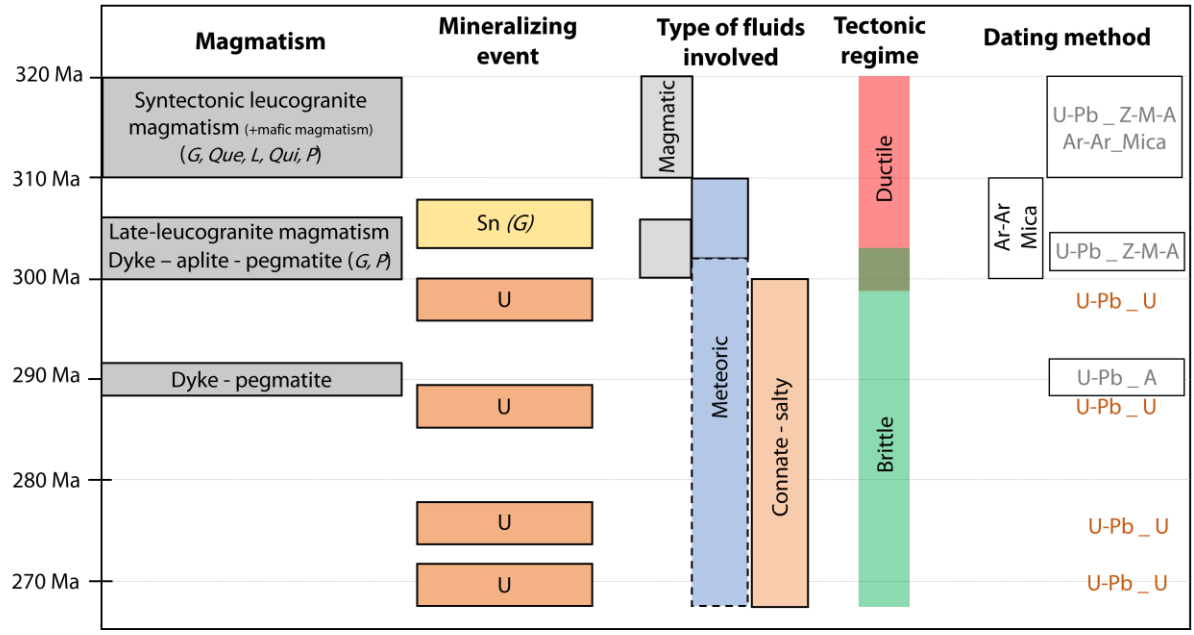

Fig. 21. Summary of the geological knowledge for the South part of the Armorican Massif (Brittany, France) during the 320-270 Ma period. This summary presents the main magmatic events, the known mineralizing events and the type of metals (Sn or U), the type of fluids involved and the related tectonic regime active in the zone. The applied dating methods and selected minerals are presented to the right of the figure (Z: zircon, M: monazite, A: apatite, C: cassiterite, U: uranium oxide). G: Guérande, Que: Questembert, L: Lizio, Qui: Quiberon, P: Pontivy.

3. Methodology

3.1. Sample strategy following the current scientific knowledge on the outcropping zone of the Vivier

Multiple geochronological and geochemical methods have been applied globally to the South Armorican Domain, and to the Quiberon Peninsula in particular with recent unpublished data acquired by researchers from Geosciences Rennes (P. Boulvais, N. Cogné and Y. Branquet) to constrain the structural-tectonic-fluid-chronological contexts. Some of these recent data have been acquired on a small outcrop to the southern part of the Quiberon peninsula: the Vivier outcrop (**Fig. 22**). This outcropping zone provides an invaluable vision of the rocks and geological processes active during the development of the detachment zones linked to the SASZ.

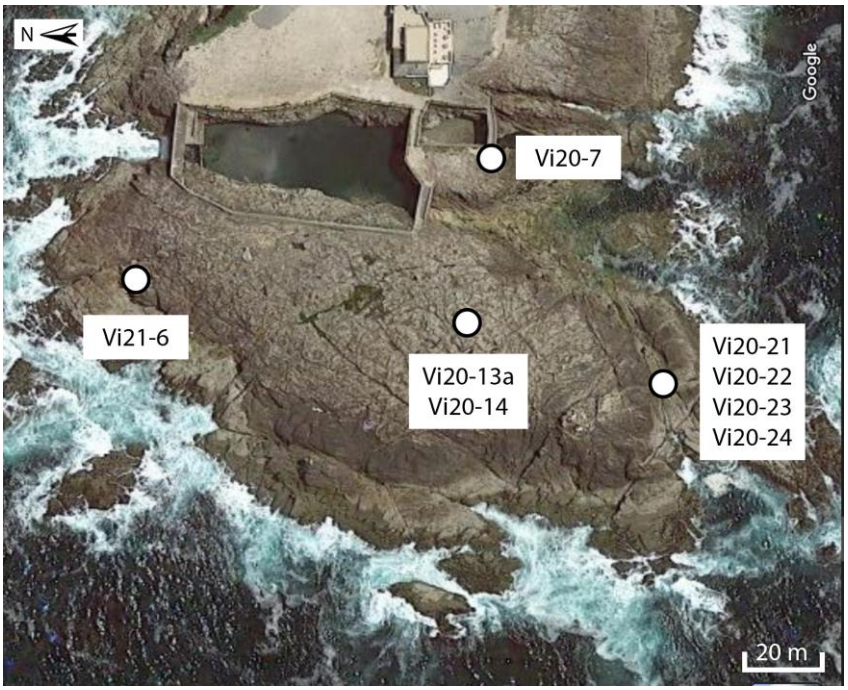

Fig. 22. Map of the Vivier zone from Google map, showing the locations of the samples analyzed in this study.

The recent geochronological results obtained at Geosciences Rennes for the Vivier using the U-Pb on apatite system demonstrate that three populations of mean age are co-existing in this area: 315.8 ± 3 Ma, 301.4 ± 1.5 Ma and 291.4 ± 2 Ma (**Table 14**). These populations of ages were acquired on the different magmatic rocks observed in the zone. The ca. 316 Ma age is within error of the zircon and monazite U-Pb ages of 317 ± 4 and 318 ± 3 Ma obtained, respectively, for the Quiberon leucogranite, and interpreted as its age of emplacement and crystallization (Dusséaux et al., 2022) (**Fig. 21**). The ca. 302 Ma age is proposed to correspond to either a major event of fluid-rock interaction linked to percolation of meteoric water within the detachment, as known in the Quiberon peninsula as well as other locations during the ca. 310-300 Ma timeframe (Tartèse et al., 2010, 2011a, 2012; Ballouard et al., 2017b; Dusséaux et al., 2019, 2022) or linked to a late magmatic episode marked by the intrusion of leucogranites, pegmatites or aplites (age of the tourmaline-rich aplite, Vi 20-7). This late magmatic episode was already dated in the Pontivy-Rostrenen and Guérande areas (Ballouard et al., 2015, 2017a). This event is also synchronous within error to a recent U-Pb age acquired on cassiterite from a quartz vein emplaced at the apical zone of the Guérande leucogranite (Ballouard, personal

communication). This demonstrates significant fluid circulations and potential mineralizing event at that period in relation to this late magmatism. The ca. 291 Ma event is proposed to correspond either to a last pegmatite magmatic event (age obtained on deformed pegmatite, Vi 20-21), or to a major fluid event affecting the SAD and related to regional U mineralizing events (Ballouard et al., 2017b, 2018). Prior to the application of the U-Pb dating method on apatite, ages younger than 300 Ma (Ar-Ar age on micas) have not been measured for the Quiberon Peninsula. Ages younger than 300 Ma are however known at the scale of the SAD and along the SASZ, with several populations measured between 300 Ma and 270 Ma in U deposits from the Guérande, Pontivy and Mortagne districts and associated leucogranites (U-Pb on apatite and uraninite, Cathelineau et al., 1990; Ballouard et al., 2017b, 2018; **Fig. 21**). Such mineralizing events are considered to be initially linked at ca. 297 Ma to deep intrusion of meteoric water along the SASZ and detachments, the source of uranium being the evolved and deformed uraninite-bearing leucrogranites crystallized at ca. 320-310 Ma (Tartèse et al., 2013; Ballouard et al., 2017b, 2018). The implication of connate waters from sedimentary basins/evaporitic systems is also considered at least for the youngest mineralizing event (ca. 270 Ma) based on study of fluid inclusions and isotopic (O, H, C, Sr, Nd) measurements from minerals coeval of uranium oxides in similar deposits from the Variscan French Massif central (Turpin et al., 1990; Cuney & Kyser, 2008).

Table 14. U-Pb ages on apatite grains from Vivier outcrop, recently acquired at Geosciences Rennes (Branquet et al., in prep). These samples were dated by in-situ LA-ICP-MS/MS measurements for Rb-Sr ages at GeoRessources.

Sample	Rock type	Description	U-Pb (Ma)	2s	n	MSWD
Vi 20-13a	Granite	deformed	316.3	5.1	47	1.5
Vi 20-14	Granite	weakly deformed	315.5	3.8	45	1.4
Vi 20-7	Aplite		302.6	10.6	41	1.0
Vi 21-6	Granite	deformed (top-east)	299.1	4.0	48	1.4
Vi 20-21	Pegmatite	deformed	288.8	8.5	46	1.4
Vi 20-23	Granite (enclave)	deformed	292.1	2.5	66	1.8
Vi 20-24	Granite	weakly deformed	291.1	3.8	45	1.8

Based on this knowledge and recent acquisition for the Vivier outcropping zone, a selection of samples was done at Geosciences Rennes. The objective was the collection of a representative set of samples of the different granitic rocks from the Vivier previously dated by U-Pb ages on apatite and representative of the three sets of ages. Following the previous works on the zone, the samples were selected to cover the different generations and deformation degrees of magmatic rocks in that zone: syntectonic weakly deformed granites, syntectonic deformed (S-C) granites, syntectonic aplites and variably deformed pegmatites crosscutting the main granitic body (details described in the next **section 3.2**).

3.2. Geology of the Vivier outcrop

The Vivier outcrop mainly consists of four rock types including a main two-mica-bearing peraluminous leucogranite facies (i.e., Quiberon leucogranite) that is crosscut by different generations of pegmatite and aplite dykes as well as quartz veins. This study was focused on granitic rocks hosting Sr ± Rb-bearing minerals, so quartz veins were not considered.

The main leucogranite facies from the Vivier is variably deformed and commonly displays S-C fabrics with C planes (shear bands) and S planes (foliation) slightly dipping toward the west and bearing an E-W oriented stretching lineation (**Fig. 23a-d).** S-C structures in the leucogranite generally indicate a top-to-the-west normal sense of hear consistent with the main deformation regime within the Quiberon detachment (Gapais et al., 2013; 2015) (**Fig. 23a** and **b**), although opposite top-to-the-east shear directions were locally observed (e.g., Sample Vi 21-6 as indicated in **Table 14**). The leucogranite, locally characterized by weak deformation where S-C fabrics are not clearly observed, is the weakly deformed leucogranite facies (**Fig. 23e** and **f**). Two-mica-bearing leucogranite samples are grouped depending on the degree of deformation as weakly deformed and deformed facies, and include two weakly deformed (Vi 20-14, Vi 20-24) and three deformed (Vi 20-13a, Vi 21-6, Vi 20-23) granite samples.

Both facies of two-mica-bearing leucogranite contain a Quartz-K-feldspar-Plagioclase-Muscovite-Biotite assemblage with a variable amount of apatite, Fe-Ti-oxide minerals, zircon or monazite (**Fig. 24a-g)**. Muscovite is dominant over biotite in weakly deformed and deformed leucogranites, and two types of muscovite are observed in the leucogranites. The first

muscovite type, that is dominant and is interpreted as primary, typically forms large (> 1 mm) euhedral to sub-euhedral flakes and commonly shows a fish-like habit. Small muscovite grains (< 100 μm), interpreted as secondary, are commonly observed in shear bands, or as recrystallization around large primary flakes (**Fig. 24c, d, e and f**). Biotite is sub-euhedral to anhedral, brown-reddish and occurs as intergrowth within or along muscovite flakes (**Fig. 24a, b, d, e, f** and **g**). Some biotite was affected by chloritic alteration, but fresh biotite was targeted in this study using SEM observation. Plagioclase is anhedral and K-feldspar are sub-euhedral. Some grain boundaries between plagioclase and K-feldspar are lobed, and K-feldspar can be found as relics within plagioclase suggesting that K-feldspar is locally replaced by plagioclase (**Fig. 24e** and **f**). Muscovite or feldspars host accessory minerals such as apatite (**Fig. 24a, b,** and **f**).

Pegmatitic dykes (~few cm to several m thick) generally spatially associated with aplites crosscut the fabrics of the leucogranite (**Fig. 23a-d**). The samples of pegmatite and aplite contain a Qz-Kfs-Pl-Msc assemblage with a variable amount of apatite, Fe-oxide, zircon, tourmaline or garnet (**Fig. 24a-g)**. These samples lack biotite. Two deformed pegmatite (Vi 20-21, Vi20-22) and one aplite (Vi 20-7) samples were analyzed for Rb-Sr dating in this study. Pegmatite is composed of coarse-grained minerals including quartz, K-feldspar, plagioclase, muscovite (**Fig. 24j** and **k**). Muscovite is commonly coarse (>1 mm) and locally have a fish-like habit. Fine muscovite grains (<0.5 mm) interpreted as secondary phases appear within shear planes (**Fig. 24l**). Two pegmatite samples contain small grains of apatite (≤0.5 mm) and small garnet grains occur in pegmatite sample Vi 20-22. Sample Vi 20-7 displays aplitic texture, contains fine muscovite flakes (<1.5 mm), plagioclase, K-feldspar, apatite, tourmaline and garnet (**Fig. 24h** and **i**). Tourmaline is generally more than 0.5 mm long and displays dark green brownish color (**Fig. 24i**). As observed in the granite samples, remnants of plagioclase are observed within K-feldspar grains, suggesting that K-feldspar has been replaced by plagioclase, potentially reflecting sodic metasomatism (i.e., albitization) (**Fig. 24h**).

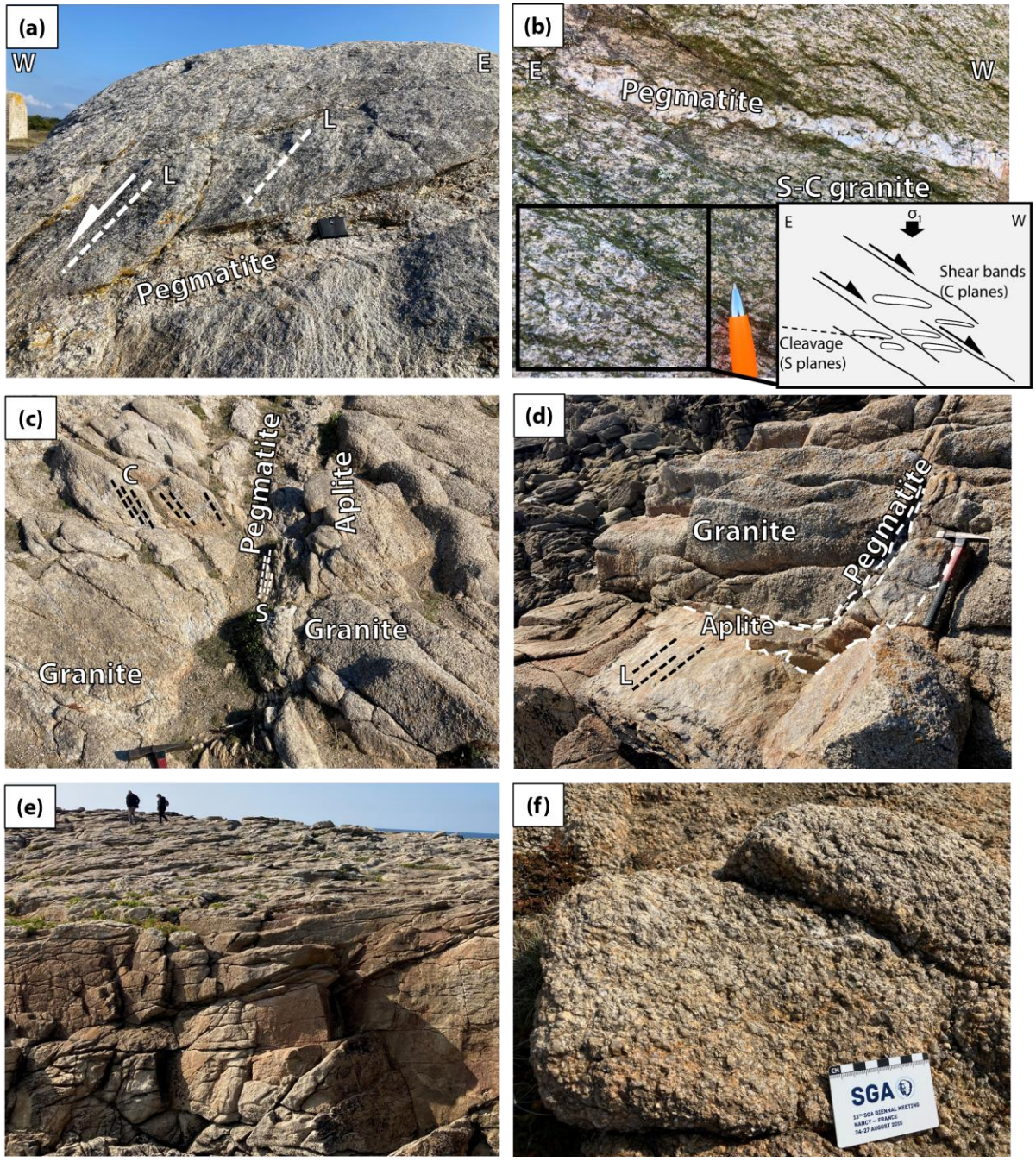

Fig. 23. Representative pictures of rock types from the Vivier outcrop. **(a, b)** S-C leucogranite within the Quiberon detachment shear zone with **(a)** stretching lineations (L) or **(b)** S-C planes, crosscut by pegmatite dykes. **(b)** S-C Quiberon leucogranite (plan view parallel to stretching lineation). Shear bands (C plane) and foliation planes (S plane) indicating top to the west normal shearing are shown. **(c, d)** Variably deformed pegmatitic and aplitic dykes crosscutting the Quiberon leucogranite. Dotted black and white lines in **(c)** indicate structural features observed in deformed granite and pegmatite. **(e, f)** Weakly deformed leucogranites.

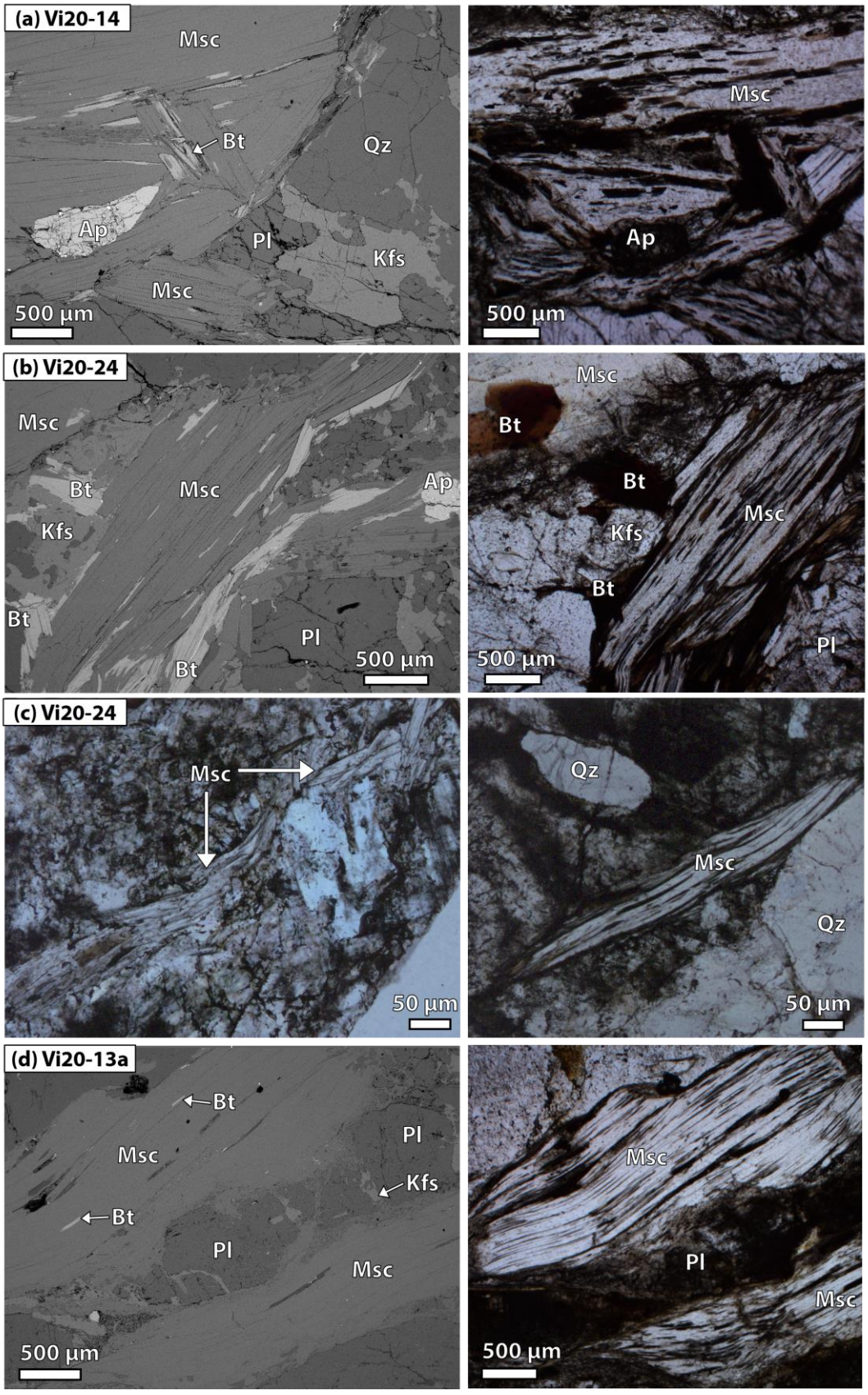
(a) Vi20-14
Msc
Bt
Qz
Ap
Pl
Kfs
Msc
500 µm
Msc
Ap
500 µm
(b) Vi20-24
Msc
Bt
Msc
Ap
Kfs
Bt
Pl
Bt
500 µm
Msc
Bt
Bt
Msc
Kfs
Bt
Pl
500 µm
(c) Vi20-24
Msc
50 µm
Qz
Msc
Qz
50 µm
(d) Vi20-13a
Bt
Pl
Msc
Kfs
Bt
Pl
Msc
500 µm
Msc
Pl
Msc
500 µm

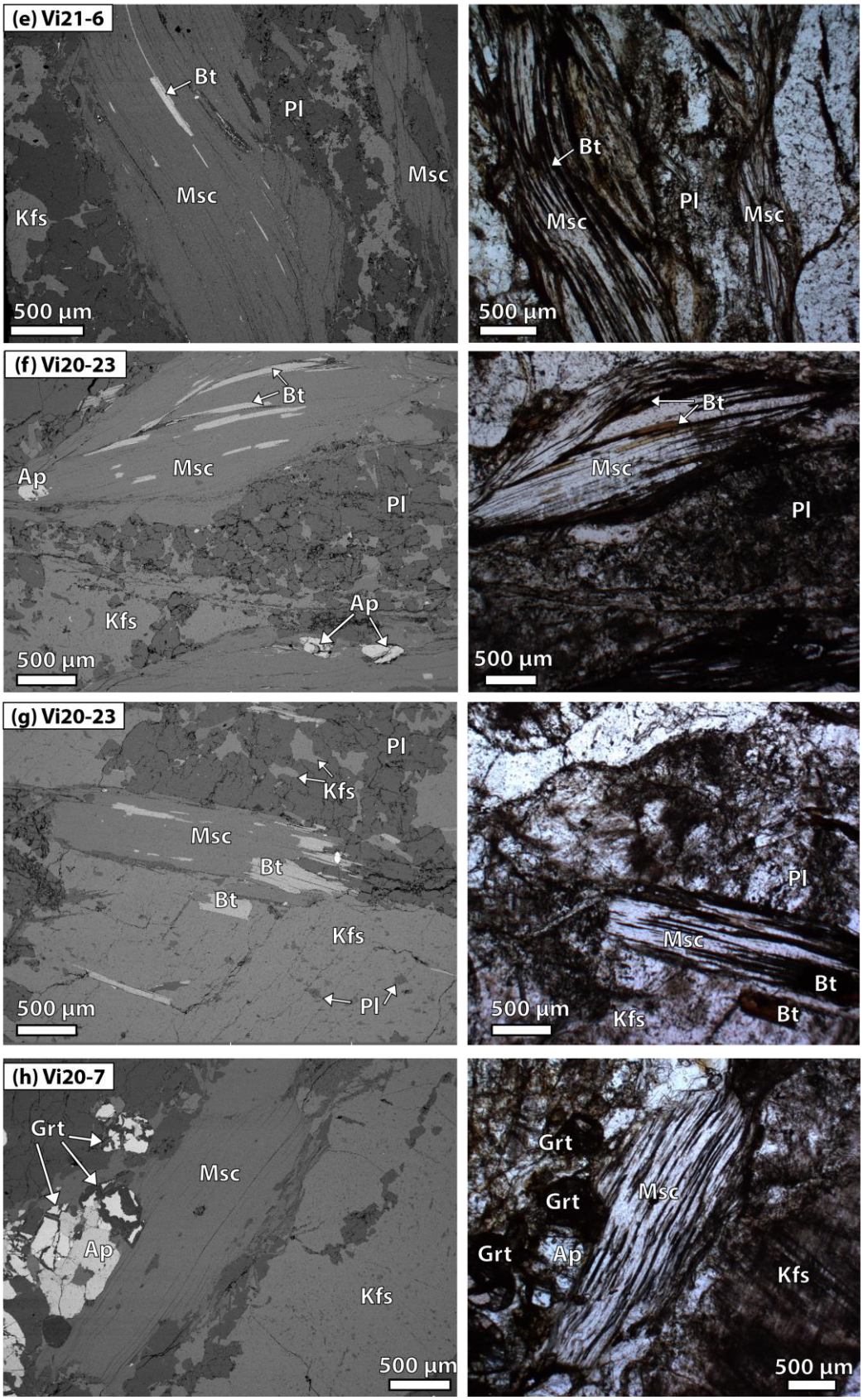
(e) Vi21-6
Bt
Pl
Msc
Msc
Kfs
500 µm
Bt
Pl
Msc
Msc
500 µm
(f) Vi20-23
Bt
Ap
Msc
Pl
Ap
Kfs
500 µm
Bt
Msc
Pl
500 µm
(g) Vi20-23
Pl
Kfs
Msc
Bt
Bt
Kfs
Pl
500 µm
Pl
Msc
Bt
500 µm
Kfs
Bt
(h) Vi20-7
Grt
Msc
Ap
Kfs
500 µm
Grt
Grt
Msc
Grt
Ap
Kfs
500 µm

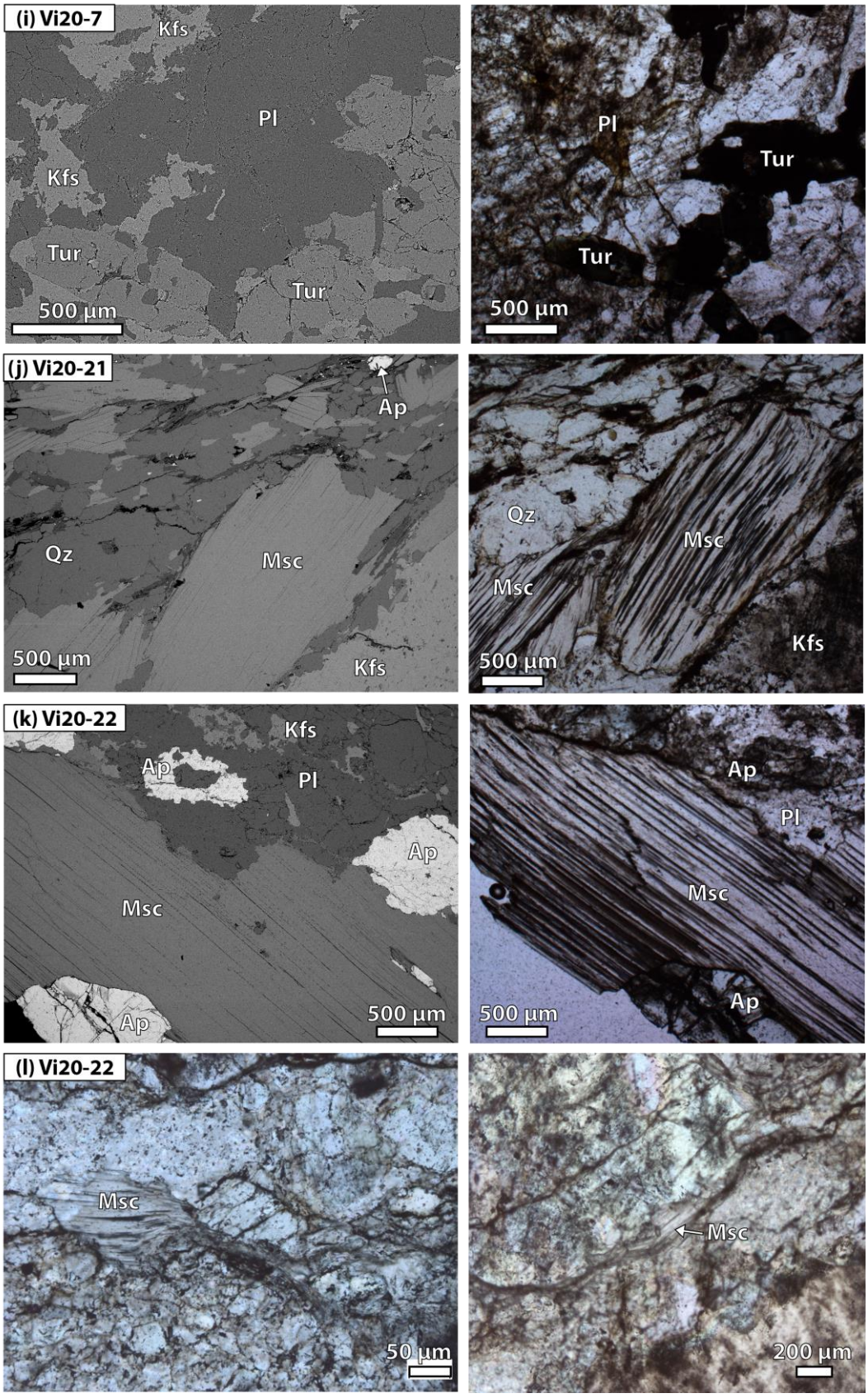
(i) Vi20-7
Kfs
Pl
Kfs
Tur
Tur
500 µm
Pl
Tur
Tur
500 µm
(j) Vi20-21
Ap
Qz
Msc
500 µm
Kfs
Qz
Msc
Msc
500 µm
Kfs
(k) Vi20-22
Kfs
Ap
Pl
Ap
Msc
Ap
500 µm
Ap
Pl
Msc
500 µm
Ap
(l) Vi20-22
Msc
50 µm
Msc
200 µm

◄

Fig. 24. Selected photomicrographs and backscattered electron (BSE) images of analyzed Rb-Sr phases (muscovite, biotite, apatite, K-feldspar, plagioclase and tourmaline) in **(a, b, c)** weakly deformed granite, **(d, e, f, g)** deformed granite, **(h, i)** aplite and **(j, k, l)** pegmatite. Msc: muscovite, Kfs: K-feldspar, Pl: plagioclase, Bt: biotite, Tur: tourmaline, Ap: apatite, Grt: garnet, Qz: quartz.

3.3. Choice of the minerals for in-situ Rb-Sr analysis at Nancy

The first mineral targeted for in-situ Rb-Sr analyses are the micas, with muscovite as first priority. Muscovite was selected as it is an ubiquitous mineral in the selected rocks; it offers large size crystals (up to several mm) on which several LA-ICP-MS spots can be targeted and have high Rb contents (304-2577 µg g^{-1}) which favor elevated Rb/Sr ratios (14.7-509) and therefore robust Rb-Sr isochrons (see **chapter 3**). The muscovites for the selected samples of the Vivier are present in different shapes and habitus, mainly dependent of the structural characteristics of the zone from which the samples were collected and of their conditions of crystallization (**Fig. 24**). When present, biotite was also analyzed as it also represents a Rb-rich phase (1076-2952 µg g^{-1}). Other mineral phases such as plagioclase, K-feldspar, apatite and tourmaline were also considered to consolidate Rb-Sr isochrons and related Rb-Sr ages. The objective was to provide the best $^{87}Sr/^{86}Sr$ initial ratio intercept (Y-axis) to favor the highest accuracy and precision as possible for Rb-Sr isochron calculations. In that respect, low-Rb phases such as apatite (≤0.6 µg g^{-1} Rb) and tourmaline (≤0.05 µg g^{-1} Rb) were prioritized. The list of minerals analyzed for each sample is indicated in **Table 15.**

Table 15. List of samples from the Vivier outcrop dated in this study. Rb-Sr phases indicate minerals analyzed for their Rb-Sr ratio. The abbreviations used in this table are as follows: Ap: apatite, Kfs: K-feldspar, Pl: plagioclase, Msc: Muscovite, Bt: Biotite, Tur: Tourmaline.

Sample	Rock type	Description	Rb-Sr phases
Vi 20-13a	Granite	deformed	Ap, Kfs, Pl, Msc, Bt
Vi 20-14	Granite	weakly deformed	Ap, Kfs, Pl, Msc, Bt
Vi 20-7	Aplite		Ap, Tur, Kfs, Pl, Msc
Vi 21-6	Granite	deformed (top-east)	Ap, Kfs, Pl, Msc, Bt
Vi 20-21	Pegmatite	deformed	Ap, Kfs, Pl, Msc
Vi 20-22	Pegmatite	deformed	Ap, Kfs, Pl, Msc
Vi 20-23	Granite (enclave)	deformed	Ap, Kfs, Pl, Msc, Bt
Vi 20-24	Granite	weakly deformed	Ap, Kfs, Pl, Msc, Bt

3.4. LA-ICP-MS/MS analytical conditions and choice of the data correction scheme for Rb-Sr isotopic analysis

Analytical conditions chosen for the analysis of the samples from the Vivier were similar to those presented in **chapter 3** of the present PhD thesis manuscript. A sum-up of conditions is presented in **Table 16**. In addition to selected minerals from the samples of Vivier outcropping zone, several reference materials (RM) were analyzed (Synthetic silicate glasses of NIST 610, and NIST 612, basalt glasses of BCR-2G and BHVO-2G, mineral powder pressed pellets of Mica-Mg and FK-N) as well as control materials in the form of mineral grains (La Posta biotite, FK-N potassium feldspar). The objective was to give the possibility to apply the analytical and data treatment schemes as defined in **chapter 3**, to obtain the best accuracy and precision for Rb-Sr isochron ages. A QAQC work was done to define which type of reference material would provide the best results considering the chemical composition of the dated minerals. NIST 610 was chosen as primary RM for calibration of $^{87}Sr/^{86}Sr$ ratios for all types of mineral phases as done in **chapter 3**. To calibrate $^{87}Rb/^{86}Sr$ ratios of muscovite and biotite, Mica-Mg in the form of powder pressed pellet is the currently best reference material which is available to calibrate micas as discussed in **chapter 3** and previous LA-ICP-MS/MS studies (Redaa et al., 2021, Rösel & Zack, 2022). $^{87}Rb/^{86}Sr$ ratios of plagioclase and K-feldspars were calibrated using powder pressed tablet of FK-N. Concerning apatite and tourmaline, with lower

Rb/Sr ratios compared to micas, NIST 610 were chosen as RM for calibration of both $^{87}Rb/^{86}Sr$ and $^{87}Sr/^{86}Sr$ ratios. In **section 4.4**, the calibration approach using matrix-matched and matrix-mismatched RMs and the correction factor (CF) were used following the methods and uncertainty propagation as described in **chapter 3**.

Table 16. LA-ICP-MS/MS parameters.

Laser ablation system		
Model		ESI NWR 193
Ablation cell		Two Volume ablation chamber (TwoVol1)
Laser wavelength	nm	193
Fluence	J cm^{-2}	ca. 6
Repetition rate	Hz	5
Ablation duration	s	50
background and washout	s	30-45
Spot diameter	µm	50
Sampling mode/pattern		Static spot ablation
Carrier gas		He
Cell carrier gas flow	ml min^{-1}	650
N_2 addition	ml min^{-1}	4
ICP-MS Instrument		
Model		Agilent 8900
Scan type		MS/MS
Sample introduction		Wire smoothing device
RF power	W	1550
Sample depth	mm	4
Ar carrier gas flow	L min^{-1}	0.64
N_2O gas flow rate	mL min^{-1}	ca. 0.20
Q1 → Q2 masses	amu	85 → 85 86 → 102 87 → 103 88 → 104
Energy discrimitation	V	-7
Wait time offset	s	2
Dwell times	ms	120 (except 85: 50 ms)
Dead time	ns	35
Typical oxide rate (^{248}ThO / ^{232}Th)	%	ca. 0.2
$^{232}Th/^{238}U$	%	ca. 99
Sensitivity of ^{85}Rb	Cps/ppm	2887-3709
Sensitivity of $^{88}Sr^{16}O$	Cps/ppm	3664-4671

3.5. Quality validation: La Posta biotite-feldspar and FK-N feldspar grains

To validate the quality of the analytical sessions (i.e., accuracy and precision of the analyses), two control materials with two different matrices were used: La Posta biotite-feldspar (LP) and FK-N feldspar grains. The objective was evaluating potential bias induce by the analytical conditions and scheme chosen. These two control materials were routinely analyzed during five analytical sessions done on samples from the Quiberon peninsula. The ages calculated for each of these 5 sessions are presented in **Fig. 25**.

The mean Rb-Sr ages and errors measured for LP and FK-N for all of these 5 sessions are identical within error to the reference values. It can be therefore considered that no bias affected these five analytical sessions, and these results validate the analytical conditions and calibration strategy applied, and related ages obtained for the samples from the Vivier.

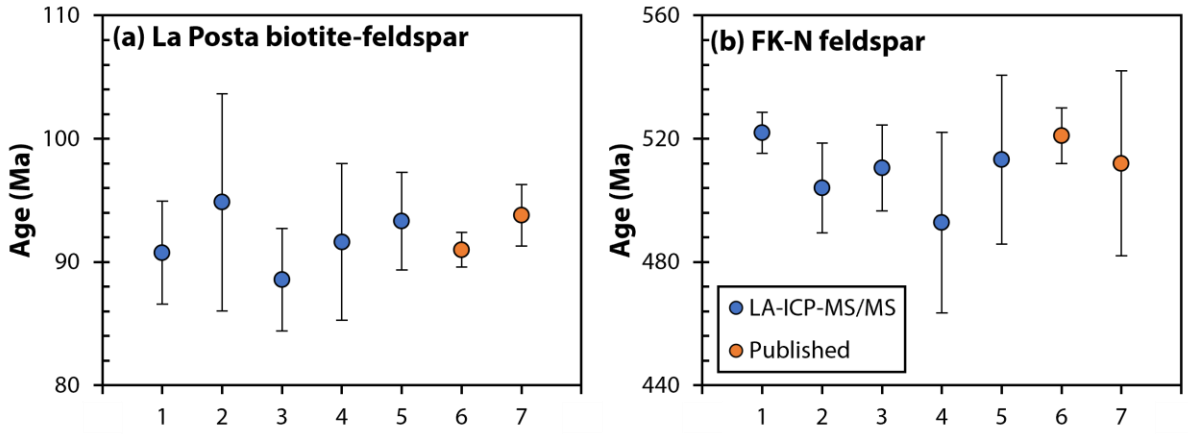

Fig. 25. Rb-Sr isochrone ages calculated for control materials La Posta biotite-feldspar and FK-N feldspar during each of the five analytical sessions (number 1 to 5) done for the samples of the Vivier outcropping zone. Two published ages are indicated for (a) La Posta as 6 and 7 are from Grove et al. (2003) and Walawender et al. (1990), respectively, and (b) FK-N feldspar as 6 and 7 are from Pandey et al. (1993) and Jegal et al. (2022), respectively. The calculated Rb-Sr ages are identical within error of the published ages.

4. Results on samples from the Vivier (Quiberon peninsula)

4.1. Preliminary study of the selected minerals before LA-ICP-QQQ-MS analyses

After an initial petrographic study of thick sections (150-200 µm) using optical microscope, targeted mineral Rb-Sr phases as indicated in **Table 15** (micas, K-feldspars, plagioclase, apatite and tourmaline) were studied by SEM-EDS analysis to control their mineralogical and chemical homogeneities at sub-micrometer scales. Small secondary muscovites are commonly occurred within shear plans or as overgrowths on primary large muscovite flakes (**Fig. 24c, d, e** and **f**). The Rb-Sr compositions and isochron ages of the secondary muscovites do not show differences from primary muscovites, therefore, Rb-Sr data and isochron ages of secondary muscovites are included in the following Rb-Sr data with primary muscovites.

The Rb and Sr contents were quantified during LA-ICP-MS/MS analyses. The muscovite has Sr and Rb concentrations of 2.2-37.9 µg g^{-1} and 304-2577 µg g^{-1}, respectively. The Sr and Rb concentrations of biotite are 2.6-29.6 µg g^{-1} and 1076-2952 µg g^{-1}, respectively. Muscovites for the different types of samples have the following ranges of Sr and Rb concentrations, respectively: 5.6-24.6 µg g^{-1} and 449-2174 µg g^{-1} for weakly deformed granite (Vi 20-14, Vi 20-24), 5.3-37.9 µg g^{-1} and 445-1599 µg g^{-1} for deformed granite (Vi 20-13a, Vi 21-6, Vi 20-23), 2.2-9.0 µg g^{-1} and 304-1977 µg g^{-1} for aplite (Vi 20-7), and 3.9-21.6 µg g^{-1} and 1316-2577 µg g^{-1} for pegmatite (Vi 20-21, 20-22). Biotites for the different types of samples display the following ranges of Sr and Rb concentrations, respectively: 2.7-6.1 µg g^{-1} and 1076-2314 µg g^{-1} for undeformed granite (Vi 20-14, Vi 20-24), 3.5-29.6 µg g^{-1} and 1405-2952 µg g^{-1} for deformed granite (Vi 20-14, Vi 21-6, Vi 20-23).

4.2. Comparison between single mineral Rb-Sr isochrons and multi-mineral Rb-Sr isochrons

The Rb-Sr isochrone ages were calculated following two approaches: i) use of muscovite only and ii) use of micas (muscovite + biotite when present) and Rb-poor minerals (apatite, tourmaline). The two ages calculated for each sample are presented in **Fig. 26** and **Table 17**.

The Rb-Sr isochrone ages calculated for each sample following the two approaches are

identical within error for all samples. $^{87}Sr/^{86}Sr$ initial ratios are also identical. The precision is increased by a minimum factor 2 when coupling low-Rb phases to micas due to a gain in precision on the calculation of the $^{87}Sr/^{86}Sr$ initial ratios (**Table 17**). The precision reached for the Rb/Sr isochron ages is comprised between 2.3% to 4.0% (including excess variance and published uncertainties of primary RMs, see **chapter 3**) for muscovite Rb-Sr isochrone ages and between 1.3% to 1.6% (including excess variance and published uncertainties of primary RMs, see **chapter 3**) for multi-mineral Rb-Sr isochron ages. Considering the difference, it is therefore proposed to use multi-phase Rb-Sr isochron ages and only these ages will be considered in the next parts of this chapter.

Table 17. Rb-Sr ages (Ma) obtained on muscovite only and multiple phases (i.e., muscovite, biotite, apatite and tourmaline). U-Pb ages (Ma) of apatite are shown for comparison.

Sample	Rock type	Description	Apatite		multiple Rb-Sr phases					Muscovite only				
			U-Pb	2s	Rb-Sr	2s	$^{87}Sr/^{86}Sr_i$	2s	n	Rb-Sr	2s	$^{87}Sr/^{86}Sr_i$	2s	n
Vi 20-13a	Granite	deformed	316.3	5.1	288.3	3.8	0.7215	0.0021	50	290.8	6.8	0.713	0.016	31
Vi 20-14	Granite	weakly deformed	315.5	3.8	283.2	4.4	0.7219	0.0023	48	282.6	8.7	0.725	0.018	24
Vi 20-7	Aplite		302.6	10.6	293.0	4.1	0.7216	0.0025	50	300	12	0.630	0.13	28
Vi 21-6	Granite	deformed (top-east)	299.1	4.0	295.5	4.6	0.7221	0.0025	44	296.9	8.6	0.719	0.017	30
Vi 20-21	Pegmatite	deformed	288.8	8.5	300.6	3.8	0.7246	0.0036	48	301.4	6.5	0.695	0.08	36
Vi 20-22	Pegmatite	deformed			289.3	3.8	0.7177	0.0024	49	291.9	11.3	0.620	0.23	31
Vi 20-23	Granite	deformed	292.1	2.5	286.8	3.9	0.7236	0.0033	51	294.0	7.5	0.725	0.013	24
Vi 20-24	Granite	weakly deformed	291.1	3.8	281.2	3.8	0.7208	0.0025	52	284.0	9	0.720	0.024	29

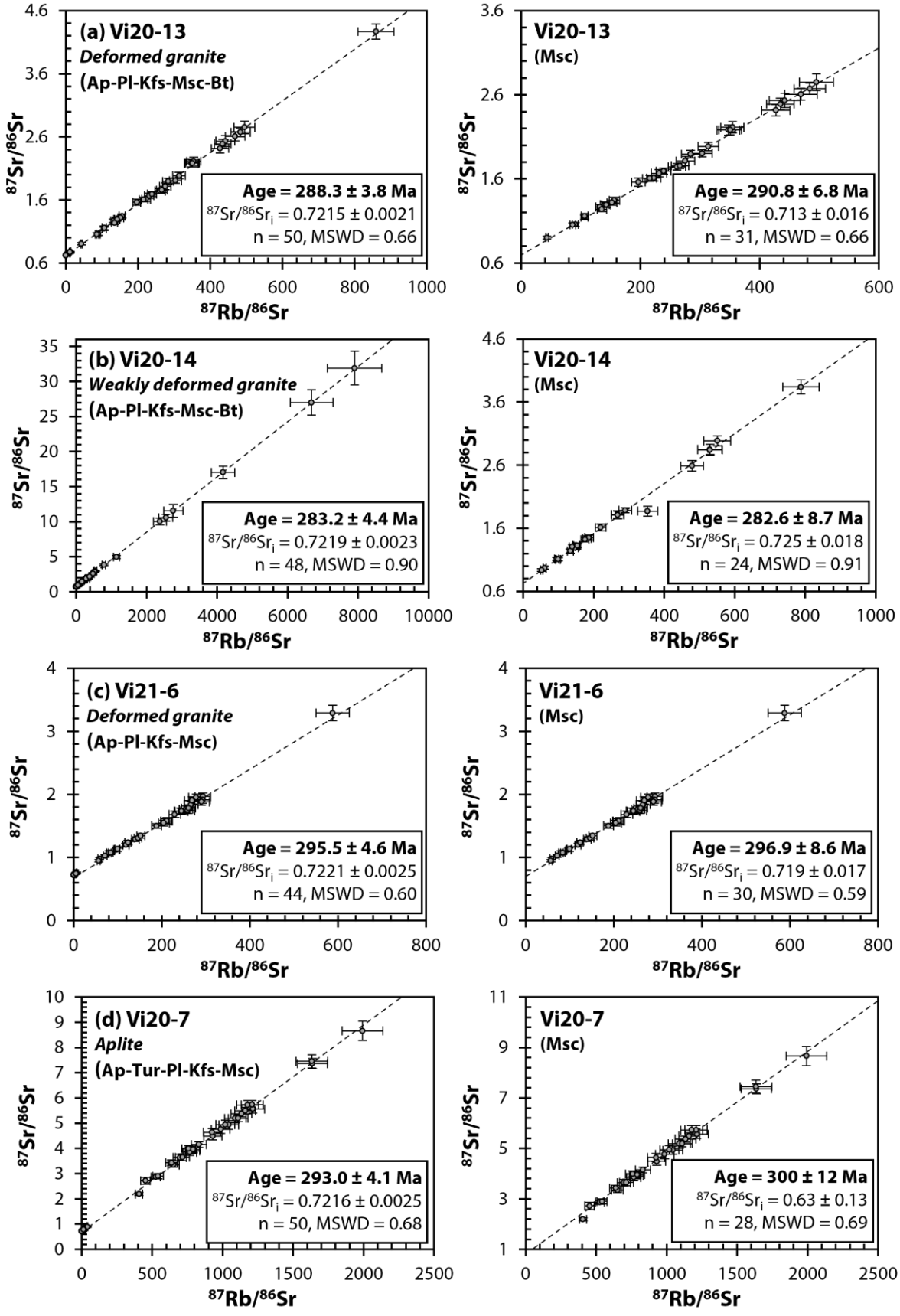
(a) Vi20-13
Deformed granite
(Ap-Pl-Kfs-Msc-Bt)
Age = 288.3 ± 3.8 Ma
87Sr/86Sri = 0.7215 ± 0.0021
n = 50, MSWD = 0.66
Vi20-13
(Msc)
Age = 290.8 ± 6.8 Ma
87Sr/86Sri = 0.713 ± 0.016
n = 31, MSWD = 0.66
(b) Vi20-14
Weakly deformed granite
(Ap-Pl-Kfs-Msc-Bt)
Age = 283.2 ± 4.4 Ma
87Sr/86Sri = 0.7219 ± 0.0023
n = 48, MSWD = 0.90
Vi20-14
(Msc)
Age = 282.6 ± 8.7 Ma
87Sr/86Sri = 0.725 ± 0.018
n = 24, MSWD = 0.91
(c) Vi21-6
Deformed granite
(Ap-Pl-Kfs-Msc)
Age = 295.5 ± 4.6 Ma
87Sr/86Sri = 0.7221 ± 0.0025
n = 44, MSWD = 0.60
Vi21-6
(Msc)
Age = 296.9 ± 8.6 Ma
87Sr/86Sri = 0.719 ± 0.017
n = 30, MSWD = 0.59
(d) Vi20-7
Aplite
(Ap-Tur-Pl-Kfs-Msc)
Age = 293.0 ± 4.1 Ma
87Sr/86Sri = 0.7216 ± 0.0025
n = 50, MSWD = 0.68
Vi20-7
(Msc)
Age = 300 ± 12 Ma
87Sr/86Sri = 0.63 ± 0.13
n = 28, MSWD = 0.69
87Sr/86Sr
87Rb/86Sr

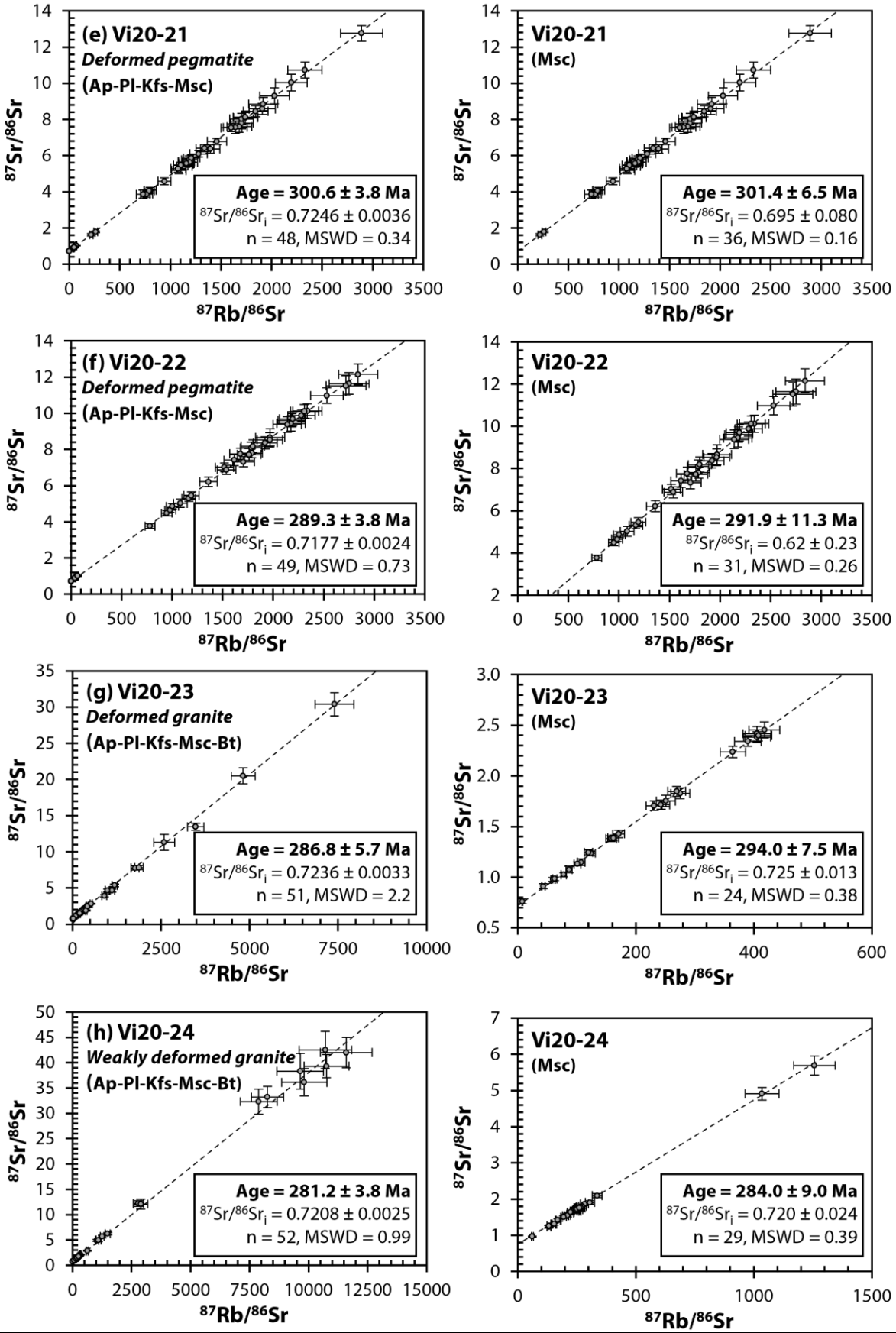
(e) Vi20-21
Deformed pegmatite
(Ap-Pl-Kfs-Msc)
Age = 300.6 ± 3.8 Ma
87Sr/86Sri = 0.7246 ± 0.0036
n = 48, MSWD = 0.34
Vi20-21
(Msc)
Age = 301.4 ± 6.5 Ma
87Sr/86Sri = 0.695 ± 0.080
n = 36, MSWD = 0.16
(f) Vi20-22
Deformed pegmatite
(Ap-Pl-Kfs-Msc)
Age = 289.3 ± 3.8 Ma
87Sr/86Sri = 0.7177 ± 0.0024
n = 49, MSWD = 0.73
Vi20-22
(Msc)
Age = 291.9 ± 11.3 Ma
87Sr/86Sri = 0.62 ± 0.23
n = 31, MSWD = 0.26
(g) Vi20-23
Deformed granite
(Ap-Pl-Kfs-Msc-Bt)
Age = 286.8 ± 5.7 Ma
87Sr/86Sri = 0.7236 ± 0.0033
n = 51, MSWD = 2.2
Vi20-23
(Msc)
Age = 294.0 ± 7.5 Ma
87Sr/86Sri = 0.725 ± 0.013
n = 24, MSWD = 0.38
(h) Vi20-24
Weakly deformed granite
(Ap-Pl-Kfs-Msc-Bt)
Age = 281.2 ± 3.8 Ma
87Sr/86Sri = 0.7208 ± 0.0025
n = 52, MSWD = 0.99
Vi20-24
(Msc)
Age = 284.0 ± 9.0 Ma
87Sr/86Sri = 0.720 ± 0.024
n = 29, MSWD = 0.39
87Sr/86Sr
87Rb/86Sr

◄

Fig. 26. Rb-Sr isochron of multiple phases (on the left) and single phase (muscovite, on the right) for individual samples **(a)** Vi 20-13 (deformed granite) **(b)** Vi 20-14 (weakly deformed granite) **(c)** Vi 21-6 (deformed granite) **(d)** Vi 20-7 (aplite) **(e)** Vi 20-21 (pegmatite) **(f)** Vi 20-22 (pegmatite) **(g)** Vi 20-23 (deformed granite) and **(h)** Vi 20-24 (weakly deformed granite). Error bars are total uncertainties including internal errors, session-based excess variance and uncertainties of primary RMs.

4.3. Rb-Sr ages

The Rb-Sr isochrone ages calculated for all selected samples of the Vivier spread between 300.6 ± 3.8 Ma (Vi 20-21, pegmatite) and 281.2 ± 3.8 Ma (Vi 20-24, granite). There is no apparent difference in terms of Rb-Sr isochrone ages between weakly deformed and deformed granites. Rb-Sr ages for weakly deformed (Vi 20-14, Vi 20-24) or deformed granites (Vi 20-13a, Vi 21-6, Vi 20-23) are significantly younger than the U-Pb ages measured on zircon (315 ± 5 Ma) and monazite (318 ± 3 Ma) for the Quiberon leucogranite, and interpreted as its age of emplacement (Dusséaux et al., 2022). Rb-Sr ages are similar or younger than published apatite U-Pb ages for the Quiberon leucogranite (313 ± 3 Ma for weakly deformed facies and 303 ± 4 Ma for deformed facies, Dusséaux et al., 2022). The oldest Rb-Sr isochrone age is obtained for an ultramylonitic pegmatite (Vi 20-21) which crosscuts the granite and therefore structurally post-date it. Compared to U-Pb ages measured on apatite on the same samples, the Rb-Sr isochrons are identical within error for the samples Vi 20-7 aplite, Vi 21-6 deformed granite and Vi 20-23 deformed granite and younger for the samples Vi 20-13a deformed granite, Vi 20-14 weakly deformed granite, Vi 20-24 weakly deformed granite (**Table 17** and **Fig. 27**). The errors calculated for the isochrone Rb-Sr age are generally smaller than those calculated for U-Pb dating on apatite from the same sample set: 1.3% to 1.6% for the Rb-Sr ages compared to 0.9-3.5% for the U-Pb apatite ages (**Table 17** and **Fig. 27**).

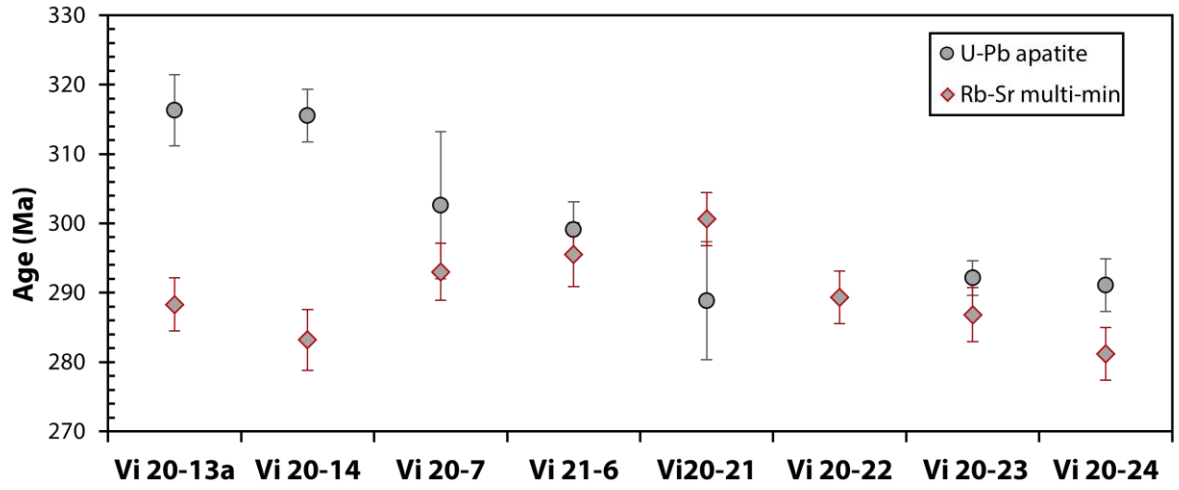

Fig. 27. Comparison between Rb-Sr ages measured on a set of minerals (micas/apatite/tourmaline/K-feldspar/plagioclase) and U-Pb apatite ages measured on apatite for seven samples from the Vivier outcrop. The sample Vi 20-22 was not dated by U-Pb on apatite.

4.4. Applications of correction factor (CF) for in-situ Rb/Sr geochronology of Quiberon sample by LA-ICP-MS/MS

In this section, matrix effects related to major element compositions and application of correction factor to the measured $^{87}Rb/^{86}Sr_{N610}$ ratios were examined by using the suggested approach in **chapter 3**. **Fig. 28a** and **28b** display the linear regressions through the data on plots of $^{87}Rb/^{86}Sr_N$ versus SiO_2 and Al_2O_3 of the RMs, respectively. The uncertainties of $^{87}Rb/^{86}Sr_N$ ratios to produce linear regressions include the U_3 and long-term excess variance of primary RMs (ε_2) calculated using all individual data from five analytical sessions for each RM conducted during the analysis of Quiberon samples, as described in **chapter 3**. The following long-term excess variance of each RM was determined by calculating a weighted mean from the repeated analyses of the RMs among all five measurement sessions using Isoplot (v. 4.14, Ludwig 2012) displayed as 'External 2s err req'd (each point)' term for $^{87}Rb/^{86}Sr$: 1.09% for NIST 610 (n = 112), 5.35% for BCR-2G (n = 111), 4.76% for BHVO-2G (n = 61), 3.84% for Mica-Mg-P (n = 110) and 5.58% for FK-N-P (n = 111). Rb-Sr isochron ages from the LA-ICP-MS/MS measurements in this study are calculated using a maximum likelihood regression of York (2004) available in the IsoplotR (v. 5.0, Vermeesch 2018) and Rb-Sr decay constant of

$1.3972 \pm 0.0045 \times 10^{-11}$ a^{-1} (Villa et al., 2015). Ages are reported as 95% confidence limits.

The linear relations in this chapter are shown by same trends from the results in **chapter 3** as $^{87}Rb/^{86}Sr_N$ has linear anti-correlation with SiO_2 and linear correlation with Al_2O_3. Following the suggested procedure in c**hapter 3**, $^{87}Rb/^{86}Sr$ ratios of La Posta sample as a secondary standard were calibrated using non-matrix matched RM (NIST 610, indicated as $^{87}Rb/^{86}Sr_{N610}$), matrix-matched RM (Mica-Mg-P for mica, FK-N for feldspar), and $^{87}Rb/^{86}Sr_{N610}$ ratios were corrected using the CF derived from the linear regressions of Al_2O_3 (CF_{Al2O3}) and SiO_2 (CF_{SiO2}) (**Fig. 28c**). All $^{87}Sr/^{86}Sr$ ratios were calibrated using NIST 610. The results show that Rb-Sr isochron ages of LP biotite and feldspar by different calibration/correction methods range from 89.3 ± 3.4 Ma (NIST 610) to 96.8 ± 3.7 Ma (CF_{SiO2}). These ages are within the uncertainties of the reported ages by Zack & Hogmalm (2016) and Walawender et al. (1990). The precision of ages is enhanced from 4.2% by Mica-Mg-P/FK-N-P to 3.8% by CF_{Al2O3}. Rb-Sr ages of Quiberon sample Vi 20-24 (weakly deformed granite, muscovite-apatite) using non-matrix matched RM (NIST 610), matrix-matched RM (Mica-Mg-P for mica, NIST 610 for apatite), CF_{Al2O3} and CF_{SiO2} range from 276.0 ± 2.9 Ma (NIST 610) to 316.4 ± 3.5 Ma (CF_{Al2O3}) (**Fig. 28d**). The Rb-Sr ages by Mica-Mg-P/NIST 610 and CF_{SiO2} are in good agreement with the Rb-Sr ages of all Rb-Sr phases (Ap-Pl-Kfs-Msc-Bt) and muscovite in **Fig. 26**. Better precision of 1.1 % is obtained by CF_{SiO2} than that by Mica-Mg-P/NIST 610. These results show that the Rb-Sr ages using NIST 610 underestimate the ages for La Posta and Quiberon Vi 20-24 samples as observed in **chapter 3**. In addition, the correction factors derived from the linear regression of $^{87}Rb/^{86}Sr_N$ vs SiO_2 and/or Al_2O_3 produced in different analytical conditions (different analytical period) can result in more precise Rb-Sr age results as suggested in **chapter 3**.

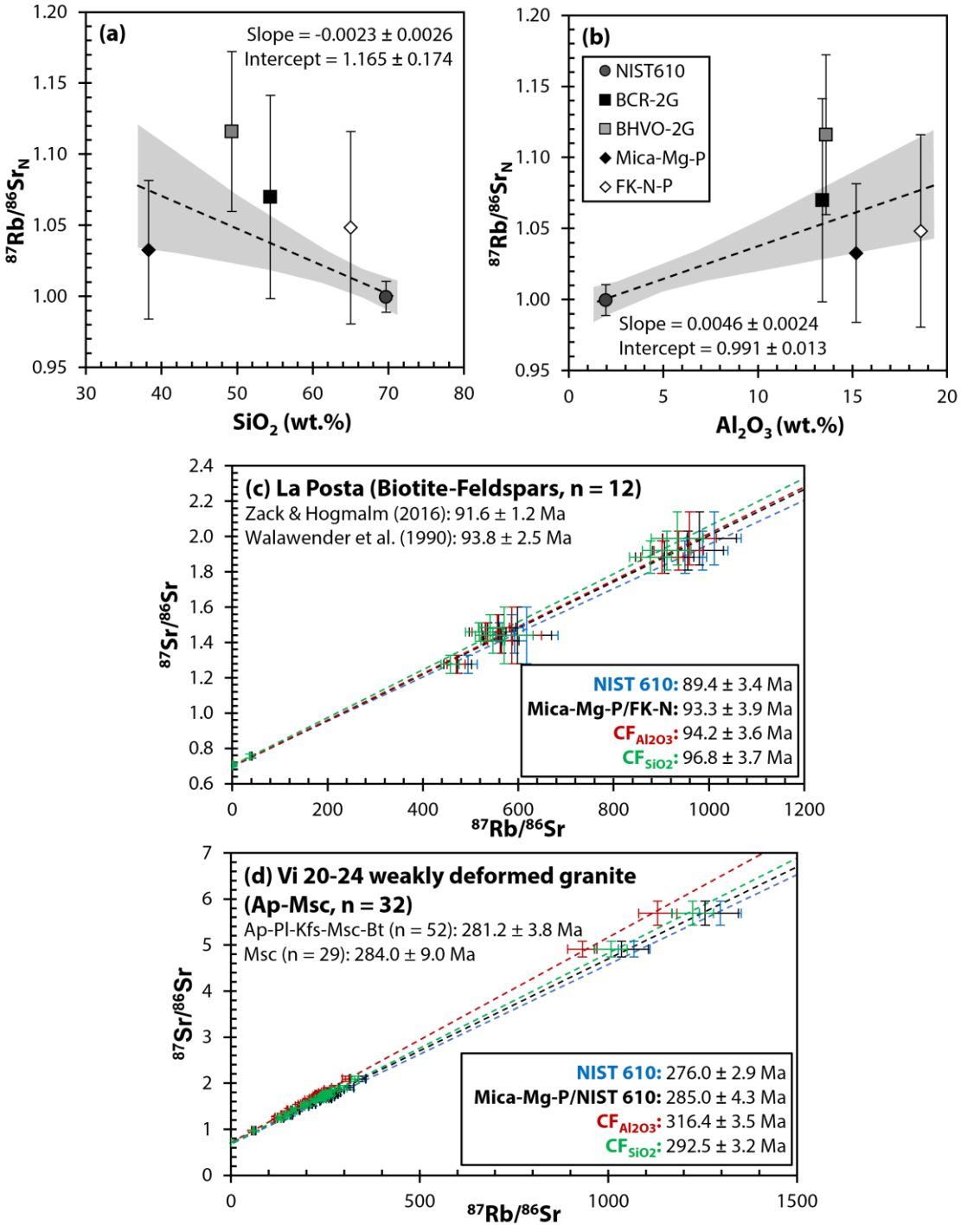

Fig. 28. (a, b) Measured $^{87}Rb/^{86}Sr_N$ (measured/published) ratios calibrated using NIST 610 for the RMs as a function of SiO_2 and Al_2O_3 contents of the RMs. **(c, d)** Rb-Sr isochrons for La Posta and Vi 20-24 samples by using different RMs and CF. Error bars in (c, d) are total uncertainties as described in **Fig. 10** of **chapter 3**.

5. Discussion

5.1. Validity and quality control of in-situ Rb-Sr ages

The Rb-Sr isochrone ages calculated for the two control materials (CM) La Posta biotite-feldspar and FK-N feldspar grains are identical within error to the two reference ages proposed for the two CM (**Fig. 25**). This result obtained for two different matrices (feldspar and mica) and two different chemical compositions firstly indicate that the analytical conditions and data treatment protocol used for the five analytical sessions dedicated to samples from the Vivier are suitable and that no systematic bias affected the quality of the data and the related calculated Rb-Sr isotopic ratios. The relative similar chemical compositions between La Posta biotite and the micas analyzed in the samples from the Vivier such as SiO_2 and FeO contents of Quiberon biotite (ca. 35 wt. % and 21 wt. % in Quiberon biotite vs 36 wt.% and 21 wt.% in La Posta biotite for SiO_2 and FeO, respectively) moreover allow excluding a specific bias by matrix effect when using Mica-Mg to calibrate the Rb/Sr ratios of micas analyzed in the samples from the Vivier. Such assumption is also validated by the fact that isochrone Rb-Sr ages using muscovite-only or multi-mineral (association of muscovite, biotite, apatite, K-feldspar, plagioclase and/or tourmaline depending on the sample) are identical within errors (**Fig. 26** and **Table 17**). It can be therefore considered that the Rb-Sr ages are analytically correct.

5.2. Comparison between Rb-Sr isochrone ages and U-Pb ages on apatites from the Vivier sample set

Seven samples from the Vivier outcrop were dated using two methods, applied on two sets of minerals: U-Pb on apatite and Rb-Sr on micas, apatite and/or tourmaline. First, the precision for the Rb-Sr isochrone ages is identical to better than the one calculated for U-Pb on apatite (**Table 17** and **Fig. 27**). This result demonstrates that the application of in-situ Rb-Sr approach is applicable and reliable compared to other isotopic systems used to date geological processes and applied at in-situ scale. The ages calculated for the two methods are identical within error for some samples (Vi 20-7, Vi 21-6 and Vi 20-23) or different for other samples (Vi 20-13a, Vi 20-14, Vi 20-21 and Vi 20-24). The largest differences (ca. 10%) between U-Pb and Rb-Sr isotopic systems are obtained for samples Vi 20-13a (316.3 ± 5.1 Ma vs 288.3 ± 3.8 Ma,

respectively) and Vi 20-14 (315.5 ± 3.8 Ma vs 283.2 ± 4.4 Ma, respectively). These two samples are weakly deformed granites. The Rb-Sr and U-Pb ages are identical within error for one sample of aplite (Vi 20-7) and pegmatite (Vi 20-21), and for two deformed granites (Vi 20-6 and Vi 20-23). When different, the Rb-Sr ages are younger than U-Pb ages on apatite except for one sample of pegmatite (Vi 20-21). When present, the difference in age between the two isotopic systems is not linked to analytical issues affecting the Rb-Sr isotopic system, as explained above in the text, and is therefore due to geological reasons. Considering that apatite and micas are co-genetic (petrographic evidence; **Fig. 24**), the difference in ages for the two systems (U-Pb and Rb-Sr) and minerals (apatite vs micas-apatite-tourmaline) indicates that the two isotopic systems do not have the same stability towards post-crystallization events. Such difference is visible for the same matrix (apatite) but also between matrices (apatite, tourmaline, micas). The U-Pb isotopic system in apatite is more stable compared to Rb-Sr whatever mineral considered. The good value of the MSWD for Rb-Sr isochrons calculated using micas and apatite demonstrates that the Rb-Sr isotopic system was synchronously reset for both micas, apatite and tourmaline. The major age difference measured for example in weakly deformed granite (Vi 20-13a, Rb-Sr age: 288.3 ± 3.8 Ma and Vi 20-14, Rb-Sr age: 283.2 ± 4.4 Ma) confirms that the stability of U-Pb and Rb-Sr isotopic systems in apatite is not identical, as U-Pb age in apatite (Vi 20-13a, U-Pb age: 316.3 ± 5.1 Ma and Vi 20-14, U-Pb age: 315.5 ± 3.8 Ma) is identical within error to the U-Pb age measured on zircon and/or monazite (Dusséaux et al., 2022). The Rb-Sr isotopic system is therefore more sensitive to reset than the U-Pb system applied to zircon, monazite and apatite. The differences in age (considering the errors) between the two isotopic systems observed for several deformed granites at the Vivier outcrop moreover indicate the reset of the Rb-Sr and U-Pb isotopic systems were linked to different geological events active in the zone during the 300-270 Ma period. The question of the nature of these events will be discussed in the following parts of the manuscript, but it could be already proposed that the coupling of several in-situ isotopic systems, like U-Pb and Rb-Sr for example, provides a more precise understanding of geological zones affected by a polyphased magmatic-hydrothermal evolution.

5.3. Comparison between Rb-Sr isochron ages and other geochronological datasets from the Armorican Massif, and geological representativeness of Rb-Sr in such geological context

The Rb-Sr ages are distributed in a range comprised between 300.6 ± 3.8 Ma (Vi 20-21, pegmatite) and 281.2 ± 3.8 Ma (Vi 20-24, granite). This range is relatively young compared to known ages within the South Armorican Domain or along the South Armorican Shear Zone. The main magmatic event, linked to the emplacement of syn-tectonic leucogranites (Questembert, Lizio, Guérande, Quiberon, Pontivy), is indeed dated between 320 and 310 Ma (**Fig. 29**) (Tartèse et al., 2011a, 2011b; Ballouard et al., 2015, 2017a; Dusséaux et al., 2022). A second magmatic event, more discrete and associated to the intrusion of leucogranitic dykes in the Guérande area (Ballouard et al., 2015), as well as the emplacement of the Langonnet leucogranite body in the Pontivy-Rostrenen complex (Ballouard et al., 2017a), is dated at ca. 303-305 Ma. This event could be linked to a Sn-mineralizing stage dated at ca. 305 Ma at the apex of the Guérande granite (Ballouard, personal communication). The ca. 300 Ma of Rb-Sr isochron age measured for Vi 20-21 pegmatite could be considered as the least affected of all samples, and similar to crystallization age for leucogranite dykes in the South Armorican Domain (304-302 Ma). A late and discrete magmatic event at ca. 290 Ma is also considered in the Quiberon peninsula (P. Boulvais, personal communication) to explain the U-Pb age measured on apatite from sample Vi 20-21. Such assumption has to be confirmed by U-Pb dating on more resistant mineral like zircon as this age could also represent a reset age, as measured for deformed granites in the same location.

The Rb-Sr systems for the other samples (deformed and weakly deformed, pegmatite and granite) are reset with ages younger than proposed crystallization ages, but also younger than ages know for the main fluid-rock interaction stages recorded by ^{40}Ar-^{39}Ar in micas. ^{40}Ar-^{39}Ar ages on micas show a large spread of distribution between ca. 319 Ma to 300 Ma in syntectonic leucogranites (Le Hébel, 2002; Tartèse et al. 2011a, 2011b; Gapais et al., 2015; Dusséaux et al. 2022). Those ages are proposed as initially be associated to the emplacement of syntectonic leucogranites (320-310 Ma), followed by fluid-rock interaction stage dominated by meteoric water between 310 and 300 Ma (e.g., Dusséaux et al., 2022). No ^{40}Ar-^{39}Ar age younger than 300 Ma has been measured in the South Armorican Domain, indicating that Ar has not been

released from micas from that time. Argon was thus less likely to be released from micas than strontium in the geological conditions which affected the South Armorican Domain during the 300-270 Ma period. U-Pb ages measured on several apatites from the Vivier outcrop however indicate that the U-Pb isotopic system was locally reset at ca. 290 Ma. Lead was therefore mobile after argon. This ca. 290 Ma reset is considered to be related to a fluid event that marked the transition between ductile to brittle conditions in the studied zone. The 300-290 Ma period is also considered to probably mark the implication of salty water in the hydrologic regime within shear zones of the South Armorican Domain. The origin of this salty water, seen in fluid inclusions from quartz of uranium oxide-bearing veins from the Guérande district (Ballouard et al., 2017b), is still unknown. However, its implication has been proposed for the formation of the U deposits distributed along the SASZ (Pontivy, Mortagne) and detachments (Guérande) and genetically linked with the leaching of U from syntectonic leucogranites (Ballouard et al., 2017b, 2018). These U deposits formed during the 300-270 Ma period, which globally corresponds to the range of ages measured at the Vivier using Rb-Sr. Although no U mineralization is known in the vicinity of the Vivier outcrop nor in the Quiberon peninsula, U mineralization dated at 300-270 Ma are known within and around the Guérande leucogranite that emplaced in a similar extensional tectonic framework as the Quiberon leucogranite (Gapais et al., 2015; Ballouard et al., 2015). The Rb-Sr ages measured at the Vivier outcrop would therefore be the expression of this global event of circulation of salty water which affected the South Armorican Domain between 300 and 270 Ma, and whose fingerprints and scale is therefore larger than previously assumed. The application of in-situ Rb-Sr dating allows therefore to better constrain the timing and duration of fluid circulation processes in complex geological zones.

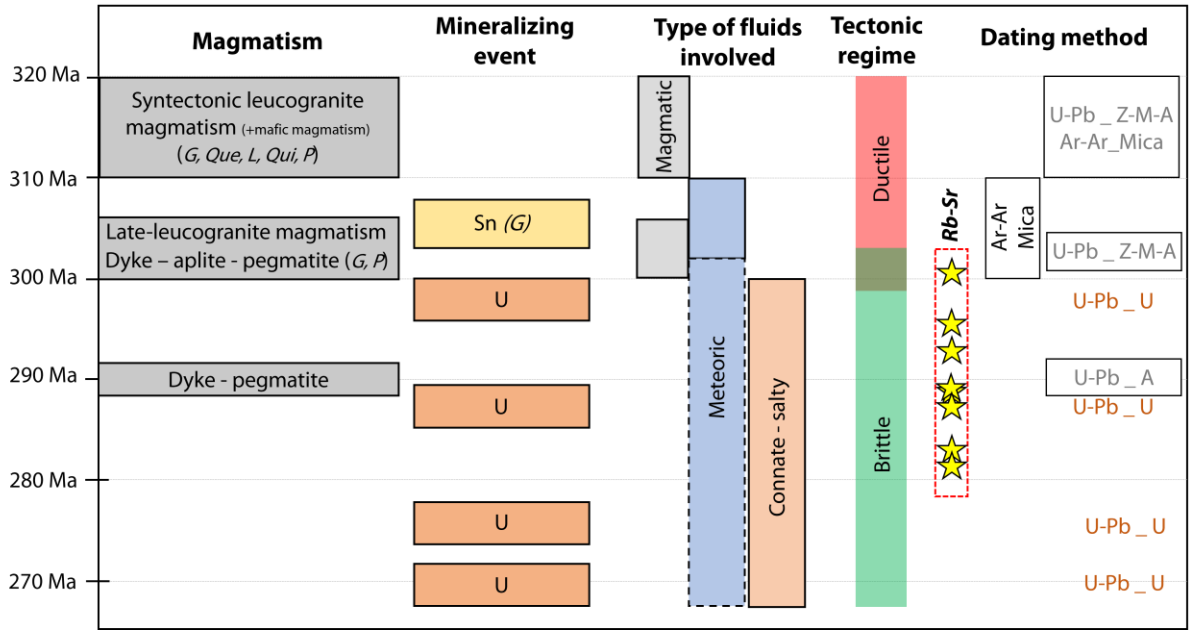

Fig. 29. Summary of the geological knowledge for the South part of the Armorican Massif (Brittany, France) during the 320-270 Ma period, with addition of the newly measured in-situ Rb-Sr ages from the Vivier outcrop (yellow stars). This summary presents the main magmatic events, the known mineralizing events and the type of metals (Sn or U), the type of fluids involved and the related tectonic regime active in the zone. The applied dating methods and selected minerals are presented to the right of the figure (Z: zircon, M: monazite, A: apatite, C: cassiterite, U: uranium oxide). G: Guérande, Que: Questembert, L: Lizio, Qui: Quiberon, P: Pontivy.

5.4. Why Rb-Sr ages give different ages than other isotopic systems for the SASZ South Armorican Domain?

The results presented in this study for the Vivier outcrop may seem surprising at first order, as Rb-Sr isochrone ages are younger to most of the ages known for this outcrop and for the South Armorican Domain. These ages are for example younger than ^{40}Ar-^{39}Ar ages measured on micas, which are commonly considered as one of the isotopic system the most sensitive in post-crystallization conditions, especially during fluid-rock interaction. As indicated above, analytical bias potentially affecting the in-situ measurements of Rb-Sr isotopic ratios can be discarded. Such apparent young Rb-Sr age are therefore linked to specific geologic conditions and processes affecting the South Armorican Domain that need to be understood. More analyses have to be done on other samples than the seven analyzed, and on different zones than the Vivier outcrop to comfort these preliminary results proposed for the evolution of this region.

It could nevertheless be considered that the range of ages for the Rb-Sr isotopic system at the Vivier outcrop is a marker of a specific event of fluid circulations and geothermometric evolutions correlated to mineralization processes of U in the South Armorican Domain that reset the Rb-Sr isotopic systems and partly the U-Pb system in apatite.

Considering the micas, ^{40}Ar-^{39}Ar and Rb-Sr systems are similar, as Sr and Ar are incompatible elements susceptible to loss by diffusion or recrystallization. ^{40}Ar-^{39}Ar are often considered as cooling ages, and closure of the Rb-Sr system is considered to occur at higher T, and therefore before, compared to K-Ar system. Some studies indicated that the closure temperature could be similar for both systems (Willingers et al., 2004) or that the closure temperature of K-Ar is even higher compared to Rb-Sr (Reiser et al., 2017). Such disconnection in age between ^{40}Ar-^{39}Ar, U-Pb and Rb-Sr in a context of regional deformation and fluid circulation processes has been previously observed in other geological contexts, but without the precision achieved in the present study. Difference in ages between Rb-Sr and U-Pb and ^{40}Ar-^{39}Ar ages were measured in the Western Domain of the Karagwe-Ankole Belt in Central Africa (Van Daele et al., 2020) as well as for western Erzgebirge, Bohemian Massif (Germany; Tichomirowa et al., 2019). For the Erzgebirge zone, most of the U-Pb ages on zircon and ^{40}Ar-^{39}Ar ages on micas are within error at ca. 315 Ma, indicating rapid cooling of the dated granites, whereas the Rb-Sr age are systematically younger of ca. 6 Ma for samples affected by late-mineralizing hydrothermal stages (Tichomirowa et al., 2019). The difference between U-Pb apatite (590-550 Ma), ^{40}Ar-^{39}Ar mica (590-570 Ma) and Rb-Sr micas (530-490 Ma) is even more important for the Karagwe-Ankole Belt.

Fluid-assisted resetting offers an explanation for the large geochronological variability on a local scale (Bosse and Villa, 2019), as viewed at the Vivier. The different isotopic systems are differently controlled by these processes, leading at the end to different ages. The mechanisms leading to a systematic rejuvenation of Rb-Sr ages compared to U-Pb and ^{40}Ar-^{39}Ar are not totally understood. No detailed explanation is proposed in the case of the Erzgebirge. An interesting approach is proposed for the Karagwe-Ankole Belt, which supports the hypothesis we supposed for the Vivier. Van Daele et al. (2020) proposed that the systematically younger ages for the Rb-Sr isotopic systems reflect a saline fluid activity know in the region at that period, and that favored recrystallization processes affecting specifically

the Rb-Sr isotopic system and not the U-Pb or ^{40}Ar-^{39}Ar. Similar thermal diffusion behavior is expected for Ar and Sr in micas (Villa, 2016), but Sr^{2+} diffusion is slower through crystal lattice than Ar due to the difference in ion size and charge. The younger Rb-Sr ages compared to ^{40}Ar-^{39}Ar ages cannot be explained by pure thermal diffusion or partial recrystallization, and a fluid-induced resetting has to be prioritized. The presence of high salinity and alkali-rich fluids could favor recrystallization process during which the Rb-Sr isotopic system is more easily disturbed than K-Ar system. This difference is based on the lower solubility of Ar in aqueous fluid with increasing salinity (Di Vincenzo et al., 2006; Jenkin et al., 2001) that lead to a higher back diffusion and retention of Ar compared to Sr. Such scenario is in agreement with the geological conditions known for the SASZ during the 320-270 Ma, with presence of salty water from 300 to 270 Ma.

In situ Rb-Sr dating reveals unnoticed events and provides additional valuable insights in sensitivity and behavior of minerals and fluids in geological systems.

6. Conclusion

The results obtained in this chapter firstly demonstrate that the application of in-situ Rb-Sr dating is a powerful approach to date complex geological case study affected by polyphased magmatic and hydrothermal activities. The precision obtained is within the range to better than other isotopic systems applied at the same scale. The precision of the Rb-Sr ages is improved in using Rb-Sr isochrons including different types of minerals (in the present case, micas, apatite, K-feldspar, plagioclase and tourmaline). Matrix effect related to major element compositions that affects the accuracy of $^{87}Rb/^{86}Sr$ ratios and correction factors from the linear regressions through the data on plots of $^{87}Rb/^{86}Sr_N$ versus SiO_2 and Al_2O_3 of the RMs were investigated, producing better precision of Rb-Sr ages by using CF compared to that by using mineral RMs. The Rb-Sr ages for the Quiberon detachment zone are globally younger than the ages obtained with other isotopic systems, whether at in-situ or mineral scale, even K-Ar. Such result was initially considered as surprising, considering that argon has been suspected to be more mobile in post-crystallization conditions than any other daughter elements in radiogenic systems. But similar results have been already obtained in other geological case studies, as

indicated by different scientific articles. The comparison of the geological conditions between the Quiberon detachment zone and these case studies points out that the late reset of the Rb-Sr isotopic system compared to K-Ar isotopic system in micas is commonly linked to late circulation of salt-rich and Ca-rich fluids in the studied geological systems. Global circulations of such type of fluids are indeed known in the Quiberon detachment zone during the 300-270 Ma period, as main drivers of formation of uranium mineralization. Our results therefore demonstrate that in-situ Rb-Sr dating is a powerful approach when coupled to other radiogenic systems to decipher discrete fluid events in polyphased geological processes.

References

Balcaen, L., (2015). Inductively coupled plasma - Tandem mass spectrometry (ICP-MS/MS): A powerful and universal tool for the interference-free determination of (ultra)trace elements - A tutorial review. *Analytica Chimica Acta 13*, 10.1016/j.aca.2015.08.053

Ballèvre, M., Bosse, V., Ducassou, C., and Pitra, P. (2009) Palaeozoic history of the Armorican Massif: Models for the tectonic evolution of the suture zones. *Comptes Rendus Geoscience*, *341,* 174–201, https://doi.org/10.1016/j.crte.2008.11.009

Ballèvre, M., Fourcade, S., Capdevila, R., Peucat, J.-J., Cocherie, A., and Fanning, C.M. (2012) Geochronology and geochemistry of Ordovician felsic volcanism in the Southern Armorican Massif (Variscan belt, France): Implications for the breakup of Gondwana. *Gondwana Research, 21*, 1019–1036, https://doi.org/10.1016/j.gr.2011.07.030

Ballèvre, M., Bosse, V., Dabard, M.-P., Ducassou, C., Fourcade, S., Paquette, J.-L., Peucat, J.-J., and Pitra, P. (2013) Histoire Géologique du massif Armoricain: Actualité de la recherche. *Bulletin de la Société Géologique et Minéralogique de Bretagne*, (D), 10-11, 5–96.

Ballouard, C., Boulvais, P., Poujol, M., Gapais, D., Yamato, P., Tartèse, R., and Cuney, M. (2015) Tectonic record, magmatic history and hydrothermal alteration in the Hercynian Guérande leucogranite, Armorican Massif, France. *Lithos*, 220–223, 1–22, https://doi.org/10.1016/j.lithos.2015.01.027

Ballouard, C., Poujol, M., Boulvais, P., and Zeh, A. (2017a) Crustal recycling and juvenile addition during lithospheric wrenching: The Pontivy-Rostrenen magmatic complex, Armorican Massif (France), Variscan belt. *Gondwana Research*, 49, 222–247, https://doi.org/10.1016/j.gr.2017.06.002

Ballouard, C., Poujol, M., Boulvais, P., Mercadier, J., Tartèse, R., Venneman, T., Deloule, E., Jolivet, M., Kéré, I., Cathelineau, M., and others (2017b) Magmatic and hydrothermal behavior of uranium in syntectonic leucogranites: The uranium mineralization associated with the Hercynian Guérande granite (Armorican Massif, France). *Ore Geology Reviews*, 80, 309–331, https://doi.org/10.1016/j.oregeorev.2016.06.034

Ballouard, C., Poujol, M., Mercadier, J., Deloule, E., Boulvais, P., Baele, J.M., Cuney, M., and Cathelineau, M. (2018) Uranium metallogenesis of the peraluminous leucogranite from the Pontivy-Rostrenen magmatic complex (French Armorican Variscan belt): the result of long-term oxidized hydrothermal alteration during strike-slip deformation. *Mineralium Deposita*, 53, 601–628, https://doi.org/10.1007/s00126-017-0761-5

Berthé, D., Choukroune, P., and Jegouzo, P. (1979) Orthogneiss, mylonite and non coaxial deformation of granites: the example of the South Armorican Shear Zone. *Journal of Structural Geology*, 1, 31–42, https://doi.org/10.1016/0191-8141(79)90019-1

Bolea-Fernandez, E., Van Malderen, S. J. M., Balcaen, L., Resano, M., & Vanhaecke, F. (2016). Laser ablation-tandem ICP-mass spectrometry (LA-ICP-MS/MS) for direct Sr isotopic analysis of solid samples with high Rb/Sr ratios. *Journal of Analytical Atomic Spectrometry*, *31*(2), 464–472. https://doi.org/10.1039/C5JA00404G

Bosse, V., Ballevre, M., and Vidal, O. (2002) Ductile Thrusting Recorded by the Garnet Isograd from Blueschist-Facies Metapelites of the Ile de Groix, Armorican Massif, France. *Journal of Petrology*, 43, 485–510, https://doi.org/10.1093/petrology/43.3.485

Bosse, V., Féraud, G., Ballèvre, M., Peucat, J.-J., and Corsini, M. (2005) Rb–Sr and $^{40}Ar/^{39}Ar$ ages in blueschists from the Ile de Groix (Armorican Massif, France): Implications for closure mechanisms in isotopic systems. *Chemical Geology*, 220, 21–45, https://doi.org/10.1016/j.chemgeo.2005.02.019

Bosse, V., & Villa, I. M. (2019). Petrochronology and hygrochronology of tectono-metamorphic events. *Gondwana Research*, *71*, 76–90. https://doi.org/10.1016/j.gr.2018.12.014

Bossiere, G. (1988) Evolutions chimico-minéralogiques du grenat et de la muscovite au voisinage de l'isograde biotite-staurotide dans un métamorphisme prograde de type barrovien: un exemple en Vendée littorale (Massif Armoricain). *Comptes rendus de l'Académie des sciences*. Série 2, Mécanique, Physique, Chimie, Sciences de l'univers, Sciences de la Terre, 306, 135–140.

Cagnard, F., Gapais, D., Brun, J.P., Gumiaux, C., and Van den Driessche, J. (2004) Late pervasive crustal-scale extension in the south Armorican Hercynian belt (Vendée, France). *Journal of Structural Geology*, 26, 435–449, https://doi.org/10.1016/j.jsg.2003.08.006

Cathelineau, M. (1981) Les Gisements Uraniferes de la Presqu'ile Guérandaise (Sud Bretagne); Approche Structurale et Metallogenique. *Mineralium Deposita*, 16, 227–240, https://doi.org/10.1007/BF00202737

Cathelineau, M., Boiron, M.C., Holliger, P., and Poty, B. (1990) Metallogenesis of the French part of the Variscan orogen. Part II: Time-space relationships between U, Au and Sn-W ore deposition and geodynamic events — mineralogical and U-Pb data. *Tectonophysics*, 177, 59–79, https://doi.org/10.1016/0040-1951(90)90274-C

Chauris, L. (1977) Les associations paragenetiques dans la metallogenie varisque du massif armoricain. *Mineralium Deposita*, 12, 353–371, https://doi.org/10.1007/BF00206172

Cuney, M., and Kyser, K. (2008) Recent and not-so-recent developments in uranium deposits and implications for exploration. *Mineralogical Association of Canada*, short course series, 39.

Cuney, M., Friedrich, M., Blumenfeld, P., Bourguignon, A., Boiron, M.C., Vigneresse, J.L., and Poty, B. (1990) Metallogenesis in the French part of the Variscan orogen. Part I: U preconcentrations in pre-Variscan and Variscan formations — a comparison with Sn, W and Au. *Tectonophysics*, 177, 39–57, https://doi.org/10.1016/0040-1951(90)90273-B

Dusséaux, C., Gébelin, A., Boulvais, P., Gardien, V., Grimes, S., and Mulch, A. (2019) Meteoric fluid-rock interaction in Variscan shear zones. *Terra Nova*, 31, 366–372, https://doi.org/10.1111/ter.12392

Dusséaux, C., Gébelin, A., Boulvais, P., Ruffet, G., Poujol, M., Cogné, N., Branquet, Y., Mottram, C., Barou, F., and Mulch, A. (2022) Timing and duration of meteoric water

infiltration in the Quiberon detachment zone (Armorican Massif, Variscan belt, France). *Journal of Structural Geology*, 156, https://doi.org/10.1016/j.jsg.2022.104546

Gapais, D. (1989) Shear structures within deformed granites: Mechanical and thermal indicators. *Geology*, 17, 1144–1147, https://doi.org/10.1130/0091-7613(1989)017<1144:SSWDGM>2.3.CO;2

Gapais, D., Lagarde, J.-L., Le Corre, C., Audren, C., Jegouzo, P., and Casas Sainz, A. (1993) La zone de cisaillement de Quiberon: témoin d'extension de la chaîne varisque en Bretagne méridionale au Carbonifère. *Comptes rendus de l'Académie des sciences*. Série 2, Mécanique, Physique, Chimie, Sciences de l'univers, Sciences de la Terre, 316, 1123–1129.

Gapais, D., Brun, J.-P., Gumiaux, C., Cagnard, F., Ruffet, G., and Veslud, C.L.C. De (2015) Extensional tectonics in the Hercynian Armorican belt (France). An overview. *Bulletin de la Société Géologique de France*, 186, 117–129, https://doi.org/10.2113/gssgfbull.186.2-3.117

Grove, M., & Harrison, T. M. (1996). 40Ar* diffusion in Fe-rich biotite. *Am. Mineral*, *81*, 940–951, https://doi.org/10.2138/am-1996-7-816

Gumiaux, C., Judenherc, S., Brun, J.-P., Gapais, D., Granet, M., and Poupinet, G. (2004a) Restoration of lithosphere-scale wrenching from integrated structural and tomographic data (Hercynian belt of western France). *Geology*, 32, 333–336, https://doi.org/10.1130/G20134.2

Gumiaux, C., Gapais, D., Brun, J.P., Chantraine, J., and Ruffet, G. (2004b) Tectonic history of the Hercynian Armorican Shear belt (Brittany, France). *Geodinamica Acta*, 17, 289–307, https://doi.org/10.3166/ga.17.289-307

Jegal, Y., Zimmermann, C., Reisberg, L., Yeghicheyan, D., Cloquet, C., Peiffert, C., et al. (n.d.). Characterisation of Reference Materials for In Situ Rb-Sr Dating by LA-ICP-MS/MS. *Geostandards and Geoanalytical Research*, https://doi.org/10.1111/ggr.12456

Jégouzo, P. (1980) The South Armorican Shear Zone. *Journal of Structural Geology*, 2, 39–47, https://doi.org/10.1016/0191-8141(80)90032-2

Jones, K.A., and Brown, M. (1990) High-temperature 'clockwise'P-T paths and melting in the development of regional migmatites: an example from southern Brittany, France. *Journal of Metamorphic Geology*, 8, 551–578, https://doi.org/10.1111/j.1525-1314.1990.tb00486.x

Le Hebel, F. (2002) Déformation continentale et histoire des fluides au cours d'un cycle subduction, exhumation, extension : exemple des porphyroïdes sud-armoricains. Rennes 1.

Le Hébel, F., Vidal, O., Kienast, J.-R., and Gapais, D. (2002) Les « Porphyroïdes » de Bretagne méridionale : une unité de HP–BT dans la chaîne hercynienne. *Comptes Rendus Geoscience*, 334, 205–211.

Lemarchand, J., Boulvais, P., Gaboriau, M., Boiron, M.-C., Tartèse, R., Cokkinos, M., Bonnet, S., and Jégouzo, P. (2012) Giant quartz vein formation and high-elevation meteoric fluid infiltration into the South Armorican Shear Zone: geological, fluid inclusion and

stable isotope evidence. *Journal of the Geological Society*, 169, 17–27, https://doi.org/10.1144/0016-76492010-186

Ludwig, K. R. (2012). Berkeley Geochronology Center Special Publication No. 5, 75.

Pandey B., Krishna V., Sastry D., Chabria T., Mary K. and Dhanaraju R. (1993) Pan-African wholerock Rb–Sr isochron ages for the granites and pegmatites of Kullampatti–Suriyamalai area, Salem District, Tamil Nadu, India. *Mass Spectrometry'IIP*, Dehra Dun, 480–482.

Tartèse, R., and Boulvais, P. (2010) Differentiation of peraluminous leucogranites "en route" to the surface. *Lithos,* 114, 353–368, https://doi.org/10.1016/j.lithos.2009.09.011

Tartèse, R., Poujol, M., Ruffet, G., Boulvais, P., Yamato, P., and Košler, J. (2011a) New U-Pb zircon and $^{40}Ar/^{39}Ar$ muscovite age constraints on the emplacement of the Lizio syn-tectonic granite (Armorican Massif, France). *Comptes Rendus Geoscience*, 343, 443–453.

Tartèse, R., Ruffet, G., Poujol, M., Boulvais, P., and Ireland, T.R. (2011b) Simultaneous resetting of the muscovite K-Ar and monazite U-Pb geochronometers: a story of fluids. *Terra Nova*, 23, 390–398, https://doi.org/10.1111/j.1365-3121.2011.01024.x

Tartèse, R., Boulvais, P., Poujol, M., Chevalier, T., Paquette, J.-L., Ireland, T.R., and Deloule, E. (2012) Mylonites of the South Armorican Shear Zone: Insights for crustal-scale fluid flow and water–rock interaction processes. *Journal of Geodynamics*, 56–57, 86–107, https://doi.org/10.1016/j.jog.2011.05.003

Tartèse, R., Boulvais, P., Poujol, M., Gloaguen, E., and Cuney, M. (2013) Uranium Mobilization from the Variscan Questembert Syntectonic Granite During Fluid-Rock Interaction at Depth. *Economic Geology*, 108, 379–386, https://doi.org/10.2113/econgeo.108.2.379

Triboulet, C., and Audren, C. (1988) Controls on P–T–t deformation path from amphibole zonation during progressive metamorphism of basic rocks (estuary of the River Vilaine, South Brittany, France). *Journal of Metamorphic Geology*, 6, 117–133, https://doi.org/10.1111/j.1525-1314.1988.tb00412.x

Turpin, L., Leroy, J.L., and Sheppard, S.M.F. (1990) Isotopic systematics (O, H, C, Sr, Nd) of superimposed barren and U-bearing hydrothermal systems in a Hercynian granite, Massif Central, France. *Chemical Geology*, 88, 85–98, https://doi.org/10.1016/0009-2541(90)90105-G

Vermeesch, P. (2018). IsoplotR: A free and open toolbox for geochronology. *Geoscience Frontiers*, *9*(5), 1479–1493. https://doi.org/10.1016/j.gsf.2018.04.001

Villa, I. M., De Bièvre, P., Holden, N. E., & Renne, P. R. (2015). IUPAC-IUGS recommendation on the half life of 87Rb. *Geochimica et Cosmochimica Acta*, *164*, 382–385. https://doi.org/10.1016/j.gca.2015.05.025

Walawender, M. J., Gastil, R. G., Clinkenbeard, J. P., McCormick, W. V., Eastman, B. G., Wernicke, R. S., et al. (1990). Chapter 1: Origin and evolution of the zoned La Posta-type plutons, eastern Peninsular Ranges batholith, southern and Baja California. In

Geological Society of America Memoirs (Vol. 174, pp. 1–18). Geological Society of America. https://doi.org/10.1130/MEM174-p1

General Conclusions

General conclusions

This PhD thesis aimed to develop in-situ Rb-Sr isotopic analysis and dating method by LA-ICP-MS/MS and SIMS and their applications to small-scale dating of geological processes. First, this thesis focused on the characterization of RMs and the establishment of their Rb-Sr isotopic values to assess as a primary RMs for calibration of in-situ Rb-Sr dating data of unknown minerals. Then, the studied RMs were applied to test the feasibility and capability of the two in-situ instruments tested at Nancy for Rb-Sr isotope measurements: LA-ICP-MS/MS and SIMS. The objectives were to optimize the analytical parameters for the two instruments, to evaluate potential analytical and matrix effects that affect the accuracy and precision of in-situ Rb-Sr isotopic data and ages, and to propose possible ways to correct them. This work was done through the use of a variety of RMs and samples of different matrices (glass, powder and mineral). Finally, the developed in-situ Rb-Sr dating approach by LA-ICP-MS/MS was applied to constrain the timing and duration of geological events based on a case study in the Quiberon detachment zone, Armorican Massif, France. This case study was selected due to the availability of detailed geological knowledge and a detailed geochronological framework. Several minerals were targeted for Rb-Sr applications (micas, feldspars, apatite, tourmaline) from undeformed and deformed leucogranites and associated dykes.

The following conclusions highlight the main outcomes of this PhD thesis and suggestion for future perspectives.

In the **first chapter**, a description of the LA-ICP-MS/MS and SIMS instrumentations along with the pioneering works of in-situ Rb-Sr isotopic analyses by LA-ICP-MS/MS and Sr isotopic analyses by SIMS were provided. To optimize the analytical conditions and operating parameters of LA-ICP-MS/MS in-situ Rb-Sr isotopic analysis, various parameters for LA system and ICP-MS/MS were assessed and evaluated during the tuning process and/or the analyses. Reaction gases O_2, N_2O and SF_6 have been tested, and N_2O was chosen based on its higher reactivity compared to other gases, confirming the results of previous studies. Better precision and accuracy of $^{87}Sr/^{86}Sr$ and $^{87}Rb/^{86}Sr$ ratios of the tested RMs (NIST 610, BCR-2G, Mica-Mg) were obtained by using the RF power at 1550 W, a wire smoothing device, detector dead time at 35 ns and dwell time of SrO^+ at 120 ms. Then, the LA-ICP-MS/MS measurements were performed with these optimized conditions to assess mass bias correction strategies

(internal, external and double corrections) of Sr isotopic ratios using RMs with a wide range of Sr contents (27.1-1650 μg g^{-1}; NIST 610, BCR-2G, Mica-Mg, MAD). It has been reported that mass discrimination corrections also affect on the precision and accuracy of the data. The results show that P/A factor calibration influences on the precision and accuracy of Sr isotopic data for samples with high Sr contents as $^{88}Sr^{16}O$ and $^{86}Sr^{16}O$ were detected in M (mixed) and P modes, respectively, resulting in its highly biased $^{87}Sr/^{86}Sr$ ratios by internal correction. External correction using NIST 610 enables to determine accurate and precise $^{87}Sr/^{86}Sr$ ratios in all investigated RMs and to avoid P/A factor issues. SIMS analyses of mica and feldspar RMs (Mica-Mg, Mica-Fe, FK-N) have been conducted to test its capability and feasibility for in-situ Rb-Sr isotope measurements. The results show that the interferences of $FeSi^+$ (mass 84, 86, 87, 88) on Sr isotopes was detected in mica RMs, which contain high Fe concentrations. These interferences could not be resolved by its maximum mass resolving power (MRP) of 40,000. The results of SIMS analysis indicate that FeSi interferences on Sr isotopes contents limit accurate Sr isotope measurements by SIMS for samples which contain Fe contents such as micas.

In **chapter 2**, four SARM RMs, including phlogopite Mica-Mg, biotite Mica-Fe, glauconite GL-O and potash feldspar FK-N, were characterized as potential reference materials for in-situ Rb-Sr isotope measurements. Indeed, one of the main obstacles for in-situ Rb-Sr dating method was a lack of appropriate RMs for high Rb mineral samples that are homogeneous and well characterized with precise $^{87}Rb/^{86}Sr$ and $^{87}Sr/^{86}Sr$ ratios. In this chapter, the four CRPG RMs were investigated in the form of grains and powder, and their isotopic compositions were measured by TIMS and MC-ICPMS after dissolution and purification. Selected grains from the investigated RMs present variable degrees of heterogeneity with chemical variation and/or inclusions observed by SEM-EDS and EPMA imaging, and chemical mapping. The mean $^{87}Rb/^{86}Sr$ and $^{87}Sr/^{86}Sr$ and their associated uncertainties of the four RMs were determined by isotope dilution TIMS and MC-ICP-MS as the mean $^{87}Rb/^{86}Sr$ ratios are 155.6 ± 4.7% (2s, as for other RMs) for Mica-Mg, 1815 ± 14% for Mica-Fe, 36.2 ± 11% for GL-O and 69.9 ± 5.9% for FK-N and the mean $^{87}Sr/^{86}Sr$ ratios are 1.8622 ± 0.36% (2s, as for other RMs) for Mica-Mg, 7.99 ± 13% for Mica-Fe, 0.75305 ± 0.12% for GL-O, and 1.2114 ± 0.17% for FK-N. The RMs present Rb/Sr isotopic heterogeneity, which potentially needs to be tested by LA-ICP-MS/MS for their use as calibration materials. The most

heterogeneous RMs are GL-O and Mica-Fe and acquired Rb-Sr isotopic results of Mica-Fe yielded unreliable Rb-Sr ages. Based on the Rb/Sr uncertainty and degree of homogeneity, Mica-Mg and FK-N are recommended as best RMs among the investigated RMs for calibration of in-situ $^{87}Rb/^{86}Sr$ data of micas and feldspars, respectively.

In the **chapter 3**, potential factors that influence on the accuracy and precision of Rb-Sr isotopic data and ages by in-situ LA-ICP-MS/MS approach were investigated based on the measured Rb-Sr isotopic data of various matrix RMs and samples. The measured $^{87}Rb/^{86}Sr$ data offsets of the RMs calibrated using NIST 610 relative to published data show a relatively strong correlation with major compositions of the RMs by yielding linear regressions with positive (for Al_2O_3, FeO, MgO and K_2O) or negative (for SiO_2, Na_2O and CaO) slopes, while the relations of the offsets with Rb-Sr compositions and ablation properties (i.e., down-hole fractionation, ablation pit volume) display no correlations. The accuracy of Rb-Sr isotopic ratios and ages could be improved by using the matrix-matched mineral RMs such as Mica-Mg for mica samples. However, there was a limitation of the external calibration using the investigated mineral RMs due to its heterogeneity and high uncertainties of $^{87}Rb/^{86}Sr$ ratios reported in the previous **chapter 2**. Therefore, alternative approaches using non-matrix matched RMs such as NIST 610 or RMs with similar major element compositions to unknown samples were proposed for enhancing the precision of in-situ Rb/Sr isotopic data and ages. The correction procedure of $^{87}Rb/^{86}Sr$ ratio calibrated using NIST 610 using correction factors calculated from major element compositions (i.e., Al_2O_3 and SiO_2) of samples and slope and intercept of the linear regressions was applied to data acquired for the mineral RMs and samples. This correction produced better precision of Rb/Sr data and ages than approaches using the mineral RMs. Finally, a recommended procedure of Rb-Sr isotope measurements by LA-ICP-MS/MS was proposed.

In the last **chapter 4**, the newly developed approaches were applied to determine the ages and duration of polyphase magmatic-hydrothermal processes. The Quiberon detachment zone (Brittany, France) was targeted, based on the previous studies done for understanding its evolution by using petrographical observations, geochemical and geochronological approaches with various isotopic systems. Representative rock samples of leucogranite and associated dykes were collected from the Vivier outcrops in the Quiberon peninsula that records geological processes active during the development of the detachment zone linked to the South

Armorican Shear Zone during the Carboniferous and Permian. In-situ Rb-Sr analysis was conducted on multiple phases of micas, feldspars, apatite and tourmaline hosted in these samples. The established in-situ Rb-Sr dating approach provides Rb-Sr globally younger than the ages obtained with other isotopic systems. The late reset of the Rb-Sr isotopic system is probably linked to late circulation of salt-rich and Ca-rich fluids. The circulations of such type of fluids are indeed known in the Quiberon detachment zone during the 300-270 Ma period, as main driver of formation of uranium mineralization. Our results therefore demonstrate that in-situ Rb-Sr dating is a powerful approach when coupled to other radiogenic systems to decipher discrete fluid events in polyphased geological processes.

Through this PhD thesis work, the in-situ Rb-Sr dating approaches by LA-ICP-MS/MS have been established at GeoRessources Nancy and could be applied in the future to numerous geological case studies. Furthermore, our measured $^{87}Sr/^{86}Sr$ and $^{87}Rb/^{86}Sr$ values and related uncertainties for the four tested RMs are recommended to use for in-situ Rb-Sr dating by LA-ICP-MS/MS of unknown samples. For future work, the development of mineral RMs for calibration of high Rb-minerals which display Rb/Sr isotopic homogeneity with low uncertainty, determined by isotope dilution methods, is still required. We also suggest ID-TIMS and MC-ICP-MS measurements of Rb-Sr isotope compositions of such RMs to be done directly on the nano-powders to minimize analytical uncertainties and limitations, derived from the degree of homogenization of the materials, or on fused glasses. In case of using fused glasses of such mineral RMs, further investigation is needed to test their Rb/Sr isotopic homogeneity at micro-scale level for in-situ method and to consider possible volatilization effects between Rb and Sr (Rb being more volatile) on Rb/Sr isotopic homogeneity. In-situ Sr isotopic measurements via SIMS is promising for mineral phases which contain Sr and do not contain Fe, such as feldspars or apatites. SIMS analysis yields better precision of Sr isotopic ratios relative to LA-ICP-MS/MS analysis. Therefore, coupling the two in-situ methods ‘LA-ICP-MS/MS’ and ‘SIMS’ for Rb-Sr isotope measurements can lead to a wide range of Rb-Sr dating and Sr isotopic tracing applications, with improved precision and accuracy of Rb-Sr isotopic data and ages in order to investigate complex geological processes, duration and timing of deposition processes in mineral and ore deposits.

List of Figures

List of Tables